Micromechanics of the Annulus Fibrosus: Role of Biomolecules in Mechanical Function

A Thesis

Submitted to the Faculty

of

Drexel University

by

Jessica Lauren Isaacs

in partial fulfillment of the

requirements for the degree

of

Doctor of Philosophy

May 2012

DEDICATIONS

I dedicate this work to my grandparents: to Barbara Isaacs, who still to this day can remember the first few words she typed of my grandfather's thesis, who always picks up the phone on my walk home from the train, and who gives me the most sound and helpful advice; to Milton Anger, who has called me "Dr. Jess" for as long as I can remember and gave me the strength and drive to work for that title; and to the memory of Dr. Peter Isaacs ז״ל and Helène Anger ז״ל.

ACKNOWLEDGEMENTS

I would like to first and foremost thank my supervisor, Dr. Michele Marcolongo, who has supported me during my years at Drexel. She has provided me with countless opportunities, and has helped prepare me for my future career. Dr. Marcolongo has also provided me with encouragement and always had the utmost faith in my abilities as a researcher and engineer.

I would like to thank Dr. Antonios Zavaliangos, a committee member, for sharing his depth of knowledge in finite element modeling and also being an ear to voice my frustrations that go along with any project, and to Dr. Ed Vresilovic, another committee member, for the many great conversations we have had about the clinical implications of our work. Special thanks to the rest of my committee members, Dr. Alan Lau and Dr. Tein-Min for your time and thoughtful guidance. And thank you to Dr. Richard Knight for always being there for a friendly hello every morning.

I would like to acknowledge the biomaterials laboratory at Drexel University, most notably Dr. Marco Cannella, Dr. Sandeep Gidvani and Dana Bonfiglio for all their work on this project. I would like to thank honorary lab member, Valerie Binetti for always smiling during our countless experiment hours, even when breaking equipment. To all the friends I have made at Drexel, in particular, Amanda Levinson, who encouraged me, listened to me complain, ate countless lunches with me and continue to share their friendship.

I especially need to acknowledge my family. To my siblings, Daniel and Alison, thank you for understanding when I was too busy or too tired to talk, for our games of Times Up, for always responding positively to every text, email, or paper I sent – even

when not understanding what they meant. To my fiancé, Zachary, thank you for knowing when all I need is a good restaurant and a few movies to get my mind off of work. After surviving your Bar Exam and my thesis, I know we can get through anything life may throw at us. Mom and Dad, I do not know where to begin. Words can never express how important you have been in making this work come to fruition. You both kept me sane during the hectic schedules, kept me fed when I would work late, and brought me back to reality when I couldn't see the finish line; your unconditional love and support are the reason that I was successful in graduate school.

TABLE OF CONTENTS

LIST OF TABLES viii

LIST OF FIGURES xii

ABSTRACT xxii

1. CHAPTER ONE: INTRODUCTION 1

2. CHAPTER TWO: BACKGROUND AND LITERATURE SURVEY 3

2.1. Anatomy of the Spine 3

2.2. Intervertebral Disc 5

2.2.1. Nucleus Pulposus 6

2.2.2. Annulus Fibrosus 6

2.2.2.1. Annular Lamellae 7

2.2.2.2. Collagen 7

2.2.2.3. Proteoglycan 8

2.2.2.4. Elastin 9

2.2.2.5. Cells of the Annulus Fibrosus 10

2.3. Loading of the Intervertebral Disc 18

2.3.1. Behavior of Soft Tissues under Loading 22

2.3.1.1. Viscoelasticity 22

2.3.1.2. Preconditioning 23

2.3.1.3. Large Deformation 23

2.4. Mechanical Properties of the Annulus Fibrosus 27

2.4.1. Lamellar Mechanics 28

2.4.1.1. Inter-lamellar Shear Strength 31

2.5. Intervertebral Disc Degeneration 41

2.5.1. Biochemical Changes Associated with Degeneration 42

2.5.2. Mechanical Changes Associated with Degeneration 43

2.5.3. Annular Tears 46
2.5.4. Intervertebral Disc Disruption and Herniation 47
2.6. Fiber Reinforced Composite Materials 54
2.6.1. Physical Properties 56
2.6.2. Failure Mechanisms 57
2.6.2.1. Fiber-Matrix Debonding 59
2.6.2.2. Matrix Micro-cracking 60
2.6.2.3. Delamination 60
2.6.3. Use of Composite Analysis in Annular Mechanics 61
2.7. Summary 62
3. CHAPTER THREE: OBJECTIVE AND SPECIFIC AIMS 70
4. CHAPTER FOUR CHARACTERIZATION OF ANNULUS FIBROSUS MIRCOMECHANICS 72
4.1. Introduction 72
4.2. Materials and Methods 75
4.2.1. Specimen Preparation 75
4.2.2. Mechanical Testing 77
4.2.3. Data Analysis 77
4.2.4. Failure Criteria for Fiber Reinforced Composites 78
4.3. Results 80
4.3.1. Intra-lamellar Samples 80
4.3.2. Inter-lamellar Samples 81
4.3.3. Failure Envelopes 82
4.4. Discussion 82
4.5. Conclusions 89
5. CHAPTER FIVE: ROLE OF BIOMOLECULES ON ANNULUS FIBROSUS MECHANICS: EFFECT OF ENZYMATIC DIGESTION ON MICROMECHANICS 102

5.1. Introduction 102
5.2. Materials and Methods 104
5.2.1. Specimen Preparation 104
5.2.2. Enzymatic Digestion 105
5.2.3. Mechanical Testing 106
5.2.4. Data Analysis 107
5.3. Results 108
5.4. Discussion 110
5.5. Conclusions 115
6. CHAPTER SIX: TOWARD A PREDICTIVE MODEL FOR ANNULAR FAILURE 125
6.1. Introduction 125
6.1.1. Lamination Theory Assumptions 128
6.2. Lamina Analysis 129
6.2.1. Mechanical Response of Lamina 130
6.2.2. Orthotropic Restrictions on Engineering Constants 132
6.2.3. Plane Stress Analysis 133
6.3. Laminate Analysis 140
6.3.1. Mechanical Response of Laminated Composite 141
6.3.2. Determination of Laminate Engineering Constants 144
6.3.2.1. Symmetric Laminate 144
6.3.2.2. Symmetric Angle-Ply Laminate 145
6.3.2.3. Antisymmetric Angle-Ply Laminate 146
6.3.3. Comparison to Lamina Data 149
6.3.4. Comparison to Literature 151
6.4. Strains and Stresses through Laminate 166
6.4.1. Symmetric Angle-Ply Laminate 167

6.4.2. Antisymmetric Angle-Ply Laminate 168
6.4.3. Digested Angle-Ply Laminate 169
6.5. Laminate Failure 178
6.5.1. Determination of Shear Strength for Lamina 179
6.5.1.1. Alternate Method for Calculation of Shear Strength 180
6.5.2. Failure Envelope 181
6.5.3. Sensitivity Analysis 183
6.6. Conclusions 193
7. CHAPTER SEVEN: CONCLUSIONS 196
7.1. Summary 196
7.1.1. Experimental Annular Mechanics 196
7.1.2. Laminated Annular Model 198
7.2. Novel Contributions 200
7.3. Future Work and Recommendations 201
APPENDIX A: LabVIEW Programs 207
APPENDIX B: Matlab Programs 214
APPENDIX C: Raw Data 219
LIST OF REFERENCES 236

LIST OF TABLES

Table 2.1: Average thickness (mean ± standard deviation) of annular lamellae from experimental data of L2-L3 and L4-L5 by Marchand and Ahmed (1990). Adapted from [14]. 16

Table 2.2: Average number of lamellae (mean ± standard deviation) from experimental data by Marchand and Ahmed (1990). Adapted from [14]. 16

Table 2.3: Collagen types in the intervertebral disc. Adapted from [26]. 17

Table 2.4: Approximate formulas for calculation of load experienced by intervertebral disc based on body weight of the individual. From [63]. 26

Table 2.5: Failure stresses and strains of single lamellae annular specimens by anatomic region (Mean ± SD) reprinted from Skaggs et al. [73]. 38

Table 2.6: Elastic tensile modulus of single lamellae annular specimens by anatomic region (Mean ± SD) reprinted from Skaggs et al. [73]. 38

Table 2.7: Elastic moduli of single lamellar AF specimens at locations ventro-lateral external (VLe), ventro-lateral internal (VLi), dorsal external (De), and dorsal internal (Di) tested with a crosshead speed of 1 mm/min. Adapted from [35]..... 38

Table 2.8: Tensile radial properties as a function of annular region (mean ± standard deviation) from Fujita et al. (1997) study). Adapted from [86]. 39

Table 2.9: Shear moduli for cube specimens (kPa, mean ± standard deviation) in study performed by Fujita et al. (2000). G_{31} is greater than G_{12}, $p = 0.01$. Adapted from [88]. 40

Table 2.10: Shear moduli for sheet specimens (kPa, mean ± standard deviation) in study performed by Fujita et al. (2000). Adapted from [88]. 40

Table 2.11: Typical matrix properties. Reproduced from [131]. 69

Table 2.12: Single ply material properties used for the lamination model by Iatridis and Gwynn (2004). Adapted from [96]. 69

Table 4.1: Intervertebral disc sample information. Intra-laminar specimens are defined to be a single annular laminar and the inter-laminar specimens are cut across the lamellae; sample preparation of samples is dependent on orientation. 100

Table 4.2: Properties of the annulus fibrosus (thickness = 150 μm) in four directions (n = 10 each): longitudinal, transverse, circumferential and radial. 100

Table 4.3: Summary of previous studies that quantified mechanical properties (σ_f = failure stress, ε_f = failure strain, E = elastic moduli, ν = Poisson's ratio) of the annulus fibrosus for the longitudinal and radial directions compared to our experimental data. Mean (Standard Deviation). 101

Table 5.1: Intervertebral disc information. 124

Table 5.2: Annular sample's group-specific buffer and enzyme assignments for digestion protocol. 124

Table 6.1: Summary of strain energy function techniques from studies used to model the AF. 138

Table 6.2: Engineering properties for individual lamina of the AF to be used for composite modeling purposes. The elastic moduli are taken in the linear range of the stress-strain relationship ($E_{75\%}$). 139

Table 6.3: Calculated shear modulus (12-direction) and Poisson's ratio (21-direction) for groups. Digested shear modulus from reduction of PBS value and digested Poisson's ratio from symmetry. [a]From [96], [b]Experimental. 139

Table 6.4: Terms of reduced stiffness matrix for experimental sample groups. 139

Table 6.5: Transformed reduced stiffness matrix for sample groups when $\theta = \pm 60°$. The terms are the same for both, only $\boldsymbol{Q16}$ and $\boldsymbol{Q26}$ change signs. 139

Table 6.6: Calculated engineering constants for AF laminate when modeled as symmetric laminate. X- and y-directions correspond to axial and circumferential, respectively. ... 162

Table 6.7: Properties of one-phase association fit, $\boldsymbol{y = Yo + P - Yo1 - e - k \cdot x}$, to engineering constants versus number of layers for a symmetric angle-ply laminate (control, Figure 6.10). 162

Table 6.8: Properties of one-phase association fit to engineering constants for an antisymmetric angle-ply laminate versus number of layers (control, Figure 6.12). 162

Table 6.9: Properties of one-phase association fit to engineering constants for an angle-ply laminate versus number of layers (control, Figure 6.14). 163

Table 6.10: Comparison of calculated in-plane engineering constants for AF model to literature data (control). 164

Table 6.11: Comparison of plateau value of calculated digested laminate elastic modulus, Ey, for AF model to experimental data (circumferential E_{LIN}). 165

Table 6.12: Calculation of stresses when biaxial stress resultant Nx = Ny = 10 N/mm applied to a symmetric 19 layer angle ply laminate. 176

Table 6.13: Calculation of stresses when biaxial stress resultant Nx = Ny = 10 N/mm applied to an antisymmetric 20 layer angle ply laminate. 177

Table 6.14: Calculated shear strengths for all digestion groups. 190

Table 6.15: Calculated shear modulus and corresponding shear strength using alternate method for all digestion groups. 191

Table 6.16: Comparison of laminate engineering constants for control sample for shear modulus value taken from literature [226] and value calculated from the shear strength of ±θ lamina being equal. 192

Table 0.1: Raw Data for intralaminar control specimens for chapter 4. 219

Table 0.2: Raw Data for interlaminar control specimens for chapter 4. 220

Table 0.3: Raw Data for longitudinal digested specimens in chapter 5..... 221

Table 0.4: Raw Data for transverse digested specimens in chapter 5..... 222

Table 0.5: Raw Data for circumferential digested specimens in chapter 5 223

Table 0.6: Raw Data for circumferential digested specimens in chapter 5 224

LIST OF FIGURES

Figure 2.1: Representative lumbar vertebrae consisting of (1) vertebral body, (2) foramen, (3) lamina, (4) pedicle, (5) spinous process, (6) superior articular process and (7) transverse process. Adapted from http://www.spineuniverse.com/anatomy/vertebral-column..... 4

Figure 2.2: Schematic of the intervertebral disc (IVD) with superior and inferior vertebral bodies. The IVD consists of three main parts: an outer annulus fibrosus surrounding an inner nucleus pulposus, with two endplates acting as buffers to the vertebrae. Reprinted from [20]. 4

Figure 2.3: A cut out portion of a normal intervertebral disc. Note the lamellar architecture of Annulus Fibrosis. Reprinted from [20]..... 12

Figure 2.4: Drawing of the annulus fibrosus with the nucleus pulposus removed. The collagen fibers are arranged in multiple concentric layers (lamellae) with consecutive rings running in alternating directions with an orientation of θ degrees. Reprinted from [60]. 12

Figure 2.5: Schematic of the intervertebral disc structure showing the regional variances in composition. Reprinted from [20]. 13

Figure 2.6: The bottle brush structure of Aggrecan, the most abundant proteoglycan in the IVD with the chemical structure of chondroitin sulfate. Reprinted from [61]. 14

Figure 2.7: Schematic view of the elastic network of the bovine tail disc. (a) Transverse section. (b) Sagittal section. Reprinted from [53]. 15

Figure 2.8: Cell morphology of the annulus fibrosus. The outer annulus is characterized by cells with a fusiform cell body and a gradual transition in process architecture, while the inner annulus consists of cells with a spherical morphology. Reprinted from [32].... 15

Figure 2.9: A comparison of the relative pressure (or load) change at different positions between a study by Nachemson (1966) and a follow-up study by Wilke et al. (1999).

Both studies compared above were performed on a 70 kg male participant. It is important to note that the Nachemson study used a 10 kg weight, while the Wilke et al. study used a 20 kg weight. Reprinted from [66]. 25

Figure 2.10: Typical stress/strain response obtained from a sample stretched in the aligned direction using continuous loading (A-B) In phase crimp progressively straightened (B) Isolated bundle sliding within intact arrays (B-C) Progressive increase in bundle sliding and separation throughout array (C) Beginning of reduced stress region from large-scale separation of fiber bundles. Adapted from [85]..... 33

Figure 2.11: The matrix in A is subjected to progressive transverse stretching in B to D to reveal an extensive interconnecting structure in the cleft region marked W. Adapted from [85]. 34

Figure 2.12: (a) Axial section of samples with four single lamellar specimens from the ventro-lateral external (VLe), ventro-lateral internal (VLi), dorsal external (De), dorsal internal (Di) regions used by Holzapfel et al. (b) Schematic diagram for a specimen from the VLe, VLi, De, or Di region. (c) Cyclic engineering stress–stretch responses of four single lamellar AF specimens for a crosshead speed of 1 mm/min. Adapted from [35].. 35

Figure 2.13: Schematic illustration of the dissection and preparation of radial tensile specimens in Fujita et al. (1997) study. Reprinted from [86]. 35

Figure 2.14: Orientation of cube specimens in order to determine shear modulus in study performed by Fujita et al. (2000). The shear moduli were measured in the plane: perpendicular to the annular lamella and parallel to the horizontal plane ($G12$), perpendicular to the annular lamella and parallel to the vertical axis of the spine ($G23$) and of the annular lamella ($G31$). Reprinted from [88]. 36

Figure 2.15: Orientation of sheet specimens in order to determine shear modulus in study performed by Fujita et al. (2000). For axial shear (G_{31}) the circumferential axis was aligned with the tensile strain (T) while the shear deformation (τ) was applied in the anatomic axial direction. For circumferential shear (G_{13}) the anatomic inferior–superior

axis of the specimen was aligned with tensile strain and the shear deformation was applied in the anatomic circumferential direction. Reprinted from [88]. 37

Figure 2.16: Changes in the major macromolecule concentrations (collagen, proteoglycan, and elastin) in the IVD with aging: annulus fibrosus (top) and nucleus pulposus (bottom). Adapted from [98-100, 121]. 49

Figure 2.17: Left: Schematic representation of specimen harvest sites in the anterolateral and posterolateral quadrants of the annulus fibrosus in Smith et al. (2008) study. Right: Image of sandpaper mounting frame with specimen prior to assembly and testing. G = gauge region; dotted lines = cutting zones following placement in the mechanical testing system grips. Reprinted from [106]. 50

Figure 2.18: Results of tensile testing study of radial samples of annulus fibrosus by Smith et al. Initial modulus, ultimate modulus, and extensibility before and after (a) elastase treatment and (b) chondroitinase ABC treatment. * Indicates significant difference between control and treatment, $p < 0.001$. Reprinted from [106]. 50

Figure 2.19: Left: Schematic representation of specimens of the annulus fibrosus in Jacobs et al. (2011) study where, $G_{r\theta}$ = radial shear modulus and $G_{\theta z}$ = circumferential shear modulus, and z = spine axial direction Right: (A) Shear testing device (B) Schematic illustration of boundary conditions (C) Schematic illustration of the shear deformation when the intervertebral disc is subjected to torsion. Reprinted from [107]. 51

Figure 2.20: Shear modulus of annulus fibrosus in Jacobs et al. (2011) study. (A) Untreated; ∗significant radial, ∗∗significant radial and 2% circ (B) treated Radial; ∗significant untreated (C) Cirum untreated vs PBS (D) treated circumferential. ∗significant to same group at 2% pre-strain. Adapted from [107]. 51

Figure 2.21: Three types of annular tears: (A) circumferential or delamination, (B) radial, (C) peripheral rim lesion. Reprinted from [122]..... 52

Figure 2.22: Representative drawing of a herniated disc. © 2011 Nucleus Medical Media, Inc. Reprinted from http://www.aurorahealthcare.org/yourhealth/healthgate/images/FX00004.jpg. 53

Figure 2.23: Schematic diagram of microstructures for short fiber CMs. The middle microstructure is representative of chopped strand mat (CSM) and sheet molding compound. The bottom microstructure is typical of injection molded parts where the fiber orientation varies through the thickness of the part due to the flow process. Reprinted from [124]. 63

Figure 2.24: Fatigue-life diagram for unidirectional CM under transverse loading. Reprinted from [129]. 64

Figure 2.25: Failure mechanisms in a unidirectional fiber composite. Reprinted from [128]. 65

Figure 2.26: Typical delamination phenomena: (a) free-edge delamination; (b) buckling-induced delamination; and (c) impact induced delamination. Reprinted from [130]. 66

Figure 2.27: (a) Schematic of fiber-reinforced laminate representation of the annulus fibrosus : axial stress (sx), in-plane shear stress (txy). (b) Schematic representation of cross section of the eight layer annulus layup 67

Figure 2.28: Stresses through the z-direction (radial) of annular layers when subjected to 10% strain in the x-direction (circumferential). AF modeled as an eight layer angle-ply laminate and 39° fiber angle. (a) Global coordinate system: x-direction (σ_x), y-direction (axial, σ_y), and xy-direction (txy, in-plane shear). (b) Material coordinate system: longitudinal direction (σ_1), transverse direction (σ_2) and for in-plane shear (τ_{12}). Reprinted from [96]. 67

Figure 2.29: Interlaminar shear stresses eight-layer angle-ply laminate (red circle) and four-layer angle-ply laminate (black square) with same thickness and 39° fiber angle. Reprinted from [96]. 68

Figure 4.1: Samples were prepared in two orientations by making either intra-lamellar or inter-lamellar cuts, relating to within a single annulus laminar slice or across lamella. The annular slices (thickness = 150 μm) are then further divided into four groups to be tested in the following directions: longitudinal, transverse, circumferential and radial. 91

Figure 4.2: Custom micro-tensile tester consisting of: a) testing stage and grips (MTI Instruments Inc., Albany, NY); b) 500 g tension/compression miniature load cell (Cooper Instruments & Systems, Warrenton, VA); c) webcam (Logitech, Fremont, CA) affixed to a stereo zoom microscope (LW Scientific, Atlanta, GA); d) power source (Ernest FF. Fullam Inc., Latham, NY); and e) signal conditioning amplifier System (Vishay Precision Group, Raleigh, NC). 92

Figure 4.3: Representative images captured from webcam (Logitech, Fremont, CA) affixed to a stereo zoom microscope (LW Scientific, Atlanta, GA) during axial loading in four directions: longitudinal, transverse, circumferential, and radial. 93

Figure 4.4: Representative stress-strain curve of an annular sample oriented in the longitudinal direction from the control digestion group (1x PBS) illustrating the failure stress (σ_f), failure strain (ε_f), elastic moduli at three locations (25%, 50%, and 75% of failure strain). Experimental results are shown with a best-fit cubic curve: $\sigma = 0.13 - 5.17\varepsilon + 114\varepsilon^2 - 148\varepsilon^3$. 94

Figure 4.5: Representative stress-strain relationships for annular samples oriented in the a) longitudinal, b) transverse, c) circumferential and d) radial directions. Experimental results are shown with a third-order polynomial best-fit cubic curve. 95

Figure 4.6: (A) Ultimate tensile strength (stress at failure) and (B) failure strain for the annulus fibrosus in four orientations: longitudinal, transverse, circumferential and radial. (* $p < 0.01$). 96

Figure 4.7: Elastic tensile modulus for the annulus fibrosus at three locations (25%-, 50%-, and 75%-failure strain) in four orientations: longitudinal, transverse, circumferential and radial. (* $p < 0.01$; ns = no significance). 97

Figure 4.8: Poisson's ratio for the annulus fibrosus in four orientations: longitudinal, transverse, circumferential and radial. (* $p < 0.01$)..... 98

Figure 4.9: Failure envelopes for annulus fibrosus orientation: a) intra-lamellae and b) inter-lamellae. Three failure criteria are compared: Maximum stress and maximum strain (limit criteria) and Tsai-Hill (interactive criterion)..... 99

Figure 5.1: Sample testing orientation. 116

Figure 5.2: Effect of buffer on mechanical properties. 117

Figure 5.4: Representative stress-strain relationships for annular samples oriented in the a) longitudinal, b) transverse, c) circumferential and d) radial directions. Experimental results are shown with a third-order polynomial best-fit cubic curve. 118

Figure 5.5: Effect of enzymatic digestion on the micromechanical properties of annular samples oriented in the longitudinal direction. (* $p < 0.05$ from control). 119

Figure 5.6: Effect of enzymatic digestion on the Poisson's ratio of annular samples oriented in the longitudinal direction: physical representative of expansion in longitudinal direction and contraction in the transverse (* $p < 0.05$ from control). 120

Figure 5.7: Effect of enzymatic digestion on the micromechanical properties of annular samples oriented in the transverse direction. (* $p < 0.05$ from control). 121

Figure 5.8: Effect of enzymatic digestion on the micromechanical properties of annular samples oriented in the radial direction. (* $p < 0.05$ from control). 122

Figure 5.9: Effect of enzymatic digestion on the micromechanical properties of annular samples oriented in the circumferential direction. (* $p < 0.05$ from control). 123

Figure 6.1: Coordinate system for lamina analysis: 1-2, principle coordinate system; x-y, off axis (global) coordinate system. Reprinted from [162]..... 130

Figure 6.2: Schematic of unidirectional fiber reinforced lamina. Reprinted from [162].136

Figure 6.3: Physical significant of compliance matrix in the anisotropic strain-stress relationship. Reprinted from [148]. 136

Figure 6.4: Above: Variations of terms of transformed reduced stiffness matrix, $\boldsymbol{Q}$, due to theta for AF lamina. Below: Zoomed in to theta = 60 ± 10 degrees..... 137

Figure 6.5: Laminate coordinate system: *x*, *y*, *z*..... 140

Figure 6.6: Laminate nomenclature. Reprinted from [223]. 154

Figure 6.7: Position directions for stress and moment resultants. Reprinted from [225]. 154

Figure 6.8: Physical significance of terms in A, B, and D matrices. Adapted from http://www.aac-research.at/downloads/Formula-collection-for-laminates.pdf 155

Figure 6.9: Three types of laminates, from left to right: symmetric (N = even), angle-ply symmetric (N = odd) and angle-ply antisymmetric (N = even). The lamina directions alter between layers from -60° (red) to +60° (blue)..... 155

Figure 6.10: Moduli (top) and Poisson's ratios (bottom) of a symmetric angle-ply laminate as a function of the number of layers for the PBS (control) samples. Values fit with one-phase association curve. ● E_x, ■ E_y, ▲ G_{xy}., ● ν_{xy} , ■ ν_{yx}. 156

Figure 6.11: a) Elastic moduli b) shear modulus and c) Poisson's ratios of a symmetric angle-ply laminate as a function of the number of layers for all sample groups: PBS, COL, ELA, and PG. Values fit with one-phase association curve. 157

Figure 6.12: Moduli (top) and Poisson's ratios (bottom) of an antisymmetric angle-ply laminate as a function of the number of layers for the PBS (control) samples. Values fit with one-phase association curve..... 158

Figure 6.13: a) Elastic moduli b) shear modulus and c) Poisson's ratios of a symmetric angle-ply laminate as a function of the number of layers for all sample groups: PBS, COL, ELA, and PG. Values fit with one-phase association curve. 159

Figure 6.14: Moduli (left) and Poisson's ratios (left) of an angle-ply laminate as a function of the number of layers for the PBS (control) samples. Values fit with one-phase association curve. 160

Figure 6.15: Modeled laminate properties (top – moduli, bottom – Poisson's ratios) are dependent on the shear modulus of the lamina, G_{12}. AF modeled as 19-layer symmetric angle ply laminate. 160

Figure 6.16: Modeled laminate circumferential modulus, Ey, is dependent on the angle of the collagen fibers, theta. AF modeled as 19-layer symmetric angle ply laminate with G_{12} = 0.3 MPa; θ = 60° depicted in red, lower than experimental. Solving for theta with experimental Ey = 11.04 ± 2.24 MPa yields θ = 71.1 ± 3.7° depicted in blue. 161

Figure 6.17: AF modeled as 8 ply symmetric laminate (ply thickness = 0.15 mm) showing the stresses through each layer in the principle coordinate system. Top: From Iatridis & Gwynn (2004) [96]. Bottom: From our experimental data. $\bullet\boldsymbol{\sigma 1}$, $\bullet\boldsymbol{\sigma 2}$, $\bullet\boldsymbol{\tau 12}$. Red layer represents -θ, blue +θ 171

Figure 6.18: AF modeled as (top) 19 layer symmetric laminate and (bottom) 20 layer antisymmetric laminate , with *t* = 0.15 mm. Red layer represents -θ, blue +θ, where θ = 60°. 172

Figure 6.19: AF modeled as (top) 19 layer symmetric laminate and (bottom) 20 layer antisymmetric laminate, with t = 0.15 mm, showing the stresses through each layer in the principle coordinate system. $\bullet\boldsymbol{\sigma 1}$, $\bullet\boldsymbol{\sigma 2}$, $\bullet\boldsymbol{\tau 12}$. Red layer represents -θ, blue +θ. 173

Figure 6.20: Stress through a symmetric angle-ply laminate (19 layer) based on the applied biaxial stress resultant applied (when $N_x = N_y$). Fit with a line, $R^2 = 1$. 174

Figure 6.21: Stress through a symmetric angle-ply laminate (19 layer) based on the applied biaxial stress resultant applied being a multiple of the other. Fit with a line, $R^2 = 1$ 174

Figure 6.22: Stress distribution a modeled AF as 19 layer symmetric laminate, with t = 0.15 mm, showing the stresses through each layer in the principle coordinate system for digested samples subjected to a tensile load of +50 N acting on a 5 mm wide cube of the AF in both the circumferential (*y*) and axial directions (*x*). Red layer represents -θ, blue +θ. 175

Figure 6.23: Failure stress resultant in the circumferential direction, N_y, when subjected to uniaxial tension is dependent on the shear strength of the lamina..... 184

Figure 6.24: Shear strength is a function of shear modulus for lamina. 185

Figure 6.25: Shape of curves for shear modulus versus shear strength all follow same trend for digested groups. 185

Figure 6.26: Shear strength as a function of shear modulus for lamina in all digestion groups. Shear strength when G_{12} = 0.3 MPa illustrated as well as location where shear strength is same for both ±θ lamina. 186

Figure 6.27: Failure envelope for control (PBS) samples when subjected to biaxial stress. Blue and red represents failures for the ±θ layers when G_{12} is taken from Iatridis & Gwynn (2004) to be 0.3 MPa [226]. Purple shows the failure envelope for the calculated G_{12} that gives same shear strength for both angled plies. 187

Figure 6.28: Failure envelope for digested samples when subjected to biaxial stress. Blue and red represents failures for the ±θ layers when G_{12} is taken to be the same decrease as elastic modulus from 0.3 MPa [226]. Purple shows the failure envelope for the calculated G_{12} that gives same shear strength for both angled plies. 188

Figure 6.29: Failure envelope for digested samples when subjected to biaxial stress for different digestion groups. The failure envelopes are for alternate shear strength technique (calculated G_{12} to produce same S). 189

Figure 6.30: Failure envelope of biaxially loaded AF model showing dependence of lamina shear modulus, G_{12} (in MPa) for +60° layers. G_{12} = 0.3 MPa was previously

reported in the model by Iatridis & Gwynn [226] and G_{12} = 0.92 MPa is the value that allows the shear strength for both ±60° to be equal. 190

Figure 7.1: Representation of three-dimensional fiber reinforced annular composite. Types of annular tears are depicted in red: A) matrix tear, parallel to fibers B) fiber tear C) matrix tear, perpendicular to fibers D) fiber/matrix interface tear E) delamination.. 205

Figure 0.1: Block diagram of webcam LabView program. Allows user to adjust the image properties prior to data acquisition. 209

Figure 0.2: Front panel of webcam LabView program..... 210

Figure 0.3 Block diagram of the acquisition LabView program. 211

Figure 0.4: Front panel of data acquisition LabView program..... 212

Figure 0.5: Block diagram of the image LabView program. 213

Figure 0.6: Front panel of image acquisition LabView program..... 213

Figure 0.1: Flow chart of Matlab Programs to get position of samples from images, leading to determination of strain. 215

ABSTRACT

Micromechanics of the Annulus Fibrosus: Role of Biomolecules in Mechanical Function

Jessica Lauren Isaacs

Advisor: Michele Marcolongo, Ph.D., P.E.

Lower back pain, caused by disc degeneration or injury, has a major effect on the United Stated economy, resulting in large medical costs – 2.5% of US health care expenditures (~50 billion dollars) annually [1]. A herniation is a common injury to the intervertebral disc that is characterized as the migration of the inner nucleus pulposus through the layers of the outer annulus fibrosus. There have been many studies quantifying the mechanical characteristics of the annulus fibrosus and modeling the response, both mathematically and computationally. There has been some work investigating the failure mechanisms of the annulus in a degenerative, micromechanical model, however the work for a larger injury model is lacking. Experimental work shows that repetitive, compressive and bending loads of the disc, causing the annulus to fail in tension, will result in catastrophic disc herniation.

The goal of this work is to characterize the failure properties of annular lamellae using a micro-mechanical testing protocol with the long-term goal of developing a failure criterion for the annulus fibrosis. Single layered annular samples were obtained from isolated cadaveric lumbar intervertebral discs in one of four orientations: longitudinal, transverse, radial, and circumferential. Uniaxial tensile tests were performed to failure and the engineering constants and failure stresses and strains determined. Key findings showed different of properties between orientations. Failure stress, elastic modulus and Poisson's ratio were higher when tested in plane to the fibers or lamellae (longitudinal and circumferential) compared to the out-of-plane orientations (transverse and radial)

with higher failure strain for out-of-plane than in-plane specimens. This was furthered by a study investigating the role of macromolecules in the intervertebral disc on the micro-mechanical behavior of the human cadaveric lumbar annulus fibrosus to determine the role these molecules play in annular mechanics.

Using composite theory, a model of the annulus fibrosus was used to determine the stresses in each lamella at different loading conditions. Failure envelopes based on the Tsai-Hill criteria were created. The properties were used to create failure envelopes for the annulus which may predict catastrophic failure of the annulus that contribute to disc herniation and lower back pain. Full understanding of the mechanical properties and failure envelopes of the annulus could potentially lead to a failure model for disc tearing and herniation.

1. CHAPTER ONE: INTRODUCTION

There is an 80% lifetime prevalence of lower back pain (LBP) and 14% or 31 million Americans suffer from LBP at any given time with an estimated cost of up to $50 billion [2-6]. There are 1.8 million days of work missed yearly due to a combination of LBP, neck-shoulder pain, and neck plus LBP in the United States [3]. LBP can be attributed to injury or degeneration. Intervertebral disc degeneration occurs in all people, to at least some extent; by age 49, 97% of lumbar IVDs showed some evidence of disc degeneration [7].

The intervertebral disc (IVD) acts like a shock absorber between two adjacent vertebral bodies. The human spine possesses 23 intervertebral discs that separate the vertebrae and provide flexibility. The intervertebral disc binds the vertebrae together and allow the series of discs and vertebrae to function as a flexible supporting column for the body [8]. The IVD is subjected to stresses from compression, torsion, and bending. The ability of the disc to bend is thought to depend on the organization of the lamellae which are only loosely interconnected and can move independently [9]. They account for 20% to 30% of the length of the spine and are composed of three distinct parts: cartilaginous plate, annulus fibrosus, and nucleus pulposus (NP). The cartilaginous plate is made up of hyaline cartilage and covers the bone of the adjacent vertebrae, acting as a shield between the bone and the rest of the IVD [10]. The outermost layer is the annulus fibrosus (AF), which is made up of dense, highly organized collagen, which merges with the posterior longitudinal ligament as well as inserts into the vertebral bodies [11]. There is a transition zone of thin fibrous tissue that separates the AF from the nucleus pulposus [12].

The annulus consists of concentric lamellae of thick collagen fibers which interlace obliquely with each layer as they cross between the endplates [13]. The AF is made up by about 20-40 lamellae; the thickness of the individual lamellae ranges from 0.14 to 0.52 mm [14]. The tissue around the collagen fibers and between lamellae is primarily aggregated proteoglycans with small amounts of elastin [15]. The individual lamellae are more distinct in the outer annulus as opposed to the middle annulus where about 40-80% are interconnecting or incomplete [14, 16]. The typical stress-strain response showed an initial toe-region and then an increase in stiffness. This nonlinear behavior has been shown in various other soft tissues; it is thought to reflect recruitment of collagen fibers with increasing tensile deformation [16]. Resistance to stress is provided by the collagen fibers; the tensile strength of which is dependent on the formation of intermolecular cross-links between the molecules making up the fibers.

Annular tears are frequently observed on magnetic resonance images (MRI) in patients with LBP [17]. Formation of annular tears, dehydration of the NP, and fissure formation in the cartilage end plate are the main early macroscopic features that characterize disc degeneration [18]. Intervertebral disc (IVD) degeneration is accompanied by a loss of collagen (COL), proteoglycan (PG) and elastin (ELA) with aging as well as an increase in enzymatic activity. Due to the localization of the biomolecular components in the IVD, the different mechanical responses and damage patterns associated with disc degeneration are likely related to the local molecular breakdown of the tissue. The biochemical compositional changes in the disc alter mechanical behavior of the disc.

2. CHAPTER TWO: BACKGROUND AND LITERATURE SURVEY

2.1. Anatomy of the Spine

The spine allows for physiological movement and flexibility of the body and protects the spinal cord from danger due to motion and trauma. The main function of the spine (vertebral column) is to transfer loads and bending moments from the head through the trunk to the pelvis [19].

The human spine consists of five main regions, from cranial to caudal: cervical, thoracic, lumbar, sacrum and coccyx. The sacrum and coccyx are composed of fused bones and are commonly referred to as a tail bone. The cervical portion of the spine relates to the area of the neck and consists of seven (C1 – C7) individual vertebrae. Moving caudal, the thoracic region (chest area) has 12 (T1 – T12) vertebrae as well as housing the ribs. The final not fused lumbar region consists of five vertebrae (L1 – L5). Each of the vertebrae has a similar shape (varying in size) except for C1 and C2, named the Atlas and Axis. This dissimilar shape allows for articulation and support of the skull. The overall shape of the rest of the vertebrae is a main vertebral body with additional posterior elements which include: foramen, lamina, pedicle, spinous process, superior articular process and transverse process (Figure 2.1).

The superior and inferior surfaces of the verbal bodies are cartilaginous plate-like structures called endplates. Between each of these endplates in the cervical, thoracic and lumbar regions, there is an intervertebral disc (IVD) which separates the adjacent vertebrae (Figure 2.2). The stability and functionality of the vertebral column is dependent on the structural integrity of these IVDs.

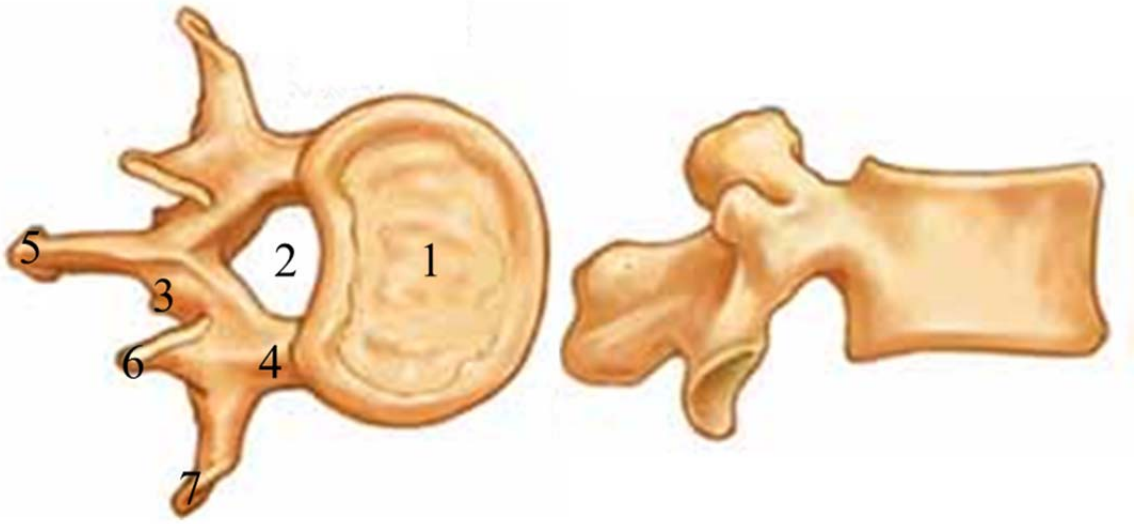

Figure 2.1: Representative lumbar vertebrae consisting of (1) vertebral body, (2) foramen, (3) lamina, (4) pedicle, (5) spinous process, (6) superior articular process and (7) transverse process. Adapted from http://www.spineuniverse.com/anatomy/vertebral-column.

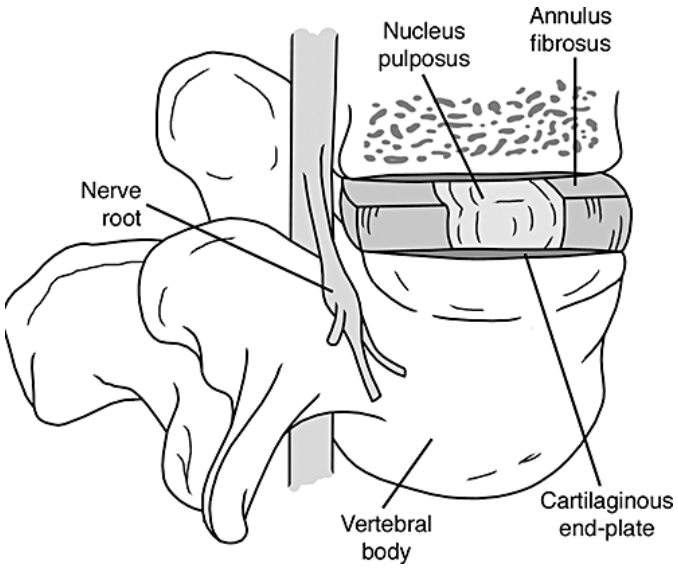

Figure 2.2: Schematic of the intervertebral disc (IVD) with superior and inferior vertebral bodies. The IVD consists of three main parts: an outer annulus fibrosus surrounding an inner nucleus pulposus, with two endplates acting as buffers to the vertebrae. Reprinted from [20].

2.2.Intervertebral Disc

Intervertebral discs (IVD) are fibrocartilagenous, hydrated structures that act as shock absorbers and the articulating surfaces between two adjacent vertebral bodies (Figure 2.3) [10, 19, 20]. They stabilize and maintain the alignment of the spine, give the spine its flexibility by allowing the movement between vertebrae and are responsible for the load distribution and energy absorption under spine loading.

The human spine possesses 23 IVDs which accounts for 20% to 30% of the height of the spine and increase in size on progression from the cervical to lumbar regions [10, 19]. IVDs have a complex donut-like structure consisting of three distinct parts: an inner nucleus pulposus (NP) surrounded by an outer annulus fibrosus (AF) and the superior and inferior bony endplates that serve as an interface between the disc and vertebrae.

The cartilaginous endplates are made up of hyaline cartilage and covers the bone of the adjacent vertebrae, acting as a shield between the bone and the rest of the IVD [10]. The outermost layer is the AF, which is made up of dense, highly organized collagen, which merges with the posterior longitudinal ligament as well as inserts into the vertebral bodies [11]. There is a transition zone of thin fibrous tissue that separates the AF from the inner NP [12].

Intervertebral discs receive nourishment through diffusion, as they are relatively avascular with nerve endings penetrating only a small part of the outer AF [21, 22]. The IVDs are made up of cells scattered in an extracellular matrix made up of water, proteoglycans, collagens, and non-collagenous proteins which will be discussed in the following sections [11].

2.2.1. Nucleus Pulposus

The central NP comprises almost half of the size of a normal IVD and is highly gelatinous, made up of predominantly water (87%, wet weight) [23] in a matrix of proteoglycan (14% wet weight) [23-25], type-II collagen [26, 27], and other matrix proteins (similar to those found in cartilage) [27-29]. Proteoglycans (PGs) are composed of glycosaminoglycan (GAG) chains attached covalently to a protein core. The sulfated GAGs are negatively charged with can associate with positively charged sodium ions (Na+) which can draw water into the tissue because of the osmotic imbalance generating a hydrostatic pressure within the NP [30]. The nucleus is rich in aggrecan and highly hydrated, with a fine collagen network which shows no apparent organization [9, 31].

2.2.2. Annulus Fibrosus

The AF serves to contain the nucleus and is made up of collagen, elastin and PGs. The AF is organized in concentric layers, called lamellae, made up of mostly collagen and are arranged in alternating angles. The composition of the AF varies as you go radially outward from the NP and thus is usually described as two separate entities, the outer annulus fibrosus (OAF) and inner annulus fibrosus (IAF).

The IAF consists of less dense matrix which has higher concentration of type-II collagen [32] and proteoglycan [25] but does not have a highly ordered lamellar organization [20]. The lamella in the IAF has been determined to have a thickness of about 300 μm [14, 33]. The OAF is made up of almost entirely type-I collagen fibers [24, 26, 32]. The thickness of the lamellae in the OAF has been reported to have an average thickness of 150 μm [14, 33]. There is no defined interface between the OAF and IAF,

instead there is a gradual transition between the two [33]. The composition of the AF will be discussed in further detail below organized by macromolecule (starting on page 7).

2.2.2.1. Annular Lamellae

Collagen fibers in individual lamella (type I in OAF and type II in IAF) of the AF are parallel with respect to the each other and have a tilt angle with respect to the sagittal axis of the disc which alternates in successive lamellae (Figure 2.4) [8, 10, 14, 34]. These collagen bundles are visible by observation without microscopy. The tilt angle of the collagen fibers within a lamellae has been discussed in the literature and ranges from 45 - 60° [14, 33, 35, 36].

Marchand and Ahmed (1990) investigated the structure of lumbar AF to determine the number of complete lamellae (Table 2.1) and the average thickness of each lamella (Table 2.2). It was determined that the AF consists of between 15 – 25 lamellae dependent on circumferential location, spine level and age [14]. The thickness of the lamellae was dependent on age and radial location, ranging from 160 – 440 μm [14]. The orientation of the collagen fibers also change due to different loadings subjected to the IVD.

The annulus contains less aggrecan than the nucleus and consists predominantly of sheets made from bundles of collagen fibers, which form concentric, cylindrical lamellae around the spinal axis [10, 15]. Collagen and PG are the primary structural components of the AF [37]. The composition and organization of the macromolecules change with the location within the disc (Figure 2.5).

2.2.2.2. Collagen

Collagen is the body's principal structural material. Consisting of long-chain protein molecules, it is made up of various amino acids and glycine arranged in a triple helix formulation [24, 26]. It frequently adopts an oriented, fibrous form, so fiber orientation is an important factor. Typical fibers are 0.2μm in diameter, with a very high aspect ratio. Collagen provides the tensile strength of the IVD, stability between the vertebrae, and resistance to disc bulging in response to loads [11].

As previously discussed, the AF of a mature lumbar disc can possess up to 25 lamellae. Collagen types I and II make up 80% of the collagen in the IVD [26], with eight other collagen types evident in the IVD (Table 2.3). Collagen accounts for as high as 70% of the dry weight of the OAF, but less than 20% of the dry weight of the central NP of young individuals [11, 26]. There is the most Type I in the outer AF and the amount decreases toward the center of the disc; there are only small amounts of type I collagen in the NP [11, 26]. In comparison, Type II collagen accounts for 80% of the collagen in the NP, and very little through the AF [26].

As the main structural component of the AF, collagen supports the tensile load and is able to maintain the tissue form and cohesiveness. Collagen can be artificially degraded using a protease specific to collagen, called Collagenase [38, 39]. Collagenase cleaves two of the three helical chains in the long, un-denatured collagen protein [39].

2.2.2.3. Proteoglycan

Proteoglycans (PGs) are hydrophilic molecules, which form strong chemical bonds with water, allowing tissues to hold water which and resist from exiting the tissue during compressive loading. PGs account for only a few percent (~5%) of the dry weight of the OAF [20], but are the most abundant macromolecules present in the NP,

accounting for as much as 65% of the dry weight and decreasing to as low as 30% with advancing age [40]. PGs contribute to tissue compressive stiffness, provide the tissue with charged properties, and play significant roles in tissue viscoelasticity through interactions with water. Similar to cartilage, IVD also derives its charged nature from PGs [38]. Proteoglycans are made of a protein core attached to a glycosaminoglycan (GAG) chain (Figure 2.6). GAGs are hydrophilic and thus attract and hold water in the IVD, absorbing the compressive loads and evenly distributing the force around the circumference of the annulus [41].

IVDs have a variety of different types of PGs in its extracellular matrix [38]. Aggrecan is the most abundant proteoglycan by weight in the IVD, it has a bottle brush structure with both chondroitin sulfate and keratan sulfate chains bound to the core GAG protein [40]. PGs contribute to the water content and disc swelling pressure as long as they remain entrapped within the center of the disc by an intact outer AF [38]. The cells of the IVD naturally break down PGs, turning them into aggregates which stay trapped within the IVD, but no longer attract water [42]. By six months of age, almost 50% of the AF proteoglycan and 30% of the NP proteoglycan has degraded into aggregates [38, 42]. There can be as must as only 10% of non-aggregated PGs by adulthood [40]. The IVD is hydrated with the water content of a NP around 90% at birth and decreases with age to 80% at 20 years, further declining to 70% at age beyond 60 years for normal discs without abnormal degeneration [43, 44]. Using the enzyme Chondroitinase ABC (ChABC) we are able to artificially break down PGs by selectively cleaving the GAG side chains from the protein core of proteoglycans [45].

2.2.2.4. Elastin

Elastin is a fibrous protein found in many soft tissues including skin, blood vessels, and lung tissue. It is an elastic material, having almost linear-elastic properties, with a low Young's modulus (around 0.6MPa) and the capacity to endure strains over 50% with good elastic recovery [46, 47]. The elastic fibers are composed of two components: centrally located amorphous elastin, surrounded peripherally by microfibrils [48]. The presence of elastic fibers in the IVD has been noted in some earlier studies [47, 49-52] and the large-scale organization of the fibers has been examined by Yu et al. [53] in bovine tail (Figure 2.7).

Inside the NP, long (greater than 150 μm) elastic fibers are orientated radially [53]. In the transitional region between nucleus and annulus, the orientation of the elastic fibers changes, producing a criss-cross pattern. Elastic fibers are densely distributed in the region between the lamellae inside the AF. In the AF, elastic fibers are apparent within the lamellae, orientated parallel to the collagen fibers [53]. Yu et al. [53] surmises that elastic fibers contribute to the mechanical functioning of the intervertebral disc and the varying organization of the elastic fibers in the different regions of the disc is related to the different regional loading patterns.

Elastase is an enzyme, found in the pancreas, which can be used to artificially degrade elastin. This is accomplished through the cleavage of peptide bonds in the target proteins. The specific peptide bonds cleaved are those on the carboxyl side of small, hydrophobic amino acids. Elastase cleaves at the peptide bond after amino acids with small side chains [54-56]. Elastase cleaves the peptide bonds in elastin, aiding in the digestibility of this elastic protein [56].

2.2.2.5. Cells of the Annulus Fibrosus

Bruehlmann et al. (2002) published a study examining the variations in cell shape, arrangement of cellular processes and cytoskeletal architecture in the OAF, IAF and between layers [32]. The OAF consisted of a dense network of cells with cord-like processes in the longitudinal direction (A: Figure 2.8), cells with lateral and reduced length longitudinal processes (B, C: Figure 2.8) and fusiform cells without processes (D: Figure 2.8). The IAF is made up of cells with twisting branches interspersed among spherical cells that sometimes contain two short processes (E, F: Figure 2.8). Between the annular lamellae there exists an adhesive-type layer of structures and cells. The inter-lamellar cells are flat, disc-shaped cells that include branches which radiate outward from the center of the cell in a star-like pattern [32]. These processes interconnect which each other to form a lattice formation.

There are also phenotypic differences between cells from the different regions of the AF with along with the previously discussed differences in morphology [57]. Chelberg et al. (1995) was identified two populations of cells within the disc, one with a chondrocytic and one with nonchondrocytic cell phenotype based on matrix synthesis [58]. Similarly, Rufai et al. (1994) showed in the rat, that the IAF is formed by cells from embryonic cartilage (the perinotochordal mesenchyme), while the OAF has contributions from surrounding fibrous mesenchymal tissue [59].

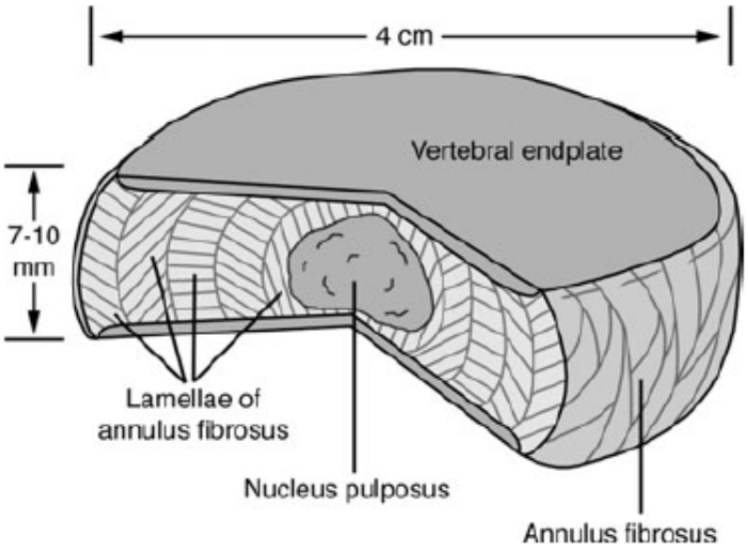

Figure 2.3: A cut out portion of a normal intervertebral disc. Note the lamellar architecture of Annulus Fibrosis. Reprinted from [20].

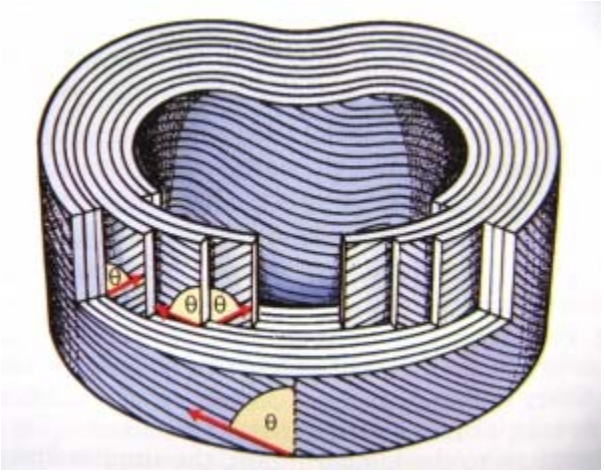

Figure 2.4: Drawing of the annulus fibrosus with the nucleus pulposus removed. The collagen fibers are arranged in multiple concentric layers (lamellae) with consecutive rings running in alternating directions with an orientation of θ degrees. Reprinted from [60].

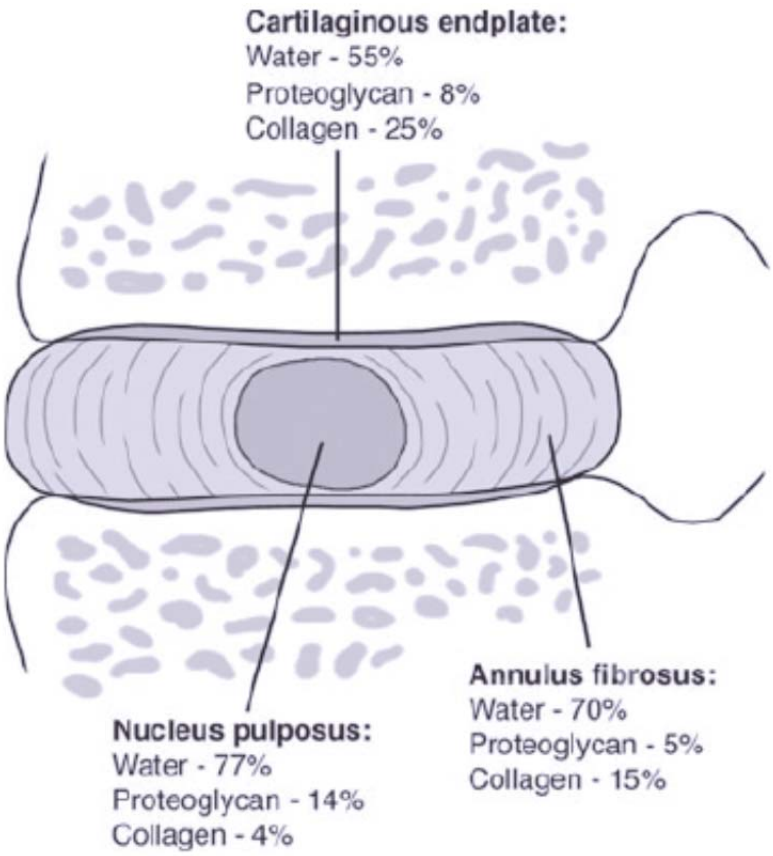

Figure 2.5: Schematic of the intervertebral disc structure showing the regional variances in composition. Reprinted from [20].

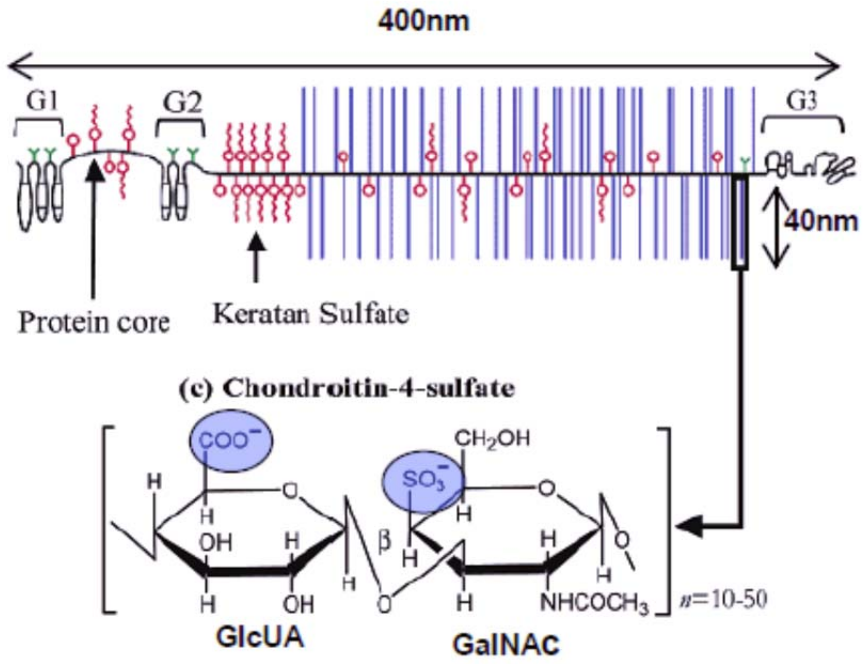

Figure 2.6: The bottle brush structure of Aggrecan, the most abundant proteoglycan in the IVD with the chemical structure of chondroitin sulfate. Reprinted from [61].

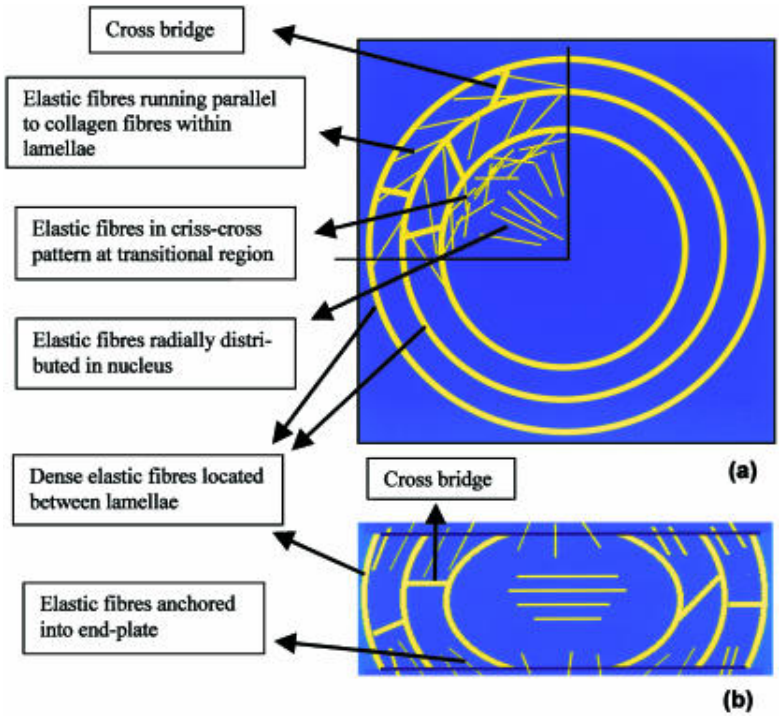

Figure 2.7: Schematic view of the elastic network of the bovine tail disc. (a) Transverse section. (b) Sagittal section. Reprinted from [53].

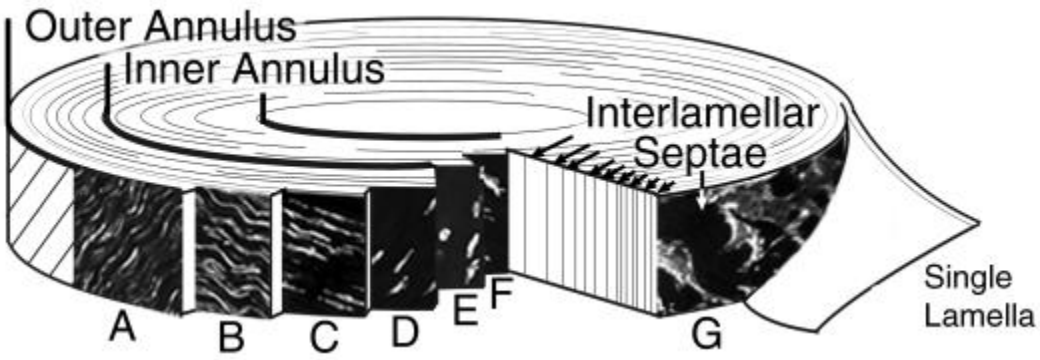

Figure 2.8: Cell morphology of the annulus fibrosus. The outer annulus is characterized by cells with a fusiform cell body and a gradual transition in process architecture, while the inner annulus consists of cells with a spherical morphology. Reprinted from [32].

Table 2.1: Average thickness (mean ± standard deviation) of annular lamellae from experimental data of L2-L3 and L4-L5 by Marchand and Ahmed (1990). Adapted from [14].

t_L (mm)		A	L	P-L	P	Mean
OUT	Young	0.14 ± 0.02	0.15 ± 0.04	0.16 ± 0.06	0.11 ± 0.03	0.14 ± 0.04
	Old	0.28 ± 0.09	0.37 ± 0.11	0.40 ± 0.08	0.29 ± 0.03	0.33 ± 0.06
MID	Young	0.18 ± 0.03	0.15 ± 0.03	0.15 ± 0.05	0.18 ± 0.04	0.16 ± 0.04
	Old	0.45 ± 0.07	0.51 ± 0.09	0.50 ± 0.06	0.37 ± 0.11	0.46 ± 0.07
IN	Young	0.23 ± 0.01	0.19 ± 0.04	0.20 ± 0.05	0.2 ± 0.05	0.20 ± 0.05
	Old	0.52 ± 0.08	0.66 ± 0.14	0.49 ± 0.14	0.4 ± 0.11	0.52 ± 0.11
ALL	Young	0.18 ± 0.02	0.16 ± 0.03	0.17 ± 0.03	0.16 ± 0.03	0.17 ± 0.03
	Old	0.42 ± 0.06	0.51 ± 0.06	0.47 ± 0.07	0.35 ± 0.09	0.44 ± 0.07

t_L = thickness of lamellae, A = anterior, L = lateral, P-L = posterolateral, P = posterior.
Young: Mean age, 23 years; range, 18 – 29 years. Old: Mean age, 63 years; range, 53 – 76 years.

Table 2.2: Average number of lamellae (mean ± standard deviation) from experimental data by Marchand and Ahmed (1990). Adapted from [14].

DL	A	L	P-L	P	Mean
Young L2- L3	20.7 ± 3	25.5 ± 2	24.0 ± 2	20.0 ± 2	22.6 ± 3
Young L4- L5	25.5 ± 2	25.0 ± 2	23.5 ± 5	22.0 ± 2	24.0 ± 2
Old L2- L3	19.0 ± 1	20.0 ± 2	18.0 ± 1	15.0 ± 2	18.0 ± 2
Old L4- L5	19.1 ± 2	21.1 ± 2	18.0 ± 2	18.0 ± 2	19.0 ± 1
Mean	21.1 ± 3	22.9 ± 3	20.9 ± 3	18.8 ± 3	20.9 ± 3

D_L = Number of distinct lamellae, A = anterior, L = lateral, P-L = posterolateral, P = posterior.
Young: Mean age, 23 years; range, 18 – 29 years. Old: Mean age, 63 years; range, 53 – 76 years.

Table 2.3: Collagen types in the intervertebral disc. Adapted from [26].

Collagen Type	Tissue Distribution	% of Total Collagen	Property
I	AF	Up to 80%	Fibrillar
II	AF, NP	Up to 80%	Fibrillar
III	Pericellular, AF, NP	?	Fibrillar, forms reticular network
IV	Not present in normal disc	–	Forms lattice backbone of basement membranes
V	AF	~3%	Fibrillar, associated with Type I
VI	Pericellular, AF, NP	10 – 20%	110 nm banded microfibrils
IX	Pericellular, AF, NP	1 – 2%	Control Type II fibril size
XI	NP	~3%	Fibrillar, codistributes with Type II

2.3. Loading of the Intervertebral Disc

The IVD is subjected to stresses from compression (primary), torsion and bending (secondary). Most natural movements of the body result in the spine being loaded in some combination of all three of these modes. The ability of the disc to provide motion is thought to depend on the organization of the lamellae which are only loosely interconnected and can move independently [9]. When the disc is loaded, mainly in compression, the NP deforms and creates an intradiscal pressure within the disc pushing outward onto the AF and the endplates. The IVD can be thought of as a thick-walled pressure vessel. As the disc is compressed (and the NP exerts intradiscal pressure on the AF) the fibers in the annulus are pushed outward and essentially loaded in tension. Having the annular lamellae loaded in tension helps to sustain the pressure inside the disc and hold the NP in place [62]. As the AF is operating in tension, it is able to transmit the loads between the separate vertebral bodies.

Maintaining this intradiscal pressure within the disc is believed to be important in preventing disc injuries or pain. There are fluxuations in intradiscal pressure during daily activities. There have been many studies measuring the intradiscal pressure at different stances and/or times of the day. From these pressure measurements, it is possible to calculate the loads experienced at the intervertebral disc. The first study to measure in vivo pressures within the disc was performed by Nachemson [63]. He used a membrane covered needle which was attached to a pressure transducer to measure the intradiscal pressures at the L3-L4 IVD of thirty participants in various positions. His work was published in a series of two papers between published in 1966 and 1970, both following the same protocol, and thus can be discussed together. Nachemson was able to correlate

the load experienced by the IVD from the measured pressures to the body weight of the participant. These formulations for a few of the positions can be seen in Table 2.4.

In the course of this study, Nachemson hypothesized that it was not the pressure (or resulting load) that was important, it was more the change in pressure/load between the different positions and maneuvers that could adversely affect the IVD. Nachemson explored the changes in pressure felt by the IVD in the various positions all compared to standing, since there is a direct relationship between pressure and load, the two terms can be used interchangeable when discussing these normalized to standing values. The largest relative increase in pressure (or load) was an increase to 275% (assume standing is 100%) when the person was leaning forward in his chair holding a 10 kg weight. Standing erect puts approximately 500 – 800 N of compressive force on the lumbar spine; bending forward to lift 10 kg puts approximately 2000 N on the lumbar spine [64]. The largest relative decrease in pressure (or load) was a decrease to 25% when the person was lying flat on his back. For more information on intradiscal pressures, Nachemson compiled all of his and his collaborators works on pressures experienced by the disc during various movements into a complete review article in 1976, which nicely summarizes all of the articles [65]. These experimental pressure changes have major clinical implications. For example, post-surgical interventions for a lumbar disc herniation, patients are advised to stand or lay down as opposed to sitting, which has a much more sever increase in pressure. There are also major experimental implications, as many subsequent spine and IVD studies published use loadings from these papers to justify loading protocols in mechanical testing setups.

There were some drawbacks to these initial *in vivo* measurements, however. The imaging techniques at this time were not as robust as current magnetic resonance imaging (MRI) which is now the norm in determining disc dimensions. With the lack of perfect imaging techniques, the disc dimensions could not be correct, thus leading to an incorrect load determination. Nachemson also reported some problems with the polyethylene membrane on the needle. Only static testing could be performed so that the membrane would stay in place. There was also a limit to the deformation the membrane could experience before it was permanently deformed, thus not allowing further testing; this created a limited to the force of the testing that was allowed.

More recently, a study by Wilke et al. (1999) reinvestigated the work performed by Nachemson and collaborators to determine if the values still head true now using more modern technologies than were available in the 60s – 70s [66]. This study was limited however by the fact that only one (male) subject was used. A pressure transducer was made by embedding a pressure sensor into a long metal tip (7mm long) which was fixed to a flexible silicon tube. This modern pressure transducer (no membrane) was inserted into the L4-L5 IVD, which was then affixed to a stabilizing belt which went around the outside of the participant's body, from which the wires were attached to a computer. The pressure transducer was surgically inserted and a test period of 24 hours began after which the implant was removed. It is interesting to note, that the paper does not discuss the recovery time and how long after the patient awoke from anesthesia the testing started. Wilke et al. compared the results for pressure change to that of Nachemson, and found that they were relatively consistent; however, the Wilke study had their participant use a 20 kg weight as opposed to the 10 kg weight used in the Nachemson study [66].

An interesting and important finding in the Wilke study was that the pressures were measured overnight as the participant slept, and the pressure was found to increase overnight as the participant was lying down. The pressure increased to 270% over the course of 7 hours of lying down, this did not depend on how the participant was lying down (i.e. back, side). This increase of pressure was explained by the IVD allowing rehydrating overnight, as there was far lower loading applied, the PGs drew in more water that was not expulsed through loading [66]. This study is cited for subsequent papers which investigate IVD mechanics over a 24 hour period, using a diurnal cycle. The diurnal cycle in reference to the disc is 16 hours of testing at physiological loads during the day (standing or sitting) then allowed for an 8 hour recovery time at a lower load, more consistent with lying down. This allows the behavior of the disc to be fully explored.

The orientation of the collagen fibers, specifically in the AF, also change due to the disc height changes which originate from the different loading states. When the disc is loaded in compression, the collagen fibers become closer together and the angle changes from ~60° in the sagittal (vertical) plane to closer to 90° [67]. However, when the disc is loaded in tension, the collagen fibers reorient themselves in the direction of the load that is being applied [68]. In the torsion loading case, the collagen fibers in alternating lamellae become slack and results in a decrease of the angle of orientation (decrease from 60°) to become closer to vertically orientation; while the alternating taut layers become more horizontal [69].

2.3.1. Behavior of Soft Tissues under Loading

Load-supporting soft tissues have important biomechanical properties, which are critical to their normal functional roles in the human body. The multiphasic nature of charged-hydrated soft tissues (like the IVD) produces unique mechanical and electrochemical behavior. Under mechanical loading, soft tissues exhibit significant viscoelastic responses, changes in ion concentration, osmotic pressure, and electrical potential response [86]. Simple elastic or viscous responses are time independent when loaded under constant stress, constant strain, or constant strain rate. However, biological materials exhibit time-dependent viscoelastic behavior. Soft tissues may be characterized as quasi-incompressible, non-homogeneous, non-isotropic, non-linear viscoelastic materials likely to undergo large deformations.

2.3.1.1. Viscoelasticity

For hydrated soft tissues (for example the AF) the viscoelasticity comes from two sources: flow dependent and flow independent. The intrinsic (flow-independent) viscoelasticity comes from intermolecular friction; the stretching and uncoiling of molecules and vibration of the long-chain polymers in the tissue [87, 88]. The flow-dependent viscoelasticity comes from the frictional drag force of interstitial fluid flow through the porous solid matrix of the tissue [89].

There exists a history-dependent component in the mechanical behavior of living tissues [90]. In extension, stress values appear higher than those at equilibrium, for the same strain, the tensile curve appears to be steeper than the one at equilibrium. When a tissue is extended and maintained at its new length, the stress gradually decreases slowly against time (stress relaxation). When the tissue is subjected to a constant tensile load, the

rate of lengthening, or expansion, will decreases as time progresses until it reaches equilibrium (creep). Under cyclic loading, the stress-strain curve shows two distinct paths corresponding to the loading and unloading trajectories (hysteresis). The stress at any instant of time depends not only on the strain at that time, but also on the history of the deformation. These mechanical properties, observed for all living tissues, are common features viscoelastic materials [90].

The IVD exhibits viscoelastic tissue properties, due to the presence of the hydrophilic PGs. During a period of sustained creep loading, the spine can lose 1-2mm of height, due to the expulsion of water from the discs [70]. With time, the tissue loses its gel-like properties and becomes less hydrated and more fibrous, decreasing its ability to transmit weight directly. As a result, a larger share of the load is sustained by the AF, which then experiences its own degeneration. These changes will be later discussed in Section 2.5 (page 33).

2.3.1.2. Preconditioning

When loading-unloading cycles are applied on the tissue successively up to the same stress level, the stress-strain curve is gradually shifted to the right. After a number of such cycles, the mechanical response of the tissue enters a stationary phase and the results become reproducible from one cycle to the next. This phenomenon is due to the changes occurring in the internal structure of the tissue, until a steady state of cycling is reached [91].

2.3.1.3. Large Deformation

In tensile tests, the relationship between the Lagrangian stresses, $\mathbf{T}$, with respect to the Lagrangian strain, $\boldsymbol{\varepsilon}$ are examined. Sometimes, Lagrangian stress is taken for the

true stress, σ, in the constitutive equation. This substitution is valid only for strains smaller than 2% of the resting length [71]. However, soft tissues are likely to exceed this limit in their physiological range of functioning, so that in most cases, this assumption no longer applies.

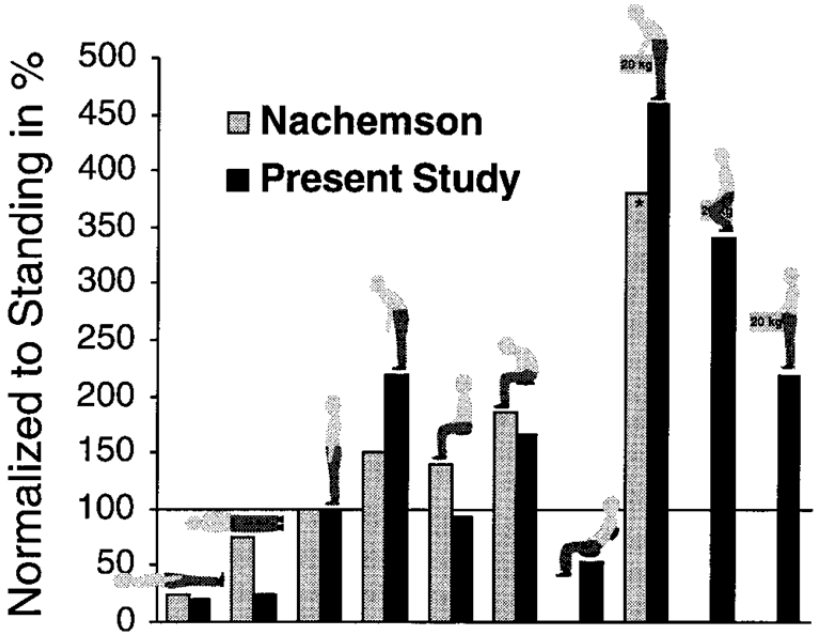

Figure 2.9: A comparison of the relative pressure (or load) change at different positions between a study by Nachemson (1966) and a follow-up study by Wilke et al. (1999). Both studies compared above were performed on a 70 kg male participant. It is important to note that the Nachemson study used a 10 kg weight, while the Wilke et al. study used a 20 kg weight. Reprinted from [66].

Table 2.4: Approximate formulas for calculation of load experienced by intervertebral disc based on body weight of the individual. From [63].

Position	Formula
Sitting upright	$P = 30 + 2.8 \cdot W$
Standing upright	$P = 15 + 2.1 \cdot W$
Sitting leaning forward (α°)	$P = 30 + 2.8 \cdot W + 3.6 \cdot W \cdot sin(\alpha)$
Standing leaning forward (α°)	$P = 15 + 2.1 \cdot W + 3.6 \cdot W \cdot sin(\alpha)$

2.4. Mechanical Properties of the Annulus Fibrosus

The material properties of the AF in tension, compression, and shear depend on disc location, orientation, age, degeneration, and loading [72-76]. Previous studies on the mechanical behavior of the AF have found it exhibits a high tendency to swell [77, 78] and behaves as a viscoelastic material in compression [79] and in tension [75, 76]. The compressive modulus of the AF was shown to vary with region in the IVD [79]. The response of the AF *in vivo* depends on its composite structure; however it is also important to understand the intrinsic mechanical behavior of the individual lamellae.

Based on a study of the tensile properties of vertebra-AF-vertebra samples, Adams and Green (1993) found that the tensile behavior was related to the mechanical properties of fiber (collagen fiber bundles), matrix, and fiber-matrix interactions [80, 81]. Using Vertical slices of annulus and bone, 5 mm thick, 15 mm long and 30 mm wide, Green et al. determined that the modulus of elasticity for the AF was 7.2 ± 3.1 MPa for the outer anterior annulus and 27.2 ± 10.2 MPa for the outer posterior annulus. The stresses at failure for the outer anterior and outer posterior AF samples were 1.7 ± 0.8 MPa and 3.8 ± 1.9 MPa, respectively. The strains to failure for the outer anterior and outer posterior AF samples were 65 ± 16 % and 34 ± 11%, respectively. They also concluded that the tensile strength of the AF was highest in line with the direction of the collagen fibers due to the intra-lamellar connections as well as the actual collagen fibers [80, 81].

There have been several other studies focusing on the mechanical properties of the AF. For multi-lamellar specimens with circumferential orientation tensile moduli have been reported to be 5.6-17.5 MPa by Elliot and Setton (2001) [82], 15-20 MPa by

Wu and Yao (1976) [83], 27.1 MPa by Acarogluet al. [72] and 5-50 MPa by Ebara et al. [74]. Brown et al. measured the distribution of the tensile strength of the AF using bone-disc-bone specimens cut from the intervertebral disc [84]. The results explained that the central portions of the AF were much weaker than the peripheral, while the anterior and posterior portions of the AF were stronger, being fused with and reinforced by fibers of the anterior and posterior longitudinal ligaments, respectively. Please refer to table 4.3 for a summary of these studies.

2.4.1. Lamellar Mechanics

Tensile testing of isolated annular specimens was first used in 1967 [76] and is still an accepted technique to determine material properties and strength of IVD tissue. Single layer annular mechanics have been qualitatively examined both parallel and perpendicular to the collagen fibers [85]. Pezowicz et al. (2005) investigated the structural and mechanical responses of fully hydrated sections from a single lamellar of the outer AF. They observed stress-strain curves for single outer lamellae (thickness 70-90 μm) of ox tail AF. The initial phase of the curve (Figure 2.10, A to B) identifies the region of response in which the in-phase collagen crimp is progressively straightened, leading to isolated bundle sliding within the intact array at point B (Figure 2.10). Sliding occurred along the entire length of the sample, indicating that these isolated bundles had detached or pulled out from each other or of the glued ends. The rapidly declining stress region (Figure 2.10, B to C) corresponds to the increase in bundle sliding and separation throughout much of the array. Point C (Figure 2.10) marks the being of the reduced stress region of behavior resulting from the large-scale separation of fiber bundles. In the same study, Pezowicz et al. (2005) also qualitatively explored the mechanical responses across

the fiber alignment direction (perpendicular). The matrix is progressively stretched until the collagen fibers begin to separate (Figure 2.11). It was shown that a network of collagen interconnections (clefts) crossed between the matrix. Upon further tension, the clefts opened further and were finally accompanied by tilting of the still intact collagen fibers. They concluded from the observation of the clefts that the inter-fiber adhesion has to be low and thus not a significant contribution to the strength of the lamellae [85].

Skaggs et al. [73] addressed the mechanical properties of single non-degenerated lamellar specimens tested in plane with the collagen fibers of the AF; this removes variables such as specimen orientation and number of lamellae in the specimen. Using a strain rate of 0.00009 sec^{-1} with grade I and II samples, they obtained samples with an average gauge dimension of 2.90 x 1.51 x 0.63 mm for length, width, and thickness, respectively. The failure stresses and strains of single lamella AF specimens varied by anatomic region ranging from 3.6 – 10.3 MPa for ultimate tensile strength and 9.2 – 15.4 % for strain (Table 2.5). The failure stress was higher for anterior than postero-lateral regions, and higher for outer than inner regions. Conversely, failure strain was higher for postero-lateral than anterior regions, and higher for inner than outer regions. Results also showed that the tensile modulus of the single lamellae ranged from 59 – 136 MPa depending on location (Table 2.6).

Holzapfel et al. [35] also investigated single lamellar mechanics of the human lumbar AF using specimens from four anatomical regions: ventro-lateral external (VLe), the ventro-lateral internal (VLi), the dorsal external (De), and the dorsal internal (Di). Non degenerate specimens from lumbar level L1-L2 were studied and the annular region remained attached to the endplates in order to provide a more physiological value of the

tensile strength (Figure 2.12). Dumbbell shaping of the lamellae was not used because it was decided the parallel fiber-alignment of the annulus lamella compromised the intended stress transfer to the narrow gage region of the dumbbell [35]. Uniaxial tests were performed on a computer-controlled and screw driven high-precision tensile testing machine. The thickness of the samples ranged from 0.4 to 0.8 mm. Specimens underwent cyclic uniaxial extension tests, which were performed with a constant crosshead speed of 1 mm/min. All tests were performed in 0.15 mol/L Sodium chloride (NaCl) solution at 37°C. Three moduli were calculated: a low-stress modulus E_{low} between 0 and 100 kPa, a medium-stress modulus E_{medium} between 100 and 500 kPa and a high-stress modulus E_{high} between 500 kPa and 1 MPa (Table 2.7).

For the investigates single lamellar specimens, Holzapfel et al. found site-specific mean values of E_{high} in the range 28-78 MPa [35]. These results are almost half of the values presented by Skaggs et al. This could be due to large specimen variance, the difference in testing protocols and investigated lumbar levels. More significant is the use of different definitions of tensile moduli. Skaggs et al. [73] reported a modulus, E, at 75% of the failure strain, while Holzapfel et al. [35] computed E_{high} as a modulus between the stresses 0.5 – 1 MPa. Seventy-five persent of mean failure stresses of 4-10 MPa from Skaggs et al. [73] is still higher than the 1MPa upper limit of Holzapfel et al. definition of E_{high}.

The radial mechanics of the AF have also been experimentally explored. Fujita et al. (1997) obtained rectangular strips of annulus, oriented in the radial direction (Figure 2.13), from non-degenerated (grade I) and moderately degenerated (grade II) human lumbar IVDs [86]. Typical stress-strain curve of the radially oriented specimens showed

the nonlinearity in the toe region of the curve at low strains. Mechanical parameters were determined from the stress-strain data, including (Table 2.8): yield stress and strain, ultimate stress and strain, and the tangent modulus. The average tangent modulus was E = 0.19 MPa at zero strain and 0.47 MPa at 70% of the yield strain [86]. The samples from the middle layers of the AF had a higher stiffness than the inner or outer AF samples which was consistent with the increased inter-laminar weaving observed in this region [14, 86]. It was also shown that the more degenerated samples (grade II) had a 30% decrease in both the ultimate and yield stresses compared to the non-degenerated samples (grade I). Thus showing that the AF becomes more weak as degeneration occurs [86].

2.4.1.1. Inter-lamellar Shear Strength

Studies have experimentally measured the shear forces in the AF. Iatridis et al. (1999) investigated the shear properties of the AF as well as evaluated the effect of different loading conditions on healthy and degenerated annular samples [87]. Cylindrical samples from L3-L4 were tested in torsional shear in a 0.15 M NaCl solution. The experiments were performed under a compressive force in order to aid with gripping. Dynamic shear properties were measured in frequency and strain sweep tests. They used the frequency range 0.1 to 100 rad/sec with a constant shear strain amplitude of 0.05 rad for the frequency sweep test and the strain sweep test was performed over an amplitude range of 0.005 to 0.15 rad at a constant frequency of 5 rad/sec [87]. The dynamic shear modulus ranged from 100 to 400 kPa and was affected by strain amplitude and frequency. Higher strain rates resulted in higher shear moduli and larger strains resulted in lower shear moduli [87].

Another study performed by Fujita et al. (2000) also investigated the shear behavior of the AF by using both cube and sheet samples [88]. Cube specimens were tested in simple shear in three orthogonal directions (Figure 2.14) to obtain the shear modulus in two locations: anterior and postero-lateral. The lamellae sheet specimens were obtained from three regions of the AF (inner, middle and outer) and the shear modulus calculated as double the slope of the relaxed shear stress versus strain curve in both an axial and circumferential testing direction (G_{31}, G_{13}, Figure 2.15) [88]. The shear moduli G_{12}, G_{23} and G_{31} for the cube specimens were calculated to be 25.34 ± 16.8 kPa, 32.12 ± 18.4 kPa and 56.04 ± 36.3 kPa (Table 2.9).

The highest shear modulus occurs when shear strain is applied in plane with the lamellae, this was hypothesized to be due to the added tensile stiffness from the inter-lamellar collagenous connections [88]. The shear properties of the sheet specimens increased from the inner to outer AF for both the axial and circumferential sample orientations (Table 2.10). The authors hypothesized this was due to the variance of collagen types through the thickness of the AF [88].

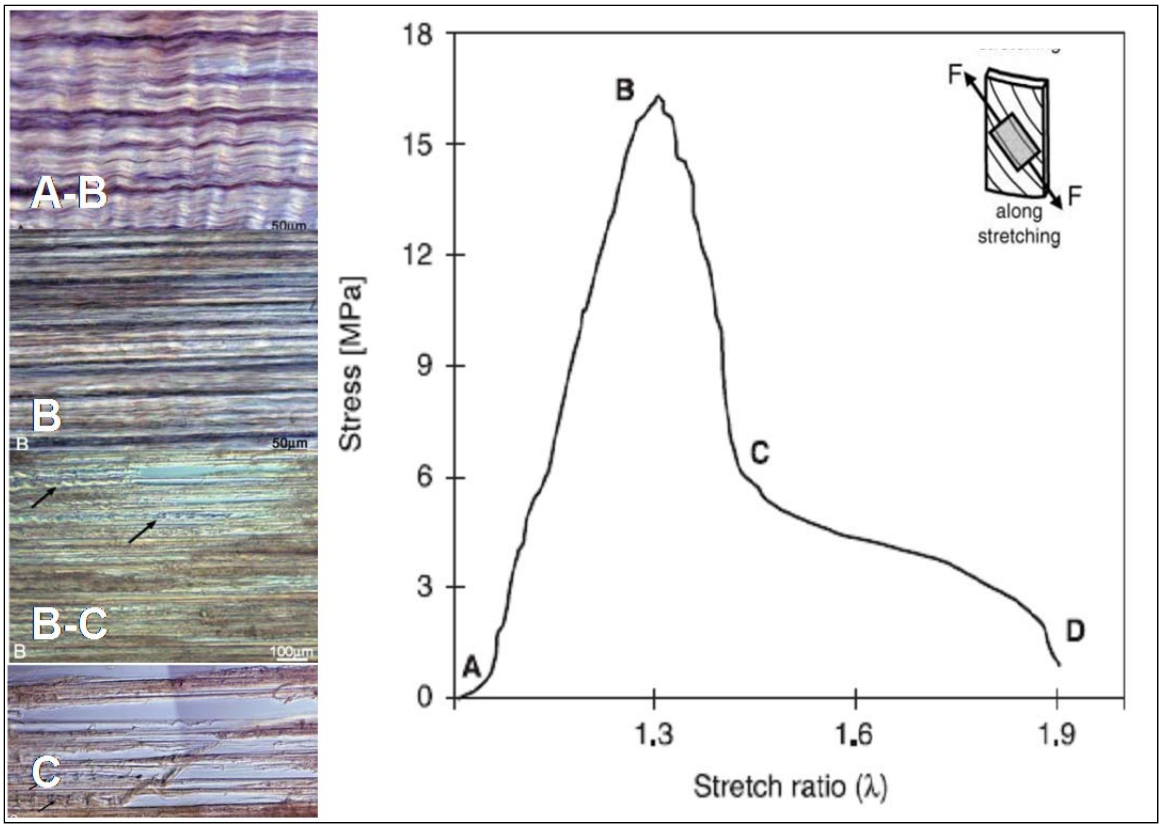

Figure 2.10: Typical stress/strain response obtained from a sample stretched in the aligned direction using continuous loading (A-B) In phase crimp progressively straightened (B) Isolated bundle sliding within intact arrays (B-C) Progressive increase in bundle sliding and separation throughout array (C) Beginning of reduced stress region from large-scale separation of fiber bundles. Adapted from [85].

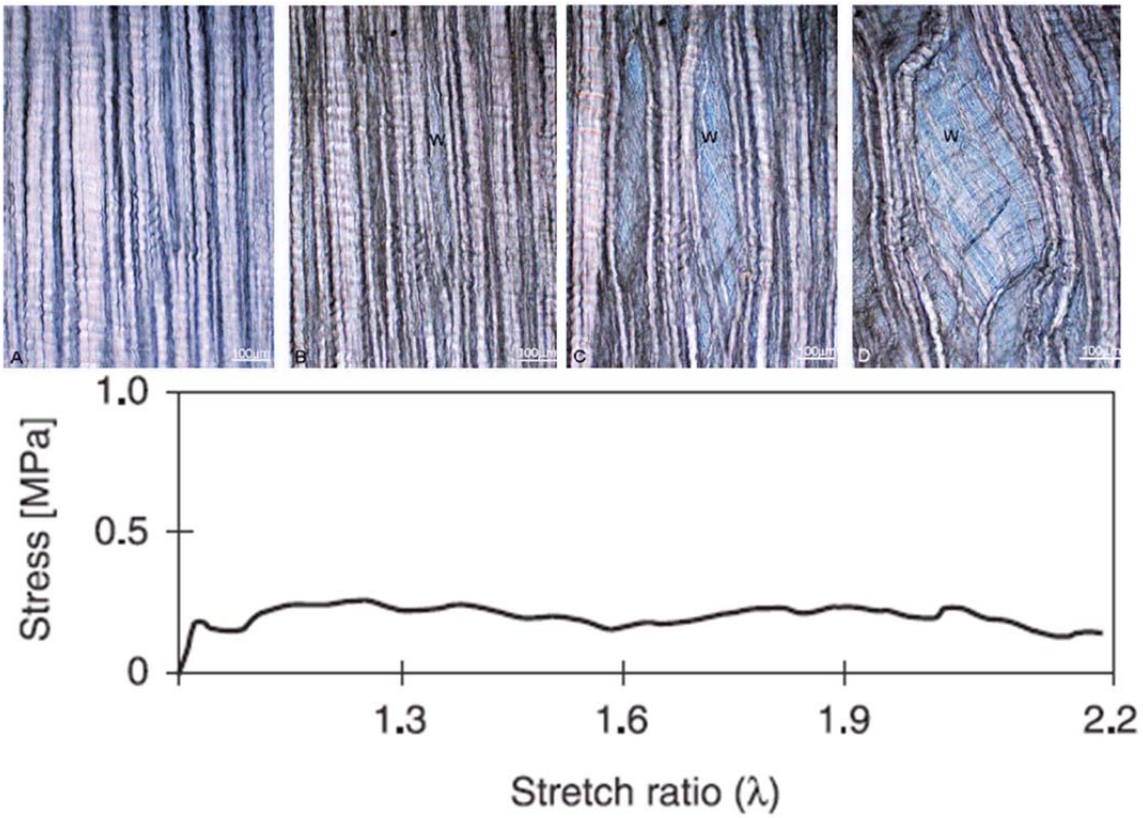

Figure 2.11: The matrix in A is subjected to progressive transverse stretching in B to D to reveal an extensive interconnecting structure in the cleft region marked W. Adapted from [85].

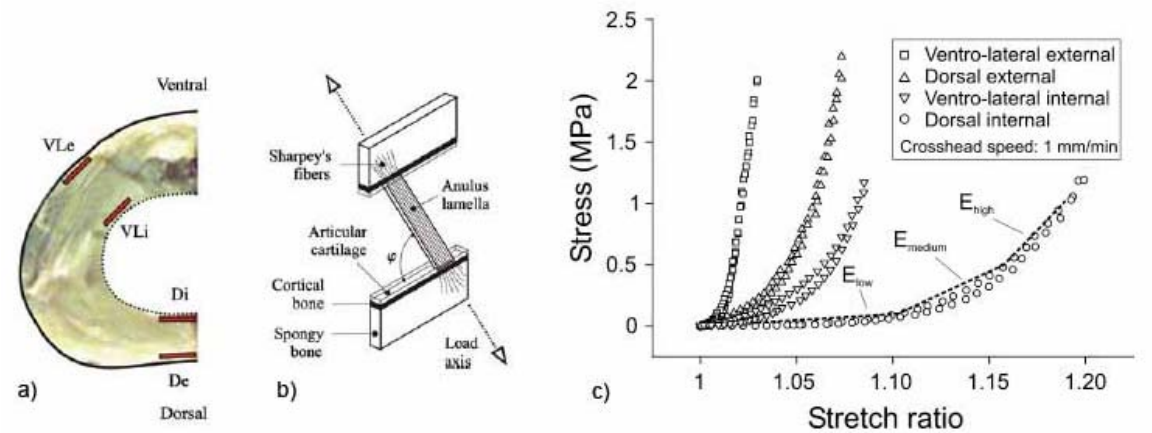

Figure 2.12: (a) Axial section of samples with four single lamellar specimens from the ventro-lateral external (VLe), ventro-lateral internal (VLi), dorsal external (De), dorsal internal (Di) regions used by Holzapfel et al. (b) Schematic diagram for a specimen from the VLe, VLi, De, or Di region. (c) Cyclic engineering stress–stretch responses of four single lamellar AF specimens for a crosshead speed of 1 mm/min. Adapted from [35].

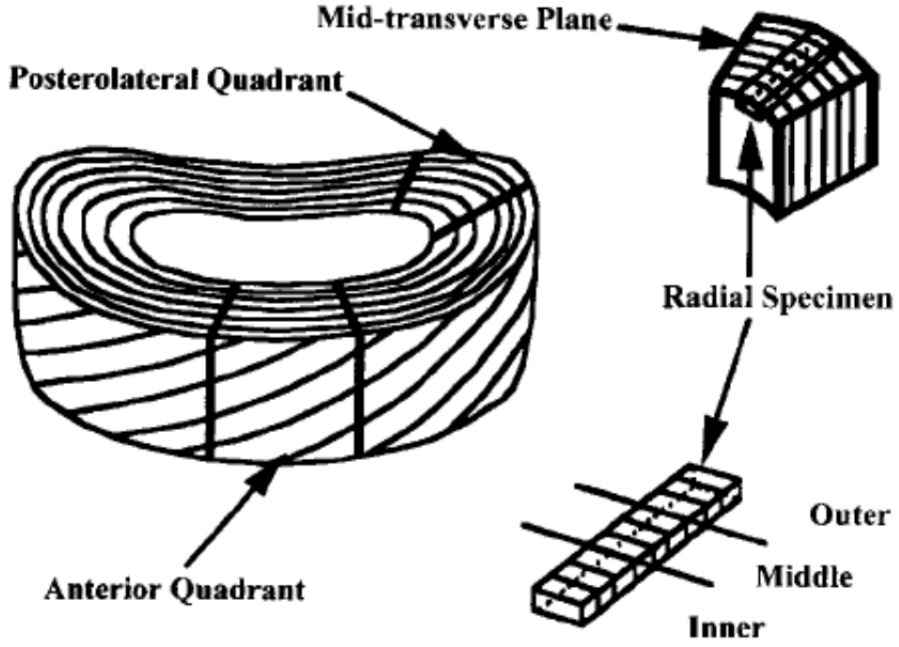

Figure 2.13: Schematic illustration of the dissection and preparation of radial tensile specimens in Fujita et al. (1997) study. Reprinted from [86].

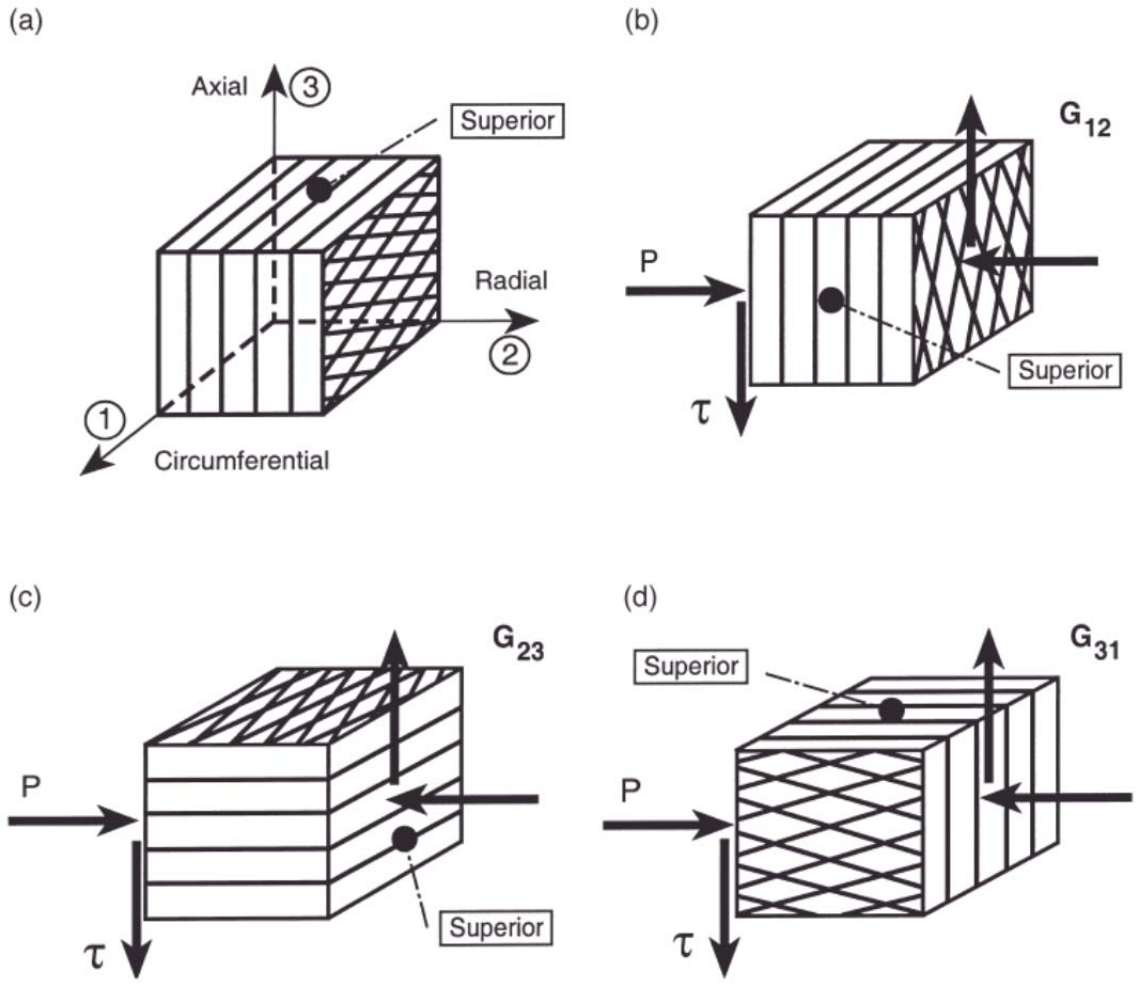

Figure 2.14: Orientation of cube specimens in order to determine shear modulus in study performed by Fujita et al. (2000). The shear moduli were measured in the plane: perpendicular to the annular lamella and parallel to the horizontal plane (G_{12}), perpendicular to the annular lamella and parallel to the vertical axis of the spine (G_{23}) and of the annular lamella (G_{31}). Reprinted from [88].

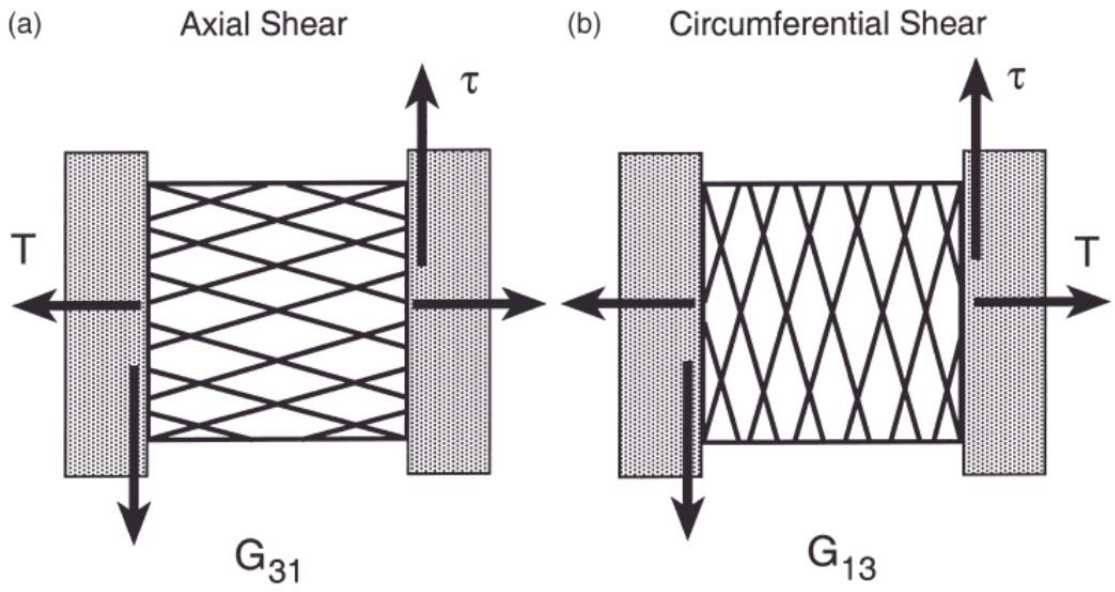

Figure 2.15: Orientation of sheet specimens in order to determine shear modulus in study performed by Fujita et al. (2000). For axial shear (G_{31}) the circumferential axis was aligned with the tensile strain (T) while the shear deformation (τ) was applied in the anatomic axial direction. For circumferential shear (G_{13}) the anatomic inferior–superior axis of the specimen was aligned with tensile strain and the shear deformation was applied in the anatomic circumferential direction. Reprinted from [88].

Table 2.5: Failure stresses and strains of single lamellae annular specimens by anatomic region (Mean ± SD) reprinted from Skaggs et al. [73].

Location	Sample size	σ_f [MPa]	ε_f [%]
AO	(n = 6)	10.3 ± 8.4	9.2 ± 3.4
AI	(n = 9)	3.6 ± 2.0	11.3 ± 6.3
PO	(n = 5)	5.6 ± 3.2	12.7 ± 2.7
PI	(n = 4)	5.8 ± 2.9	15.4 ± 3.0

A = anterior, P = posterolateral, O = outer, I = inner.

Table 2.6: Elastic tensile modulus of single lamellae annular specimens by anatomic region (Mean ± SD) reprinted from Skaggs et al. [73].

	Anterior	Posterolateral	Average
Outer	136 ± 50	82 ± 43	108 ± 67
Inner	76 ± 50	59 ± 41	67 ± 45
Average	106 ± 72	70 ± 42	

Table 2.7: Elastic moduli of single lamellar AF specimens at locations ventro-lateral external (VLe), ventro-lateral internal (VLi), dorsal external (De), and dorsal internal (Di) tested with a crosshead speed of 1 mm/min. Adapted from [35].

Location	E_{Low} [MPa]	E_{Medium} [MPa]	E_{High} [MPa]
VLe	5.96 ± 3.05	32.5 ± 12.1	77.6 ± 20.0
VLi	3.79 ± 2.61	13.9 ± 8.13	27.5 ± 12.8
De	8.01 ± 6.5	24.1 ± 12.3	64.8 ± 48.6
Di	3.8 ± 5.02	14.0 ± 8.63	31.2 ± 19.8

Table 2.8: Tensile radial properties as a function of annular region (mean ± standard deviation) from Fujita et al. (1997) study). Adapted from [86].

	Mean (n=183)	Inner (n=59)	Middle (n=60)	Outer (n=67)	Anterior (n=89)	Posterolateral (n=97)
Tangent Modulus, MPa	0.47 ± 0.33	0.44 ± 0.46	0.64 ± 0.46*	0.42 ± 0.45	0.49 ± 0.47	0.51 ± 0.48
Yield Stress, MPa	0.23 ± 0.13	0.25 ± 0.13	0.27 ± 0.13	0.21 ± 0.13	0.24 ± 0.19	0.24 ± 0.2
Yield Strain	0.8 ± 0.4	0.89 ± 0.38	0.74 ± 0.39	0.77 ± 0.41	0.79 ± 0.38	0.81 ± 0.39
Ultimate Stress, MPa	0.3 ± 0.16	0.34 ± 0.23	0.33 ± 0.23	0.28 ± 0.16	0.32 ± 0.19	0.31 ± 0.2
Ultimate Strain	1.24 ± 0.66	1.39 ± 0.61	1.02 ± 0.62*	1.32 ± 0.62	1.25 ± 0.66	1.23 ± 0.69

* Significant difference ($p<0.01$) between middle and both inner and outer regions.

Table 2.9: Shear moduli for cube specimens (kPa, mean ± standard deviation) in study performed by Fujita et al. (2000). G_{31} is greater than G_{12}, p = 0.01. Adapted from [88].

	G_{12}	G_{23}	G_{31}
Overall (n = 30)	25.34 ± 16.8	32.12 ± 18.4	56.04 ± 36.3
Anterior (n = 14)	28.92 ± 8.4	40.16 ± 8.0	58.86 ± 18.4
Postero-lateral (n = 16)	22.20 ± 8.4	25.10 ± 8.5	53.60 ± 18.4

Table 2.10: Shear moduli for sheet specimens (kPa, mean ± standard deviation) in study performed by Fujita et al. (2000). Adapted from [88].

Pre-Strain	Harvest Site					
	Inner (n = 18)		Middle (n = 20)		Outer (n = 20)	
	Axial	Circum.	Axial[a]	Circum.	Axial[a,b]	Circum.
0%	73.4 ± 32	61.0 ± 36	137.4 ± 96[c]	54.8 ± 22	223.6 ± 112[c]	110.6 ± 56
5%	88.2 ± 48	71.0 ± 36	159.6 ± 92	69.2 ± 34	324.0 ± 99	124.0 ± 60
10%	97.2 ± 60	72.2 ± 36	193.6 ± 104	76.2 ± 32	461.0 ± 174	138.6 ± 64

[a]:Axial > circumfernteial, $p < 0.001$

[b]: 0%<5%<10%, $p<0.001$

[c]: Inner>middle>outer, $p<0.001$

2.5. Intervertebral Disc Degeneration

Intervertebral disc degeneration occurs in everyone, to at least some extent. Miller et al. (1988) showed that by age 49, 97% of lumbar IVDs showed some evidence of disc degeneration [7]. It is not uncommon that disc denegation is asymptomatic and a person is unaware of the ailment [89, 90]. It is not clearly understood who is at risk for severe and early onset degeneration which causes pain. Male discs degenerate earlier than female discs and also have more degeneration than their age-matched female counterparts [7]. Disc degeneration can also be exasperated by smoking, "heavy lifetime occupational and leisure physical loading," exposure to whole body vibrations and there may also be a genetic predisposition to degeneration [91-94]. There is an 80% lifetime prevalence of lower back pain (LBP) and 14% (or 31 million) Americans suffer from LBP at any given time with an estimated cost of up to $50 billion [2-6]. There are 1,800,000 days of work missed yearly due to a combination of LBP, neck-shoulder pain, and neck plus LBP in the United States [3].

The IVD can be subject to degenerative changes caused by normal aging as well as injury, loading or genetically induced accelerated disc degeneration [95]. The exact mechanism of IVD degeneration is not well understood and is a broader topic of study in the literature, and will not be addressed in the scope of this thesis. IVD degeneration is characterized by mechanical changes, biological degradation, and loss of nutritional pathways. "Understanding mechanical failure mechanisms in the annulus fibrosus due to loading will allow researchers to predict damage propagation and to isolate mechanical damage from biological degradation in the degeneration process" [96].

2.5.1. Biochemical Changes Associated with Degeneration

The intervertebral disc experiences irreversible chemical and structural changes due to aging and degeneration. As the IVD ages, blood vessels in the endplates become less numerous and can completely disappear by age 30 [11]. The most substantial change in macromolecules due to degeneration is the loss of PGs [97]. This decrease in the amount of PGs in the disc causes a reduction in the osmotic pressure and the water content. This reduction of the hydration in the disc, changes its shape and volume, which affects the ability to absorb and distribute loads effectively [11]. Olczyk (1993 and1994) correlated the changes in IVD PG and GAG with age, Figure 2.16 [98, 99]. The study showed that in both the AF and NP, PG content decreases starting from birth.

IVD degeneration is also accompanied by a loss of collagen; the physical as well as chemical properties of collagen change with age. Olczyk (1992) correlated the changes in IVD collagen with age (Figure 2.16), showing that significant age-related changes in the solubility of disc collagen was found [100]. The age related decrease in collagen solubility has been attributed to an increase in intermolecular cross-links [101]. Olczyk also found that the total amount of collagen in the IVD of normal subjects increases significantly during the first 5 decades of life and subsequently remains at the same level [100]. It was also found that the aging process is accompanied by an increase in the insoluble collagen content in the AF. The AF contains mainly type II collagen with significantly less type I collagen and only trace amounts of type III collagen [100]. The quantity of type II collagen gradually increased between 1 and 45 years and remains almost unchanged after that [100].

2.5.2. Mechanical Changes Associated with Degeneration

The biochemical compositional changes in the disc alter mechanical behavior of the disc. The loss of PG has a major effect on the behavior of the disc. The NP becomes more stiff and is less able to dissipate energy [72]. Intradiscal pressure measurements in degenerated discs are lower than those of normal discs and the pressure within the degenerated disc is unevenly distributed in the superior/inferior and lateral directions [102]. This could cause high stresses at specific points in the disc, causing the development of localized tissue damage [11]. As the NP degenerates, the AF plays a more prominent role in the absorbing the load [103]. However, since the AF is also affected by degeneration and a loss of PG content, the AF becomes more stiff and weaker as well which can lead to failures [62, 74]. Due to the localization of the biomolecular components in the IVD, the different mechanical responses and damage patterns associated with disc degeneration are likely related to the local molecular breakdown of the tissue [97].

Enzyme treatments have been used with mechanical testing to explore mechanical properties of different connective tissues in terms of the contributions of macromolecules, for example elastin and GAGs [104, 105]. There have been studies that have experimentally explored if degradation of these specific macromolecules have an effect on the IVD's mechanical behavior and perhaps may contribute to the progression of degeneration.

Smith et al. (2008) investigated the mechanics of radial AF samples that have been subjected to an enzymatic digestion in either elastase or chondroitinase ABC [106]. Radial samples (Figure 2.17) were tested in one of three groups: control, elastase and

chondroitinase ABC (nonhuman, derived from bacteria). The chondroitinase ABC group was included in order to account for the fact that elastase can have an effect on GAGs [106]. The control samples were soaked in 0.15 M phosphate buffer saline for 1 hour prior to testing. The elastase group was soaked in 3 U of high purity pancreatic elastase in 1 mL of 0.2 M Tris–HCl (pH 8.6) with protease inhibitors (10 mM N-ethylmaleimide and 5 mM benzamidine hydrochloride). The chondroitinase ABC group's solution consisted of 1 U of chondroitinase ABC in 1 mL of 0.05 M Tris–HCl plus 0.06 M sodium acetate buffer (pH 8.0) with protease inhibitors (10 mM N-ethylmaleimide and 5 mM benzamidine hydrochloride and 1 mM phenylmethanesulfonyl fluoride). Both enzyme soaks were carried out for 36 hours at 37°C. The samples were mechanically tested in tension with a strain rate of 0.0025 s^{-1}. The initial and ultimate elastic moduli as well as extensibility of the sample, the intersection of the moduli tangent lines, were determined for each sample from the quasi-static stress-strain curves (Figure 2.18).

By degrading the elastin fibers there was a significant reduction in both the initial modulus and the ultimate modulus, and a significant increase in the extensibility of the radial AF samples. The elastase treatment did result in non-specific degradation of collagen [106]. It was shown that elastin is important in the initial toe-region of the stress-strain curve as it aids in de-crimping of the collagen bundles, an important factor in energy absorption of the tissue [62, 106]. Following treatment with chondroitinase ABC, specimens also had a significant reduction in initial modulus and increase in extensibility, however there was no significant change in ultimate modulus.

A more recent study investigated the effects of enzymatic degradation of GAGs and elastin on AF shear mechanical properties. Using bovine caudal discs, Jacobs et al.

(2011) obtained circumferential and radial AF samples (Figure 2.19) and in each orientation assigned to one of 4 groups (n = 6 per group): untreated, 0.15 M phosphate buffered saline (PBS) control, chondroitinase- ABC treatment (ChABC), and elastase treatment (elastase) [107]. Enzymatic treatments followed the same protocols as previously described [106]. The shear modulus for all the samples were determined as well as the GAG content using the dimethylmethylene blue (DMMB) assay for 2% pre-strain in both orientations as well as at 10% pre-strain in the circumferential direction.

The study showed that the effect of pre-strain on the circumferential samples was significant; the circumferential 2% pre-strain shear modulus was 8 times higher than the 2% radial shear modulus and 44 times higher than the circumferential 10% pre-strain modulus (Figure 2.20). The only group to show a significant different in the radial shear modulus was the PBS treatment group. However, there was no difference in the circumferential shear modulus between the untreated and PBS groups. The DMMB assay was used to determine the GAG removal, with both the radial and circumferential orientations being pooled together for the results. The PBS group had a 51% decrease in compared to untreated ($p < 0.05$). The ChABC treatment resulted in a reduction of 36% ($p < 0.05$) and elastase treatment a reduction of 70% ($p < 0.05$) compared to PBS control [107].

The authors hypothesize that if the ChABC was able to more fully degrade annulus GAG (it was unable to degrade keratin sulfate), the increase in modulus with respect to PBS treatment may have been greater [107]. They suggest that interactions between GAG and collagen *increases* overall stiffness when GAG is selectively digested. The elastase treated samples did not affect the circumferential shear modulus

which supports the hypothesis that it is dominated by collagen fiber stretch. However the elastase group had less GAG than the PBS or ChABC treated groups, which could indicate that elastic fibers provide a smaller mechanical support to AF in shear [107].

2.5.3. Annular Tears

Annular tears are frequently observed on magnetic resonance images (MRI) in patients with LBP [17]. Lower back pain could be attributed to impingement on nerves due to excessive deformation of the AF due to tearing; the meningeal nerve and branches from the ventral ramus of the somatic spinal nerve both innervate the AF [17, 21]. If annular tears occur, these nerve endings could be irritated by acid metabolites contained in the herniated disc material. Annular tears or disc herniation could be responsible for lower back pain even without nerve root compression [17]. There are three types of annular tears: peripheral or rim lesions, circumferential (concentric) and radial (Figure 2.21). Peripheral tears are discrete tears of theater layers of the annulus fibrosus, parallel and adjacent to one or both end-plates [108]. These usually lead to circumferential tears, seen as separation of the individual annular lamellae. Circumferential tears are the most common annular defect. Radial tears happen with more advanced degeneration, forming clefts with radiate from the nucleus pulposus to the outer lamellae of the annulus in a plane parallel or oblique to the endplate [108]. Peripheral tears are more frequent in the anterior disc, circumferential tears are seen equally in the anterior and posterior parts of the AF, while radial tears are almost exclusively seen in the posterior AF [108]. Failure initiation and propagation of the tears has been simulated with compressive and bending forces [18].

Formation of annular tears, dehydration of the NP, and fissure formation in the cartilage end plate are the main early macroscopic features that characterize disc degeneration [18]. Mechanical stress applied to the disc appears to accelerate the development of all degenerative changes [18]. Animal models of disc degeneration exist in the literature. Key and Ford [109] studied the progression of a transverse surgical incision on the AF of a canine IVD and found that nuclear prolapse occurred and also that the original gelatinous NP turned into a more structured matrix. A rabbit model was used by Smith and Walmsley [110] to study the healing processes in a motion segment that was transversely cut into the NP. They concluded that healing occurred only in the superficial layers [110]. Osti et al. [108] studied disc degeneration in an ovine model in which a rim lesion was surgically introduced in the AF. They found that the discrete peripheral tears led to progressive failure of the inner AF [108].

2.5.4. Intervertebral Disc Disruption and Herniation

The most common IVD disorder or injury is a herniated disc (Figure 2.22) [97]. A herniation is characterized by the ejection of the NP through the AP and can be classified as either a protrusion or prolapse [111]. A protrusion is when the nuclear material is still encased in the AF but there is an annular bulge with extends into the spinal canal in the posterior direction. A prolapse is when the NP actually extrudes through the AF and into the spinal canal.

It has been shown that during protrusion and eventual prolapse, the NP is pressed against the inner layers of the AF until clefts form in the lamellar at the weakest location, allowing nuclear material to propagate through to the adjacent layer of AF [112, 113]. Clinically, herniation's of the disc are usually observed in the posterior or posterior-

lateral direction of the IVD [114, 115]. It has been hypothesized that this is due to the greater number of incomplete layers found in the posterior region of the annulus which could cause a reduction in its strength relative to the anterior annulus [14, 36].

There have been *in vitro* studies which have explored which loading conditions can cause herniation of the IVD. Adams & Hutton (1982) showed that that static hyperflexion combined with compression can initiate herniation and delamination [116]. Gordon et al. (1991) also showed that it can be caused by repetitive compressive loading and combined flexion [117]. There have been multiple studies indicating that repetitive flexion combined with compression will lead to herniation [118-120].

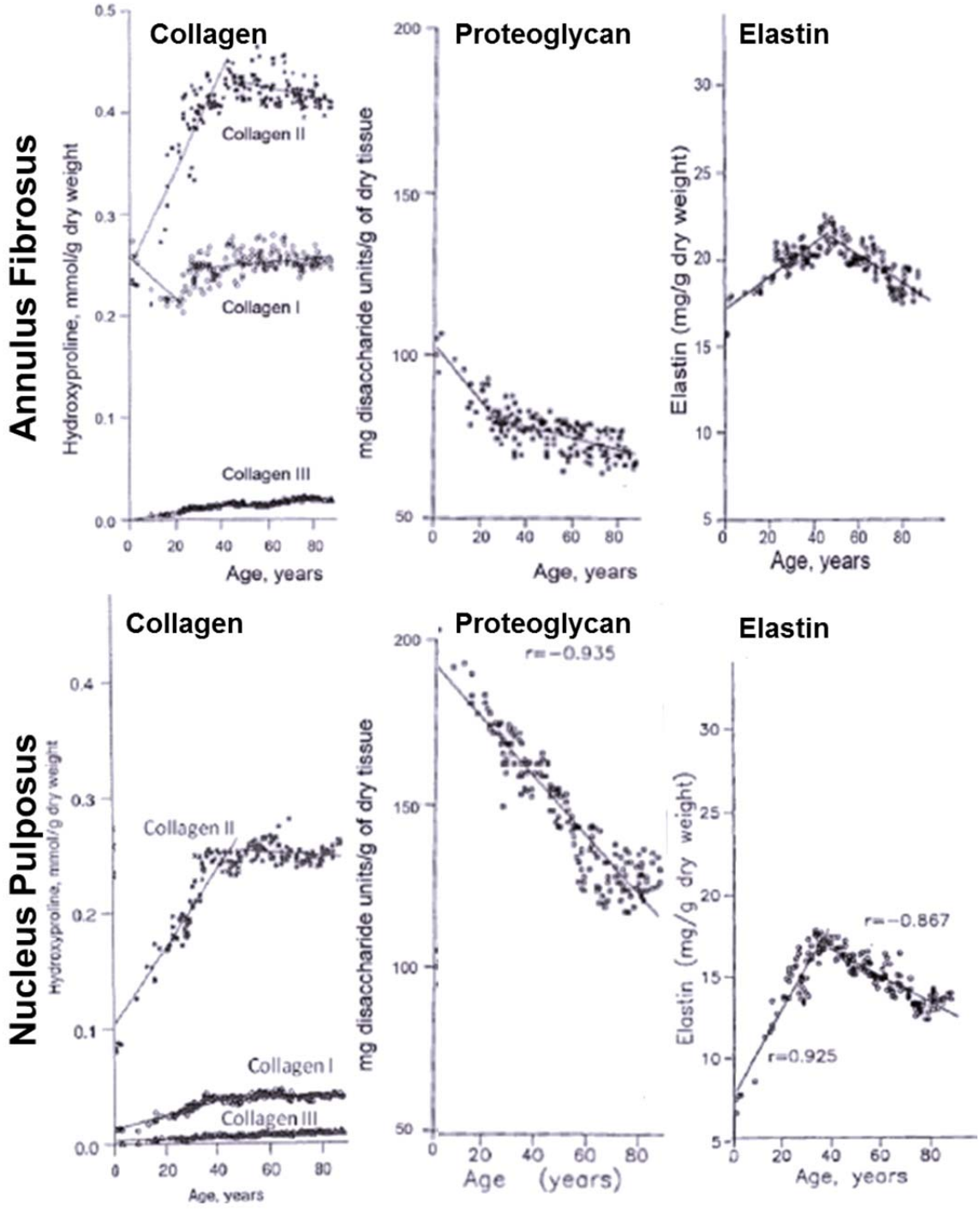

Figure 2.16: Changes in the major macromolecule concentrations (collagen, proteoglycan, and elastin) in the IVD with aging: annulus fibrosus (top) and nucleus pulposus (bottom). Adapted from [98-100, 121].

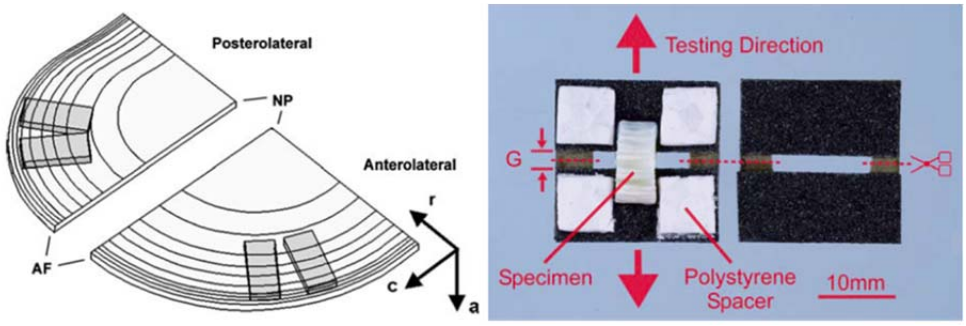

Figure 2.17: Left: Schematic representation of specimen harvest sites in the anterolateral and posterolateral quadrants of the annulus fibrosus in Smith et al. (2008) study. Right: Image of sandpaper mounting frame with specimen prior to assembly and testing. G = gauge region; dotted lines = cutting zones following placement in the mechanical testing system grips. Reprinted from [106].

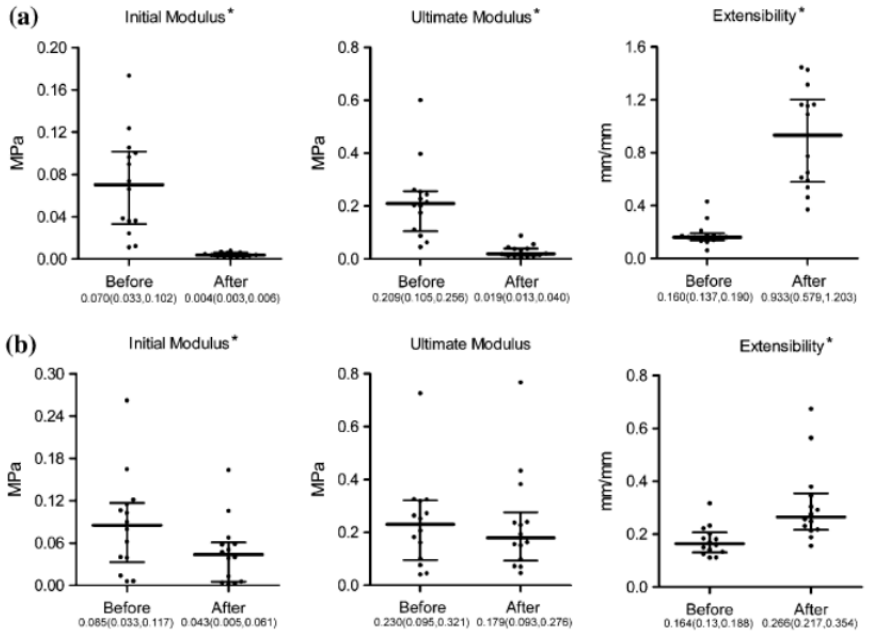

Figure 2.18: Results of tensile testing study of radial samples of annulus fibrosus by Smith et al. Initial modulus, ultimate modulus, and extensibility before and after (a) elastase treatment and (b) chondroitinase ABC treatment. * Indicates significant difference between control and treatment, $p < 0.001$. Reprinted from [106].

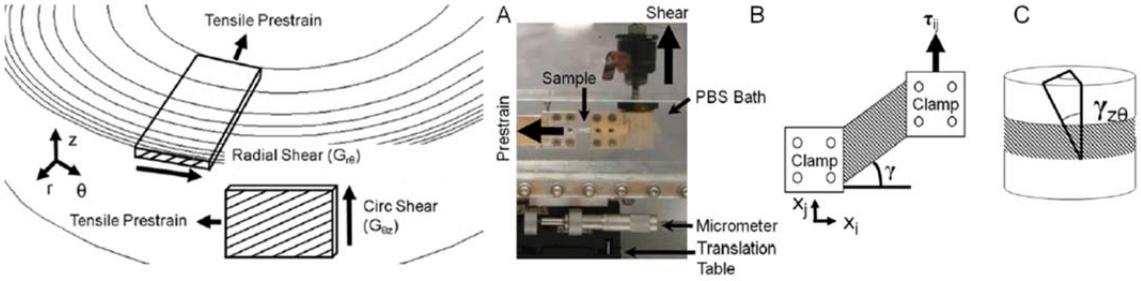

Figure 2.19: Left: Schematic representation of specimens of the annulus fibrosus in Jacobs et al. (2011) study where, $G_{r\theta}$ = radial shear modulus and $G_{\theta z}$ = circumferential shear modulus, and z = spine axial direction Right: (A) Shear testing device (B) Schematic illustration of boundary conditions (C) Schematic illustration of the shear deformation when the intervertebral disc is subjected to torsion. Reprinted from [107].

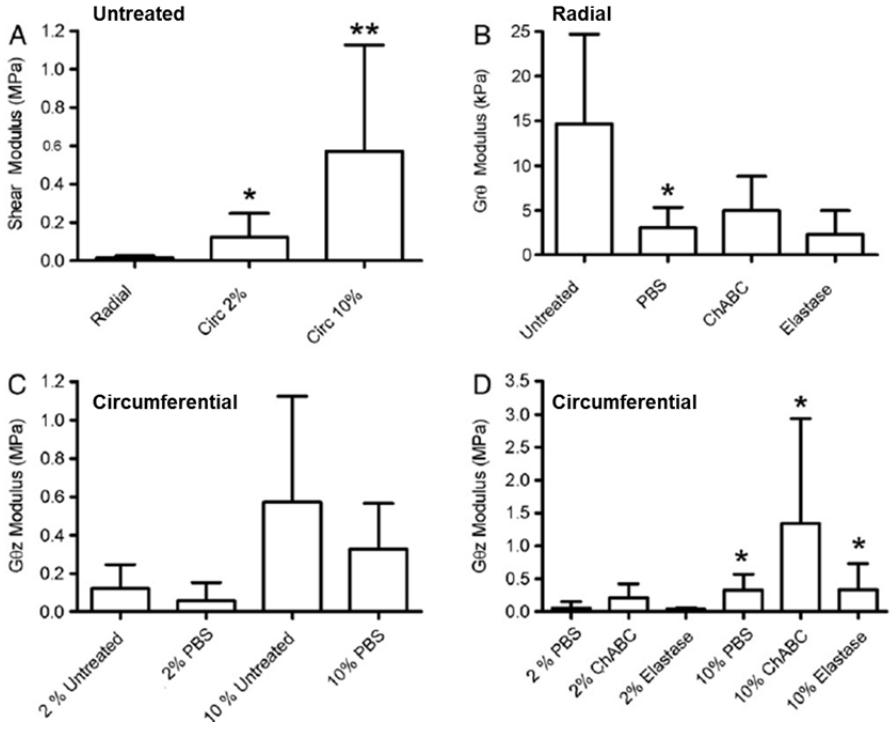

Figure 2.20: Shear modulus of annulus fibrosus in Jacobs et al. (2011) study. (A) Untreated; * significant radial, **significant radial and 2% circ (B) treated Radial; *significant untreated (C) Cirum untreated vs PBS (D) treated circumferential. *significant to same group at 2% pre-strain. Adapted from [107].

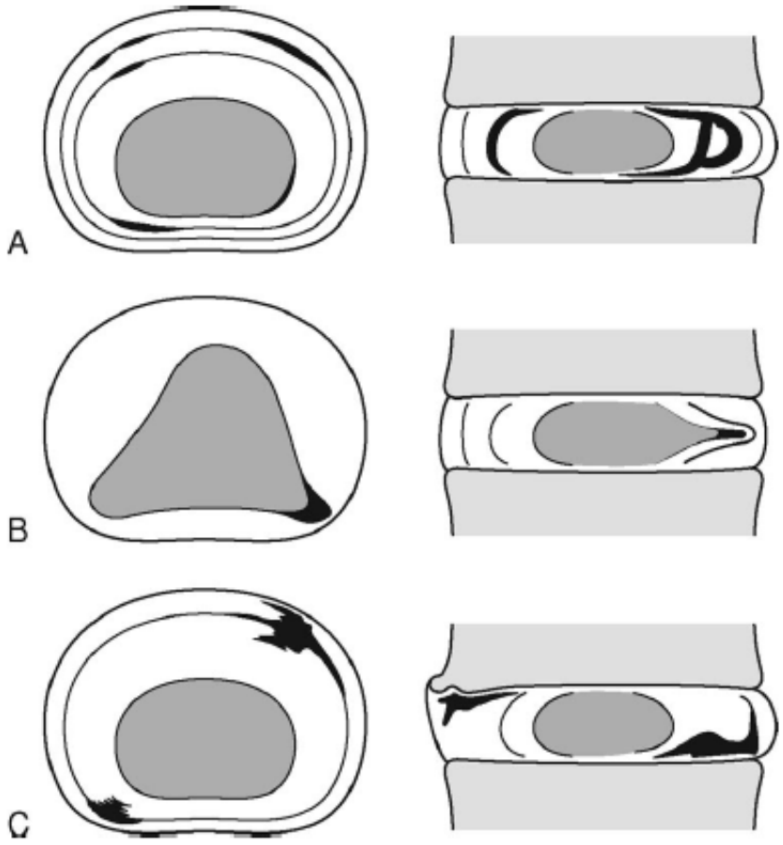

Figure 2.21: Three types of annular tears: (A) circumferential or delamination, (B) radial, (C) peripheral rim lesion. Reprinted from [122].

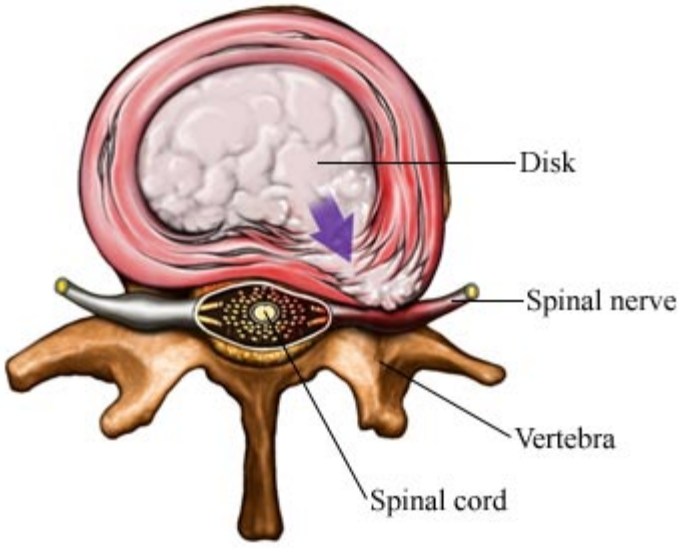

Figure 2.22: Representative drawing of a herniated disc. © 2011 Nucleus Medical Media, Inc. Reprinted from http://www.aurorahealthcare.org/yourhealth/healthgate/images/FX00004.jpg.

2.6.Fiber Reinforced Composite Materials

A composite material (CM) is a combination of two materials in which one of the materials, called the *reinforcing phase*, is in the form of fibers, sheets, or particles, and are embedded in the other materials called the *matrix phase*. CMs are used because overall properties of the composites are superior to those of the individual components. The reinforcement system in a CM determines the achievable properties. It is common to classify composites according to these characteristics of the reinforcement, including the shape, size, orientation, composition, distribution, and manner of incorporation of the reinforcement. They can be classified by their geometry of the reinforcement: either particle reinforced (a particulate composite) or fiber reinforced (a fibrous composite).

Fibers have a very high aspect ratio of length to diameter compared with particles and whiskers, and the smaller the diameter, the greater is the strength of the fiber due to a reduction in surface flaws. Many properties of a composite are determined by the length, orientation, and volume fraction of fibers of a given type. CMs can be made using continuous fibers or short discontinuous fibers (Figure 2.23). Fibers are often manufactured as continuous filaments, with diameters in the range of 5 to 50 μm, which are used to fabricate continuous-fiber composites. Filaments can be cut to form short fibers ranging in length from 3 to 50 mm that are used to make discontinuous or short-fiber composites, more commonly for low-cost applications or small intricate parts.

The continuous fibers can be in the matrix in a single layer in which they are aligned in a single direction. These unidirectional composites are very strong and stiff in the fiber direction, but not as much in the transverse direction. Short fiber composites are less advantageous due to the presence of fiber ends which cause lower stiffness values

and strength than the continuous fibers. An advantage of short fiber composites are that since they are more likely to fail by propagation of a single crack, fracture mechanics (FM) and single crack growth techniques can be used for modeling [123]. Mandell [124] stated that most data for short fiber composites in the literature are in regards to commercially significant types: random chopped-strand-reinforced thermosets with glass fibers, discontinuous fibers aligned in a unidirectional layer and injection-molded reinforced thermoplastics.

Continuous and short fibers can be oriented in one, two, or three dimensions, resulting in unidirectional, planar, and random reinforcement systems. The volume fraction of fibers oriented in a given direction strongly affects the physical properties of a composite in that direction. Unidirectional and planar reinforced composites are anisotropic. Laminate composites are a type of fiber-reinforced composite consisting of anisotropic layers or plies bonded together that can differ in relative fiber orientation and volume fraction. This allows high-fiber-volume fractions and three-dimensional orientation not achievable in isotropic short-fiber composites [125].

The matrix serves several important functions in a CM. It holds the fibers or particles in place; in oriented composites it maintains the preferred direction of fibers. The matrix transfers the applied load to the reinforcement and redistributes the stress. When used with brittle fibers, the matrix helps increase fracture toughness because it is typically of a lower stiffness material and can tolerate greater elongation and shear forces than the reinforcement [125]. The matrix also determines the environmental durability of the composite by resisting and protecting the reinforcement from chemical and thermal stresses [125].

The transfer and distribution of stresses from the matrix to the fibers occur through the separating interface. The area of the interface and the strength of the bond affect the final composite properties and long-term property retention [126]. Interfacial shear strength determines the fiber-matrix de-bonding process. Strong interfaces in polymer matrix composites make ductile matrices very stiff but also lower the fracture toughness. Weak interfaces in a ceramic matrix make brittle matrices tough by promoting matrix crack but also lower strength and stiffness [127].

2.6.1. Physical Properties

CMs can be designed to have a wide range of physical and biochemical properties. There are three approaches to predicting the basic mechanical properties of a composite [127, 128]: mechanics of materials models, theory of elasticity models and semiempirical models.

The mechanics of materials model uses analytical equations to determine the properties using simplifying assumptions about the stress and strain distribution in a representative volume element of the composite. The rule of mixtures equations for composites is where properties are relative to the volume fraction of the fibers and matrix. The rule of mixtures is useful in estimating the upper and lower values of mechanical properties of an oriented fibrous composite, where both the matrix and fibers are isotropic orthotropic, respectively. The equations for composite moduli can be given as below, where E and G are the elastic and shear moduli, respectively.

$$\boldsymbol{E_{1C} = E_{1f}V_f + E_mV_m} \tag{2.i}$$

$$\frac{\boldsymbol{1}}{\boldsymbol{E_{2C}}} = \frac{\boldsymbol{V_f}}{\boldsymbol{E_{2f}}} + \frac{\boldsymbol{V_m}}{\boldsymbol{E_m}} \tag{2.ii}$$

$$\frac{\boldsymbol{1}}{\boldsymbol{G_{12C}}} = \frac{\boldsymbol{V_f}}{\boldsymbol{G_{12f}}} + \frac{\boldsymbol{V_m}}{\boldsymbol{G_m}} \tag{2.iii}$$

The rule of mixtures equations assumes strain compatibility between the phases, which is unlikely due to the different Poisson's ratios of the elements. These equations are used to predict experimental results in unidirectional composites. A limitation occurs when the matrix material yields, and the stress becomes constant in the matrix while continuing to increase in the fiber [125]. In the *Theory of Elasticity Models*, no assumptions are made about the stress and strain distributions per unit volume. The fiber geometry and the difference in Poisson's ratio between the fiber and matrix is taken into account. Curve-fitting parameters are used in semi-empirical and generalized equations to predict experimental results.

2.6.2. Failure Mechanisms

Damage process and failure modes in unidirectional laminates, depend on the loading conditions (tension or compression), and on direction of applied load (parallel or at some angle to the fiber direction). For the case where the fatigue load is applied parallel to the direction of the fibers, breaks occur at initial defects in the fibers. These isolated fiber breaks may lead to cracking of the surrounding matrix region, plasticity of the surrounding matrix, or de-bonding between the fiber and the matrix material.

Talreja (1987) suggested that the matrix undergoes a fatigue process of crack initiation and crack propagation in which the cracks align in an orientation perpendicular to the applied tensile stress [129]. If the strains are larger than some threshold value, the cracks cause breaks in the fibers and are able to propagate. Failure occurs when enough adjacent fiber breaks coalesce to cause instability and crack propagation without increasing the load. Talreja also stated that different mechanisms may dominate for different cyclic strain ranges [129]. The lower limit to Figure 2.24 corresponds to the

fatigue limit of the matrix material, ε_m, the strain below which cracks in the matrix remain arrested by the fibers. The upper strain limit is the strain-to-failure of the composite, ε_c. Talreja suggests that the third region of the fatigue-life diagram is where a progressive failure mechanism is dominant. Within the region, matrix cracking and fiber-matrix interfacial shear failure lead to strain-dependent damage. For off-axis fatigue loading of unidirectional continuous fiber composites, cracks along the fiber-matrix interface are subjected to mixed-mode loading conditions. The limiting value of the crack opening displacement and fatigue depends on the off-axis angle.

The damage mode in continuous fiber laminated CMs is matrix cracking. Matrix cracks initiate in directions perpendicular to the fibers (transverse direction) in plies which experience tensile stresses greater than the strength of the ply. Crack initiation is estimated by laminate analysis combined with a failure criterion (maximum strain, maximum stress, or the Tsai-Wu criterion). Moderate amounts of micro-cracking have a small effect, or even no effect, on the strength of a lamina or laminate [123]. However, global stiffness can be drastically affected by the formation of micro-cracks. Under cyclic loading conditions, micro-cracks play a critical role in the development of subsequent damage; fiber fracture can develop in adjacent plies near the matrix crack tips. De-bonding can also occur near the broken fiber ends [123].

A unique characteristic of fiber fracture is that an individual fiber can break many times inside a CM system. The matrix material around the fibers holds the ends of the fibers that break, and transfers stress back into these fibers by shear forces along the length of the fiber. Fiber fracture is also highly coupled; it is interactive with other fiber

fractures, matrix cracking, and delamination, and the interactions are influenced by the coupling between the fibers and the matrix materials.

Damage occurs at the microscale in CMs with fiber rupture in tension and fiber buckling in compression, possibly accompanied by microcracks in the matrix (Figure 2.25). At the mesoscale, damage processes are fiber-matrix debonding and transverse matrix cracking. Damage is also present at the macroscale where macroscopic debonding of mesoscale characteristics occur (delamination).

The basic mechanical behavior of composite laminates can be examined by first looking at the behavior of a single lamina. A unidirectional single lamina loaded longitudinally has a behavior governed by the fibers. Therefore, the response is usually elastic-brittle with almost no plasticity [130]. The fiber strength governs the lamina strength in the longitudinal direction. In single unidirectional laminas loaded longitudinally in compression the behavior is also governed by fiber properties; however, the interaction with matrix behavior is stronger than in the case of unidirectional tension. In the case of a single lamina loaded transversely, the behavior is matrix dominated and failure occurs due to transverse matrix cracking.

2.6.2.1. Fiber-Matrix Debonding

The Fiber-matrix interface is important in the mechanical behavior of CMs as load transfers from the matrix to the fibers. The failure mechanics of the fiber-matrix interfaces change the mechanical response of the composite and can be the initiator of the damage processes [130]. In order to have high modulus and high strength, there must be strong adhesion between the fibers and matrix.

To measure interface resistance experimentally, there are numerous methods including the single fiber pull-out and the single fiber push-out or pushdown tests. These tests promote a debonding process between the fibers and matrix by moving the fibers with respect to the matrix. Typical values of debonding shear stress for polymer matrix composites derived from pull-out tests are in the range 5-100 MPa [131].

2.6.2.2. Matrix Micro-cracking

The matrix's functions include transferring stresses between fibers, stabilizing fibers when loaded in compression, and increasing the resistance to impact damage. It is difficult to determine *in situ* matrix mechanical properties because the behavior of the matrix when in a fiber-reinforced composite differs from that of the pure matrix material [130]. As stated in section 1.2, polymer matrices are most common and can be divided into two main classes: thermosetting and thermoplastic. Values for two main polymer matrices can be seen in Table 2.11. Mechanical properties of polymer matrices are rate dependent, which can affect both the elastic and inelastic properties [131].

Matrix damage mechanisms control the composite's mechanical behavior in laminas loaded tangentially or in plane shear and is usually the first form of damage which is evident in laminate composites. This can trigger other damage mechanisms, like delamination, which can lead to complete failure of the CM [132]. In cross-ply laminates, the damage initiates in 90° plies which form the cracks perpendicular to the loading (parallel to the fiber in transverse loading).

2.6.2.3. Delamination

Delamination is caused by interlaminar stresses in laminates mainly at the free edges, around holes or nearby internal pre-existent flaws (Figure 2.26). The interlaminar

stresses are formed due to a mismatch in mechanical properties between adjacent layers of the laminate CM. Delamination starts due to tensile loading and can propagate from the edge toward the interior; internal defects then propagate due to delamination which can be activated by compressive loading and subsequent local buckling of the delaminated area [130]. Impact loading can also initiate delamination. Delamination involves mixed-mode propagation in laminate CMs. In order to computational model this phenomenon, first the energy needed to make delamination cracks propagate must be determined (the interlaminar fracture energy, G) experimentally by means of interlaminar fracture tests [133].

2.6.3. Use of Composite Analysis in Annular Mechanics

The AF can be treated as a fiber reinforced composite material, with the collagen bundles acting as the fibers, embedded in a proteoglycan matrix. The structure of the annular lamellae lends itself to be analyzed as an angle-ply laminate structure. Composite theory has been previously discussed, and the well understood concepts can help in understanding of the complex annular tissue. There are however limitations in using composite theory (specifically *Classical Lamination Theory*, CLT) in regard to the AF. There is an assumption of linear elasticity and small strain in composite theory; further, lamination theory assumes that there is no slip between the fibers and matrix, the layers are perfectly bonded, and an average property for the fiber and matrix properties [123-126, 128, 129, 131, 133]. In regards to the AF, this is an oversimplification of the complex molecular interactions and structure [96].

A study by Iatridis and Gwynn (2004) uses composite lamination theory to calculate the stresses in annular layers and interlaminar shear stresses [96]. They assumed

that the AF was a symmetric angle-ply laminate consisting of eight layers. Data from the literature [73, 134] was used for the material constants, Table 2.12, and the fiber and matrix volume fractions used were $V_f = 0.15$ and $V_m = 0.85$, respectively.

The stresses in the 1-2 and *x*-*y* coordinate systems were estimated using CLT when subjected to 10% tensile strain in the *x*-direction (Figure 2.27). It was determined that the longitudinal stress was ~8 MPa and the transverse and in-plane shear stresses were both less than 0.1 MPa (Figure 2.28) [96]. The value for the longitudinal stress was lower than experimental values in the literature (10.3 MPa [73]). The maximum stress in both the fibers and matrix were also found: $\sigma_{f,max} = 54$ MPa, $\sigma_{m,max} = 0.03$ MPa [96].

Interlaminar stresses were estimated based on the CLT results using preexisting methodology [135, 136] and the effect of layer thickness and amount of layers determined. The interlaminar stresses were linear through each layer and had the same maximum values at each $\pm\theta$ interface (Figure 2.29). The interlaminar stresses ranged from 0.4 to 1 MPa, which was within the range of previously reported data in literature [137]. Also, as the number of layers is halved (which doubles the layer thickness), the magnitude of the shear stress increases [96].

2.7. Summary

Initiation and progression of injuries to the IVD, for example disc herniation, is related to the tensile strength of the annular lamellae. The stronger layers will be less susceptible to breakage, while the more weak lamellae will be more easily broken by the NP. Understanding the tensile strength, along with the other mechanical properties, of the AF is necessary to begin to understand how disc injuries are able to begin and propagate through the IVD.

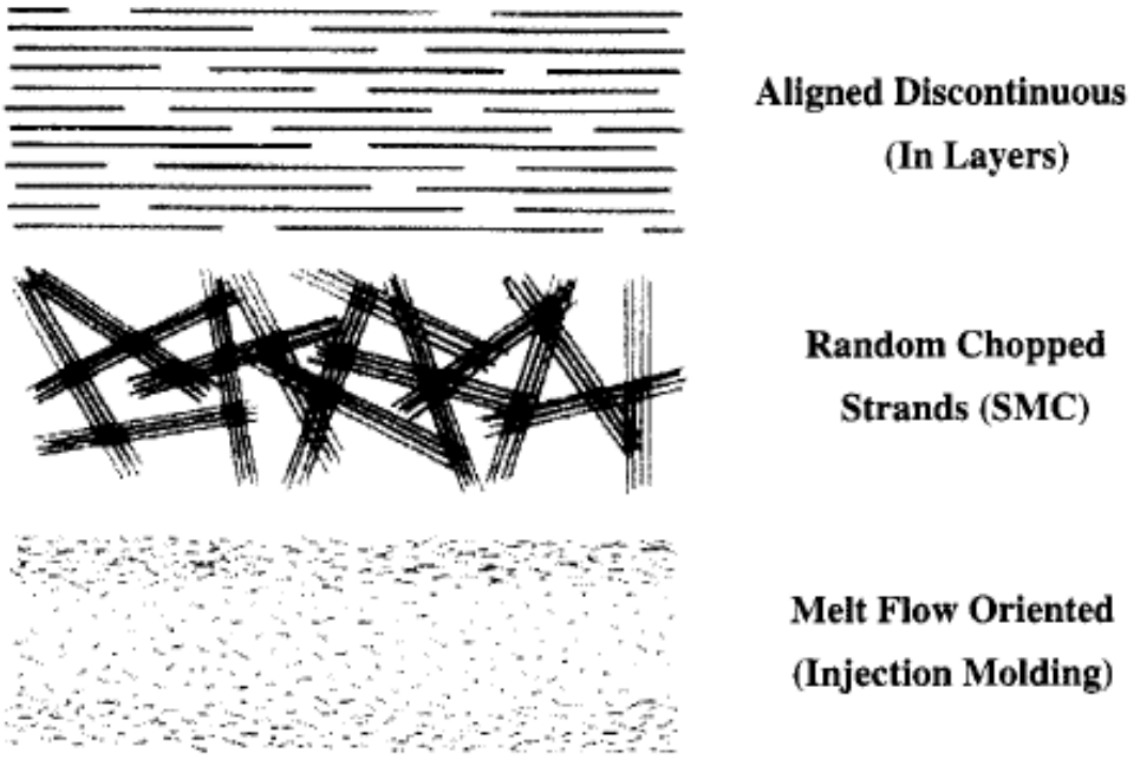

Figure 2.23: Schematic diagram of microstructures for short fiber CMs. The middle microstructure is representative of chopped strand mat (CSM) and sheet molding compound. The bottom microstructure is typical of injection molded parts where the fiber orientation varies through the thickness of the part due to the flow process. Reprinted from [124].

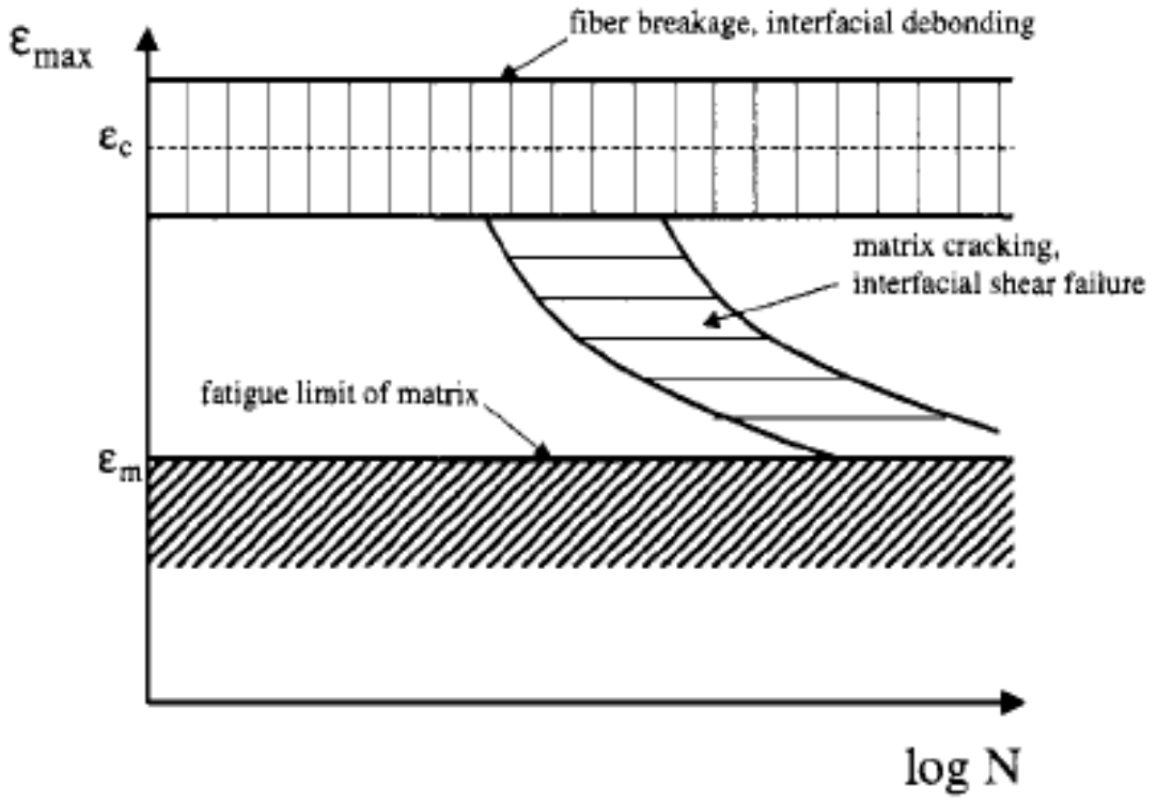

Figure 2.24: Fatigue-life diagram for unidirectional CM under transverse loading. Reprinted from [129].

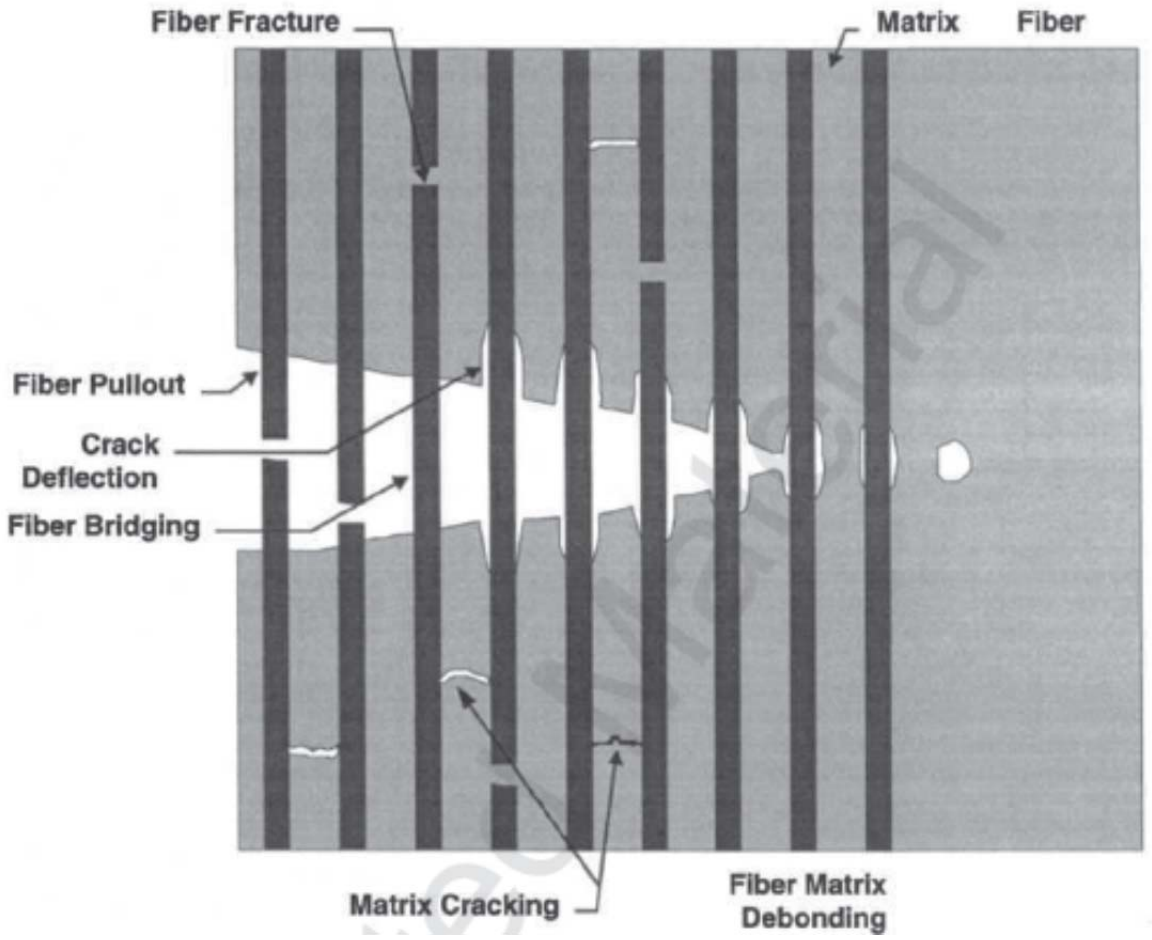

Figure 2.25: Failure mechanisms in a unidirectional fiber composite. Reprinted from [128].

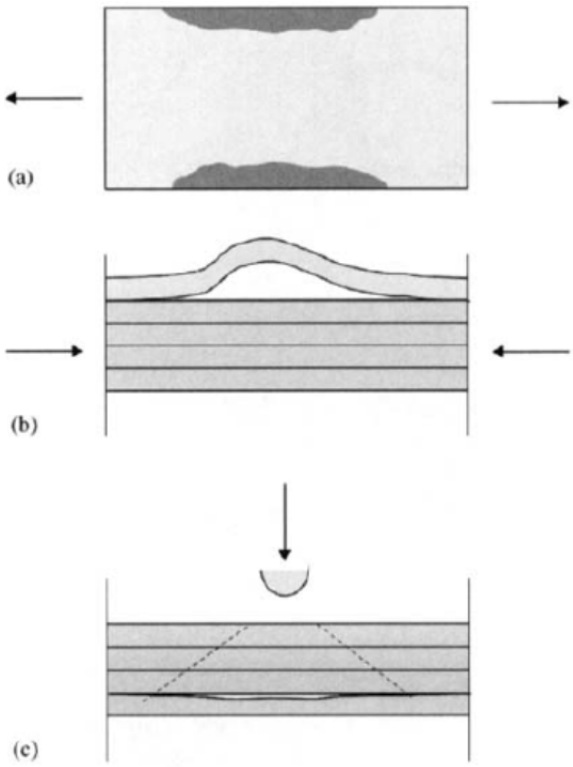

Figure 2.26: Typical delamination phenomena: (a) free-edge delamination; (b) buckling-induced delamination; and (c) impact induced delamination. Reprinted from [130].

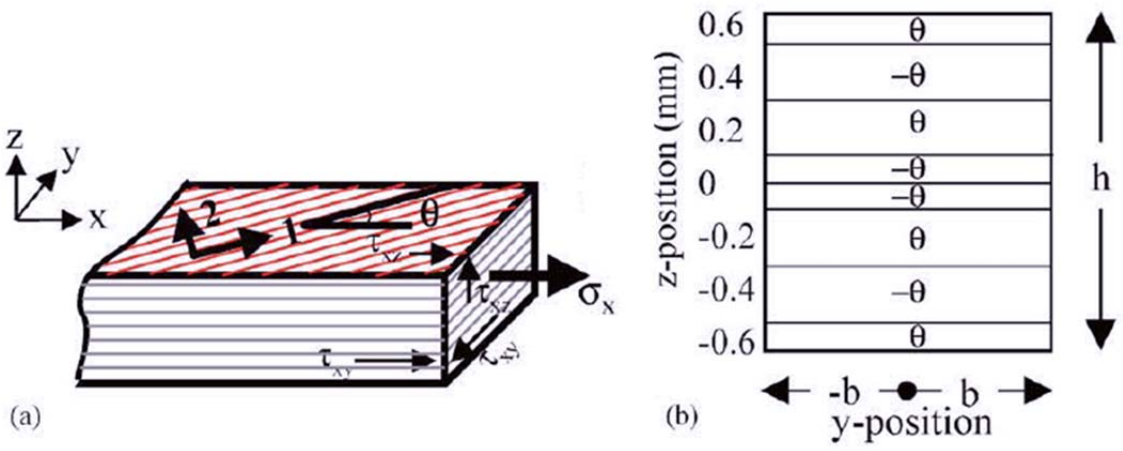

Figure 2.27: (a) Schematic of fiber-reinforced laminate representation of the annulus fibrosus : axial stress (s_x), in-plane shear stress (t_{xy}). (b) Schematic representation of cross section of the eight layer annulus layup

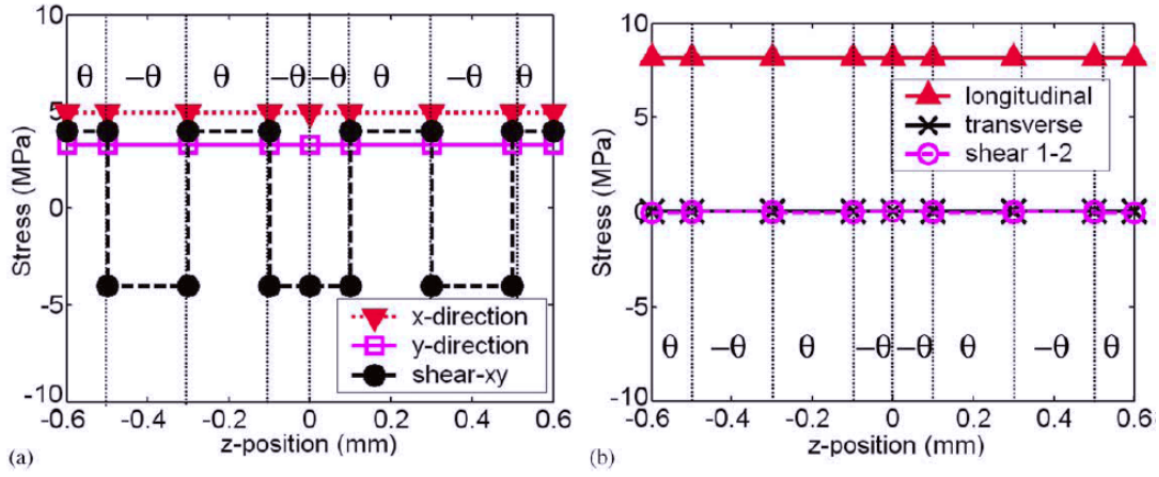

Figure 2.28: Stresses through the z-direction (radial) of annular layers when subjected to 10% strain in the x-direction (circumferential). AF modeled as an eight layer angle-ply laminate and 39° fiber angle. (a) Global coordinate system: x-direction (σ_x), y-direction (axial, σ_y), and xy-direction (txy, in-plane shear). (b) Material coordinate system: longitudinal direction (σ_1), transverse direction (σ_2) and for in-plane shear (τ_{12}). Reprinted from [96].

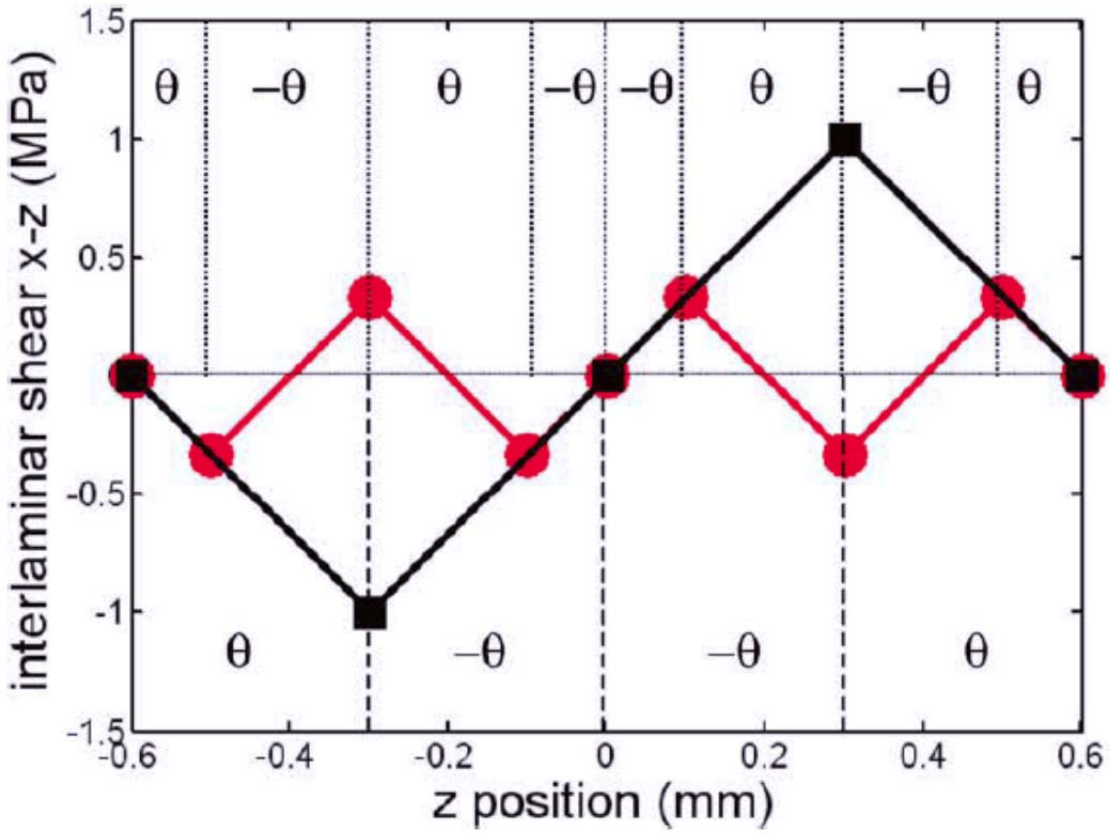

Figure 2.29: Interlaminar shear stresses eight-layer angle-ply laminate (red circle) and four-layer angle-ply laminate (black square) with same thickness and 39° fiber angle. Reprinted from [96].

Table 2.11: Typical matrix properties. Reproduced from [131].

Matrix	Young's Modulus [GPa]	Poisson's Ratio	Tensile Strength [GPa]	Failure Strain [%]
Thermoset epoxy resin	3 – 6	0.38 – 0.4	0.035 – 0.1	1 – 6
Thermoplastic PEEK	3.6	0.3	0.17	50

Table 2.12: Single ply material properties used for the lamination model by Iatridis and Gwynn (2004). Adapted from [96].

Property		Value	Source
V_f[a]	Fiber volume fraction	0.15	[73]
V_m	Matrix volume fraction	0.85	$V_m = 1 - V_f$
E_f[a]	Fiber modulus	904 MPa	$E_f = (E_1 - E_m V_m)/V_f$
E_m[a]	Matrix modulus	0.5 MPa	[134]
ν_{12}[a]	In-plane Poisson's ratio	0.3	Chosen[b]
G_{12}[a]	In-plane shear modulus	0.3 MPa	Non-linear regression
θ[a]	Fiber angle	39°	Non-linear regression
E_1	Longitudinal modulus	136 MPa	[73]
E_2	Transverse modulus	0.76 MPa	Halpin-Tsai Equation

[a]Independent material constant required for the linearly elastic plane stress analysis
[b]Parametric student demonstrated insensitivity of in-plane stiffness matrix to this parameter

3. CHAPTER THREE: OBJECTIVE AND SPECIFIC AIMS

The objective of this work is to quantify the mechanical properties (engineering constants) of the annulus fibrosus on two levels: laminate and laminar. The laminar level being the properties of a single lamellae of the annulus; and the laminate, the more physiologically relevant loading mode. Within these two levels, we can test both in and out of plane to either the collagen fibers or the lamellae themselves, leading to four testing orientations. By allowing the testing to go until annular failure, we will be able to quantify the loading conditions needed to allow the annulus to fail in each of the orientations. From these characterizations, we can model the AF as an angle ply composite. Using composite theory we can create failure envelopes based on the Tsai-Hill Criterion and explore what biaxial loads will cause the annular laminate to fail. The follow specific aims are proposed:

Specific Aim One (Chapter 4)

The goal of this aim is to characterize the failure properties of annular lamellae using a micro-mechanical testing protocol. This is accomplished by uniaxial failure tests in one of four orientations: longitudinal, transverse, radial, and circumferential. The properties were used to create failure envelopes for the annular lamina which may predict formation of microscopic tears in the annulus fibrosus that contribute to disc herniation and lower back pain.

Specific Aim Two (Chapter 5)

The goal of this aim is to investigate the effect of digesting the main macromolecules in the intervertebral disc on the micro-mechanical behavior of the human cadaveric lumbar annulus fibrosus to determine the role these molecules play in

annular mechanics. The enzymatic digestion protocol will allow for a quantitative assessment of the effect the main macromolecules within the intervertebral disc have on annular mechanics.

Specific Aim Three (Chapter 6)

In this aim, using composite theory, the annulus is modeled as an angle-ply laminated composite. Using the mechanical properties defined in aim one, the shear strength is calculated. The Tsai-Hill Failure Criteria is implemented to create a biaxial failure envelope of the annulus. This is expanded to include the cases of enzymatically digested samples.

4. CHAPTER FOUR CHARACTERIZATION OF ANNULUS FIBROSUS MIRCOMECHANICS

4.1. Introduction

The annulus fibrosus (AF) consists predominantly of sheets made from bundles of collagen fibers, which form concentric lamellae around the spinal axis [10, 15]. The outer AF is made up of type-I collagen fibers embedded within a proteoglycan matrix. Collagen fibers in individual lamella of the AF are parallel with respect to the each other and at a ±60° with respect to the spinal-longitudinal axis which alternates in successive lamellae [8, 10, 14, 34]. The inner AF consists of less dense matrix which has higher concentration of type-II collagen and proteoglycan but lacks the clearly distinct lamellar organization of the outer AF. An elastic component within the disc ensures adequate recovery of the network organization after deformations. In the annulus, elastic fibers appear densely distributed in the region between the lamellae and are also found within single lamellae [138].

There have been several studies focusing on the micromechanical properties of the AF [72, 86, 139-141]. Skaggs and colleagues (1994) examined single human lamellae and found that, when stretched parallel to the collagen fibers (longitudinal) at a very slow strain rate (0.00009 sec^{-1}), failure stresses for anterior annulus tissue were higher than for posterior-lateral annulus tissue and failure stresses for outer annulus samples were higher as compared to those from the inner annulus. These reported failure stresses (mean ± standard deviation) were 10.3 ± 8.4 MPa in the anterior outer region, 3.6 ± 2.0 MPa in the anterior inner region, 5.6 ± 3.2 MPa in the posterior outer region, and 5.8 ± 2.9 MPa in the posterior inner region [139].

Holzapfel et al., (2005) examined the elastic moduli of individual lamellae from human lumbar IVD. They examined both the tensile strength in the directions parallel (longitudinal) and perpendicular (transverse) to the collagen fibers. They found a mean elastic modulus for the perpendicular (transverse) samples of 0.22 MPa while the moduli for the tensile tests conducted on the parallel (longitudinal) samples were over 100 times this magnitude (28 – 78 MPa) [140].

Numerous theoretical studies have estimated the value of Poisson's ratio for the annulus by matching a numerical model with experimental predictions resulting in values around 0.45 [142-144]. Poisson's ratio for the annulus fibrosus has also been experimentally measured [72, 145]. Acaroglu et al. (1995) determined that the effective Poisson's ratio of a normal annulus by testing circumferentially (thickness = 1.8 mm) and measuring displacement using a video dimension analyzer system and reported a value of 1.36 ± 0.63 [72]. Similarly, Elliott and Setton (2001) determined that the Poisson's ratio of a normal outer annulus (7.7 x 2.9 x 1.4 mm samples) by measuring strain using a digital image system and reported a values of 0.6 ± 0.7 circumferentially and 0.51 ± 0.1 radially [145]. The values reported were consistent with biological tissue Poisson's ratio values of 2.0 ± 1.9 for ligament (Ischiofemoral) [146] and 1.9 ± 1.1 for the surface of articular (patella) cartilage [147]. These values indicate the anisotropy of the tissues due to the requirement that the shear modulus and bulk modulus have positive values, the upper limit of Poisson's ratio is 0.5 for isotropic materials [148].

Annular tears have observed on magnetic resonance images (MRI) in patients with degenerated discs [17, 149, 150]. Annular tears could be responsible for radicular pain due to weakening of the annular wall, leading to bulging and thus nerve compression

[17, 21]. If annular tears occur and nucleus expulsion follows (herniation), these nerve endings could be irritated by acid metabolites contained in the herniated disc material [151]. Annular tears or disc herniation could be responsible for lower back pain even without nerve root compression [17]. Irritation to the outer portion of the annulus fibrosus could be caused from the innervated branches of the sinuvertebral nerve [152]. Failure initiation and propagation of the tears have been numerically simulated with compressive and bending forces [18].

A composite material (CM) is a combination of two materials in which one of the materials, called the reinforcing phase, is in the form of fibers, sheets, or particles, and are embedded in the other materials called the matrix phase. They can be classified by the geometry of the reinforcement, for example a fiber reinforced composite. The continuous fibers can be in the matrix in a single layer in which they are aligned in a single direction. Damage process and failure modes in unidirectional laminates, depend on the loading conditions (tension or compression), and on direction of applied load (parallel or at some angle to the fiber direction).

One can analyze the annulus fibrosus as a fiber-reinforced composite lamellae structure; having uniaxial collagen and elastin fibers embedded in a proteoglycan matrix [142, 144, 153-156]. Accurate and reliable prediction of failure in composite materials is required for advanced analysis of damage and failure in composite structures. Although failure in composites has been studied for over 40 years (for review, see [157]), predictions of failure by leading failure criteria often differ significantly from experimental results [158]. A failure criterion predicts the safe limits of a material under multi-axial stress states. Failure criteria can be written in several forms, including: stress-

based, strain-based, energy-based, damage-based, and empirical [159]. The function that governs the interaction of stresses and strengths is the failure criterion.

There are numerous failure theories for predicting lamina failure, including limit and interactive criteria [160]. Limit criteria predict lamina failure load by separately comparing lamina stresses with corresponding strengths and identifies failure with a piecewise linear function [160]. Simplicity is the main advantage of this approach; however it assumes no stress interactions between orientations. Interactive criteria predicts failure load using a single polynomial equation involving all stress components creating a continuous smooth failure envelope [160]. Again, the simplicity of a polynomial representation is the main advantage with the ability to model stress interactions, however failure prediction is dependent on irrelevant strength parameters (e.g. tensile failure prediction depends on compressive strength). In this chapter, two limit criteria (Maximum Stress Criterion and Maximum Strain Criterion) and one interactive (Tsai-Hill Criterion) criterion will be discussed. Material properties were determined for the annulus fibrosus in multiple orientations and various failure criteria were compared to determine onset of fracture.

4.2. Materials and Methods

4.2.1. Specimen Preparation

Ten intervertebral discs were isolated from fresh-frozen cadaveric spines, dissecting sharply at the superior and inferior endplates. Spines were obtained from an approved tissue source (National Disease Research Interchange, Philadelphia, PA) and ranged in age from 51 – 82 years with an average of 68.9 years (Table 4.1). Upon isolation, the nucleus pulposus and inner annulus was removed. Sections in the anterior

(n = 10) and postero –lateral (n = 10) positions of the outer annulus were separated for dissection. These were then mounted to the freezing stage of a cryostat (Model CM 3050S, Leica, Nussloch, Germany) using Cryomatrix™ (Shandon Cryomatrix, Fisher Scientific) and cut using a D profile Tungsten Carbide knife (Delaware Diamond Knives, Wilmington, DE). Samples were cut to a uniform thickness of 150μm in the appropriate orientation and frozen at -22°C until testing.

Annulus samples were prepared for: intra-laminar (n = 20, 10 anterior and 10 postero-lateral) and inter-laminar (n = 20, 10 anterior and 10 postero-lateral) (Figure 4.1). We define the intra-laminar specimens to be a single annular lamellae allowing for examination of laminar properties within the outer annulus. The inter-laminar specimens were used to investigate the failure properties between the lamellae. Inter-laminar specimens were prepared in the spinal-axial plane and tested in the circumferential (n = 10) and radial directions (n = 10). The circumferential and radial directions relate to preparation on the horizontal plane of the body at 0- and 90-degrees respectively; with the collagen fibers of individual lamellae oriented at ±60° to the sagittal-axis. All samples were tested in two orientations, giving a total of four testing groups. Intra-laminar specimens were tested parallel and perpendicular to the axis of the collagen fibers. Longitudinal (n= 10) and transverse (n= 10) directions relate to the preparation of a single lamellae, with the collagen fibers oriented at 0-degrees for longitudinal (parallel) and 90-degrees (perpendicular) for transverse. A total of 40 samples were kept frozen at -20°C until mechanical testing was performed.

4.2.2. Mechanical Testing

Prior to testing, the annular slices were allowed to thaw in room temperature in 1x phosphate buffered saline (Sigma Aldrich, St Louis, MO) overnight and examined for tears; damaged samples were discarded. Length, width and thickness of the specimens were measured with a digital caliper (Mitutoyo, Aurora, IL). The average dimensions of the test specimen were 5 x 2 x 0.15 mm for length, width, and thickness, respectively. The samples were secured with fine grit sandpaper glue (3M Company, St. Paul, MN) using Scotch® brand super glue (3M Company, St. Paul, MN) via clamping grips into an adapted tensile stage (MTI Instruments Inc., Albany, NY) (Figure 4.2) with a 500g tension/compression miniature load cell (Cooper Instruments & Systems, Warrenton, VA). Displacement was optically determined using a webcam (Logitech, Fremont, CA) affixed to a stereo zoom microscope (LW Scientific, Atlanta, GA) under which the device was placed. Displacement was measured by the position of the two grips (axial-displacement, δ) as well as the sample's width displacement (transverse-displacement, δ_t). A custom designed LabVIEW (National Instruments Corporation, Austin, TX) program was used to record the load and an image every second of a uniaxial tensile test (1 Hz sampling rate). Please refer to Appendix A (page 207) for a detailed description of the software. Samples were preconditioned to 10% strain for five cycles then loaded until failure at a 20 μm/s strain rate.

4.2.3. Data Analysis

Stress (σ) and axial strain (ε, from axial displacement δ) were calculated from the force and displacement data exported from the custom software. Contractile strain, ε_t, of the sample was also determined from the width disablement for Poisson's ratio

calculations. The failure strain (ε_f) was defined as the strain corresponding to the failure (maximum) stress (σ_f) as determined from the stress-strain curve. Poisson's ratio was calculated from the negative relationship between the contractile strain normal to the applied load and the axial strain in the direction of the applied load, $\nu = -\varepsilon/\varepsilon_t$. Poisson's ratio was calculated using strains within the linear-region [145-147, 161]. For this study, a cubic function was used to fit the tensile stress-strain behavior [139]: $\sigma = D + C\varepsilon + B\varepsilon^2 + A\varepsilon^3$, where the coefficients were determined using a nonlinear regression curve-fitting procedure. Tensile moduli were found by differentiating the stress-strain relationship based on Skaggs et al. [139] at a low, medium and high percentage of failure strain due to non-linearity: $E_{25\%}$-, $E_{50\%}$- and $E_{75\%}$-ε_f (Figure 4.4).

A total of 40 samples, from 10 human lumbar intervertebral discs, were mechanically tested and analyzed. A two-way analysis of variance (ANOVA) was performed with a Bonferroni post-test to compare each mechanical property and orientation. All statistical analyses were performed using Prizm software (Graphpad Software, San Diego, CA) with significance set at $P \leq 0.05$.

4.2.4. Failure Criteria for Fiber Reinforced Composites

The maximum stress criterion and the maximum strain criterion, two common limit criteria, are reviewed in the following. The maximum stress criterion states that stress in principal material coordinates must be less than respective strengths, otherwise failure occurs [148]. In tension, the maximum stress criterion can be written as,

$$\frac{\sigma_x}{X} = \mathbf{1}; \quad \frac{\sigma_y}{Y} = \mathbf{1} \tag{4.i}$$

where X and Y are the ultimate tensile strengths in the x- and y-direction, respectively. The x-direction indicates the load is applied at 0-degrees to the fibers or lamellae

(longitudinal and circumferential) and the y-direction indicates 90-degree loading (transverse and radial). For single lamellae testing, longitudinal and transverse are the x- and y-directions, respectively. It is possible to predict the strength of the whole laminate from the strength profiles of the individual lamina using classical lamination theory (CLT). So, if all lamina stresses are known, then stresses in each lamina can be compared to a failure criterion and uniformly scaled upward to determine the load at which failure occurs. However, CLT assumes that strains are small and orthotropic properties are linear, which is not the case for the annulus [148, 162]. We, instead, expanded the failure criteria for lamina for inter-lamellar samples, by allowing the principle directions to relate to the orientation of the laminar layers; x- and y-directions depict the circumferential and radial directions.

An alternative limit criterion is formulated in terms of strain. The maximum strain criterion states that strain in principal material coordinates must be less than respective maximum strains, otherwise failure occurs [148]. In terms of strains, the maximum strain criterion is,

$$\frac{\varepsilon_x}{X_\varepsilon} = \mathbf{1};\ \ \frac{\varepsilon_y}{Y_\varepsilon} = \mathbf{1} \tag{4.ii}$$

where X_ε and Y_ε are the maximum tensile normal strain in the x- and y-directions, respectively. In the x-y plane, the failure envelope is skewed due to the inclusion of poison's effect; while in the x-z and y-z planes, maximum strain criterion is coincident with the maximum stress criterion. The strain based failure criterion can be written in terms of stresses, using the Poisson's ratio [148].

$$\frac{\nu_{xy}\sigma_y + X}{\sigma_x} = \mathbf{1};\ \ \frac{\nu_{yx}\sigma_x + Y}{\sigma_y} = \mathbf{1} \tag{4.iii}$$

The Tsai-Hill criterion, a common interactive criterion, is a generalization of the von Mises criterion [163-165]. The criterion is formulated using Taylor series expansion, similar to the von Mises criteria, but for orthotropic materials such as the annulus. This results in a generalized polynomial function where the coefficients can be found using uniaxial strength tests [148, 165]. If plane stress conditions are assumed, the criterion is simplified to the following [148].

$$\frac{\sigma_x^2}{X^2} - \frac{\sigma_x \sigma_y}{X^2} + \frac{\sigma_y^2}{Y^2} + \frac{\tau_{xy}^2}{S^2} = \mathbf{1} \qquad \text{(4.iv)}$$

A drawback to the Tsai-Hill criterion is that it cannot account for intra-lamellar biaxial strengthening effects [148]. The Tsai-Hill stress interaction always predicts a biaxial weakening effect; this does not always agree with experimental data and is considered a conservative estimate [165].

4.3. Results

Typical stress-strain tensile responses for specimens in all orientations exhibited nonlinear and anisotropic behavior (Figure 4.5). There was no statistical difference between the anterior and postero-lateral groups within each orientation. Previous studies have shown that annular properties are site specific [139, 166]; we attribute our lack of statistical significance to our small sample size. Mechanical properties of the annular samples can be seen in Table 4.2.

4.3.1. Intra-lamellar Samples

Comparison of the failure properties within a single lamellae, showed a decrease of 85% in ultimate tensile strength (failure stress) between the longitudinal (0°) and transverse (90°) directions (Figure 4.6). Conversely, there was a significant increase in the failure strain when comparing the parallel to perpendicular testing directions. There

was a 26% increase in failure strain between longitudinal and transverse directions. The elastic moduli showed an average 87.5 ± 1.5% reduction between the longitudinal and transverse directions (Figure 4.7). There was a statistically significant increase in both directions when comparing the modulus at 25% strain to the two higher strain percentages. However, there was no statistically significant different between the moduli at 50% and 75% strain in either the longitudinal or transverse directions. The intra-lamellar longitudinal samples showed a Poisson's ratio of 0.44 ± 0.05 and the transverse samples shows a Poisson's ratio of 0.097 ± 0.02 (Figure 4.8). Based on the two directionalities, Poisson's ratio in the longitudinal and transverse directions are defined as ν_{LT} and ν_{TL}, respectively.

4.3.2. Inter-lamellar Samples

The inter-lamellar samples had a 60% reduction in the ultimate tensile strength when comparing the circumferential samples to the radial samples. Alternately, the failure strain showed an increase of 50% between the circumferential (parallel to lamellae layers) and radial (perpendicular to laminar sheets) directions. There was an 84 ± 2% reduction in the elastic moduli comparing the circumferential to the radial directions. For both directions, there was an increase when comparing the modulus at 25% strain to the two higher strain percentages. However, there was no statistically significance difference between the moduli at 50% and 75% strain in either direction. The circumferential samples had a Poisson's ratio (ν_{CR}) of 0.44 ± 0.04 and the radial samples (ν_{RC}) show a Poisson's ratio of 0.159 ± 0.009.

4.3.3. Failure Envelopes

We can assume that each of these orientations relates to a unidirectional lamina with known failure strengths. Using this information, we developed failure envelopes for the annulus using the three failure criteria discussed previously for a unidirectional lamina subjected to uniaxial stress (Figure 4.9). The maximum stress and strain theories produce less accurate results than more robust criteria, however are used due to their simplicity and conservative estimates [162]. Shear strength has not been experimentally measured in the literature and we assume does not play a role in the failure envelope of our samples due to the uniaxial tensile loading. Thus, we simplify equation 4.iv and do not include the fourth shear term. In order to determine the most accurate criteria, biaxial testing of the annulus would need to be completed and plotted against the failure envelopes.

4.4. Discussion

We have quantified the mechanical tensile behavior of intra-lamellae and inter-lamellae samples of the annulus fibrosus. This was achieved by dissecting the annulus in two orientations and then testing those in two directions each, in- and out-of-plane to either the collagen fibers or sheets of lamellae, resulting in the four testing directions: longitudinal, transverse, circumferential and radial.

We compared our data for the longitudinal samples to similar studies reported in literature (summarized in Table 4.3). Skaggs et al. (1994) reported location-specific failure stress values between 3.6 ± 2 MPa (inner anterior) and 10.3 ± 8.4 MPa (outer anterior) in the longitudinal direction for single lamellae testing [139]. Our value of 2.37 ± 0.26 MPa is within this range for the outer annulus. The study also reported failure

strains ranging from 9.2 ± 3.4% (inner anterior) to 11.3 ± 6.3% (outer annulus) which is slightly lower than our value of 19 ± 2% reported (longitudinal). If we consider only the anterior longitudinal samples (n = 5) in our study, we have a failure strain of 13 ± 3% which is within the previous study's range [139]. Holzapfel et al. (2005) studied the elastic moduli of the AF and determined the tensile modulus of longitudinally oriented samples at three locations: low, medium and high. Our moduli compared well to their E_{Low}, E_{medium} and E_{high} values (8 ± 6.5, 24 ± 12, and 65 ± 48.6 MPa respectively) within their posterior outer annular groups [140]. Our data for radially oriented samples is within the range presented by Fujita et al. (1997) presented values for ultimate stress and strain (0.3 ± 0.16 MPa and 80 ± 40 %, respectively) [86]. That study also determined an elastic modulus of 0.47 ± 0.33 MPa, which is slightly lower than our reported 75% strain modulus ($E_{75\%}$-ε_f = 1.76 ± 0.29 MPa). Smith et al. (2007) also quantified the initial and ultimate radial moduli for the AF at anterior and posterolateral positions. The study reported values for initial modulus values of 0.096 ± 0.062 MPa (anterior) and 0.055 ± 0.040 MPa (postero-lateral) and for the ultimate modulus 0.272 ± 0.178 MPa and 0.167 ± 0.103 MPa for the anterior and postero-lateral samples [141]. Our values are on the order of ten-times higher than these reported ranges, however our values had smaller standard deviations. These differences in moduli could be due to differences in sample location, population, grade, or testing protocol.

In this study, we quantified the mechanical characteristics of single lamellae of the annulus fibrosus using a uniaxial testing technique. Failure stress is higher in the longitudinal (0°) direction than the transverse (90°) direction samples as expected. There is an increase in failure strain when comparing the transverse to longitudinal samples.

Testing in line with the axis of the fibers (longitudinal) allows the collagen fibers to be the main load-bearing elements in the sample. The conclusion that the collagen fibers are giving the tensile strength to the annulus is supported. The proteoglycan and elastin fiber matrix does not allow for as high of loads before failure, as evident by the lower tensile strength in the transverse direction where the collagen fibers do not contribute. However, one benefit that manifests during the transverse loading is the increase the amount of deformation that can occur before failure (increase in failure strain). The higher failure strain is more reflective of the property for elastin fibers, which have been found to be oriented parallel to the collagen fibers as well as crossing perpendicular between collagen bundles within single lamellae [167]. The elastic moduli in the longitudinal direction are higher at all strain locations when compared to the transverse elastic moduli. However, consistent in both testing directions (longitudinal and transverse) there is an increase in modulus from the low region ($E_{25\%}\varepsilon_f$) to the higher locations and no statistical difference between the moduli at 50% and 75% strain. In the future, this will allow calculation of the modulus at only a low and high percentage of strain (25% and 75% with respect to our study). This inversion of failure properties, high strength and low deformation for longitudinal samples versus lower strength and higher allowable deformation for transverse samples is what gives the annulus its unique properties. This has been seen in other tissues that exhibit nonlinear and anisotropic behavior, such as the aortic valve cusp [168, 169] and meniscus [170-172].

This work also quantified the effective mechanical characteristics of the annulus fibrosus in the circumferential and radial directions. The circumferential direction showed a higher failure stress than the radially tested samples. Alternatively, there is an

increase in failure strain when comparing the two (radial > circumferential). Testing in the inter-laminar orientation has the collagen fibers oriented in a plane normal to the uniaxial radial axis at ±60°. We hypothesize that the collagen fibers are able to redistribute the load and due to the small thickness of our samples, are able to rotate into the plane of load. Across the lamellae, there are an abundance of elastin fibers which work as cross-bridges between lamellae [141, 173]. This intra-laminar structure, while not as strong (evident in lower failure stress) allows the higher failure strain in the radial direction. The cross-bridge elastin fibers allow for high deformation prior to failure. The elastic moduli in the circumferential direction are higher than the radial moduli at all strain locations. In both testing directions (circumferential and radial) there is an increase in modulus from the low region (E25%εf) to the higher locations on the stress-strain curve and no statistical difference between the moduli at 50% and 75% strain indicating a typical non-linear stress-strain behavior as seen with other biological composite tissues [168-172].

Capturing concurrent images of the samples as they were being tested enabled calculation of Poisson's ratio of the annulus in the two orientations (intra- and inter-lamellae). Using the definition of Poisson's ratio, the ratio of transverse contraction strain to longitudinal extension strain in the direction of stretching force, we were able to measure the deformations in both directions of the images, for use in strain calculations. From the longitudinally tested samples, we were able to calculate ν_{LT} and from the transverse, ν_{TL} (Figure 4.8) which are the major and minor Poisson's ratios in the intra-laminar specimens, respectively. For inter-laminar specimens, we were able to quantify the major and minor Poisson's ratio from the circumferential and radial directions,

respectively. We can compare our major Poisson's ratio for the inter-lamellar samples ($\nu_{CR} = 0.43 \pm 0.05$) to the experimental work done by Acaroglu et al. (1995) and Elliott and Setton (2001) and see that our value is within the range previously reported (1.36 ± 0.63 and 0.6 ± 0.7) with a much smaller standard deviation [72, 145]. Our values for all directions are below the $\nu = 0.5$ boundary limits for isotropic materials. Poisson's ratio is beneficial in computational modeling techniques to analyze the annulus and also in calculating failure envelopes for the annulus. Interestingly, some synthetic materials (honeycombs and foam structures) report negative values of Poisson's ratio; the lower bound for is obtained by deforming a body and assuming that its volume remains constant [174, 175].

Reported values for Poisson's ratio for different biological tissues have exceeded the 0.5 theoretical threshold for linearly elastic isotropic materials ($-1 < \upsilon < 0.5$) [176]. This material behavior has been attributed to the anisotropy of the biological tissues tested (disc, ligament and cartilage) [72, 145-147]. Due to the positive requirement of strain energy density, Ting and Chen (2005) showed that Poisson's ratio for anisotropic elastic materials can have an arbitrarily large positive or negative value [176]. For composite laminate theory, which describes the theoretical behavior of anisotropic linear composites with assumptions of perfect bonding between reinforcing fiber and matrix, this theoretical boundless condition for Poisson's ratio also holds true. Theoretically, this behavior is explained by the anisotropy and inhomogeneity of the substructures of the material [176, 177]. As previously mentioned, there are materials with negative Poisson's ratio values., including micro-porous polyethylene [178], α-cristobalite [179], some cubic metals [180], plasmas as well as other extreme matter [181]. Only some of

these are anisotropic [178, 182]. Lakes and Witt (2002) states that anisotropy is not a necessary condition for negative Poisson's ratio [158]. We hypothesize that anisotropy is not the mitigating factor that allows biological tissues to experimentally have a Poisson's ratio greater than 0.5. To the authors' knowledge, there exists only one synthetic, anisotropic material with a Poisson's ratio greater than 0.5: open-cell foam [183]. Conversely, there are alternate studies that show the Poisson's ratio of open-cell foam to be less than 0.5 [184, 185]. We hypothesize that there is another unique characteristic of biological tissues which allows the high Poisson's ratio. We hypothesize that the high Poisson's ratio sometimes reported for fibrous biological tissues in general and for the annulus fibrosus, specifically is due to the nonhomogeneous, substructure of the AF and not the anisotropic nature of the material. We suggest that biological materials, which follow the general morphology of a synthetic anisotropic composite are also actually non-continuous, non-linear, and not perfectly bonded, thus allowing for a vast range in values, even those exceeding a Poisson's ratio of 0.5. [72, 145].

For orthotropic materials, the major and minor Poisson's ratios within an orientation can be related by the elastic moduli; the relationship between the Poisson's ratio and the elastic modulus in that principle direction are equal in both directions (for example: $\nu_{LT}/E_L = \nu_{TL}/E_T$) [148, 186]. From this relationship we can calculate the expected Poisson's ratio in the alternate direction and compare to our experimental results. For example, using the Poisson's ratio in the longitudinal direction, ν_{LT}, and the elastic modulus in both the longitudinal and transverse directions ($E_{75\%\varepsilon f}$ chosen), we can calculate the expected ν_{21}; When doing this, we get a value of 0.053 ± 0.01. This calculated value is 200% less than the experimental value. A limitation of using this

relationship is that its validity assumes linear stress-strain relationship, where we have a non-linear relationship. A single modulus value was chosen, however to acknowledge the non-linear stress-strain behavior of the annulus, the initial and ultimate moduli would need to be considered in the relationship. We are also able calculate the predicted major Poisson's ratio value for inter-lamellar samples from the radial Poisson's ratio to get a value of $\nu_{CR,predicted} = 0.33 \pm 0.14$, which is not statistically different from our experimental value. The differences in these statistical significances between the predicted and actual intra- and inter-laminar samples are limited in the fact that the predicted values are still based on experimental data. However, this is the first attempt at experimentally determining the intra-lamellar major and minor Poisson's' ratios.

Our results are limited by testing isolated annulus fibrosus specimens; upon cutting the collagen fibers, stress-free edges are created. However, this is a common technique to determine the material properties and strength of annulus tissue [72, 74, 82, 86, 139, 187, 188]. Our samples are limited to a low aspect ratio (5:2) due to preparation constraints. By using failure envelopes to predict catastrophic failure instead of classical lamination theory for the inter-lamellar samples, the assumption of small strain in CLT was not violated. Special consideration would have to be given to failure envelopes involving the inter-laminar stresses, when the annulus will be considered one bulk laminate composite, however that is beyond the scope of this text. Another limitation to using failure envelopes is the significance of shear stress. In this study, shear stresses of the AF were not considered. However shear stress can play a significant role in lamina failure since it contributes to the magnitude of stresses in various directions [162]. While these may not hold at our failure stress and strain levels, the purpose of this study was to

show how the mechanical properties that were experimentally determined could be used to provide insights into failure of the annulus fibrosus and not provide a rigorously validated constitutive failure model.

Using these mechanical properties of the annulus fibrosus and fiber reinforced composite theory this failure work can be expanded using CLT. The structure of the layered unidirectional lamellae within the annulus can be viewed as an angle-ply laminate ($\theta = \pm 60°$). Using laminate analysis, mid surface strains and curvatures can be determined for the whole laminated annular structure. After the mid-surface strains and curvatures are determined, the laminate can be analyzed for stresses and subsequent failure using one of the aforementioned failure criteria. Future work should also entail including shear and biaxial testing in order to use a more robust interactive failure criteria. This can be based on work done previously in the literature to determine the shear failure stresses in the annulus [189-191]. A limitation to this technique is the assumption of small strain in CLT. The overall objective is to work toward a predictive model for annulus fibrosus failure.

4.5. Conclusions

In this chapter, we were able to quantify baseline mechanical properties of the annulus fibrosus, including an experimentally determined Poisson's ratio in four directions, longitudinal and transverse (intra-lamellae) as well as circumferential and radial (inter-lamellae). These properties were applied to three failure criteria in order to provide insight into failure envelopes of the annulus fibrosus as an initial step to using fiber reinforced composite theory for a laminated composite to predict failure of the

annulus. Full understanding of these mechanical properties of the annulus could potentially lead to a failure model for disc tearing and herniation.

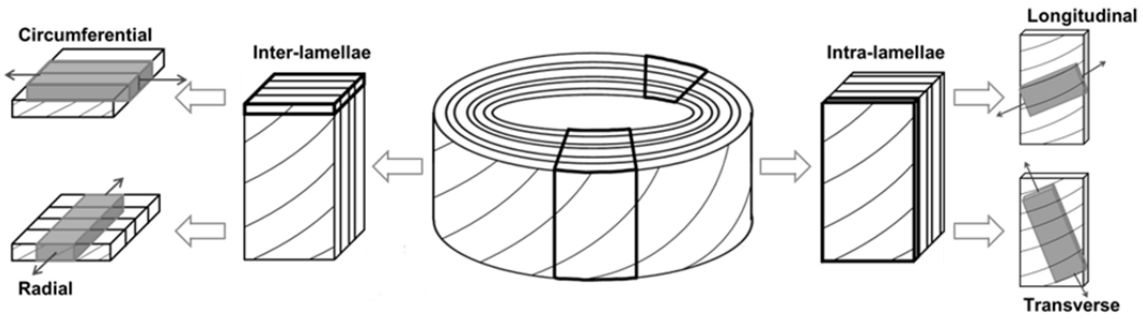

Figure 4.1: Samples were prepared in two orientations by making either intra-lamellar or inter-lamellar cuts, relating to within a single annulus laminar slice or across lamella. The annular slices (thickness = 150 µm) are then further divided into four groups to be tested in the following directions: longitudinal, transverse, circumferential and radial.

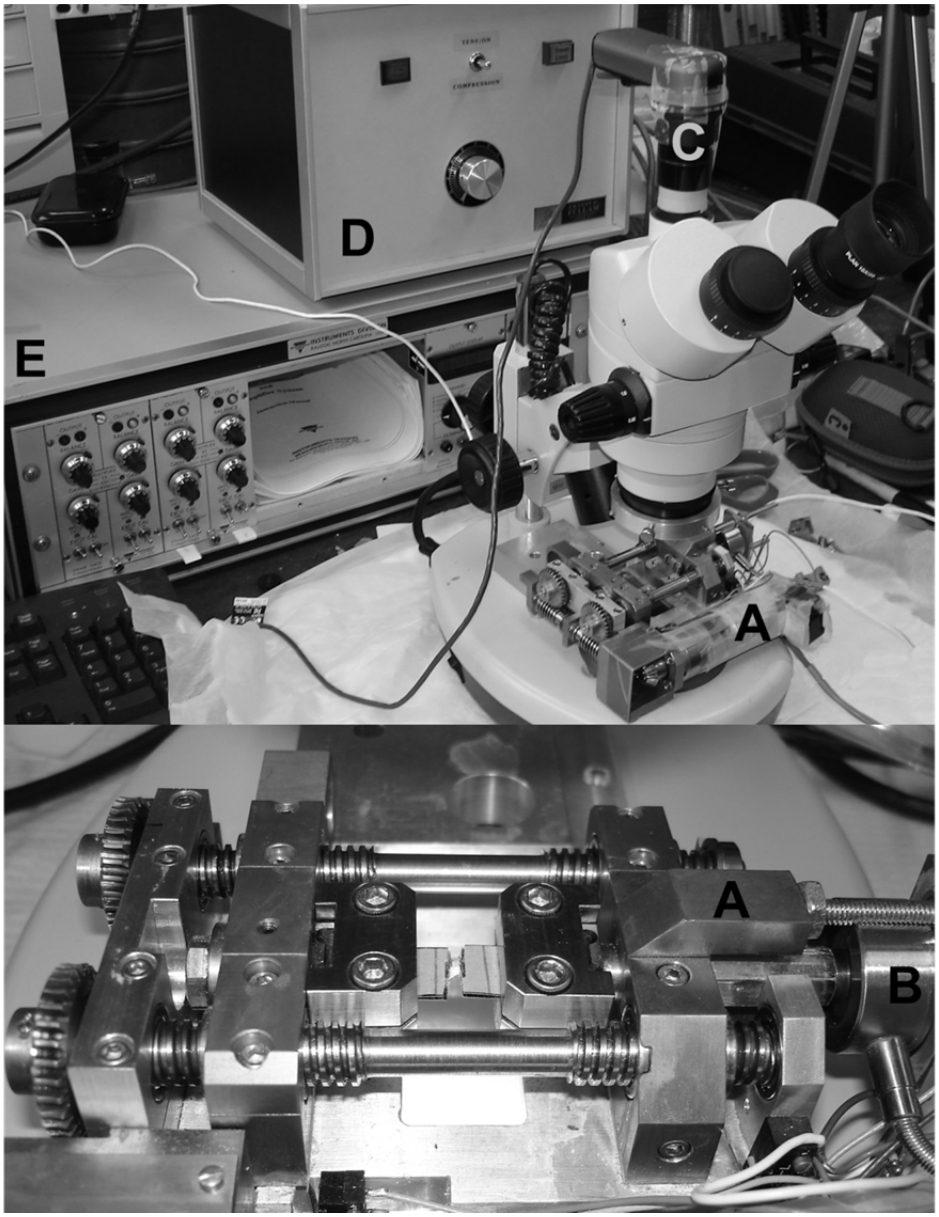

Figure 4.2: Custom micro-tensile tester consisting of: a) testing stage and grips (MTI Instruments Inc., Albany, NY); b) 500 g tension/compression miniature load cell (Cooper Instruments & Systems, Warrenton, VA); c) webcam (Logitech, Fremont, CA) affixed to a stereo zoom microscope (LW Scientific, Atlanta, GA); d) power source (Ernest FF. Fullam Inc., Latham, NY); and e) signal conditioning amplifier System (Vishay Precision Group, Raleigh, NC).

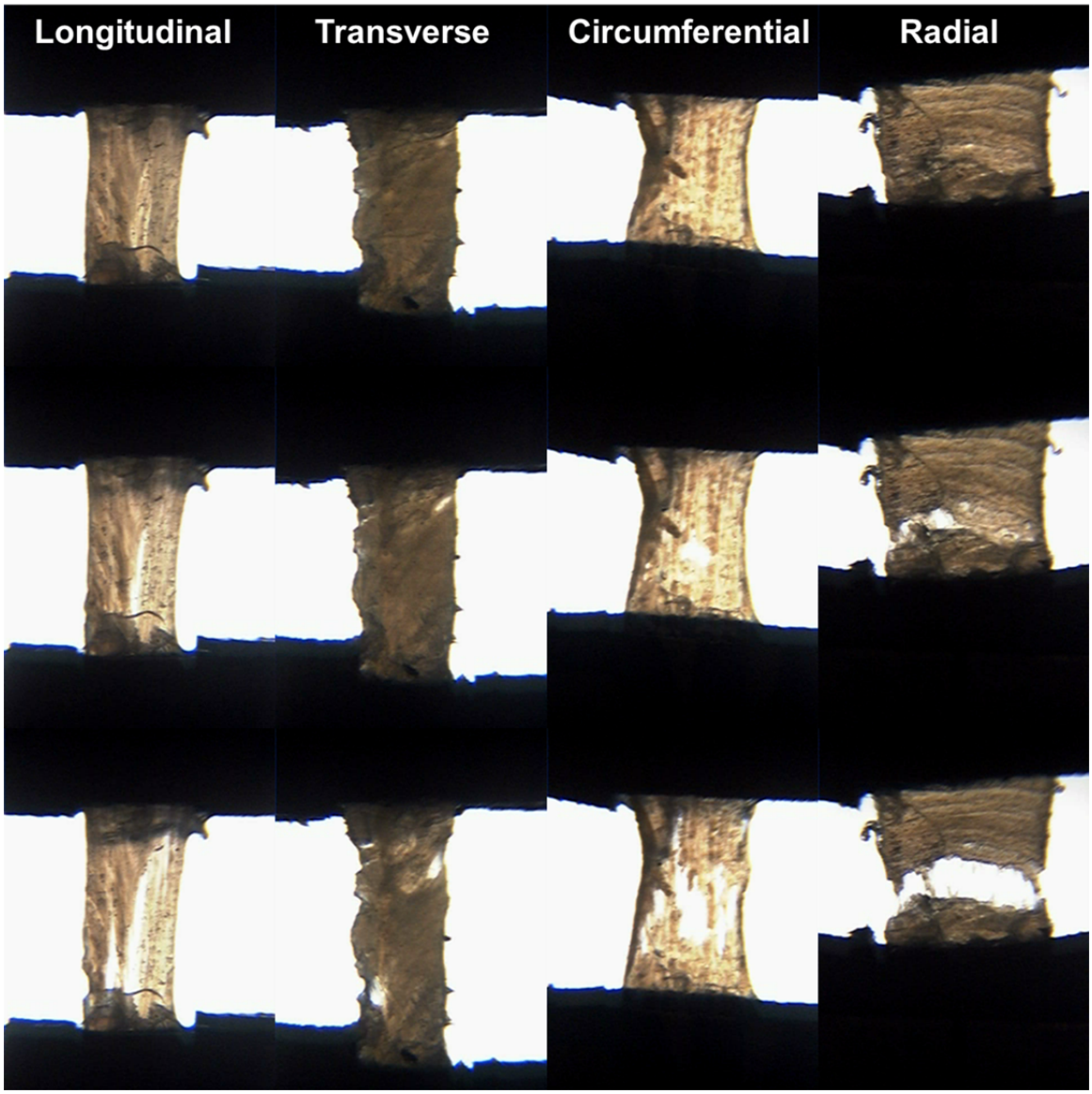

Figure 4.3: Representative images captured from webcam (Logitech, Fremont, CA) affixed to a stereo zoom microscope (LW Scientific, Atlanta, GA) during axial loading in four directions: longitudinal, transverse, circumferential, and radial.

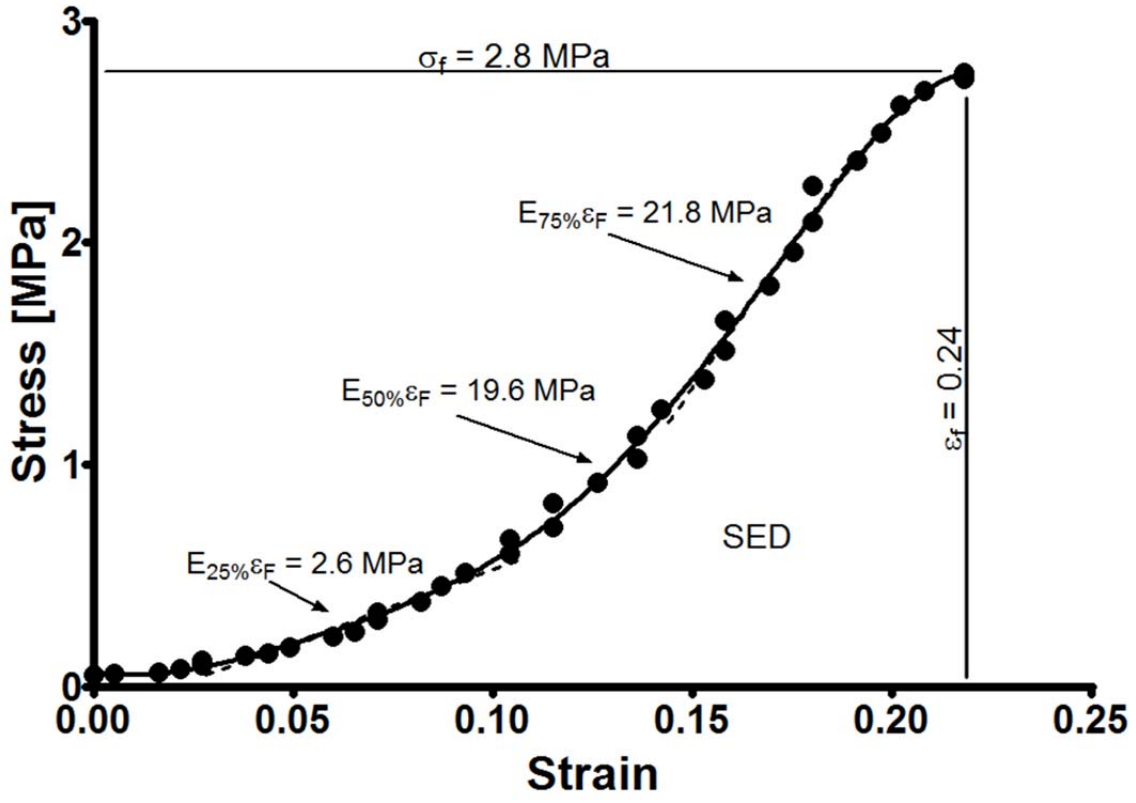

Figure 4.4: Representative stress-strain curve of an annular sample oriented in the longitudinal direction from the control digestion group (1x PBS) illustrating the failure stress (σ_f), failure strain (ε_f), elastic moduli at three locations (25%, 50%, and 75% of failure strain). Experimental results are shown with a best-fit cubic curve: $\sigma = 0.13 - 5.17\varepsilon + 114\varepsilon^2 - 148\varepsilon^3$.

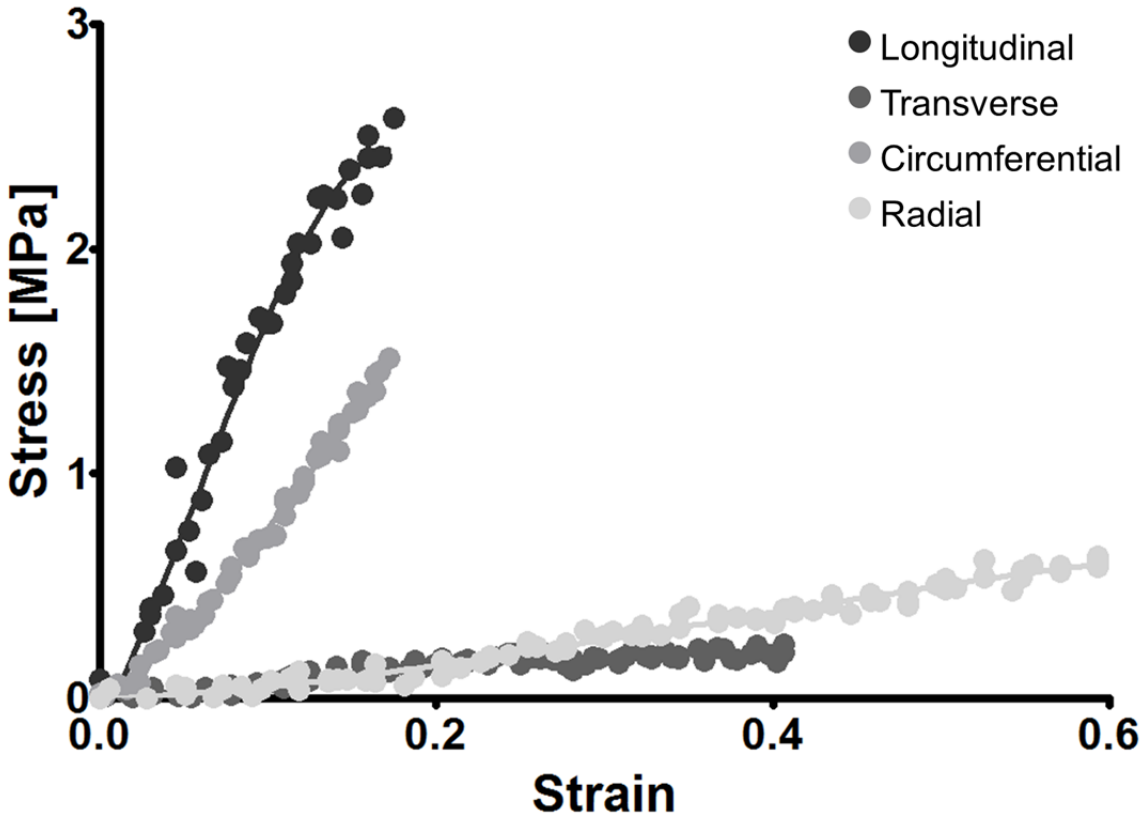

Figure 4.5: Representative stress-strain relationships for annular samples oriented in the a) longitudinal, b) transverse, c) circumferential and d) radial directions. Experimental results are shown with a third-order polynomial best-fit cubic curve.

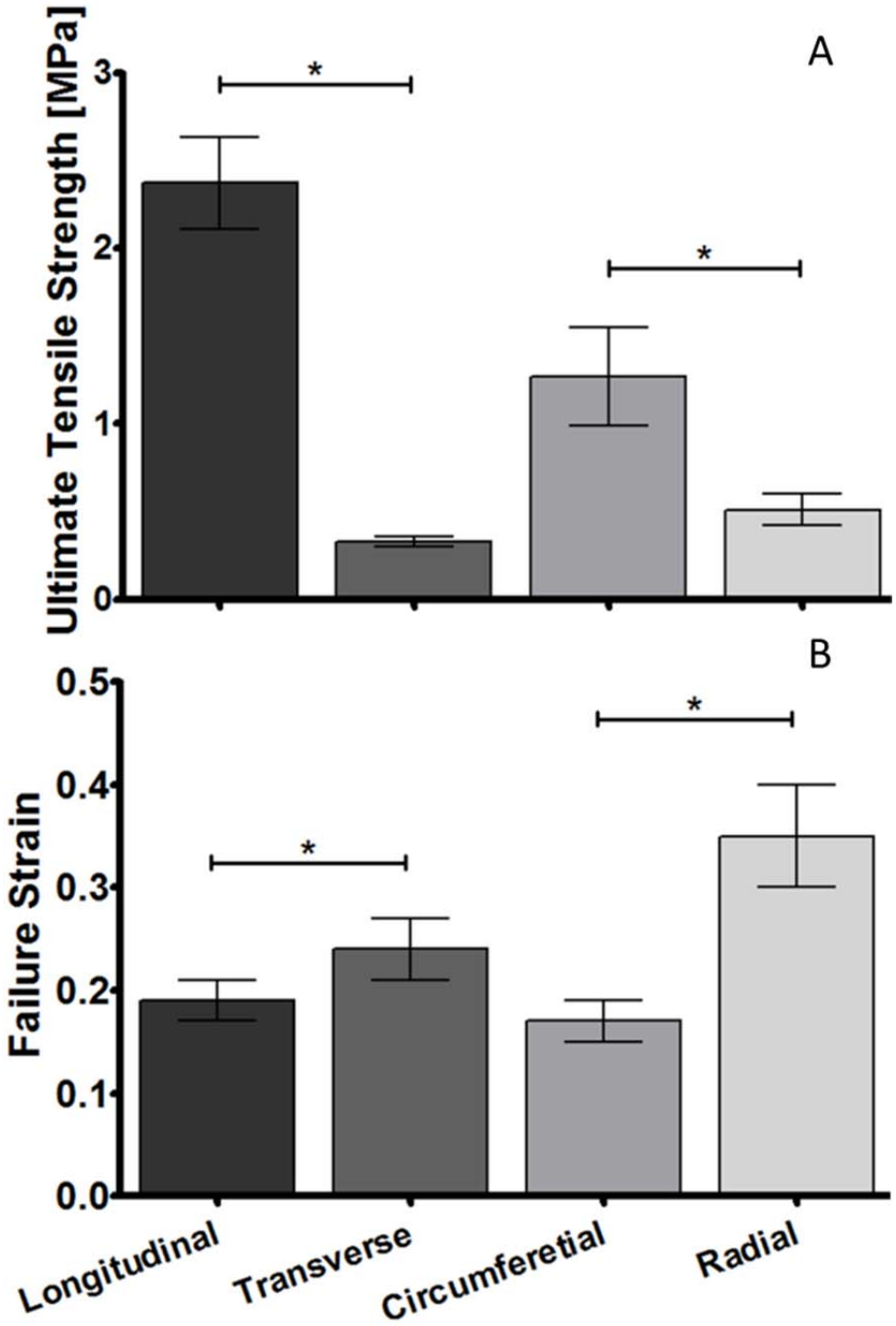

Figure 4.6: (A) Ultimate tensile strength (stress at failure) and (B) failure strain for the annulus fibrosus in four orientations: longitudinal, transverse, circumferential and radial. (* $p < 0.01$).

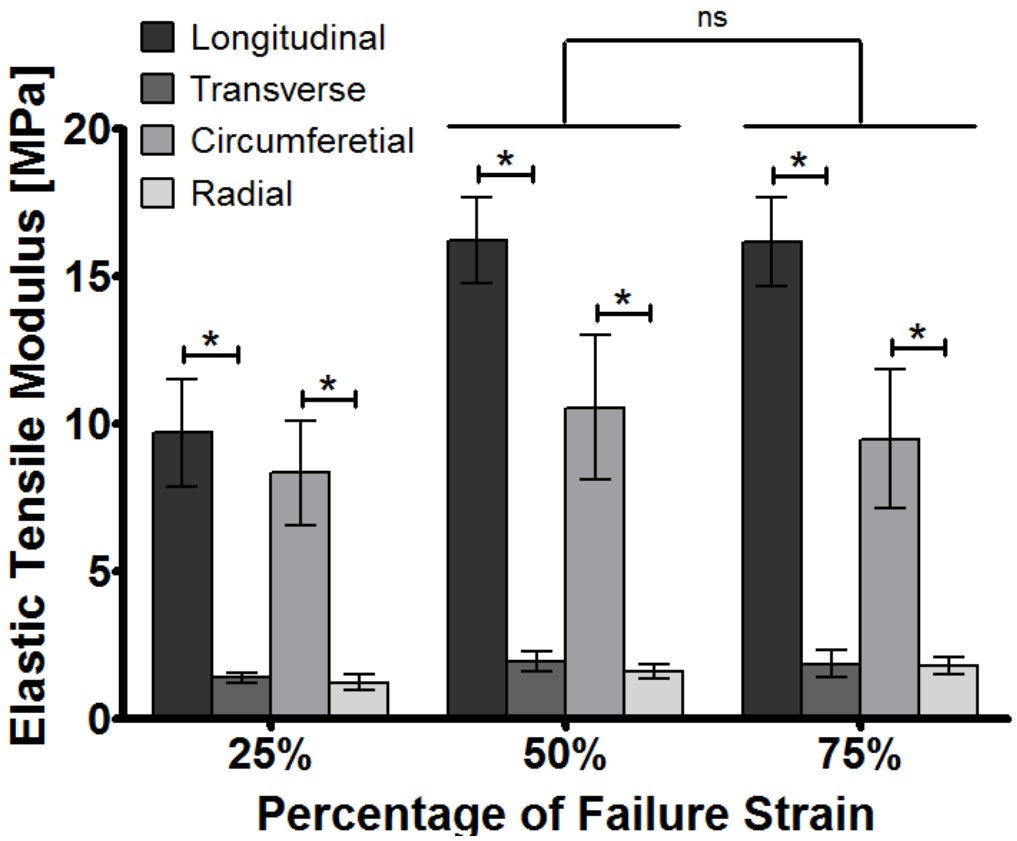

Figure 4.7: Elastic tensile modulus for the annulus fibrosus at three locations (25%-, 50%-, and 75%-failure strain) in four orientations: longitudinal, transverse, circumferential and radial. (* $p < 0.01$; ns = no significance).

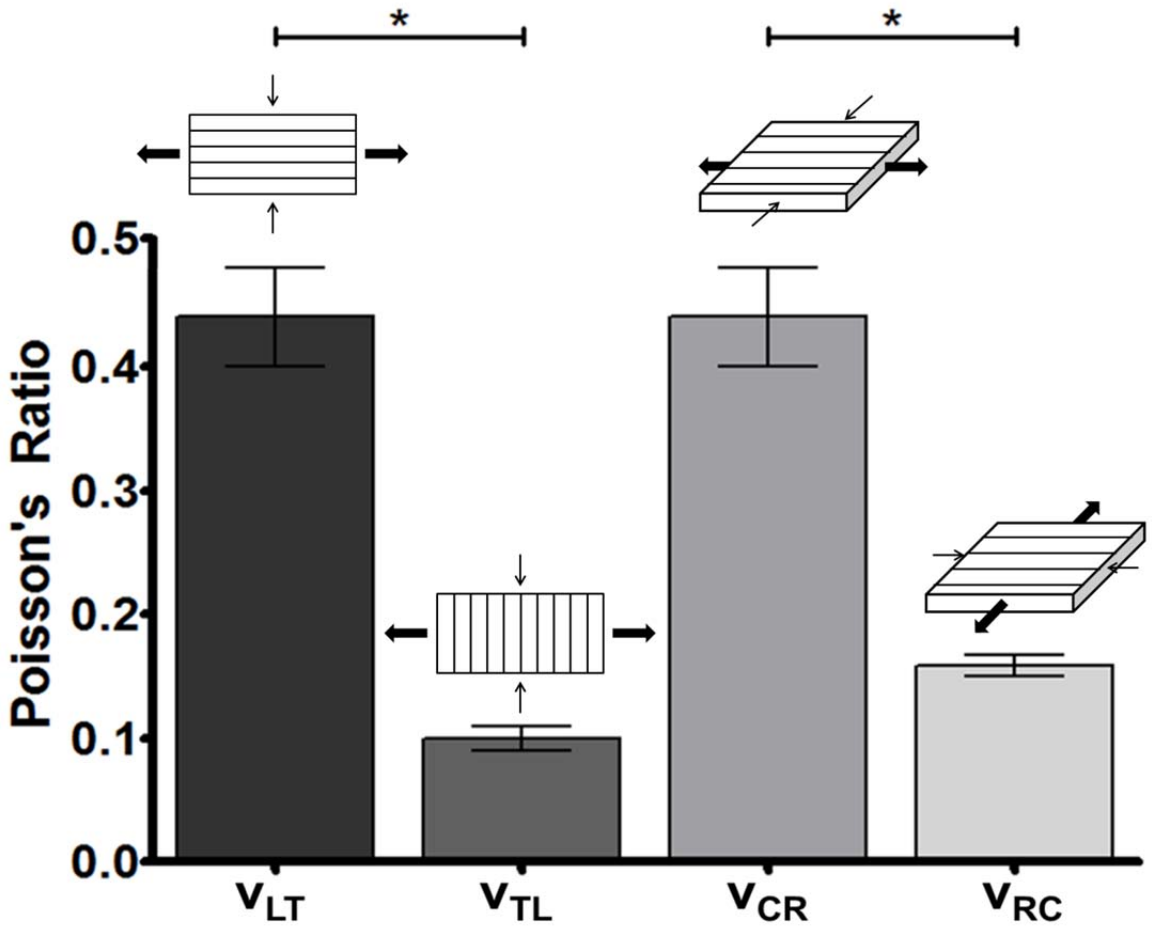

Figure 4.8: Poisson's ratio for the annulus fibrosus in four orientations: longitudinal, transverse, circumferential and radial. (* $p < 0.01$).

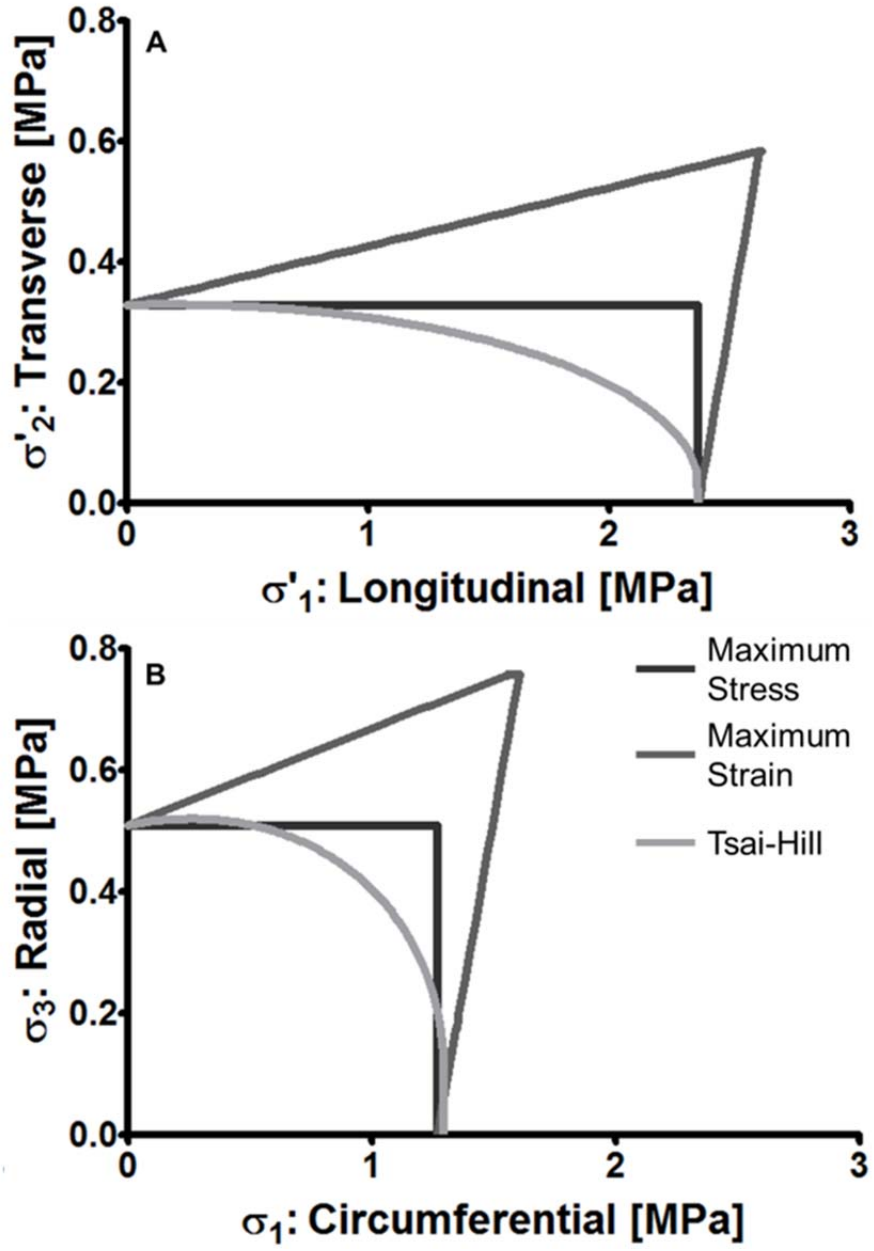

Figure 4.9: Failure envelopes for annulus fibrosus orientation: a) intra-lamellae and b) inter-lamellae. Three failure criteria are compared: Maximum stress and maximum strain (limit criteria) and Tsai-Hill (interactive criterion).

Table 4.1: Intervertebral disc sample information. Intra-laminar specimens are defined to be a single annular laminar and the inter-laminar specimens are cut across the lamellae; sample preparation of samples is dependent on orientation.

	Age	Gender	Level	Grade
Inter-lamellae				
	62	F	L2 – L3	2
	67	F	T12 – L1	2
	82	M	T11 – T12	2
	51	M	L3 – L4	3
	51	M	L1 – L2	3
Intra-lamellae				
	78	F	L5 – S1	3
	74	F	L4 – L5	3
	70	M	L4 – L5	2
	70	M	L2 – L3	2
	67	M	L1 – L2	3

Table 4.2: Properties of the annulus fibrosus (thickness = 150 µm) in four directions (n = 10 each): longitudinal, transverse, circumferential and radial.

	Failure	Failure	Elastic Modulus			Poisson's
	Stress	Strain	25% ε_f	50% ε_f	75% ε_f	Ratio
	[MPa]		[MPa]	[MPa]	[MPa]	
Intra-lamellae						
Longitudinal	2.37 ± 0.26	0.19 ± 0.02	9.67 ± 1.82	16.2 ± 1.45	16.15 ± 1.52	0.44 ± 0.05
Transverse	0.33 ± 0.03	0.24 ± 0.03	1.38 ± 0.17	1.91 ± 0.34	1.85 ± 0.47	0.097 ± 0.017
Inter-lamellae						
Circumferential	1.27 ± 0.28	0.17 ± 0.02	8.32 ± 1.76	10.52 ± 2.45	9.47 ± 2.34	0.44 ± 0.039
Radial	0.51 ± 0.09	0.35 ± 0.05	1.21 ± 0.26	1.6 ± 0.24	1.76 ± 0.29	0.159 ± 0.009

Table 4.3: Summary of previous studies that quantified mechanical properties (σ_f = failure stress, ε_f = failure strain, E = elastic moduli, ν = Poisson's ratio) of the annulus fibrosus for the longitudinal and radial directions compared to our experimental data. Mean (Standard Deviation).

Research Group	Sample Orientation	Sample Preparation	Mechanical Properties					
			σ_f, MPa	ε_f, %	E_{low}, MPa	E_{medium}, MPa	E_{high}, MPa	ν
[a]Skaggs et al. (1994) [139]	Longitudinal	• Single lamellae • Dumbbell shaped • Tested in 0.15M NaCl (room temperature)	AO = 10.3 (8.4) AI = 3.6 (2.0) PO = 5.6 (3.2) PI = 5.8 (2.9)	AO = 9.2 (3.4) AI = 11.3 (6.3) PO = 12.7 (2.7) PI = 15.4 (3.1)				
[b]Holzapfel et al. (2005) [140]	Longitudinal	• Single lamellae • Vertebral body grips • Dabbed with 0.15M NaCl and tested at room temperature			VLe = 5.96 (3.05) VLi = 3.79 (2.61) De = 8.01 (6.50) Di = 3.80 (5.02)	VLe = 32.5 (12.1) VLi = 13.9 (8.13) De = 24.1 (12.3) Di = 14.0 (8.63)	VLe = 77.6 (20) VLi = 27.5 (12.8) De = 64.8 (48.6) Di = 31.2 (19.8)	
[c]Fujita et al. (1997) [86]	Radial Inter-lamellae	• 1 ± 0.1 mm thick • Equilibrated in 0.15M NaCl prior to testing • Tested at room temperature	0.30 (0.16)	124 (66)			0.47 (0.33)	
[d]Smith et al. (2008) [141]	Radial Inter-lamellae	• 2 mm thick • Tested in 0.15M PBS at room temperature			AL = 0.096 (0.062) PL = 0.055 (0.04)		AL = 0.272 (0.178) PL = 0.167 (0.103)	
[e]Acaroglu et al. (1995) [72]	Inter-lamellae	• 1.8 mm thick • Dumbbell shaped • Tested in 0.15M NaCl at room temperature						ν_{CR} = 1.36 (0.63)
[e]Elliott & Setton (2001) [145]	Inter-lamellae	• 7.7 x 2.9 x 1.4 mm sample (L x W x t) • Tested in 0.15M PBS at room temperature						ν_{CR} = 0.6 (0.7) ν_{RC} = 0.51 (0.2)
[g]Current Study	Intra-lamellae	• Single lamellae • Dabbed with PBS • Tested at room temp	L = 2.37 (0.26) T = 0.33 (0.03)	L = 19 (2) T = 24 (3)	L = 9.67 (1.82) T = 1.38 (0.17)	L = 16.2 (1.45) T = 1.91 (0.34)	L = 16.15 (1.52) T = 1.85 (0.47)	ν_{LT} = 0.44 (0.05) ν_{TL} = 0.097 (0.017)
	Inter-lamellae	• 0.15 mm thick • Dabbed with PBS • Tested at room temp	C = 1.27 (0.28) R = 0.51 (0.09)	C = 17 (2) R = 35 (5)	C = 8.32 (1.76) R = 1.21 (0.26)	C = 10.52 (2.45) R = 1.6 (0.24)	C = 9.47 (2.34) R = 1.76 (0.29)	ν_{CR} = 0.44 (0.039) ν_{RC} = 0.159 (0.009)

[a]AO = anterior/outer (n = 6); AI = anterior/inner (n = 9); PO = posterolateral /outer (n = 5); PI = posterolateral/inner (n = 4). Uniaxial test with strain rate = 0.00009 sec^{-1}. [b]VLe = ventro-lateral external (n = 11); VLi = ventro-lateral internal (n = 9); De = dorsal external (n = 11); Di = dorsal internal (n = 8). Uniaxial test with strain rate = 1 mm/min. [c]Tangent modulus calculated at 30% strain. Strain rate = 0.5% sec^{-1}. [d]AL = anterolateral; PL = posterolateral. Strain rate = 0.0025 sec^{-1}. [e]Strain rate = 0.0001 sec^{-1}. [g]L = Longitudianl direction; T = Transverse direction; R = Radial direction; C = Circumferential Direction.

5. CHAPTER FIVE: ROLE OF BIOMOLECULES ON ANNULUS FIBROSUS MECHANICS: EFFECT OF ENZYMATIC DIGESTION ON MICROMECHANICS

5.1. Introduction

The main macromolecular components of the annulus fibrosus are fibrillar collagens (type I and II collagen), proteoglycans (mostly aggrecan) and elastin. The composition and the organization of these macromolecules differ across the regions. The annulus consists predominantly of sheets made from bundles of collagen fibers, which form concentric lamellae around the spinal axis [10, 15]. Collagen fibers in individual lamella of the annulus are parallel with respect to the each other and have an angle of 60° with respect to the sagittal axis of the disc which alternates in successive lamellae [8, 10, 14, 34]. Collagen provides the tensile strength of the annulus, stability between the vertebrae, and resistance to disc bulging in response to loads [11]. In the annulus of young, normal discs, collagen makes up 67% of the dry weight [11]. An elastic component within the disc ensures adequate recovery of the network organization after deformations. The presence of elastic fibers in the annulus has been noted in some earlier studies [47, 49-52] and the large-scale organization of the fibers has been examined by Yu et al. [53] in bovine tail. In the annulus, elastic fibers appear densely distributed in the region between the lamellae and also across the lamellae [138]. Proteoglycans are glycosaminoglycan (GAG) chains attached to a protein core in a bottle brush arrangement. GAGs are hydrophilic and thus attract and hold water in the intervertebral disc, absorbing the compressive loads and evenly distributing the force around the circumference of the annulus [41], in addition to providing electrostatic repulsion

between molecules which accounts for 50% of their mechanical contribution [61, 192, 193]. Intervertebral discs have a variety of proteoglycans in its extracellular matrix [38]; aggrecan is the most abundant proteoglycan by weight (10-20% dry weight) [194].

The intervertebral disc experiences irreversible chemical and structural changes due to aging. Intervertebral disc degeneration is accompanied by a loss of collagen, proteoglycan and elastin with aging as well as an increase in enzymatic activity. Due to the localization of the biomolecular components in the intervertebral disc, the different mechanical responses and damage patterns associated with disc degeneration are likely related to the local molecular breakdown of the tissue. Olczyk correlated the changes of aldehyde contents of collagen with age (from 0.17 mmol/g dry weight at 30 years old to 0.07 mmol/g dry weight at 80 years old) and showed that significant decreases in collagen solubility was attributed to an increase in intermolecular cross-links and age [100, 101]. Elastin and proteoglycan concentration in the annulus also decrease with age and degeneration; from around 23 mg/g dry weight at 50 years old to about 17 mg/g dry weight at 80 years old for elastin and from 100 mg disaccharide units/g dry tissue at birth to about 70 mg disaccharide units/g dry tissue at 80 years old for proteoglycan [98, 121].

The material properties of the annulus in tension, compression, and shear depend on disc location, age, degeneration, sample orientation within the disc, and loading rate [72-76]. Previous work has been completed studying the effect of enzymes on elastin and proteoglycans on annular tensile mechanics which showed a significant reduction in the initial and ultimate modulus, and a significant increase in the extensibility, of radially oriented annulus fibrosus specimens [141]. In this novel study, we examined the effect of removing the main macromolecules (collagen, elastin and proteoglycan) using enzymatic

digestion of the annulus fibrosus. To determine the mechanical function of these macromolecules we have developed a protocol to test the effect of digested conditions on annular inter- and intra-laminar biomechanics. In this work, using micromechanical testing, we investigated the degenerative mechanics that occur longitudinally, transversely, circumferentially and radially in the annulus.

5.2. Materials and Methods

5.2.1. Specimen Preparation

Ten intervertebral discs were isolated from eight fresh-frozen human cadaveric lumbar spines (age range, 51–82 years; mean, 68.9 years; Table 5.1) that were obtained from an approved tissue source (National Disease Research Interchange, Philadelphia, PA) using a sharp dissection at the superior and inferior endplates. Using a modified Thompson scale [195], the isolated discs were assigned a degenerative grade (1–5 scale; Grade 1, nondegenerate; to Grade 5, degenerate) based on observations of gross morphology made by two independent observers. The outer annulus was dissected from each isolated disc in two locations: anterior and postero-lateral. Each segment was mounted on the freezing stage of a cryostat (Model CM 3050S, Leica, Nussloch, Germany) using Cryomatrix™ (Shandon Cryomatrix, Fisher Scientific). Samples were cut using a D profile Tungsten Carbide knife (Delaware Diamond Knives, Wilmington, DE) to a uniform thickness of 150μm and frozen at -22°C until testing.

Samples were prepared in two orientations, inter-lamellar (across lamellae: circumferential and radial) and intra-lamellar (within a single lamellae: longitudinal and transverse) to obtain samples in four testing directions: longitudinal (L), transverse (T), radial (R) and circumferential (C). We define the intra-laminar specimens to be a single

annular laminar and the inter-laminar specimens to be cut across the lamellae, sample preparation of samples is dependent on orientation. Samples were prepared by making either a) intra-lamellar or b) inter-lamellar cuts, relating to within a single annulus laminar slice or across lamella. The annular slices are then further distributed into four groups to be tested in the following orientations: longitudinal, transverse, circumferential and radial.

The intra-lamellar orientations investigate the properties of individual lamina of the annulus, while the inter-lamellar orientations give insight into the characteristics between layers of the annulus. The inter-lamellar samples were examined to determine that collagen fibers were evident in only direction, thus assuring no more than one annular lamellae was obtained; samples with more than one lamellae evident were discarded. In relation to the collagen fibers of a single lamellae, longitudinal samples are at 0°, while transverse are oriented 90° to the loading direction. Similarly, the intra-lamellar specimens were cut so that the length, width and thickness aligned with the axis of the intervertebral disc. Circumferential samples were oriented so that there would be tension along the perimeter of the annular layers, while the radial samples were loaded in tension out of plane to the individual lamella. In relation to stacks of lamellae, circumferential samples are at 0°; while radial are oriented 90° to the loading direction.

5.2.2. Enzymatic Digestion

Within the four orientation groups, the samples were randomly assigned to four digestion groups (n = 10 for longitudinal and circumferential, n = 5 both anterior and posterior-lateral; due to small sample size, n = 7 for transverse and radial with n = 3 anterior and n = 4 posterior-lateral): Control, COL, ELA, and PG. Pilot studies were

performed to bracket the enzymatic digestion protocol time, holding enzyme concentration constant. It was determined that an 18 hour soak maintained viable samples, while providing adequate degeneration of the samples to show a mechanical consequence. Each annular sample was thawed at room-temperature in a group-specific buffer solution for 2 hours (Table 5.2). Samples were then immersed in the appropriate buffer solution with enzyme for 18 hours at 37°C under gentle agitation. The samples were then allowed to reach equilibrium at room-temperature in 1x phosphate buffered saline (PBS). The control group consisted of 5 mL of 0.15 M (1X) Phosphate Buffered Saline with no enzyme. The COL treatments group consisted of 5 mL of 50mM N-[Tris(hydroxymethyl)methyl]-2-aminoethanesulfonic acid (TES) and 2mM Calcium Chloride (CaCl) with the enzyme 2 U/mL of Collagenase (from *Clostridium histolyticum*). The ELA treatments group consisted of 5 mL of 0.1M Tris(hydroxymethyl)aminomethane (TRIS) with 2 U/mL of Elastase (from *Porcine pancreas*; Elastin Products Company, Owensville, MO) as the enzyme. Finally, the PG treatment group consisted of 5 mL of 50mM of TRIS and 60mM of Sodium Acetate in 0.02% Bovine Serum Albumin (BSA) with 0.125 U/mL of Chondroitinase ABC (from *Proteus vulgaris*) as the enzyme being activated. Pilot studies showed there were no significant differences in mechanical properties when immersed in the different buffer solutions (Figure 5.2). All reagents were obtained from Sigma Aldrich (St Louis, MO) unless otherwise noted.

5.2.3. Mechanical Testing

Prior to testing, samples were examined for tears; these broken samples were discarded. Annular samples were gripped with fine grit sandpaper glue (3M Company,

St. Paul, MN) using Scotch® brand super glue (3M Company, St. Paul, MN) and secured in a mechanical testing system (Model 4442, Instron, Norwood, MA) with screw side action grips (#2710-004, Instron, Norwood, MA). Width and length of the gauge section were measured with a digital caliper (Mitutoyo, Aurora, IL). The average dimensions of the gauge region of the intra-laminar test specimens were 5 x 2 x 0.15 mm for length, width, and thickness, respectively. In the same frame of reference, the inter-laminar specimens had dimensions for length, width, and thickness of 0.15 x 2 x 5 mm. Two different low-profile static load cells were used: ±50 N (Instron, Norwood, MA) for longitudinal and circumferential orientations and ±5 N (Instron, Norwood, MA) for transverse and radial orientations. Samples were preconditioned to 10% strain cyclically for five cycles at a strain rate of 0.005 sec^{-1}. Each sample was then loaded in tension at a strain rate of 0.005 sec^{-1} until macroscopic failure occurred. This slow rate was chosen to help minimize the effect of frictional drag and the viscoelasticity of the annular solid matrix [139, 170]. The data acquisition rate was dependent on the load cell, 1 Hz and 10 Hz for the ±5 N and ±50 N load cells respectively.

5.2.4. Data Analysis

Stress and strain were calculated from the force and displacement data. Stress (σ) was computed as force divided by original cross-sectional area and strain (ε) was computed as displacement of grips divided by the initial gauge length. The failure strain (ε_f) was defined as the strain corresponding to the failure (maximum) stress (σ_f) as determined from the stress-strain curve. For this study, a cubic function was used to fit the tensile stress-strain behavior [139]: $\sigma = D + C\varepsilon + B\varepsilon^2 + A\varepsilon^3$, where the coefficients were determined using a nonlinear regression curve-fitting procedure. Tensile moduli

were found by differentiating the stress-strain relationship based on Skaggs et al. [139] at a low and high percentage of failure strain due to non-linearity, 25%ε_f and 75%ε_f, we label as elastic toe modulus (E_{Toe}) and linear modulus (E_{Lin}), respectively. A total of 128 samples, from ten human lumbar intervertebral discs, were mechanically tested and analyzed. Digested mechanical properties within each orientation were normalized to the control group. Student's *t*-test was performed on the mechanical parameters to test for the effect of digestion. All statistical analyses were performed using Prizm software (Graphpad Software, San Diego, CA) with significance set at $P \leq 0.05$.

5.3. Results

The annular tensile response exhibited expected nonlinearity and anisotropic behavior. A typical stress-strain response for a longitudinal specimen from the control group (1x PBS) is shown in Figure 4.4. Our previous work [196] discussed the procedural validation; to summarize, the control values for the longitudinal and radial samples were in range of those in literature [86, 139-141]. The shape of the stress-strain relationships varied depending on orientation of the samples.

In the longitudinal orientation, samples underwent the digestion protocol, but without enzymes to determine if there was an effect of digestion buffer solutions on the properties; there was no statistically significant difference between the control (1x PBS) samples and the digestion buffer solutions. Normalized digested mechanical properties within each orientation were examined.

In the longitudinal orientation (Figure 5.4), among all digestion groups there was a statistically significant decrease ($P < 0.001$) in properties from the control, except for failure strain. The only digestion group that showed a significant change in the failure

strain was the COL group which had a 63% increase. The COL group had an average decrease of 85 ± 3 % for the rest of the properties from the control group. The elastase- and chondroitinase ABC-treated groups (ELA, PG) showed average decreases of 66 ± 4 % and 58 ± 9 % respectively in all properties except for failure strain.

All digestive groups of the longitudinal samples were tested using the microscope setup described in section 4.2. With the recorded images, the Poisson's ratios, ν_{LT}, were able to be determined. Previously, we experimentally found that Poisson's ratio for the PBS sample was equal to $\nu_{LT} = 0.44 \pm 0.05$. There was a significance decrease in the Poisson's ratio for the COL and PG samples from the control group ($p < 0.05$), and no difference between the ELA and PBS (control) group. The values of the in-plane intra-lamellar Poisson's ratios were (Figure 5.5): 0.37 ± 0.02, 0.42 ± 0.05, and 0.33 ± 0.02 for the COL, ELA and PG groups, respectively.

Within the transversely oriented samples, the effect of digestion was more varied (Figure 5.6). The COL group showed a significant decrease (average 55 ± 8 %) in the failure stress and elastic moduli from the control group. The ELA group had an average 70 ± 20 % decrease in all properties from control. Samples within the PG digestion group showed a decrease in moduli of about 53% from the control group. While there was a 36% increase in the failure strain for digested specimens.

The effect of the different digestion groups was varied within the radially oriented samples (Figure 5.7). Enzymatic digestion had no effect on the linear elastic modulus (E_{Lin}). The only digestion group to affect the elastic toe modulus (E_{Toe}) was ELA with a 70% decrease. Failure strain was the only property to have a significant change when subjected to chondroitinase ABC (PG group) with a 48% increase from the control. There

was an average increase by about half in failure strain within the COL and PG groups. There was an average 37 ± 6 % decrease of the failure stress in the COL and ELA groups.

Specimens in the circumferential orientation (Figure 5.8) showed a decrease in properties, excluding failure strain, in all digestions except for the chondroitinase ABC-treated (PG). The PG group only had an effect on failure strain, decreasing it from the control group by a quarter. The collagenase- and elastase-treated groups (COL, ELA) showed average decreases of 43 ± 5 % and 50 ± 10 % respectively in all properties except for failure strain in which there was no statistically significant change.

5.4.Discussion

Disc degeneration is associated with changes in mechanical properties which may lead to instabilities and herniation [197-200]. We examined the role of individual molecules of collagen, elastin and proteoglycan on the mechanical behavior of intra- and inter-lamellar specimens of the annulus fibrosus which were oriented in four directions: longitudinal, transverse, circumferential and radial.

The properties of single non-degenerated annulus lamellar specimens has been studied by Skaggs et al. [139] in plane with the collagen fibers (longitudinal); our longitudinal control samples are within this range. Collagenase attacks and cleaves amino acids at specific binding sites of the collagen molecule [201, 202]. When treated with the COL enzymatic digestion, there is a loss in all examined mechanical properties except failure strain. This follows the theory that the collagen fibers are the main load bearing elements within the annulus [8, 50]. Enzymatic digestion of some collagen and the resulting decrease in failure stress demonstrates the importance of collagen to the tensile

strength of the annulus. Failure strain does not follow this trend. We hypothesize that upon removal of the collagen fibers, the elastin fibers which are aligned parallel to the collagen fibers [141, 173] are able to become the load bearing elements the strain reflects that of elastin which has a higher failure strain that collagen. It has been previously shown, that collagenase was not active against elastin [203]. Elastase is a highly active elastin-decomposing enzyme and degrades amino acids at sites of the elastin molecule [204, 205]. Samples within the ELA and PG groups showed no significant change in the failure strain suggesting that collagen plays an important role in the failure strain of the control group and does not allow the closely connected elastin fibers to act as structural reinforcement. Conversely, failure stress and elastic moduli, were negatively affected in the elastase- and chondroitinase ABC-treated groups. This suggests that the elastic fibers and PG matrix are playing an important role within the annulus acting as an extracellular matrix to help engage the collagen fibers during loading. We hypothesize that upon removal of the proteoglycans, the collagen fibers are no longer as strong since there are no interactions between them without the surrounding matrix. Similarly, in removing elastin fibers there is a loss of the mutual interactions between collagen and elastin which produce the overall mechanical response of the annulus.

Transverse lamina specimens allowed for testing out of plane of the collagen fibers. The COL samples had a similar trend as the longitudinal samples; there was a decrease in all properties except failure strain. This suggests that due to the proteoglycan matrix and elastin fibers, even when orientated at 90°, the collagen fibers still play an active role in laminar mechanics. Again, failure strain was not reduced; the property is more indicative of the elastin fibers. There was also an increase in failure strain in the PG

group. This occurred due to a similar mechanism; the proteoglycan matrix no longer restricted the elastin fibers, and the failure strain was allowed to increase to a value more reflective of elastin. The PG samples showed no difference in the failure stress however. The reduction in properties within the elastase-treated group (ELA) was expected due to the placement of elastin fibers within a single lamellae; It has been suggested that some elastin fibers are anchored to collagen fibers within a lamellae [141, 167] and can aid in the collagen fiber bundles working together during tension. Removal of these elastin fibers disrupts the collagen fibers and proteoglycan matrix, thus leading to a reduction in all mechanical properties (failure stress, failure strain and elastic moduli).

The radial properties of non-degenerated annulus specimens has been previously studied [86]; our control samples in this orientation are within this range. Due to the stacked lamellae structure, we hypothesize that testing in this orientation should be a good approximation of the inter-laminar matrix because this direction of testing is perpendicular to the primary collagen architecture. Similar to the other out-of-plane orientation (transverse), when tested radially samples in the COL and PG groups showed an increase in failure strain. Between lamellae, elastin is positioned in three-dimensional bundles which branch from collagen fibers in adjacent lamellae [141, 173]. Removing the alternate biomolecules, allows these elastin fibers to be tensed uniaxially, thus allowing a higher failure strain. This is further evidenced by the decrease in failure strain in the ELA group. The ELA samples also showed a decrease in the failure stress, again demonstrating that the elastin fibers play a major role in inter-laminar mechanics, this also suggests that they play a role in maintaining lamellar cohesion. Distributions of proteoglycans are low between lamellae, thus evident by the lack of change in the failure

stress, strain and moduli when compared to the control group. Interestingly, the only other property that the collagenase-treated group (COL) had an effect on was a decrease in failure stress. In this orientation, the collagen fibers are ±30° in a perpendicular plane to the force. This suggests that the geometry of the lamellae play a role in the radial mechanics; this could be related to the out-of-plane ply interactions within a cross-ply laminate [148, 206, 207].

Testing in the circumferential direction, the PG group showed no significant change in properties, except for failure strain. However, in this orientation there was an unexpected decrease in failure strain. We hypothesize that the removal of proteoglycans disrupts the matrix in which the collagen network is embedded in the perpendicular plane, thus not allowing the anchored elastin fibers to bear load. No other treatment groups had an effect on failure strain. The COL and ELA groups had similar negative effects on the rest of the mechanical properties. This implies that the structure and mechanics of the individual lamina play a large role in the mechanics of the whole structure (laminate), following composite theory [207].

The findings presented here should be considered in light of some limitations. The sample preparation and dimensions may allow for the introduction of edge effects [208]. However, Skaggs et al. [139] determined that the advantage of the dumbbell shape is not fully recognized in the uniaxial testing on longitudinal annulus lamellae and stress concentrations at the grips may not be relieved. Annular mechanics are strain-rate dependent, so for this study, a slow strain rate was chosen in order to represent the intrinsic properties of the annulus in tensile loading. It is also important to point out that the enzymes may have a non-specific effect on the non-targeted biomolecules. It has

been previously reported that elastase treatment of the annulus can result in non-specific degradation of collagen, however it is not considered to have a significant effect on the mechanical properties [141]. There has also been evidence that elastase can have an effect on the glycosaminoglycans within the annulus [141]. In this study, no attempt was made to confirm the specificity and extent of degradation of collagen, elastin and proteoglycan produced by the enzymatic treatments. However, from the results it appears that the enzymatic digestion is appropriate to study the mechanical contributions of the specific macromolecules. Biochemical assays should be performed in order to quantify the amount of biomolecules that are removed following digestion in each enzyme group.

In this paper, we quantified the effects of enzymatic digestion on different testing orientations of the annulus fibrosus in order to give insight into role of the biomolecules within the annulus. These properties provide insight into the mechanical behavior and molecular component interactions within the annulus. This may be important in diagnosis, prevention and repair of debilitating intervertebral disc disorders and manufacturing of tissue-engineered annulus. Fiber-reinforced numerical models of the annulus fibrosus have been commonly used in the analysis of the mechanical behavior of the intervertebral disc [142, 144, 153-156]. A future goal of this work is to create a damage criterion to predict failure in the annulus fibrosus by treating the annulus as a fiber reinforced angle-ply laminate. The experimentally determined material properties determined in this study can be used together with composite theory to determine the role of the lamellae and biomolecular influences in annular failure.

5.5.Conclusions

Uniaxial tension was applied to enzymatically digested single lamellar human cadaveric annulus fibrosus specimens to investigate changes in annular mechanics due to the loss of the main biomolecules. The purpose of this chapter was to investigate the effect of digesting the main macromolecules in the intervertebral disc on the micro-mechanical behavior of the human cadaveric lumbar annulus fibrosus to determine the role these molecules play in annular mechanics. The enzymatic digestion protocol allowed for a quantitative assessment of the effect the main macromolecules within the intervertebral disc have on annular mechanics. The collagenase- and elastase-treated groups had the most significant effect on the mechanical properties within all the orientation groups, decreasing the failure properties except failure strain. The chondroitinase ABC-treated group only had a significant impact on the single layer orientations (longitudinal and transverse) decreasing the failure properties except failure strain. Collagenase-treated groups showed an increase in the failure strain following enzymatic digestion in all orientations except for circumferential. The digested properties described provide insights into the laminar mechanical behavior and how the separate molecular components contribute to the effective properties of the annulus fibrosus. This may prove insightful in diagnosis, prevention and repair of debilitating intervertebral disc disorders and manufacturing of tissue-engineered annulus.

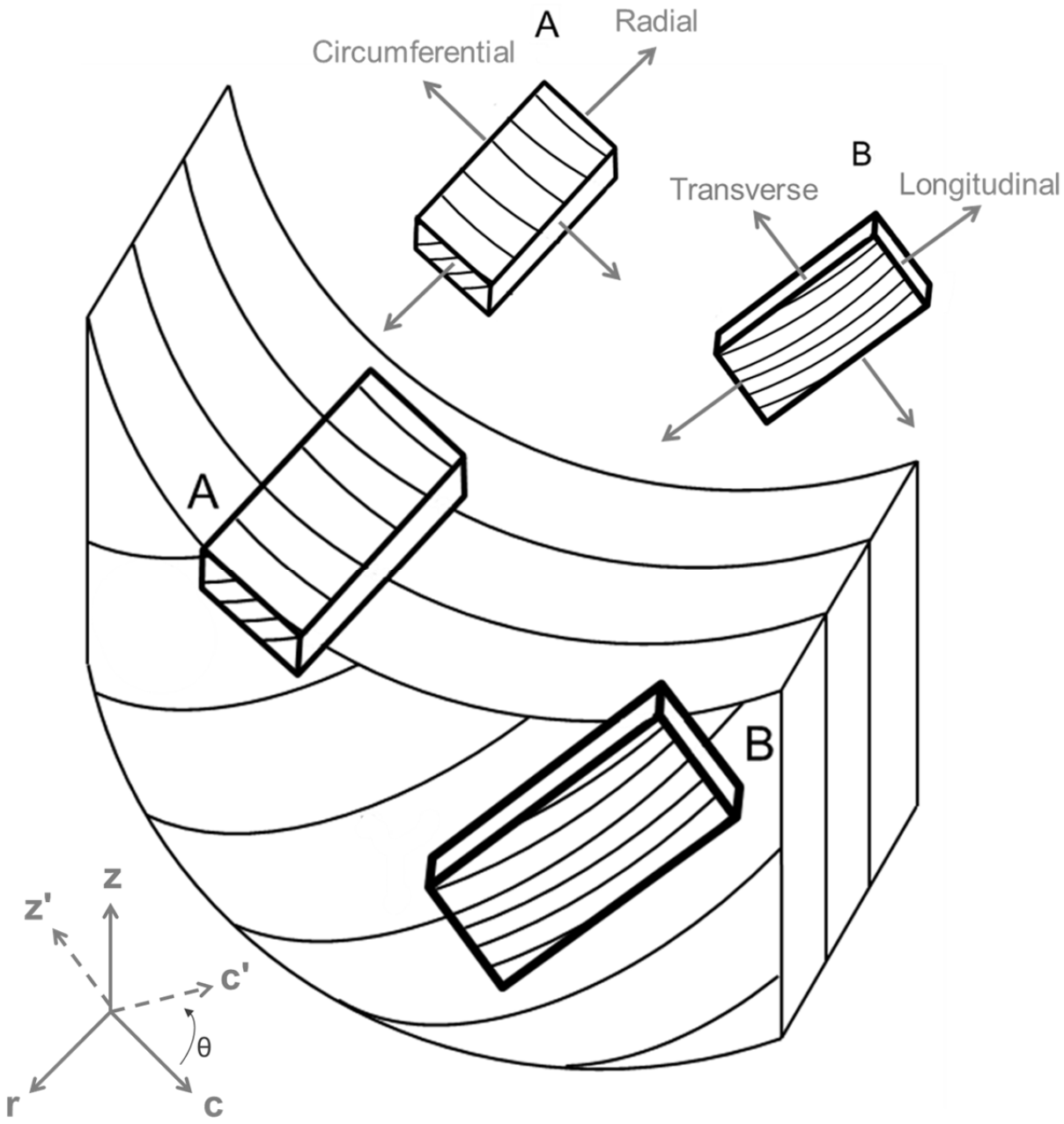

Figure 5.1: Sample testing orientation.

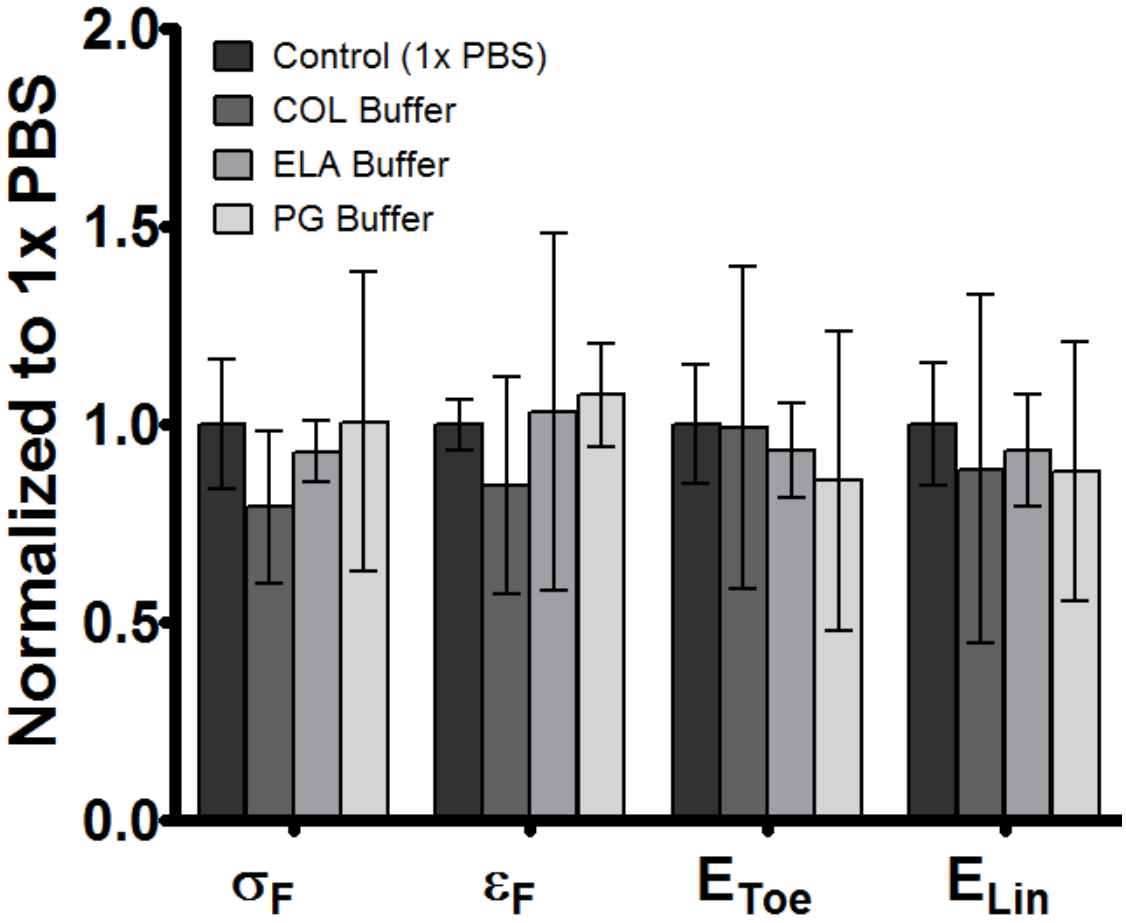

Figure 5.2: Effect of buffer on mechanical properties.

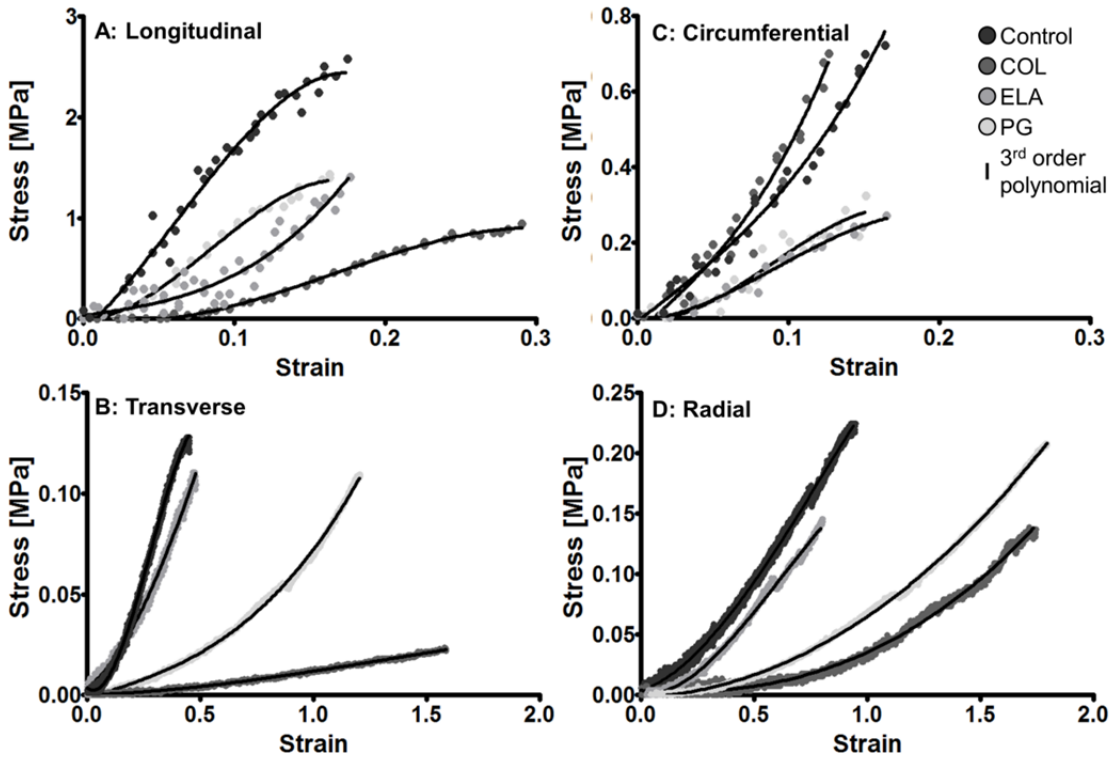

Figure 5.3: Representative stress-strain relationships for annular samples oriented in the a) longitudinal, b) transverse, c) circumferential and d) radial directions. Experimental results are shown with a third-order polynomial best-fit cubic curve.

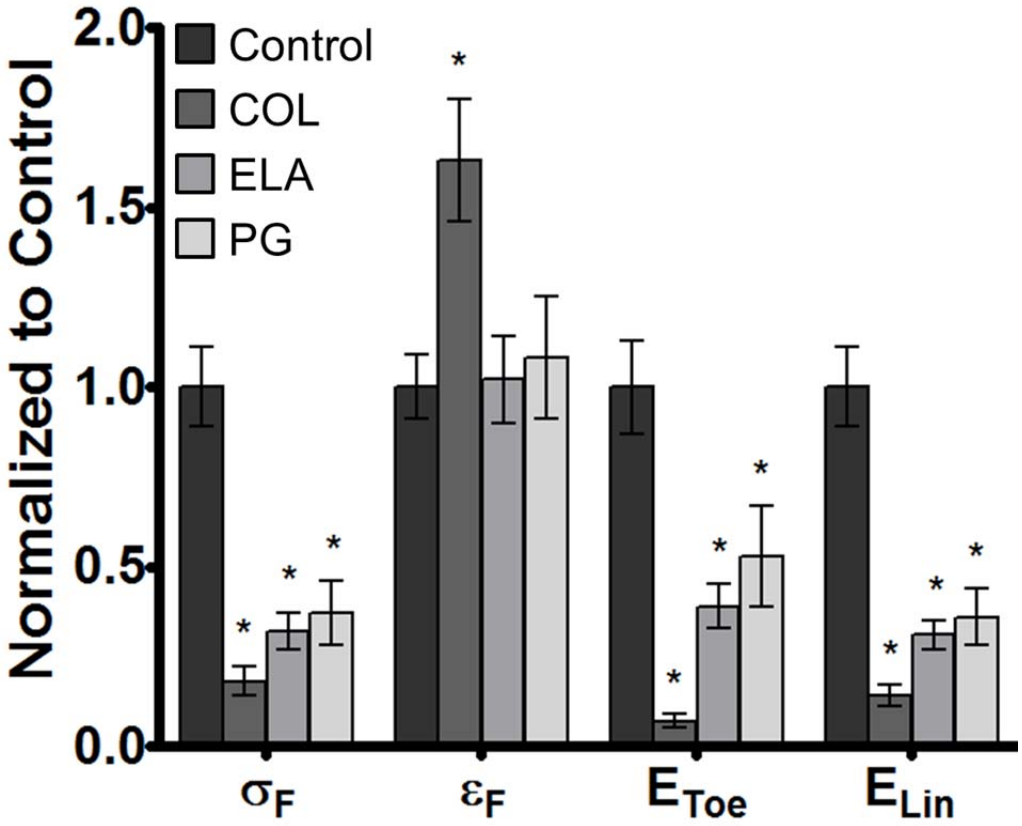

Figure 5.4: Effect of enzymatic digestion on the micromechanical properties of annular samples oriented in the longitudinal direction. (* $p < 0.05$ from control).

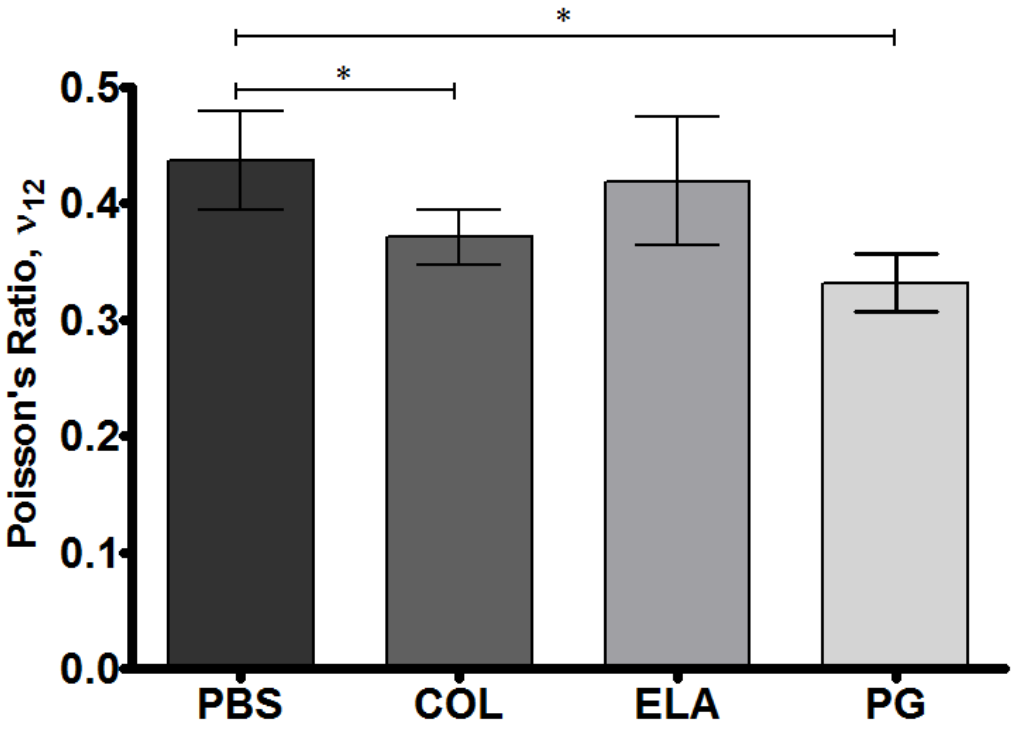

Figure 5.5: Effect of enzymatic digestion on the Poisson's ratio of annular samples oriented in the longitudinal direction: physical representative of expansion in longitudinal direction and contraction in the transverse (* $p < 0.05$ from control).

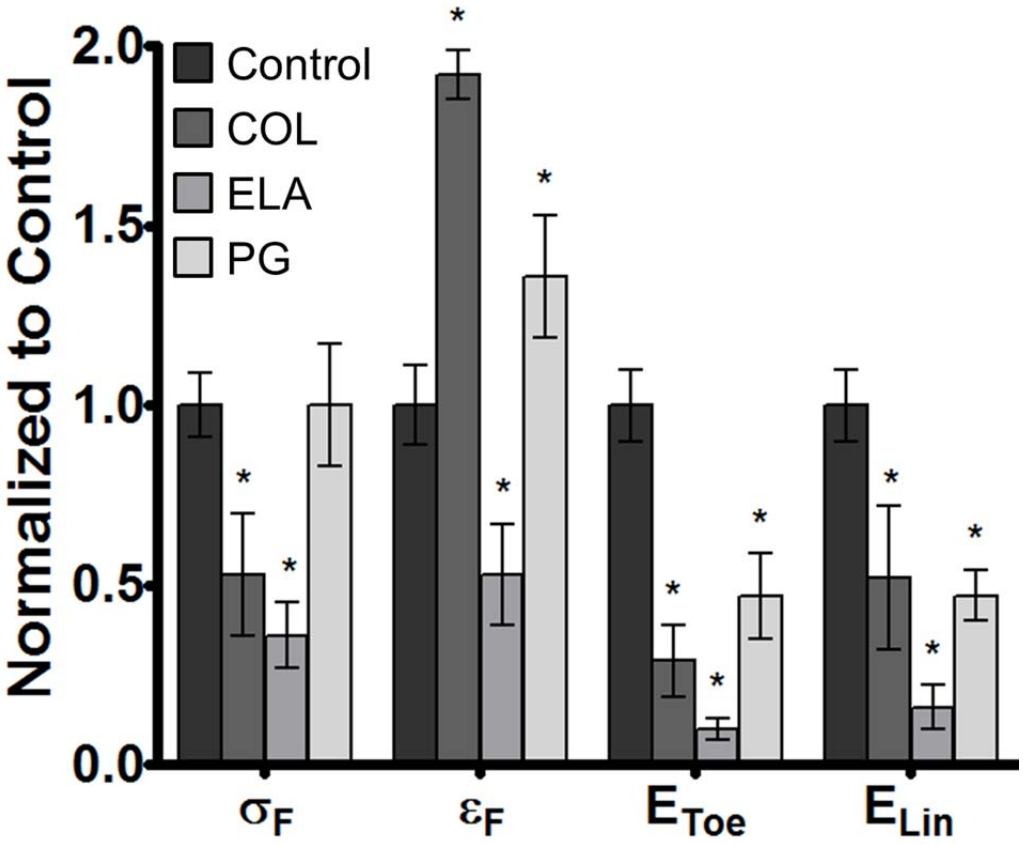

Figure 5.6: Effect of enzymatic digestion on the micromechanical properties of annular samples oriented in the transverse direction. (* $p < 0.05$ from control).

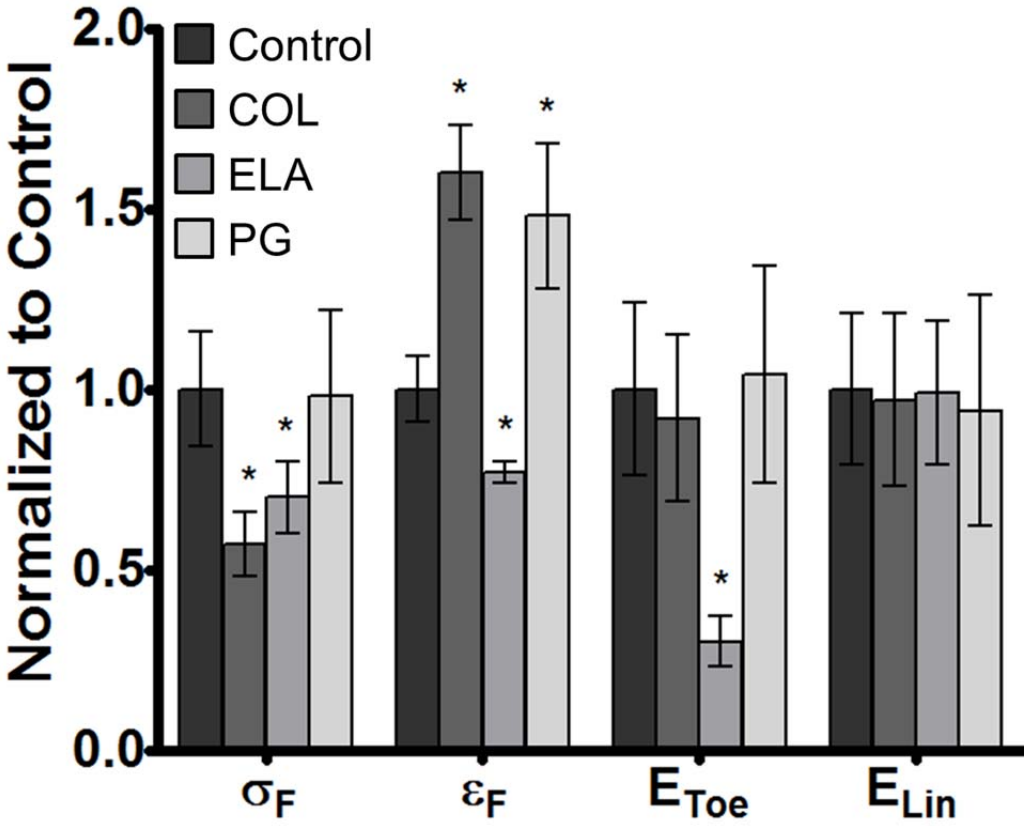

Figure 5.7: Effect of enzymatic digestion on the micromechanical properties of annular samples oriented in the radial direction. (* $p < 0.05$ from control).

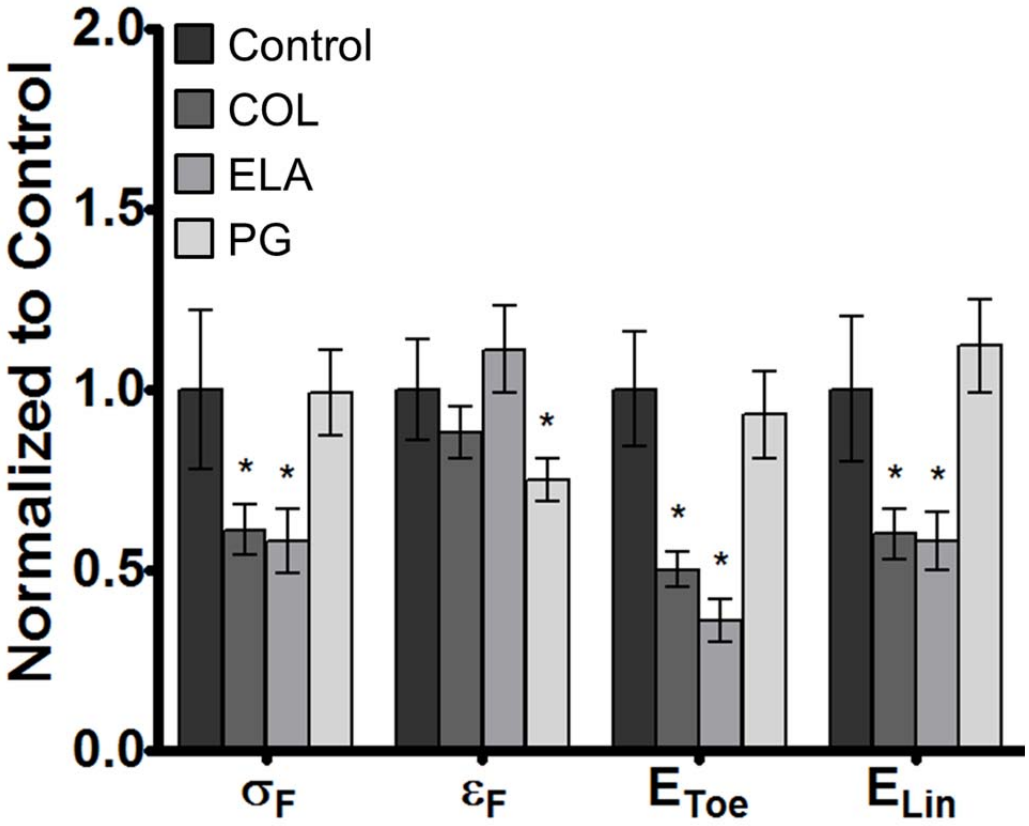

Figure 5.8: Effect of enzymatic digestion on the micromechanical properties of annular samples oriented in the circumferential direction. (* $p < 0.05$ from control).

Table 5.1: Intervertebral disc information.

	Age	Gender	Level	Grade
Inter-lamellae				
	62	F	L2 – L3	2
	67	F	T12 – L1	2
	82	M	T11 – T12	2
	51	M	L3 – L4	3
	51	M	L1 – L2	3
Intra-lamellae				
	78	F	L5 – S1	3
	74	F	L4 – L5	3
	70	M	L4 – L5	2
	70	M	L2 – L3	2
	67	M	L1 – L2	3

Table 5.2: Annular sample's group-specific buffer and enzyme assignments for digestion protocol.

Group	pH	Buffer	Enzyme
Control	7.5	1X PBS	
COL	7.4	50mM TES, 2mM CaCl in 1X PBS	10 U Collagenase
ELA	8.5	0.1M TRIS in 1X PBS	10 U Elastase
PG	8.0	50mM TRIS, 60mM Sodium Acetate in 0.02% BSA	0.625 U Chondroitinase ABC

6. CHAPTER SIX: TOWARD A PREDICTIVE MODEL FOR ANNULAR FAILURE

6.1. Introduction

Previous work in this thesis has experimentally measured the longitudinal and transverse engineering constants for lamellae of the AF. There have been other studies which have also characterized these material properties of the IVD in various loading conditions: tension [72, 76, 86, 139, 145, 166, 209], compression [79, 134], and shear [87, 88]. A better understanding of the mechanical behavior of the AF on a laminar level can improve theoretical, mathematical and computational models of both the AF and the whole IVD.

There has been work to model the behavior of the AF. Studies have related the fiber reinforced composition of the AF with material properties using strain energy functions with linear, nonlinear and hyperelastic models to describe the mechanical behavior of the AF [68, 145, 156, 210-217]. The fiber reinforced strain energy models do not require input of separate fiber and matrix properties, however they include many invariant terms which are hard to uniquely determine and do not always have a physical significance. These models have all been based on the initial work of Spencer (1984) using the principle invariants of the deformation tensor and separate structural tensors to represent the embedded collagen fibers and can be further broken into two categories [218]: the use of two equivalent fiber families [156, 212, 217] or two equivalent transversely isotropic materials [68, 211, 216]. In one study, the collagen fibers were modeled to only resist tensile loading [216]; alternatively, the collagen fibers can be modeled to resist both tension and compression [68, 211-213, 215].

Wu and Yao (1976) used a hyperelastic model and defines a strain energy function with two invariants for two families of collagen fibers and included fiber-fiber interactions in their work [217]. Klisch and Lotz (1999) derived a nonlinear, orthotropic model for the AF using the principle stretches of the material based on an annular strain energy function dependent on nine material coefficients, however it violated the traction free boundary conditions [156]. Elliott and Setton (2000, 2001) furthered this work by using a quadratic strain energy function in a linear anisotropic model and included fiber-matrix interactions in addition to the fiber-fiber interactions [145, 210]. Wagner and Lotz (2004) modeled the AF behavior using an orthotropic model with separate strain energy terms to represent the annular constituent contributions: matrix, fiber, interactions [212]. Guerin and Elliott (2007) developed a nonlinear anisotropic hyperelastic model which also used separated strain energy terms for the matrix, fiber and interactions [68]. However, they described the interaction terms in both shear and normal directions. A follow up to this work quantified the behavior of degenerated AF [211]. More recent work has examined interlaminar shear by use of a hyperelastic constitutive model [191] and examined the effectiveness of both the use of two equivalent fiber families or two equivalent transversely isotropic materials to include shear deformations [213]. The goal of these papers was to implement a material model of the AF in order to determine a complete set of model properties and prediction of annular material characteristics. A summary of these studies can be seen in Table 6.1. However, none of these models expanded the work to include investigation of failure of the AF.

These composite models give good insights into the influence of the laminate structure as well as the microstructure of the collagen fibers on the constitutive behavior;

however they do not investigate the failure or damage propagation in the AF. There has been substantial work in the field of composite theory, specifically laminated composites and corresponding failure [219, 220]. The author suggests a good review article on failure methods for composite materials by Orifici et al. (2008) [221]. These techniques that allow for understanding and prediction of failure of composite materials (either damage or fracture mechanics) can be used in order to examine the failure of the AF. In composite materials (including the degenerative AF), failure does not often occur catastrophically with no warning, it is usually progressive.

In the AF, there are tears that can become evident due to loading: radial (perpendicular to the end plates), circumferential (between annular layers, delamination), and rim lesions (radial tears along the endplate) [149, 195]. Propagation of these tears can be simulated with both compressive and bending loading procedures [113, 120, 153]. Iatridis and Gywnn (2004) investigated the failure mechanisms of the AF in terms of composite theory and calculated the interlaminar shear stress, stresses in AF lamellae and stress concentrations around a fiber break. They discuss observed failure patterns from rat tail IVD in an SEM, including fiber failure, matrix cracking, and delamination. However, they do not make any link to the calculated stresses in the AF and to observed failure.

In this aim, we use composite theory for laminated fiber reinforced composites to model a physiologically relevant AF (by use of an angle-ply laminate). Composite theory is well defined for use with laminated composited and is a standard in the field for use with fiber reinforced composites. The author points to the following texts for a summary of the equations and theory used in this aim: [126, 128, 129, 131, 148, 162, 186]. We will expand this theory to our biological material. Using the material properties

experimentally determined in previous aims, we were able to predict the AF laminate properties and use an established failure criterion in order to determine when catastrophic failure will occur in the annular model. We then expanded this work to include the digested cases to investigate the role the macromolecules play in whole laminate failure. It is important to note, that this aim will not attempt to model the specific failure mechanisms and propagation (degenerative model), instead we are considering catastrophic, one time failure (injury model).

6.1.1. Lamination Theory Assumptions

In general, laminates can be created with any combination of continuous fiber, short fiber or woven fiber composite lamina; however they must follow the assumptions of classical thin plate theory. The basic assumptions of laminated plate theory state that every lamina must obey linear stress-strain relations and that within the laminate there is a state of plane stress. For our purposes, we will take a lamina to be reinforced with continuous fibers at some angle, θ, which remains constant.

We assume that the laminate is constructed of any number of lamina which is considered to be orthotropic sheets bonded together. The orthotropic axes (*1-2* axes, principle directions) of material symmetry for each lamina do not need to coincide with the *x-y* axes of the laminate. It is assumed that each lamina is perfectly bonded together and is infinitesimally thin, as well as not shear-deformable. These assumptions allows for the displacements to be treated as continuous across lamina boundaries so that no lamina can slip relative to another.

The thickness of the laminate should be much smaller than the other dimensions (width and length). Meaning, the deflections and strains are small compared to the

thickness of the laminate. This allows the assumption that the strains vary linearly through the thickness and we can negate the interlaminar deformations at the interior regions of the laminate. However, we cannot ignore interlaminar stresses at geometric discontinuities, such as free edges. This region where the stress transfer between lamina is due to interlaminar stresses is called the boundary layer, and this area violates the basic assumptions of lamination theory [148, 162, 222-225]. Interior regions where lamination theory is valid can be considered locations where the boundary layer diminishes within one laminate thickness from the free edge [148, 162, 222-225].

We also assume that the laminate is in a state of plane-stress, or that all loads applied to the lamina act in the midplane direction, and are symmetric with respect to the midplane. Also, that the normal and shear stress components in the *z* direction are either zero or negligible. Lamina that have large elastic to shear moduli ratios (E_1/G_{13} and E_1/G_{23}) are susceptible to delamination (failure through the thickness of the laminate) because their effective transverse shear moduli (G_{12} and G_{23}) are smaller than the elastic modulus in the fiber direction (E_1) [222]. Lamination theory (due to plane stress assumption) does not take the *z*-direction shear or normal stresses into consideration, and thus is a limitation to using this theory on composites that are likely to failure in the *z*-direction.

6.2. Lamina Analysis

Each individual lamellae of the AF will have its own mechanical response due to loading based on the individual mechanical properties of those lamellae – which will now be referred to as lamina to be consistent with composite theory terms. In the case of the AF, each lamina is hypothesized to have the same mechanical response, as seen with the

experimental data in chapter four, starting on page 72. From the mechanical properties experimentally determined, we can determine how each lamina will respond to an applied loading condition or stress (Figure 6.2).

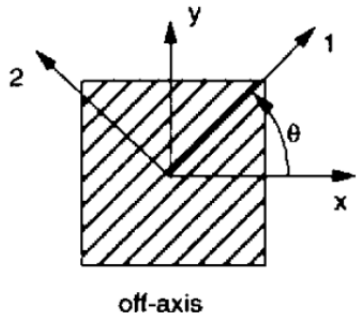

Figure 6.1: Coordinate system for lamina analysis: 1-2, principle coordinate system; x-y, off axis (global) coordinate system. Reprinted from [162].

6.2.1. Mechanical Response of Lamina

For this work, each lamina will be considered as a unidirectional fiber reinforced composite with all the fibers oriented in the same direction and perfectly straight. The assumption that the lamina behaves linear elastically is also made. It has been previously shown that the AF exhibited nonlinear and anisotropic behavior, however other studies have also treated the AF as a linear elastic material in order to use composite theory techniques to give insight into the failure strengths or mechanisms [210, 226]. In order to treat the lamina as linearly elastic the elastic moduli in the ultimate linear region of the specimens will be used. The 1-direction refers to the longitudinal orientation (parallel to the collagen fibers) and the 2-direction, the transverse (perpendicular to the collagen fibers, Table 6.2).

There exists a relationship in order to relate the stresses and strains. This is analogous to the one-dimension case for a linear elastic material; the stress is proportional to the strain through the elastic modulus.

$$\sigma = E\varepsilon \tag{6.i}$$

The *generalized Hooke's Law* takes on the form,

$$\sigma_i = C_{ij}\varepsilon_j \tag{6.ii}$$

where σ_i are the stress components, ε_j the strain components and C_{ij} a 6x6 stiffness matrix. The law states that stress is proportional to the gradient of the deformation occurring in the material. From symmetry we know that $C_{ij} = C_{ji}$ and thus there are only 21 independent constants in the matrix. Similarly, the inverse of this relationship, relating strain to stress, can be related using the compliance matrix, S_{ij}.

$$\varepsilon_i = S_{ij}\sigma_j \tag{6.iii}$$

When the compliance matrix is fully populated, each term has a physical significance to the material (Figure 6.3).

If the assumption that the lamina is an orthotropic material is made, meaning extension and shear are uncoupled (there is no interaction between the normal stresses and shearing strains or shearing stresses and normal strains) [148, 162]. This reduces the number of independent constants in the compliance (and the stiffness) matrix to nine; the only nonzero terms are: S_{11}, S_{22}, S_{33}, S_{44}, S_{55}, S_{66}, S_{12}, S_{13}, S_{23}. Since each term in the compliance matrix has a physical representation, they can be written in terms of engineering constants,

$$S_{11} = \frac{1}{E_1} \quad S_{22} = \frac{1}{E_2} \quad S_{33} = \frac{1}{E_3}$$
$$S_{12} = -\frac{\nu_{12}}{E_1} \quad S_{13} = -\frac{\nu_{31}}{E_3} \quad S_{23} = -\frac{\nu_{32}}{E_3}$$
$$S_{44} = \frac{1}{G_{23}} \quad S_{55} = \frac{1}{G_{31}} \quad S_{66} = \frac{1}{G_{12}} \tag{6.iv}$$

where *E* are the elastic moduli, *G* are the shear moduli and *ν* the Poisson's ratios.

6.2.2. Orthotropic Restrictions on Engineering Constants

There exist restrictions on the values that the engineering constants may have for orthotropic materials; this is analogous to the restricted range of Poisson's ratio ($-1 < \nu < 0.5$) for isotropic materials. These constraints are based on the first law of thermodynamics (showing that the stiffness and compliance matrices must be positive definite) and help determine if the engineering constants are valid in an elastic model [227]. Each of the shear and elastic moduli must be greater than zero (non-negative) and the following relationship between elastic moduli and Poisson's ratio must hold true:

$$|\nu_{ij}| < \sqrt{\frac{E_i}{E_j}} \tag{6.v}$$

These constraints can be used to help validate the experimental data from Table 6.2. For all experimental groups, the constraints hold true. There exists a value for the in-plane shear modulus, G_{12}, in the literature from Iatridis and Gwynn (2004), we use $G_{12} = 0.3$ MPa for our testing since that was not covered in the scope of the characterization study in Chapter 3 [226]. Similarly, there exists no experimental data for the shear modulus for the digested cases. For our purposes, we assume the same percent decrease as from the elastic moduli for the shear moduli in the digested sample groups. For example, the collagenase-treated groups had an 85% decrease in the linear elastic modulus from the

control group, thus we assume an 85% decrease from the shear modulus as well ($G_{12,COL}$ = 0.045 MPa). This was similarly done for each of the digested groups to estimate the shear moduli in the 12-direction (Table 6.3).

Poisson's ratio for the digested samples was only experimentally measured in the 12-direction, to determine the 21-direction we use the symmetry condition and use the relationship between the ν_{12} and related elastic moduli to get $\nu_{12,COL}$, $\nu_{12,COL}$, and $\nu_{12,COL}$ to be 0.188, 0.034, and 0.081 respectively (which all hold to the constraint, Table 6.3).

$$\frac{\nu_{ij}}{E_i} = \frac{\nu_{ji}}{E_j} \tag{6.vi}$$

6.2.3. Plane Stress Analysis

Experimental values relating to the 3-direction of the lamina are not reported in the literature. We hypothesize this is due to the thickness of the lamina (~0.15 mm [14]) being very small compared to the other dimensions. If plane stress is assumed, the stresses in the 3-direction are equal to zero ($\sigma_3 = \tau_{23} = \tau_{31} = 0$) and the compliance matrix simplifies to:

$$S_{PBS} = \begin{bmatrix} S_{11} & S_{12} & 0 \\ S_{12} & S_{22} & 0 \\ 0 & 0 & S_{66} \end{bmatrix} = \begin{bmatrix} 0.62 & 0.027 & 0 \\ 0.027 & 0.54 & 0 \\ 0 & 0 & 3.33 \end{bmatrix} MPa^{-1} \tag{6.vii}$$

From the fact that $C_{ij} = S_{ij}^{-1}$, the stiffness matrix for an orthotropic lamina with plane stress (denoted as Q_{ij}, called the reduced stiffness matrix), in terms of the engineering constants, is equal to the following.

$$Q_{ij} = \begin{bmatrix} \frac{E_1}{1-\upsilon_{12}\upsilon_{21}} & \frac{\upsilon_{12}E_2}{1-\upsilon_{12}\upsilon_{21}} & 0 \\ \frac{\upsilon_{12}E_2}{1-\upsilon_{12}\upsilon_{21}} & \frac{E_2}{1-\upsilon_{12}\upsilon_{21}} & 0 \\ 0 & 0 & G_{12} \end{bmatrix} \quad \text{(6.viii)}$$

The terms of the reduced stiffness matrix can be calculated for each of the sample groups (Table 6.3).

The reduced stiffness matrix relates the stress and strain of the lamina when loaded in the principle coordinate system (1-2). However, in the case of the AF, the fibers are at an angle (θ = 60°) from the circumferential direction [67, 69]. We can transform the reduced stiffness matrix in order to account for loading for any offset from the 1-2 system (θ) into an xy-coordinate system (Figure 6.2).

The transformed reduces stiffness matrix can be found using two transformation matrices, where $\overline{Q_{ij}} = [T_\sigma]^{-1} Q_{ij} [T_\varepsilon]$. The transformation matrices are defined as:

$$[T_\sigma] = \begin{bmatrix} cos^2\theta & sin^2\theta & 2cos\theta sin\theta \\ sin^2\theta & cos^2\theta & -2cos\theta sin\theta \\ -cos\theta sin\theta & cos\theta sin\theta & cos^2\theta - sin^2\theta \end{bmatrix}$$
$$[T_\varepsilon] = \begin{bmatrix} cos^2\theta & sin^2\theta & cos\theta sin\theta \\ sin^2\theta & cos^2\theta & -cos\theta sin\theta \\ -2cos\theta sin\theta & 2cos\theta sin\theta & cos^2\theta - sin^2\theta \end{bmatrix} \quad \text{(6.ix)}$$

If we take the y-direction to be our circumferential direction then θ = ±60°, and the terms of the reduced stiffness matrix can be found for the control (PBS) and digested sample groups (Table 6.5).

There will be a variation of each of the reduced stiffness matrix components due to the angle, θ. It has been reported that the fiber angle can vary by ±10 degrees [68] (for non-degenerated and degenerated samples), we can see that varying theta from 50 – 70 degrees allows an error for the terms (Figure 6.4). The largest difference is seen in the

$\overline{Q_{22}}$ term which shows a 65% range from 6.8 – 13.5 MPa between θ = 50-70°. This variance in the reduced stiffness matrix due to the rotation angle will be explored in more detail in the next section (Laminate Analysis) to see how this carries through to further calculations.

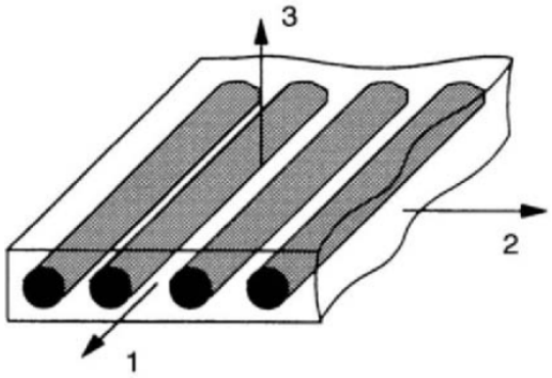

Figure 6.2: Schematic of unidirectional fiber reinforced lamina. Reprinted from [162].

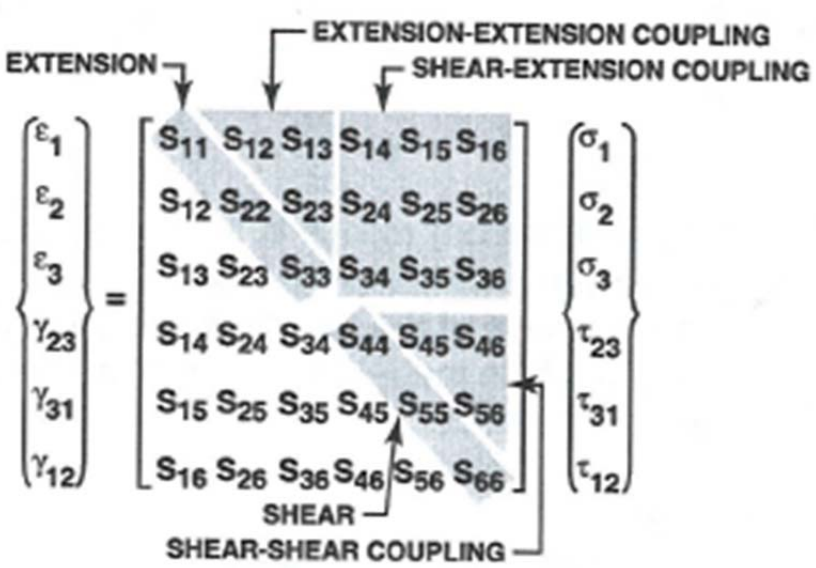

Figure 6.3: Physical significant of compliance matrix in the anisotropic strain-stress relationship. Reprinted from [148].

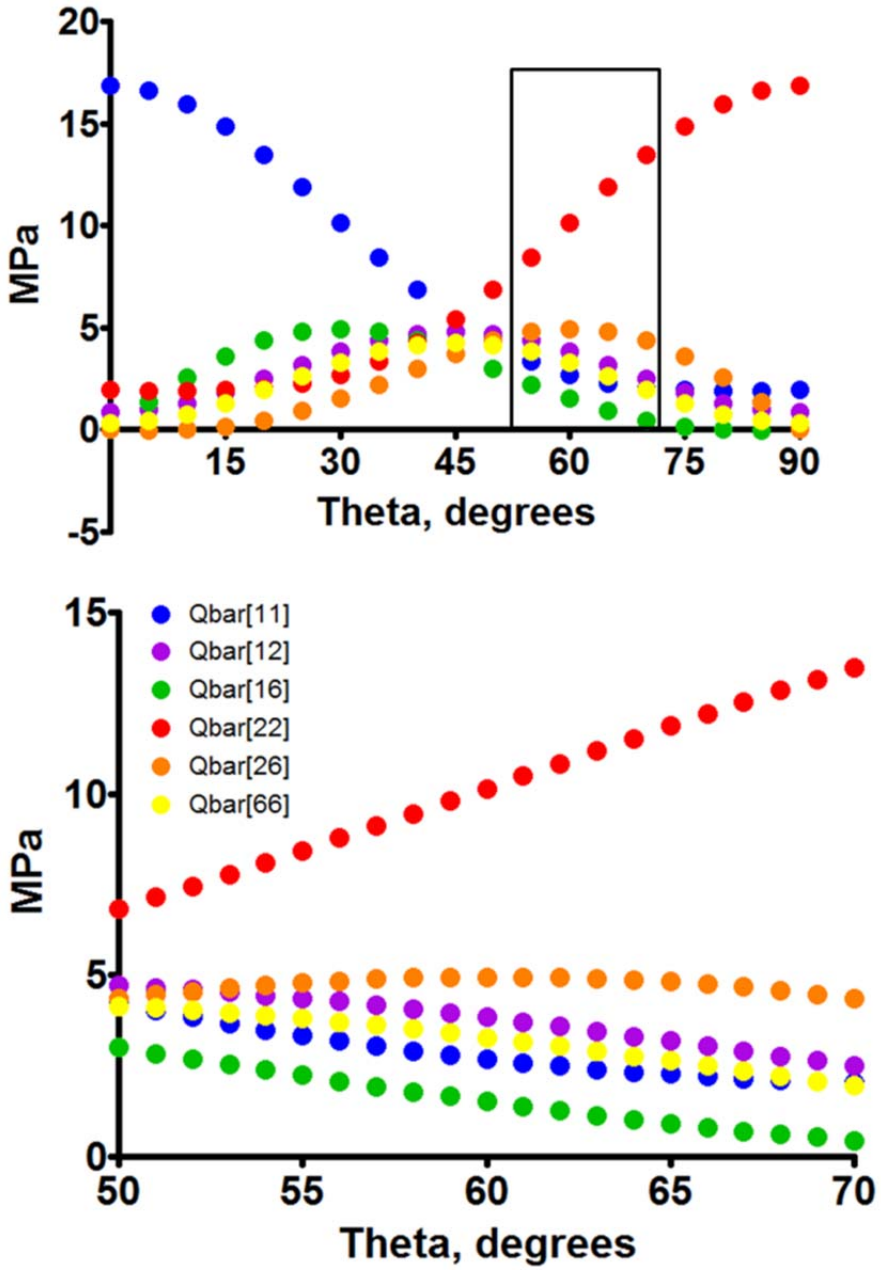

Figure 6.4: Above: Variations of terms of transformed reduced stiffness matrix, $[\bar{Q}]$, due to theta for AF lamina. Below: Zoomed in to theta = 60 ± 10 degrees.

Table 6.1: Summary of strain energy function techniques from studies used to model the AF.

	Strain Energy Function	Model	Assumptions	Advantages	Limitations
Wu & Yao (1976) [217]	• Nonlinear • Exponential	• 11 material properties • Determined by matching model predictions to material tests	• Orthotropic • Constant fiber angle • Material incompressibility • Small strain	• First to use strain energy function to model AF	• Large variation in experimental data for material properties • Incompressible
Klisch & Lotz (1999) [156]	• Nonlinear • Exponential	• 11 material properties • Determined by matching model predictions to material tests	• Orthotropic • Constant fiber angle • Small strain	• Added compressibility to above model • Exponential functions instead of polynomial (fewer material coefficients needed)	• Large variation in experimental data for material properties • Traction-free boundary conditions not included • Non-unique material properties
Elliott & Setton (2000) [210]	• Linear • Anisotropic	• Determined from uniaxial material tests from literature and thermodynamic constraints (6/9 properties)	• Shear isotropy • Constant fiber angle • Small strain • Determined remaining 3 properties assuming symmetry	• Reduced material constants to set of seven • Interactions terms discussed: fiber-fiber and fiber-matrix	• Determined remaining 3 properties from assumptions • Neglected contributions of fibers to shear stiffness • Non-unique material properties • Only tensile loading studied
Elliott & Setton (2001) [82]	• Linear • Orthotropic	• 9 material properties from independent, uniaxial material tests from literature	• Constant fiber angle • Small strain	• Unique material properties	• Independent moduli and Poisson's ratios did not satisfy equation 6.vi. • Large variation in experimental data
Wagner & Lotz (2004) [212]	• Nonlinear • Orthotropic	• 9 material properties determined from independent, uniaxial material tests from literature	Crosslinks occur between fibers within a single lamellae only No residual stress	• Separate terms to represent contributions from constituents: matrix, fiber, interaction • Developed mathematical form of interaction constituent	• Not fully validated • Interaction restricted to fiber crosslinking • Large variation in experimental data
Guerin & Elliott (2007) [68]	• Nonlinear • Anisotropic • Hyperelastic	• Material properties taken from uniaxial material tests in literature	• Small strain • Fiber angle constant throughout specimen	• Incorporated the contribution of both shear and normal interactions	• Large variation in experimental data

Table 6.2: Engineering properties for individual lamina of the AF to be used for composite modeling purposes. The elastic moduli are taken in the linear range of the stress-strain relationship ($E_{75\%}$).

Sample Group	E_1 [MPa]	E_2 [MPa]	ν_{12}	ν_{21}
PBS: control	16.15	1.851	0.44	0.097
COL: collagenase-treated	2.19	1.113	0.37	–
ELA: elastase-treated	4.55	0.363	0.42	–
PG: chondroitinase ABC-treated	5.27	1.295	0.33	–

Table 6.3: Calculated shear modulus (12-direction) and Poisson's ratio (21-direction) for groups. Digested shear modulus from reduction of PBS value and digested Poisson's ratio from symmetry. [a]From [96], [b]Experimental.

Sample Group	G_{12} [MPa]	ν_{21}
PBS	0.3[a]	0.097[b]
COL	0.045	0.19
ELA	0.102	0.033
PG	0.126	0.082

Table 6.4: Terms of reduced stiffness matrix for experimental sample groups.

Sample Group	Q_{11} [MPa]	Q_{12} [MPa]	Q_{22} [MPa]	Q_{66} [MPa]
PBS	16.87	0.85	1.93	0.3
COL	2.35	0.44	1.19	0.045
ELA	4.61	0.15	0.37	0.102
PG	5.42	0.44	1.33	0.126

Table 6.5: Transformed reduced stiffness matrix for sample groups when θ = ±60°. The terms are the same for both, only $\overline{Q_{16}}$ and $\overline{Q_{26}}$ change signs.

Sample Group	$\overline{Q_{11}}$ [MPa]	$\overline{Q_{12}}$ [MPa]	$\overline{Q_{16}}$ [MPa]	$\overline{Q_{22}}$ [MPa]	$\overline{Q_{26}}$ [MPa]	$\overline{Q_{66}}$ [MPa]
PBS	2.69	3.83	±1.51	10.15	±4.96	3.28
COL	1.02	0.91	±0.02	1.59	±0.52	0.51
ELA	0.63	0.95	±0.46	2.75	±1.38	0.90
PG	1.35	1.45	±0.30	3.39	±1.46	1.13

6.3.Laminate Analysis

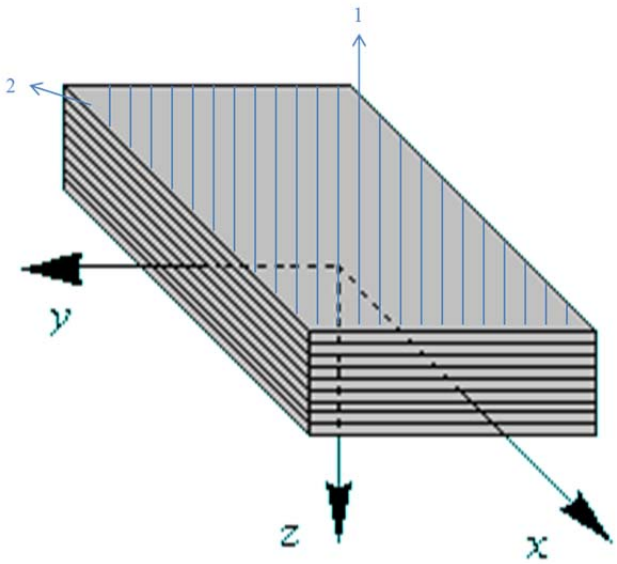

Figure 6.5: Laminate coordinate system: *x*, *y*, *z*.

A laminate can be defined as "two or more lamina bonded together to act as an integral structure element" [148]. A laminate is some collection of lamina, regardless of material or fiber direction, that are stacked adjacent to one another. The properties of this new laminate material are able to be found based on the known properties of the individual lamina that make up the structure by a set of procedures called *Classical Lamination Theory* (CLT) [148, 162, 224, 228-230]. In the case of the AF, we can model an annular laminate as a sequence of lamina as alternating angles, [$\pm\theta = 60°$]. In order to use the CLT technique the assumptions we made on a laminar level must still hold true: linear elasticity, and plane stress. Using this technique (based on an explanation of the Love-Kirchhoff theory for thin plates) also introduces some further fundamental assumptions [162, 225]:

1. The thickness of the laminate is small compared to its other dimensions.
2. The thickness of the plate does not change during a deformation.

3. The lamina are perfectly bonded together (there is no slip between lamina).
4. Each lamina obeys generalized Hooke's law.
5. Fibers are continuous within a lamina and unidirectional.

6.3.1. Mechanical Response of Laminated Composite

For this next section, we must think of each lamina in the laminate as a separate entity, each having its own stress-strain relationship for the k^{th} lamina of an n-layered laminate. The stacking sequence is based on the first layer being at the bottom with the midplane of the laminate going through the N/2 lamina. The z-axis is considered positive in the downward direction (Figure 6.6).

The strain of each lamina in the laminate can be written as the sum of the midplane strains (ε^0) and curvatures (K), where z is the thickness of the lamina:

$$\begin{Bmatrix} \varepsilon_x \\ \varepsilon_y \\ \gamma_{xy} \end{Bmatrix} = \begin{Bmatrix} \varepsilon_x^0 \\ \varepsilon_y^0 \\ \gamma_{xy}^0 \end{Bmatrix} + z \begin{Bmatrix} \kappa_x \\ \kappa_y \\ \kappa_{xy} \end{Bmatrix} \tag{6.x}$$

Using the transformed reduced stiffness matrix we can calculate the stresses in the k^{th} lamina of the laminate.

$$\begin{bmatrix} \sigma_x \\ \sigma_y \\ \sigma_{xy} \end{bmatrix}_k = [\bar{Q}]_k \begin{Bmatrix} \varepsilon_x^0 \\ \varepsilon_y^0 \\ \gamma_{xy}^0 \end{Bmatrix} + [\bar{Q}]_k z_k \begin{Bmatrix} \kappa_x \\ \kappa_y \\ \kappa_{xy} \end{Bmatrix} \tag{6.xi}$$

The transformed reduced stiffness matrices have already been determined for ±60° AF lamina and the mid-plane strains and curvatures can be determined from the stress and moment resultants (Figure 6.7).

The constitutive equations which relate the stress and moment resultants can be written as:

$$\begin{Bmatrix} N \\ \dots \\ M \end{Bmatrix} = \begin{bmatrix} [A] & | & [B] \\ \dots & \dots & \dots \\ [B] & | & [D] \end{bmatrix} \begin{Bmatrix} \varepsilon^0 \\ \dots \\ \kappa \end{Bmatrix} \tag{6.xii}$$

where the A, B, and D matrices are based on the sum of the products of the transformed reduced stiffness matrix and thickness characteristic for each lamina.

$$[A] = \sum_{k=1}^{N} [\bar{Q}]^k (h_k - h_{k-1})$$
$$[B] = \frac{1}{2} \sum_{k=1}^{N} [\bar{Q}]_k \left({z_k}^2 - {z_{k-1}}^2 \right)$$
$$[D] = \frac{1}{3} \sum_{k=1}^{N} [\bar{Q}]_k \left({z_k}^3 - {z_{k-1}}^3 \right) \tag{6.xiii}$$

These matrices have physical meanings relating to the stress and moment resultants (Figure 6.8): A – extensional stiffness, B – extension-bending coupling, D – bending stiffness [162]. The [A] and [D] matrices physically represent the stiff due to extension separately; all the terms are never zero in the matrix, however some terms may be zero depending on the symmetry of the laminate. The [B] matrix, however, is an indication of the coupling between extensions and bending. For example, if the [B] matrix was partially populated, then it would mean that as a laminate is stretched, it will also bend even when no external bending force is indicated.

Based on the type of laminate, the terms of the ABD matrix can be simplified. We can now define three different types of laminates that will be discussed in the following sections (Figure 6.9): symmetric, angle-ply symmetric, and angle-ply antisymmetric. Each of these types will be discussed in regards to an annular model, thus the lamina will alternate between $\theta = \pm 60°$ as discussed previously. A symmetric laminate is defined as a

laminate that is symmetric around the mid-plane (z) axis. For this case (any symmetric laminate), the B matrix will be zero. A special type of symmetric is called a symmetric angle-ply laminate; this has an odd number of layers that alternate between ±θ with the mid-plane z- axis being through the center lamina. The terms of the A and D matrices can easily be directly correlated to the transformed reduced stiffness matrix (again recall that the transformed reduced stiffness matrix will have the same terms for the ±θ lamina except for a sign change in the 16 and 26 places), the total height of the laminate (sum of all the lamina thicknesses), h, and number of layers, N [148].

1. $(A_{11}, A_{22}, A_{12}, A_{66}) = h(\bar{Q}_{11}, \bar{Q}_{22}, \bar{Q}_{12}, \bar{Q}_{66})$
2. $(A_{16}, A_{26}) = \frac{h}{N}(\bar{Q}_{16}, \bar{Q}_{26})$
3. $(D_{11}, D_{22}, D_{12}, D_{66}) = \frac{h^3}{12}(\bar{Q}_{11}, \bar{Q}_{22}, \bar{Q}_{12}, \bar{Q}_{66})$
4. $(D_{16}, D_{26}) = \frac{h^3(3N^2-2)}{12N^3}(\bar{Q}_{16}, \bar{Q}_{26})$

Similarly, we can have an antisymmetric angle-ply laminate, which is not symmetric around the z-axis with an even number of layers. In this case, the B matrix is non-zero, but only the shear terms are present. The shear terms of the A and D matrix also now become zero. For the antisymmetric angle-ply, the above four relationships hold true with the following additions [148]:

1. $A_{16} = A_{26} = D_{16} = D_{26} = 0$
2. $(B_{16}, B_{26}) = -\frac{h^2}{2N}(\bar{Q}_{16}, \bar{Q}_{26})$
3. As $N \rightarrow \infty$, $(B_{16}, B_{26}) \rightarrow 0$

6.3.2. Determination of Laminate Engineering Constants

Since each of the components of the ABD matrix has a physical meaning relating to the laminate, the engineering constants for the laminate (E_x, E_y, G_{xy}, ν_{xy}, ν_{yx}) can be determined from these terms, based on the known engineering constants of the individual lamina. In regards to the AF, we can predict the annular properties based on the individual lamellar properties. Since we are in the plane stress condition, we will only be able to predict the axial (x) and circumferential (y) properties, (radial properties relate to the z-axis).

6.3.2.1. Symmetric Laminate

The definition of the elastic modulus in the *x*-direction is: $E_x = {\sigma_x}/{\varepsilon_x} = {N_x/h}/{\varepsilon_x}$. Since we have a symmetric laminate, the B matrix is zero and the constitutive equation reduces to relating the stress resultants directly to the midplane strains.

$$[N] = [A][\varepsilon^0] \tag{6.xiv}$$

Since for the case of the elastic modulus in the *x*-direction we only want to relate N_x and ε_x, a load is applied only in the *x*-direction. We are able to put ε_y^0 and γ_{xy}^0 in terms of ε_x^0 only from components 2 and 3 of equation 5.vi and substitute back into the first component. Simplifying this will give an equation for the ratio of ${N_x}/{\varepsilon_x}$; dividing this by height gives the laminate elastic modulus, E_x, in terms of the components of the A matrix. A similar procedure can be followed in order to find the other engineering constants [225]:

$$E_x = \frac{A_{11} + A_{12}\left(\frac{A_{26}A_{16} - A_{12}A_{66}}{A_{22}A_{66} - {A_{26}}^2}\right) + A_{16}\left(\frac{-A_{16}}{A_{66}} + \frac{A_{26}A_{12}A_{66} - {A_{26}}^2 A_{16}}{A_{22}{A_{66}}^2 - A_{66}{A_{26}}^2}\right)}{h} \quad (6.xv)$$

$$E_y = \frac{A_{12}\left(\frac{A_{16}A_{26} - A_{12}A_{66}}{A_{11}A_{66} - {A_{16}}^2}\right) + A_{22} + A_{26}\left(\frac{-A_{26}}{A_{66}} + \frac{A_{16}A_{12}A_{66} - {A_{16}}^2 A_{26}}{A_{11}{A_{66}}^2 - A_{66}{A_{16}}^2}\right)}{h} \quad (6.xvi)$$

$$G_{xy} = \frac{A_{66} - \frac{{A_{26}}^2}{A_{22}} + \frac{2A_{12}A_{16}A_{26}A_{22} - {A_{12}}^2{A_{26}}^2 - {A_{16}}^2{A_{22}}^2}{A_{11}{A_{22}}^2 - A_{22}{A_{12}}^2}}{h} \quad (6.xvii)$$

$$\upsilon_{xy} = \frac{-{\varepsilon_y}^0}{{\varepsilon_x}^0} = \frac{A_{12} - \frac{A_{16}A_{26}}{A_{66}}}{A_{22} - \frac{{A_{26}}^2}{A_{66}}} \quad (6.xviii)$$

$$\upsilon_{yx} = \frac{-{\varepsilon_x}^0}{{\varepsilon_y}^0} = \frac{\frac{A_{16}A_{26}}{A_{66}} - A_{12}}{\frac{{A_{16}}^2}{A_{66}} - A_{11}} \quad (6.xix)$$

For any symmetric laminate of $[\pm\theta]_{N,SYM}$, with layers the same thickness, the engineering constants are the same (regardless of angle sign of first layer). For the control case (PBS): The elastic moduli are Ex = 1.24 MPa and Ey = 4.69 MPa, the shear modulus is Gxy = 3.28 MPa, and Poisson's ratios νxy = 0.37 and νyx = 1.42. Similarly, we can calculate the engineering constants for the three digested cases (Table 6.6).

6.3.2.2. Symmetric Angle-Ply Laminate

The symmetric angle ply laminate is simply a specialized form of the symmetric laminate. The engineering constants are still determined by equations 5.xv – 5.xix, however they are now dependent on the number of layers. Since each of the components of [A] is a component of the transformed reduced stiffness matrix multiplied by height (a

function of N, $h = Nt$ where t = thickness of each lamina) the size of the laminate is important in determining the engineering constants. We can determine the engineering constants for different laminate sizes (Figure 6.10).

For all engineering constants, a one-phase associate function, $y = Y_o + (P - Y_o)(1 - e^{-k \cdot x})$, was a good fit to the data ($R^2 > 0.99$, Table 6.7), where *x* is the number of layers (lamina of same thickness) and *y* the engineering property. We can see that by a height of 11 lamina, the constants are within 3% of the plateau value. We can then consider any symmetric laminate of more than 11 layers to have the same engineering constants.

We can also find the modeled laminate engineering constants for the digested groups (Figure 6.11). For the elastic moduli, all the digested groups calculated laminate engineering constants were less than the control. There is a decrease in properties for E_x of about 60-, 75- and 40% for the COL, ELA and PG groups. Similarly, there is a difference of ~80-, 70-, and 60% for COL, ELA and PG groups for E_y. The same trend follows for the shear modulus with the most decrease being the COL group (~85%) and the least the PG group (65%). The Poisson's ratios are distinctly different from the moduli. For the in-plane Poisson's ratio (ν_{xy}), only the ELA group has a decrease from control (<10%), conversely the COL and PG groups have a 50- and ~13% increase from the control group (PBS). The alternate holds true for the out of plane Poisson's ratio (ν_{yx}); The ELA group has a ~5% decrease and there are 37% and ~25% increases for COL and PG from the control group.

6.3.2.3. Antisymmetric Angle-Ply Laminate

The engineering constants for an antisymmetric angle ply laminate can be determined in a similar manner as for a symmetric laminate, however [B] is now nonzero, thus leading to more complex equations [225].

$$E_x = \frac{1}{h}\frac{det\begin{vmatrix} A & B \\ B & D \end{vmatrix}}{det\begin{vmatrix} A_{22} & A_{26} & B_{12} & B_{22} & B_{26} \\ A_{26} & A_{66} & B_{16} & B_{26} & B_{66} \\ B_{12} & B_{16} & D_{11} & D_{12} & D_{16} \\ B_{22} & B_{26} & D_{12} & D_{22} & D_{26} \\ B_{26} & B_{66} & D_{16} & D_{26} & D_{66} \end{vmatrix}} \tag{6.xx}$$

$$E_y = \frac{1}{h}\frac{det\begin{vmatrix} A & B \\ B & D \end{vmatrix}}{det\begin{vmatrix} A_{11} & A_{12} & B_{11} & B_{12} & B_{16} \\ A_{16} & A_{22} & B_{12} & B_{22} & B_{26} \\ B_{11} & B_{12} & D_{11} & D_{12} & D_{16} \\ B_{12} & B_{22} & D_{12} & D_{22} & D_{26} \\ B_{16} & B_{26} & D_{16} & D_{26} & D_{66} \end{vmatrix}} \tag{6.xxi}$$

$$G_{xy} = \frac{1}{h}\frac{det\begin{vmatrix} A & B \\ B & D \end{vmatrix}}{det\begin{vmatrix} A_{11} & A_{12} & B_{11} & B_{12} & B_{16} \\ A_{12} & A_{22} & B_{12} & B_{22} & B_{26} \\ B_{11} & B_{12} & D_{11} & D_{12} & D_{16} \\ B_{12} & B_{22} & D_{12} & D_{22} & D_{26} \\ B_{16} & B_{26} & D_{16} & D_{26} & D_{66} \end{vmatrix}} \tag{6.xxii}$$

$$\nu_{xy} = -\frac{det\begin{vmatrix} A_{12} & A_{26} & B_{12} & B_{22} & B_{26} \\ A_{16} & A_{66} & B_{16} & B_{26} & B_{66} \\ B_{11} & B_{16} & D_{11} & D_{12} & D_{16} \\ B_{12} & B_{26} & D_{12} & D_{22} & D_{26} \\ B_{16} & B_{66} & D_{16} & D_{26} & D_{66} \end{vmatrix}}{det\begin{vmatrix} A_{22} & A_{26} & B_{12} & B_{22} & B_{26} \\ A_{26} & A_{66} & B_{16} & B_{26} & B_{66} \\ B_{12} & B_{16} & D_{11} & D_{12} & D_{16} \\ B_{22} & B_{26} & D_{12} & D_{22} & D_{26} \\ B_{26} & B_{66} & D_{16} & D_{26} & D_{66} \end{vmatrix}} \tag{6.xxiii}$$

$$\nu_{yx} = -\frac{det\begin{vmatrix} A_{12} & A_{16} & B_{11} & B_{12} & B_{16} \\ A_{16} & A_{66} & B_{16} & B_{26} & B_{66} \\ B_{12} & B_{16} & D_{11} & D_{12} & D_{16} \\ B_{22} & B_{26} & D_{12} & D_{22} & D_{26} \\ B_{16} & B_{66} & D_{16} & D_{26} & D_{66} \end{vmatrix}}{det\begin{vmatrix} A_{11} & A_{16} & B_{12} & B_{22} & B_{26} \\ A_{16} & A_{66} & B_{16} & B_{26} & B_{66} \\ B_{11} & B_{16} & D_{11} & D_{12} & D_{16} \\ B_{12} & B_{26} & D_{12} & D_{22} & D_{26} \\ B_{16} & B_{66} & D_{16} & D_{26} & D_{66} \end{vmatrix}} \quad \text{(6.xxiv)}$$

Since [B] is nonzero, both [B] and [D] now play roles because the full set of constitutive equations is needed. Each of the components of [ABD] is a component of the transformed reduced stiffness matrix multiplied by height (a function of N, $h = Nt$ where t = thickness of each lamina) the size of the laminate is important in determining the engineering constants, similar to the symmetric angle ply laminate. We can determine the engineering constants for different laminate sizes (Figure 6.12).

For the antisymmetric angle-ply engineering constants, a one-phase associate function was also a good fit to the data ($R^2 > 0.99$, Table 6.8). We can see that by a height of 14 lamina, the constants are within 3% of the plateau value. We can then consider any symmetric laminate of more than 14 layers to have the same engineering constants.

We can also find the modeled laminate engineering constants for the digested groups (Figure 6.13) . For the elastic moduli, all the digested groups calculated laminate engineering constants were less than the control. There is a decrease in properties for E_x of about 60-, 75- and 40% for the COL, ELA and PG groups. Similarly, there is a difference of 83-, 72-, and 60% for COL, ELA and PG groups for E_y. The same trend follows for the shear modulus with the most decrease being the COL group (~85%) and the least the PG group (65%). The Poisson's ratios are distinctly different from the moduli. For the in-plane Poisson's ratio (ν_{xy}), only the ELA group has a decrease from

control (<8%), conversely the COL and PG groups have a 50- and 13% increase from the control group (PBS). The alternate holds true for the out of plane Poisson's ratio (ν_{yx}); The ELA group has a ~7% decrease and there are 38% and 25 % increases for COL and PG from the control group.

We can graph the two different angle-ply laminates (symmetric and antisymmetric) together to see if we can make any statements about the angle-ply laminate as a whole for the control samples (PBS, Figure 6.14). The goodness of fit (R^2, Table 6.9), does slightly decrease (average 0.972) from when the anti- and symmetric were treated separately. However, for laminates more than 15 layers, there is less than a 1% difference between the plateau value (when fit with one-phase association) and calculated constant.

6.3.3. Comparison to Lamina Data

It is interesting to compare these changes for the angle-ply laminate engineering constants (Table 7.8) to the experimental changes that were seen on a lamina level due to digestion. We previously examined the changes due to digestion in the longitudinal and transverse directions. In the longitudinal direction there were average decreases of 85-, 66- and 58% for COL, ELA and PG elastic moduli and Poisson's ratio (Figure 5.4). And in the transverse direction for COL, ELA and PG, decreases of 55-, 70-, and ~50% (Figure 5.6). The calculated elastic and shear moduli are functions of the elastic moduli (E_1, E_2), shear modulus (G_{12}) and Poisson's ratios (ν_{12}, ν_{21}) of the lamina. Since for each of the lamina constants (12-direction) there is a decrease in the properties dependent on digestion group, most for COL and least for PG, we would expect the same trend to follow with the laminate properties. This is also more pronounced, since these exact

reductions were used to assume values for the shear moduli (G_{12}); this will be discussed in more detail in section 6.5.3.

The calculated Poisson's ratios for the laminate do not hold with this trend, however. When comparing the digested in-plane lamina Poisson's ratios (ν_{12}), we see that the ELA has the smallest difference from PBS (<5% decrease), while the PG had the largest (15%). For the control samples (PBS), the out of plane Poisson's ratio (ν_{21}) was experimentally determined and did not follow equation 7.vi. Whereas, the digested ν_{21} were calculated based on that equation. If we use the relationship between elastic moduli and Poisson's ratios to determine ν_{21} (0.05) for the PBS group then the plateau values for the laminate Poisson's ratios would become: $\nu_{xy} = 0.12$, and $\nu_{yx} = 0.47$. If we compare these new values to the digested values, then we can examine if a trend results. The in-plane laminate Poisson's ratio (ν_{xy}), now has an increase of about 375-, 190- and 250% from the control for the COL, ELA and PG groups. While the out-of-plane laminate Poisson's ratio (ν_{xy}), now has an increase of about 90-, 221- and 128% from the control for the COL, ELA and PG groups It makes sense that the Poisson's ratio would increase from control, since the elastic moduli are decreasing (this must occur to fulfill equation 6.vi). It is interesting, that they do not follow the same trend as the moduli, with which digestion group delivers the most change. In the case of the Poisson's ratios, for the in-plane (ν_{xy}), the COL group has the most drastic increase, while the ELA the smallest; for out-of-plane (ν_{yx}), it is the opposite: COL has the smallest and ELA the largest (this opposition is expected due to the relationship between ν_{xy} and ν_{yx}. This follows the same trend that we saw with the digested lamina Poisson's ratios.

6.3.4. Comparison to Literature

There exists data in the literature for experimentally determined laminate engineering constants to which we can compare our control calculated model data (PBS, Table 6.10); we remember that the model x-direction compares to the IVD's axial direction and *y* to the IVD's circumferential orientation. When comparing the model data to the experimental, we can see that the in-plane elastic modulus (E_x), and Poisson's ratios (ν_{xy} , ν_{yx}) are within the experimental range reported in literature [68, 72, 82, 212, 231]. However, for the circumferential elastic modulus (E_y) and the shear modulus (G_{xy}) the data do not fit. There are various papers which investigate the circumferential modulus, for two of these papers our value (average 4.65) is within the range [72, 82]; however, for the majority of values reported [68, 74, 212], including our experimental data, the model value is an underestimate of what has been seen experimentally. The opposite is true for the shear modulus; the values reported in the literature [87, 88] are significantly lower than the model prediction (average 3.2).

We hypothesize that there could be various reasons for these discrepancies. First, in the innate assumptions made in order to predict the laminate properties from those of the lamina, namely perfect bonding between layers. In assuming that each layer is perfectly bound together with no interplay between, we negate this densely populated *in vivo* elastin fiber area. In doing so in the model, the stress-strain curve would change to no longer allow high strain, but the same stress would still be modeled, thus leading to a higher shear modulus (akin to the relationship between stress and strain during shearing).

The lamina shear modulus is also taken to be 0.3 from Iatridis and Gwynn (2004), however this was not experimentally determined. We can see in Figure 6.15 that the

laminate values are also sensitive to the lamina shear modulus value. For example for the circumferential data to fit our experimental value (11.04 ± 2.24 MPa), the lamina shear modulus would have to be equal to 2.7 ± 1.4 MPa. A good experimentally determined value for shear modulus is necessary to have a more realistic model of the AF.

The underestimation of the circumferential modulus could follow similar logic. We can also compare the circumferential modulus for the digested samples to the experimental values obtained (Table 6.11). We see that the model values are also less than the experimental. Upon using CLT to model the AF as a laminate, we look at each lamina as a separate, self-contained entity and base calculations accordingly. When the AF is loaded in circumferential tension, the collagen fibers are allowed to reorient themselves and align more in the direction of the loading [68]. AF mechanics are altered by changes in fiber angle values: As the fiber angle increases, the circumferential modulus and compressive motion segment will become stiffer (higher E_y) [154, 232-235]. As the AF is loaded, the fibers will realign with the loading and thus allow for the larger experimental circumferential modulus that is not reflected in the model (this was seen earlier in terms of the transformed reduced stiffness matrix, Figure 6.4). If we model the AF as a 19 ply symmetric angle-ply laminate, we can plot the laminate values of the circumferential modulus (E_y) between the angles of 50° - 70° (Figure 6.16). At an angle of 70°, the modulus is equal to 10.4 MPa while at an angle of 50 degrees, 1.6 MPa. There is a large variance in the modulus dependent on the angle of fibers chosen. We can solve for the angle that will allow the circumferential modulus to be within the range of our experimental data (11.04 ± 2.24 MPa), yielding an angle of $\theta = 71.1 \pm 3.7°$.

While there are many finite models of the IVD in literature [143, 154, 233, 234, 236, 237]. Many model the AF as a homogenous material with known properties (using experimental laminate values, such as those seen in Table 6.10) [143, 237]. There are some models that will model the lamina using rebar elements embedded in homogenous isotropic material elements to represent the collagen fibers embedded in the proteoglycan matrix [154, 233, 234, 236]. These studies manipulate the fiber content, volume, spacing and properties in order to allow the AF to behave as seen experimentally (Table 6.10). Therefore making a comparison between our calculated and modeled data and computational model properties would be redundant.

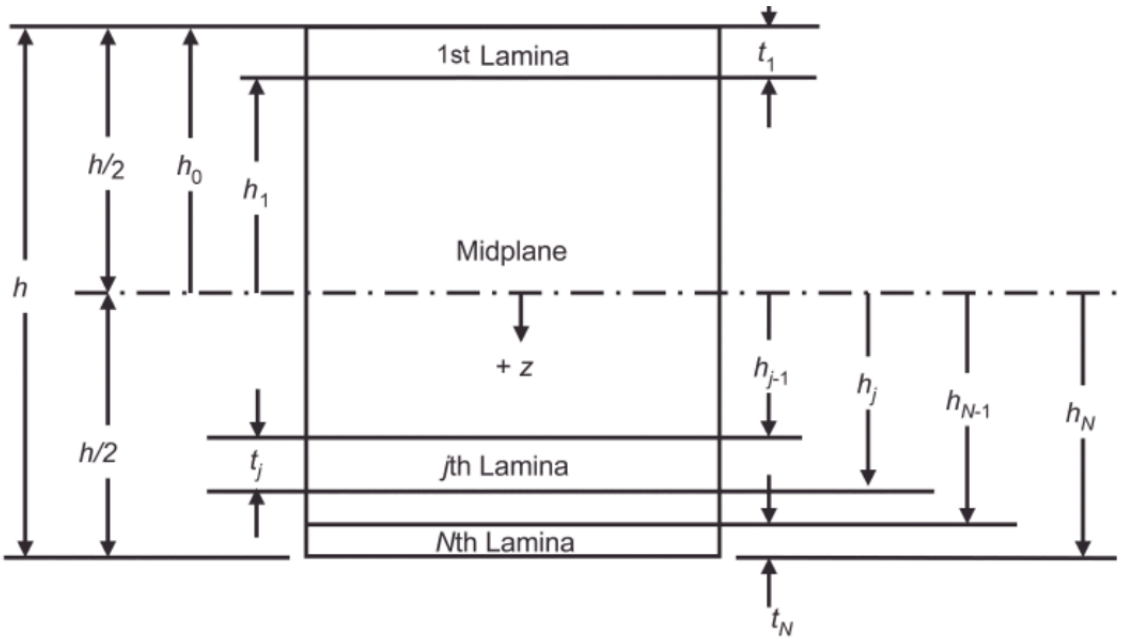

Figure 6.6: Laminate nomenclature. Reprinted from [223].

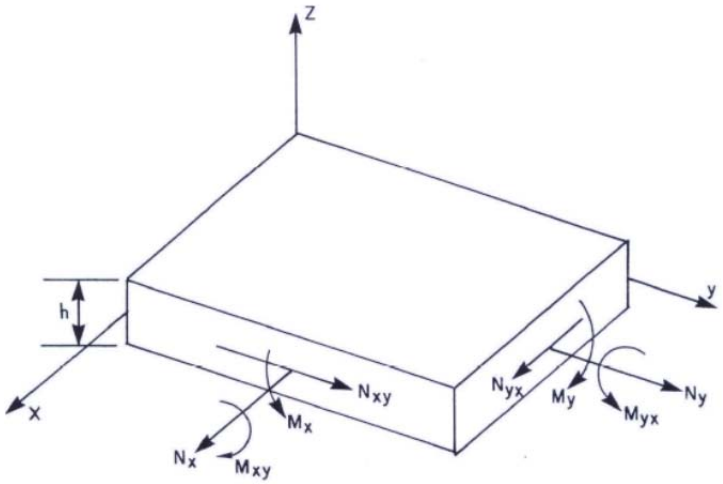

Figure 6.7: Position directions for stress and moment resultants. Reprinted from [225].

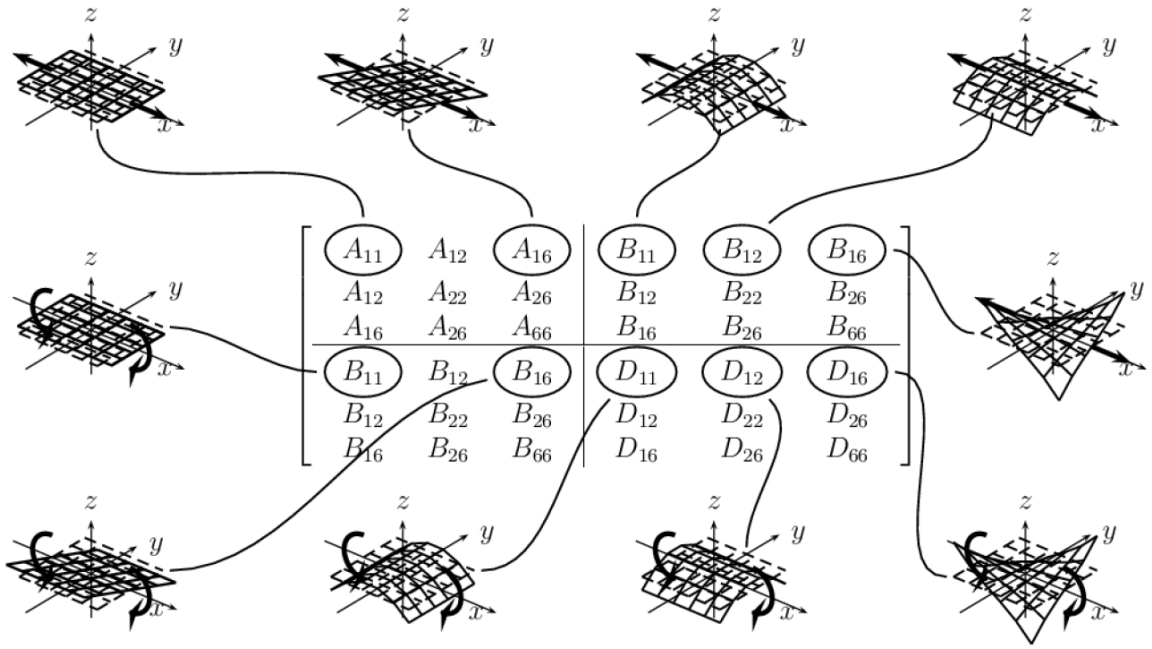

Figure 6.8: Physical significance of terms in A, B, and D matrices. Adapted from http://www.aac-research.at/downloads/Formula-collection-for-laminates.pdf

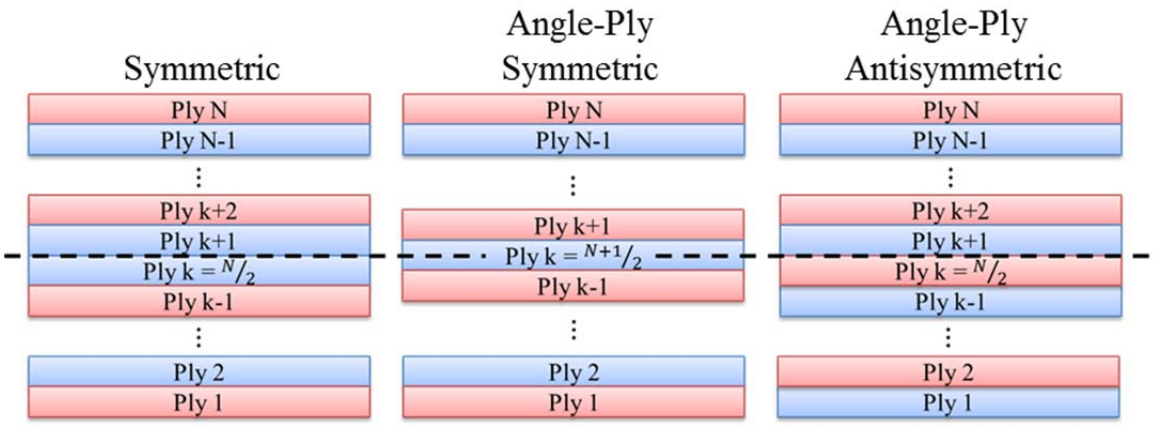

Figure 6.9: Three types of laminates, from left to right: symmetric (N = even), angle-ply symmetric (N = odd) and angle-ply antisymmetric (N = even). The lamina directions alter between layers from -60° (red) to +60° (blue).

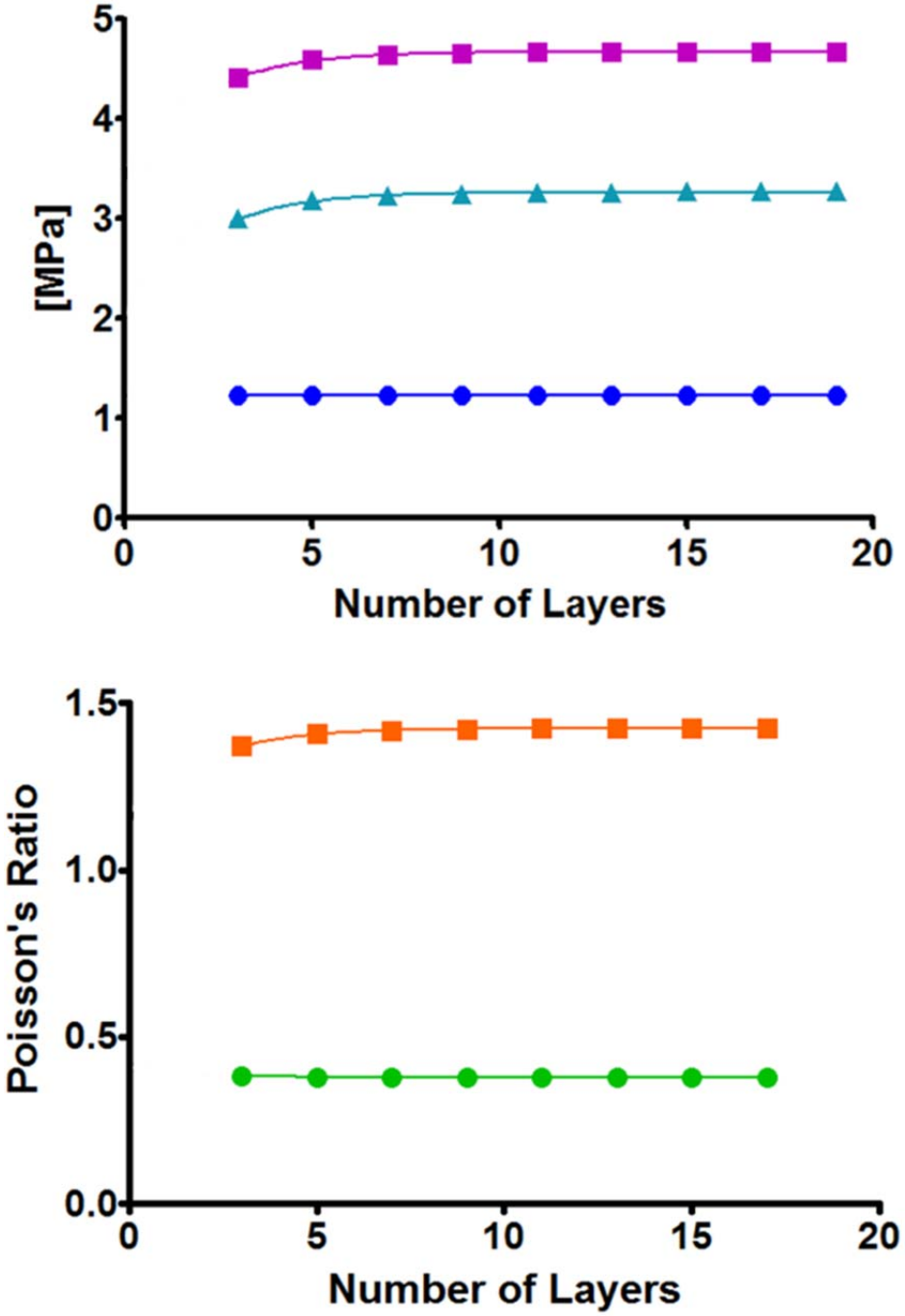

Figure 6.10: Moduli (top) and Poisson's ratios (bottom) of a symmetric angle-ply laminate as a function of the number of layers for the PBS (control) samples. Values fit with one-phase association curve. E_x, E_y, G_{xy}., ν_{xy} , ν_{yx}.

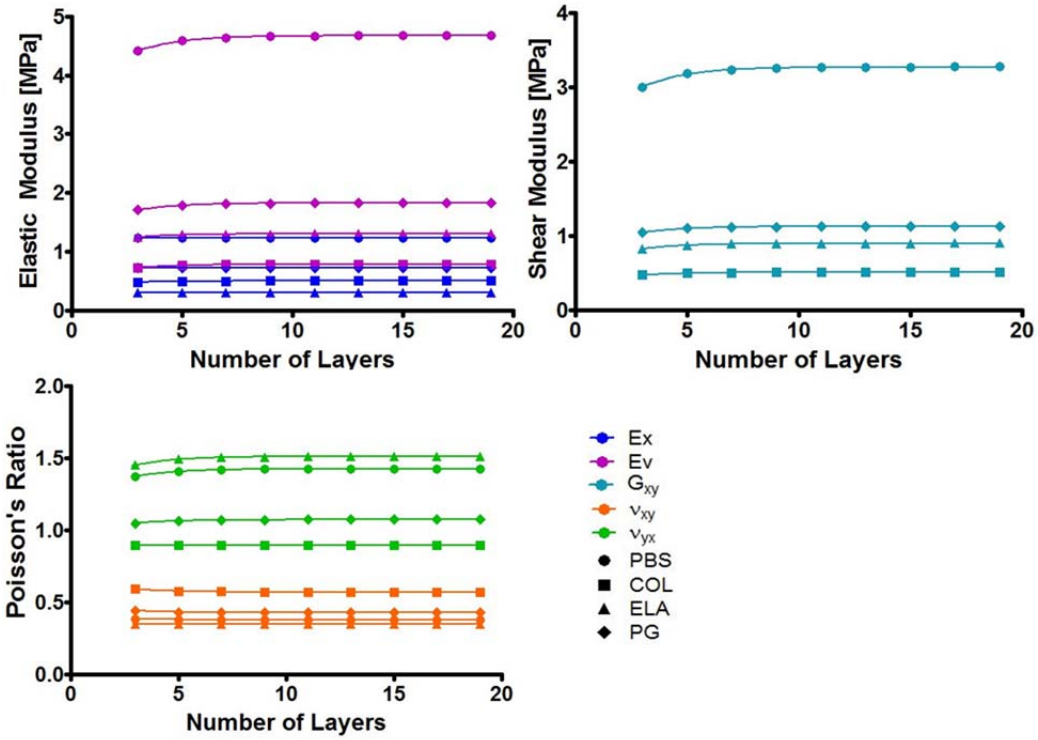

Figure 6.11: a) Elastic moduli b) shear modulus and c) Poisson's ratios of a symmetric angle-ply laminate as a function of the number of layers for all sample groups: PBS, COL, ELA, and PG. Values fit with one-phase association curve.

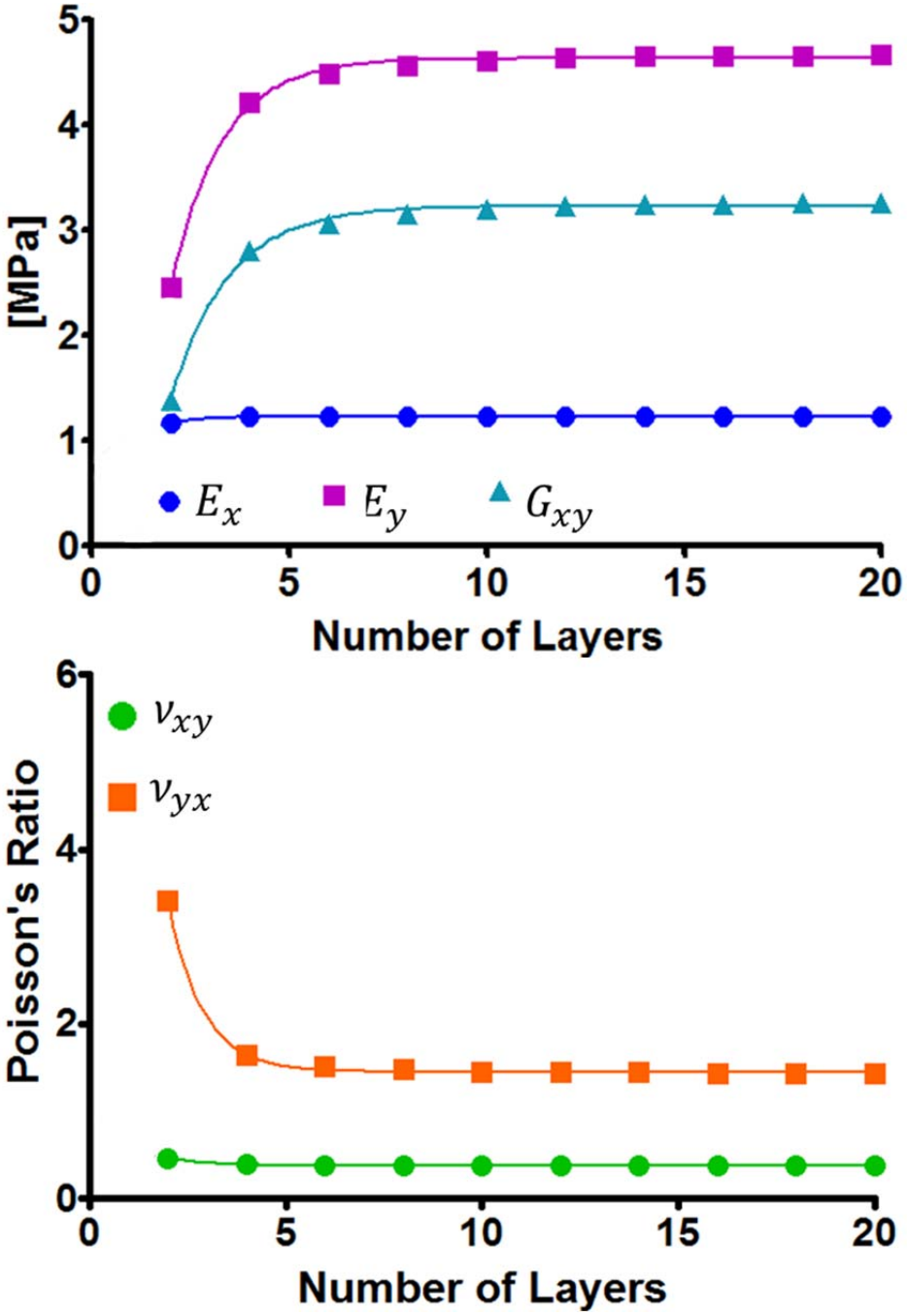

Figure 6.12: Moduli (top) and Poisson's ratios (bottom) of an antisymmetric angle-ply laminate as a function of the number of layers for the PBS (control) samples. Values fit with one-phase association curve.

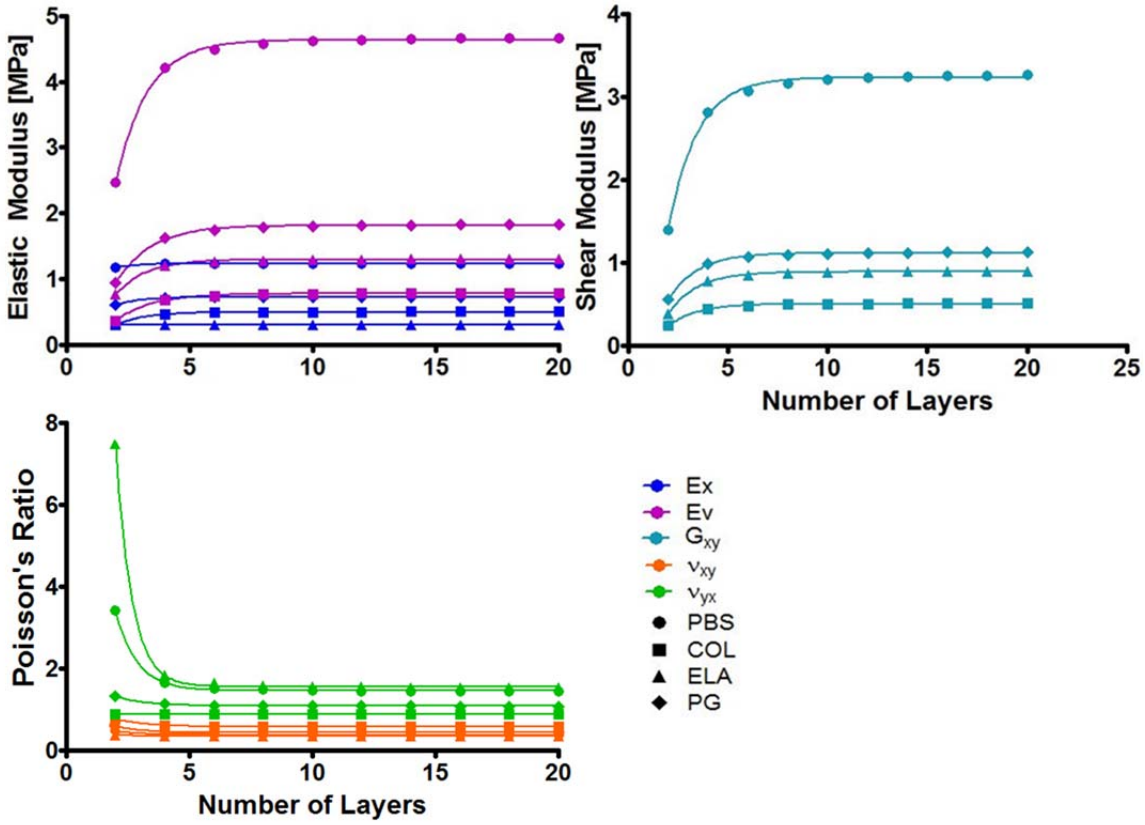

Figure 6.13: a) Elastic moduli b) shear modulus and c) Poisson's ratios of a symmetric angle-ply laminate as a function of the number of layers for all sample groups: PBS, COL, ELA, and PG. Values fit with one-phase association curve.

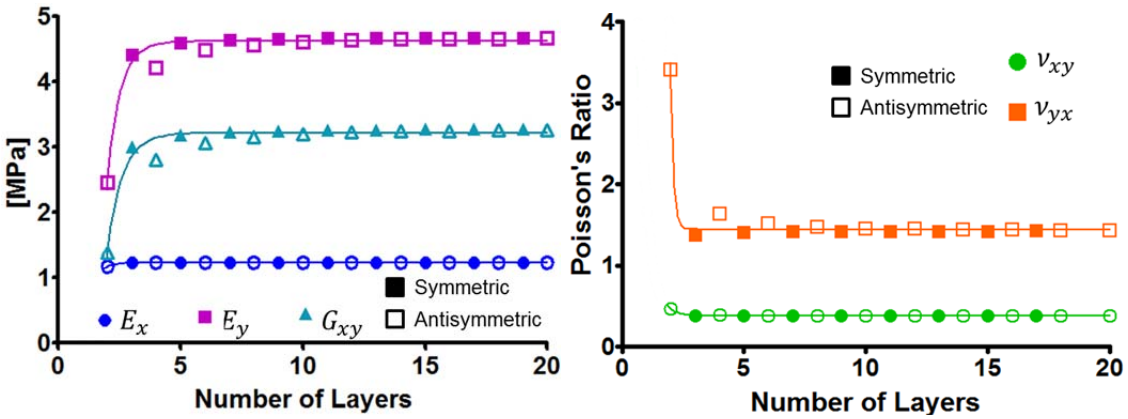

Figure 6.14: Moduli (left) and Poisson's ratios (left) of an angle-ply laminate as a function of the number of layers for the PBS (control) samples. Values fit with one-phase association curve.

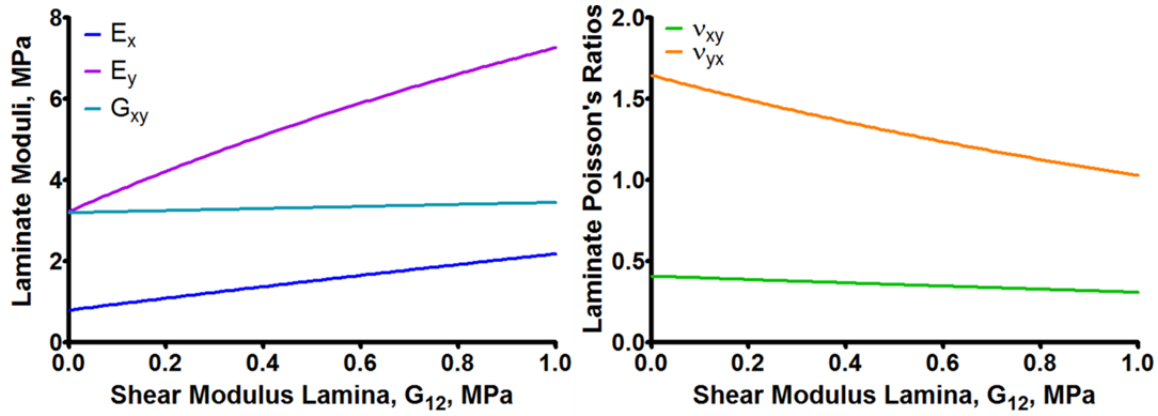

Figure 6.15: Modeled laminate properties (top – moduli, bottom – Poisson's ratios) are dependent on the shear modulus of the lamina, G_{12}. AF modeled as 19-layer symmetric angle ply laminate.

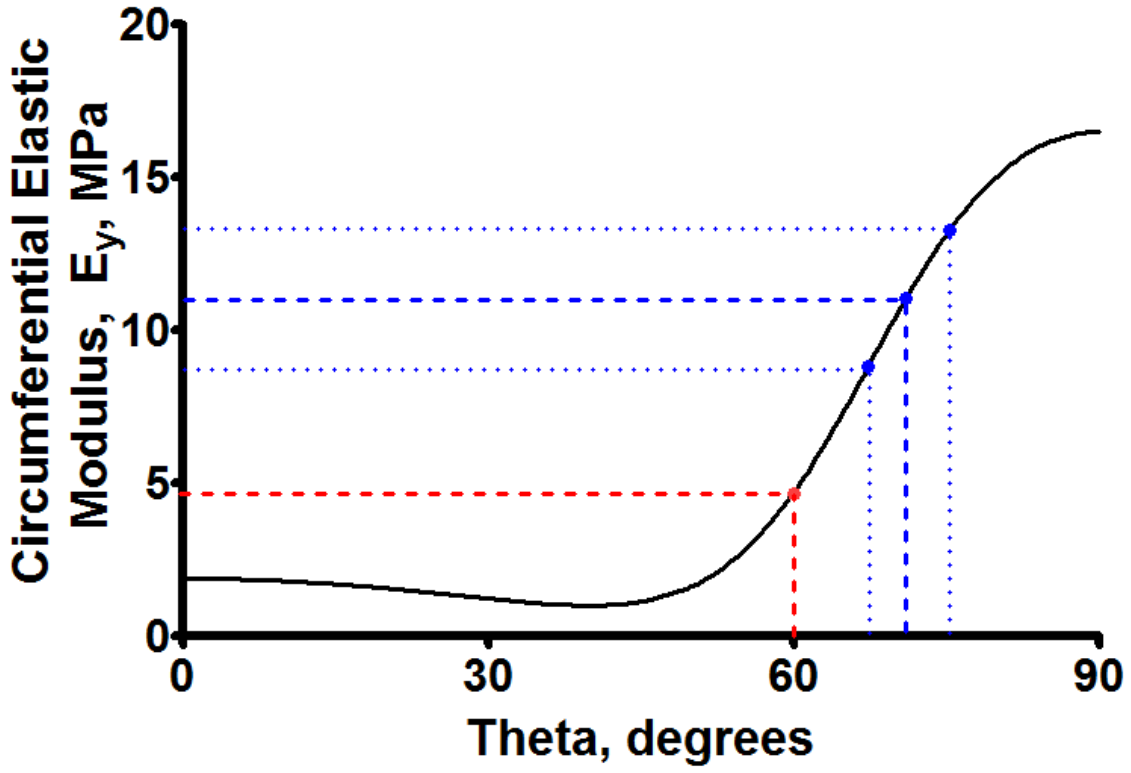

Figure 6.16: Modeled laminate circumferential modulus, Ey, is dependent on the angle of the collagen fibers, theta. AF modeled as 19-layer symmetric angle ply laminate with G_{12} = 0.3 MPa; θ = 60° depicted in red, lower than experimental. Solving for theta with experimental Ey = 11.04 ± 2.24 MPa yields θ = 71.1 ± 3.7° depicted in blue.

Table 6.6: Calculated engineering constants for AF laminate when modeled as symmetric laminate. X- and y-directions correspond to axial and circumferential, respectively.

Sample Group	E_x [MPa]	E_y [MPa]	G_{xy} [MPa	ν_{xy}	ν_{yx}
PBS	1.24	4.69	3.28	0.37	1.42
COL	0.5	0.79	0.51	0.57	0.89
ELA	0.3	1.3	0.91	0.35	1.52
PG	0.73	1.84	1.13	0.43	1.07

Table 6.7: Properties of one-phase association fit, $y = Y_o + (P - Y_o)(1 - e^{-k \cdot x})$, to engineering constants versus number of layers for a symmetric angle-ply laminate (control, Figure 6.10).

	E_x [MPa]	E_y [MPa]	G_{xy} [MPa]	ν_{xy}	ν_{yx}
Y_0	1.22	3.42	2.02	0.41	1.17
P, Plateau	1.24	4.67	3.27	0.378	1.424
K	0.54	0.52	0.51	0.55	0.53
Span	0.02	1.25	1.25	-0.03	0.26
R^2	0.9970	0.9971	0.9971	0.9975	0.9976

Table 6.8: Properties of one-phase association fit to engineering constants for an antisymmetric angle-ply laminate versus number of layers (control, Figure 6.12).

	E_x [MPa]	E_y [MPa]	G_{xy} [MPa]	ν_{xy}	ν_{yx}
Y_0	0.72	-5.77	-4.16	1.09	20.7
P, Plateau	1.24	4.63	3.23	0.379	1.451
K	1.05	0.78	0.69	1.05	1.15
Span	0.5	10.4	7.4	0.71	19.27
R^2	0.9998	0.9978	0.9975	0.9988	0.9991

Table 6.9: Properties of one-phase association fit to engineering constants for an angle-ply laminate versus number of layers (control, Figure 6.14).

	E_x [MPa]	E_y [MPa]	G_{xy} [MPa]	ν_{xy}	ν_{yx}
Y_0	-11.63	-93.15	-43.24	18.7	1.4e+08
P, Plateau	1.24	4.62	3.22	0.38	1.45
K	2.7	1.9	1.6	2.67	9.05
Span	-11.63	-93.15	-43.24	18.7	1.4e+08
R^2	0.9839	0.9597	0.9463	0.9841	0.9854

Table 6.10: Comparison of calculated in-plane engineering constants for AF model to literature data (control).

		Height (mm)	**Est. Num. of Layers**	E_x (MPa)	E_y (MPa)	G_{xy} (MPa)	ν_{xy}	ν_{yx}
Experimental	Elliott & Setton (2001) [82]	1.37 ± 0.30	11	0.82 ± 0.71	17.45 ± 14.29	–	0.66 ± 0.22	1.77 ± 0.65
	Duncan & Lotz (1998) [231]	~2.5	16	2.2 ± 1.7	–	–	–	–
	Fujita et al. (2000) [88]	3.2 ± 0.15	21	–	–	0.11 ±0.056	–	–
	Wagner & Lotz (2004) [212]	~5	33	–	13.2 ± 5.00	–	0.40 ± 0.15	–
	Ebara et al. (1996) [74]	~2.3	15	–	50 ± 30[a] 20 ± 15[b]	–	–	–
	Acaroglu et al. (1995) [72]	~1.8	12	–	26 ± 17[a] 14 ± 10[b]	–	–	1.13 ± 0.67[a] 1.2 ± 0.4[b]
	Guerin & Elliott (2006) [68]	2.83 ± 0.38	19	–	29.35 ± 21.92	–	–	4.64 ± 4.12
	Iatridis et al. (1999) [87]	1.67 ± 0.24	12	–	–	0.1 – 0.4	–	–
	Aim 1 Experimental Data	~2.1	13	–	11.04 ± 2.24	–	–	–
Calculated	**Symmetric Laminate**	All height values	All height values	1.24	4.69	3.28	0.37	1.42
	Angle Ply Laminate	All heights greater than 2.25	Thicker than15	1.24	4.67	3.27	0.378	1.42
	Antisymmetric Angle Ply	All heights greater than 2.1	Thicker than14	1.24	4.63	3.23	0.379	1.45

[a]Anterior
[b]Posterior
All samples are cadaveric human lumbar IVD

Table 6.11: Comparison of plateau value of calculated digested laminate elastic modulus, Ey, for AF model to experimental data (circumferential E_{LIN}).

	PBS	COL	ELA	PG
Aim 1 Experimental Data	11.04 ± 2.24	6.66 ± 0.80	6.35 ± 0.85	12.40 ± 1.43
Symmetric Laminate	4.69	0.79	1.3	1.84
Symmetric Angle Ply	4.67	0.79	1.3	1.83
Antisymmetric Angle Ply	4.65	0.78	1.3	1.81

6.4.Strains and Stresses through Laminate

Previously, we determined the stresses through each ply of a laminate to be a function of the transformed reduced stiffness matrix and the midplane strains and curvatures (7.xi). From the definition of the midplane strains and curvatures, we can rewrite them in terms of the loading conditions, N and M:

$$\begin{Bmatrix} \varepsilon^0 \\ \dots \\ \kappa \end{Bmatrix} = \begin{bmatrix} [A]^* & | & [B]^* \\ \dots & \dots & \dots \\ [C]^* & | & [D]^* \end{bmatrix} \begin{Bmatrix} N \\ \dots \\ M \end{Bmatrix} \tag{6.xxv}$$

Where the definitions of $[ABCD]^*$ are as follows.

$$\begin{aligned} [A^*] &= [A]^{-1} - (-[A]^{-1}[B])([D] - [B][A]^{-1}[B])^{-1}[B][A]^{-1} \\ [B^*] &= -[A]^{-1}[B]([D] - [B][A]^{-1}[B])^{-1} \\ [C^*] &= -([D] - [B][A]^{-1}[B])^{-1}[B][A]^{-1} \\ [D^*] &= ([D] - [B][A]^{-1}[B])^{-1} \end{aligned} \tag{6.xxvi}$$

From these two equations, the stresses in each ply of the laminate can be found as a function of the reduced transformed stiffness matrix, [ABD] matrices and the loading conditions.

$$\begin{bmatrix} \sigma_x \\ \sigma_y \\ \sigma_{xy} \end{bmatrix}_k = [\bar{Q}]_k\{([A]^*[N] + [B]^*[M]) + z_k([C]^*[N] + [D]^*[M])\} \tag{6.xxvii}$$

This can be converted into the stresses in the principle coordinate system by multiplying by the transformation matrix for stress, equation 6.ix.

Previous work by Iatridis and Gwynn (2004) modeled the AF as a symmetric laminate with 8 layers [96]: E_1 = 136 MPa, E_2 = 0.76, G_{12} = 0.3 MPa, ν_{12} = 0.3, θ = 51°. The longitudinal modulus was the only experimental value taken from a study by Skaggs et al. (1994) [73]. The transverse modulus was determined based on the Halpin-Tsai

equation which relates the modulus to the fiber modulus and matrix modulus (E_m = 0.5 MPa [134] and E_f = 904 MPa). The fiber angle and in plane shear modulus were both determined using nonlinear regression. The study subjected the model laminate to 0.10 tensile strain in the *y*-direction (circumferential) and determined the maximum stresses. They report that the maximum stress in the longitudinal direction was 8MPa and transverse and shear had "magnitudes less than 0.1 MPa" [96]. Using our above technique, we were able to determine that the transverse maximum stress was 0.044 MPa and shear stress ±0.03 MPa in their model laminate (Figure 6.17).

Their model is limited, in part, to the fact that the value that they use for the longitudinal modulus (and base other constants from) has a standard deviation of ± 50 MPa (more than 1/3 of the average value). We can follow the same methodology (model the AF as an 8 ply symmetric laminate $[\pm 60°]_{8,sym}$) using our experimental values – in this case, only shear modulus and angle are not experimentally determined – to calculate the maximum stresses in the principle direction for each ply. In our case, the maximum stress in the longitudinal direction is 1.29 MPa and transverse and shear stresses are 0.11 and ±0.026 MPa respectively (Figure 6.17). This model is also limited in the fact that the AF is not a symmetric laminate of only 8 layers. We propose, in order to most accurately model the AF, using a 19-ply symmetric angle-ply laminate and a 20-ply antisymmetric laminate [14].

6.4.1. Symmetric Angle-Ply Laminate

In this section, we model the AF as a symmetric angle-ply laminate with 19 layers (Figure 6.18), where t = 0.15 mm. If we subject the laminate to 0.1 strain the *y*-direction, we get the same values for the stresses in the principle coordinate system as from the

symmetric 8 ply model. This makes sense, since the [B] matrix is zero (for all symmetric) the stress is not in terms of *z* or the overall height of the laminate.

In vivo, the AF is subjected to biaxial tension when the IVD is loaded in compression. We can imagine that we are looking a small cube section of the AF and determine the stresses through each layer during biaxial tension. If we assume that there is a tensile load of +25 N acting on a 2.5 mm thick cube of the AF in both the circumferential (*y*) and axial directions (*x*), we can determine the stresses in the principle coordinate system. In this case, the stress resultants are $N_x = N_y = {}^{25}/_{2.5}\,\frac{N}{mm}$.

We can see that the stresses are constant for each +60 or -60 layer (Figure 6.19, Table 6.12). The longitudinal stresses are 4.33 MPa in the –θ layers and 4.57 for the +θ layers, transverse stresses are 2.58 MPa and 2.56 MPa in the –θ and +θ layers, respectively. Finally, the shear stresses through the laminate are ±0.4 MPa. If we assume that $N_x = N_y$ then there is a perfect linear fit between the magnitude of the applied stress resultants and the stresses through the laminate (Figure 6.20). This linear fit also holds if the stress resultant in one direction is a multiple of the other (for example, $N_x = 2N_y$ or $2N_x = N_y$, Figure 6.21). If the loading of the AF is known, we are able to determine the stresses in the principle directions for each layer.

6.4.2. Antisymmetric Angle-Ply Laminate

We can also model the AF as an antisymmetric angle-ply laminate with 20 layers (Figure 6.18), where $t = 0.15$ mm. Now the [B] matrix is nonzero and the stresses will depend on the location of the layer (*z*-dependent) when a load is applied. However, in the case of applying a strain, the stresses will still be constant through each layer (it's the strain that will vary by thickness, thus propagating through to the stress). So, if we

subject the laminate to 0.1 strain the *y*-direction, we get σ_1 = 1.28 MPa, σ_2 = 0.11 MPa, and τ_{12} = ±0.026 MPa(same as from the symmetric 8 ply model).

If we assume that there is a tensile load of +50 N acting on a 5 mm wide cube of the AF in both the circumferential (*y*) and axial directions (*x*), we can again determine the stresses in the principle coordinate system. In this case, the stress resultants are $N_x = N_y = 10\frac{N}{mm}$. We can see that the stresses are not constant for the layers (Figure 6.19, Table 6.13). There is a linear relationship between the values in the +60 and -60 layers that relates the stress to the position on the *z*-axis:

$$\sigma_1 = \begin{cases} -0.015t + 2.4 & if \quad -\theta \\ 0.0148t + 2.44 & if \quad +\theta \end{cases}$$
$$\sigma_2 = \begin{cases} 0.022t + 4.2 & if \quad -\theta \\ 0.204t - 0.013 & if \quad +\theta \end{cases}$$
$$\tau_{12} = \begin{cases} 0.0047t + 0.51 & if \quad -\theta \\ 0.0044t - 0.51 & if \quad +\theta \end{cases} \qquad \text{(6.xxviii)}$$

Due to the complex nature of the antisymmetric angle ply laminate (the dependence of *z*), from now on we will model the AF as the 19 layer symmetric laminate.

6.4.3. Digested Angle-Ply Laminate

We are also able to find the stresses through the symmetric angle-ply laminate for the digested samples (Figure 6.22) subjected to a tensile load of +50 N acting on a 5 mm wide cube of the AF in both the circumferential (*y*) and axial directions (*x*). Again, the digested shear moduli (G_{12}) are assumed to follow the same trend as the elastic moduli as stated above. We can see that the stresses will decrease as the engineering constants are also decreased between digestion groups.

These models are idealized cases to examine the laminate if the whole sample was digested. Using this technique, different layers in the AF model could be substituted with

different digested states ([ABD] would change depending on layout) and the change in stress distributions examined. A full examination of how the macromolecules help to transfer stresses throughout the laminate is outside the scope of this study, but would make for an interesting follow-up study. In order to properly develop this, a micromechanical model of the AF would have to be integrated at the lamina level to determine how the principle stresses in each lamina are distributed between the fibers and matrix. Once at the lamina level, the modes of failure can be examined, for example: fiber breakage in tension, fiber matrix shearing, matrix breakage.

While it is interesting to determine the principle stresses in each lamina based on the laminate loading, this does not yet account for failure. We previously discussed failure envelopes on a laminar level (on page 82), the next section will expand this to the laminate level, allowing us to develop failure envelopes for the whole AF model.

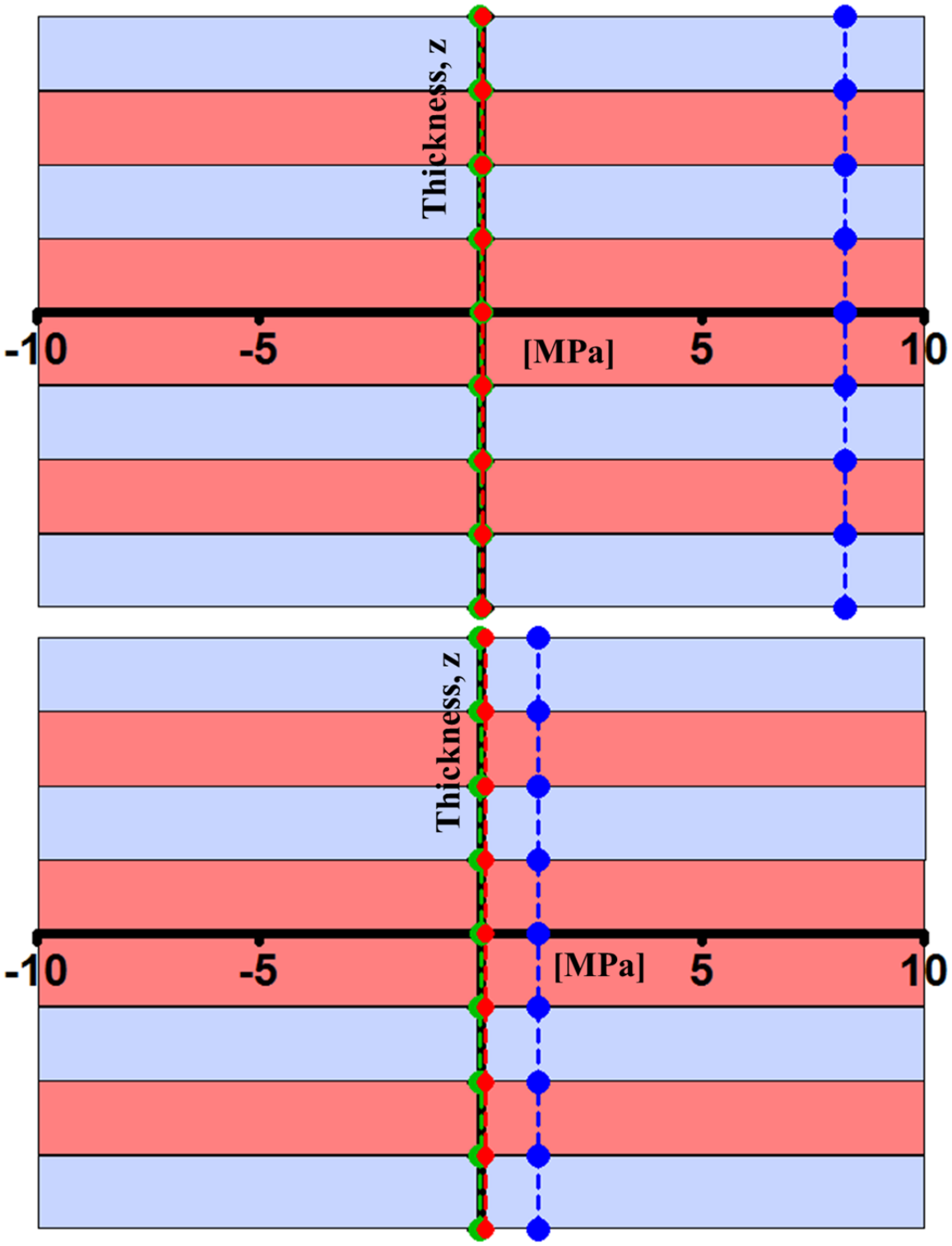

Figure 6.17: AF modeled as 8 ply symmetric laminate (ply thickness = 0.15 mm) showing the stresses through each layer in the principle coordinate system. Top: From Iatridis & Gwynn (2004) [96]. Bottom: From our experimental data. ●σ_1, ●σ_2, ●τ_{12}. Red layer represents -θ, blue +θ.

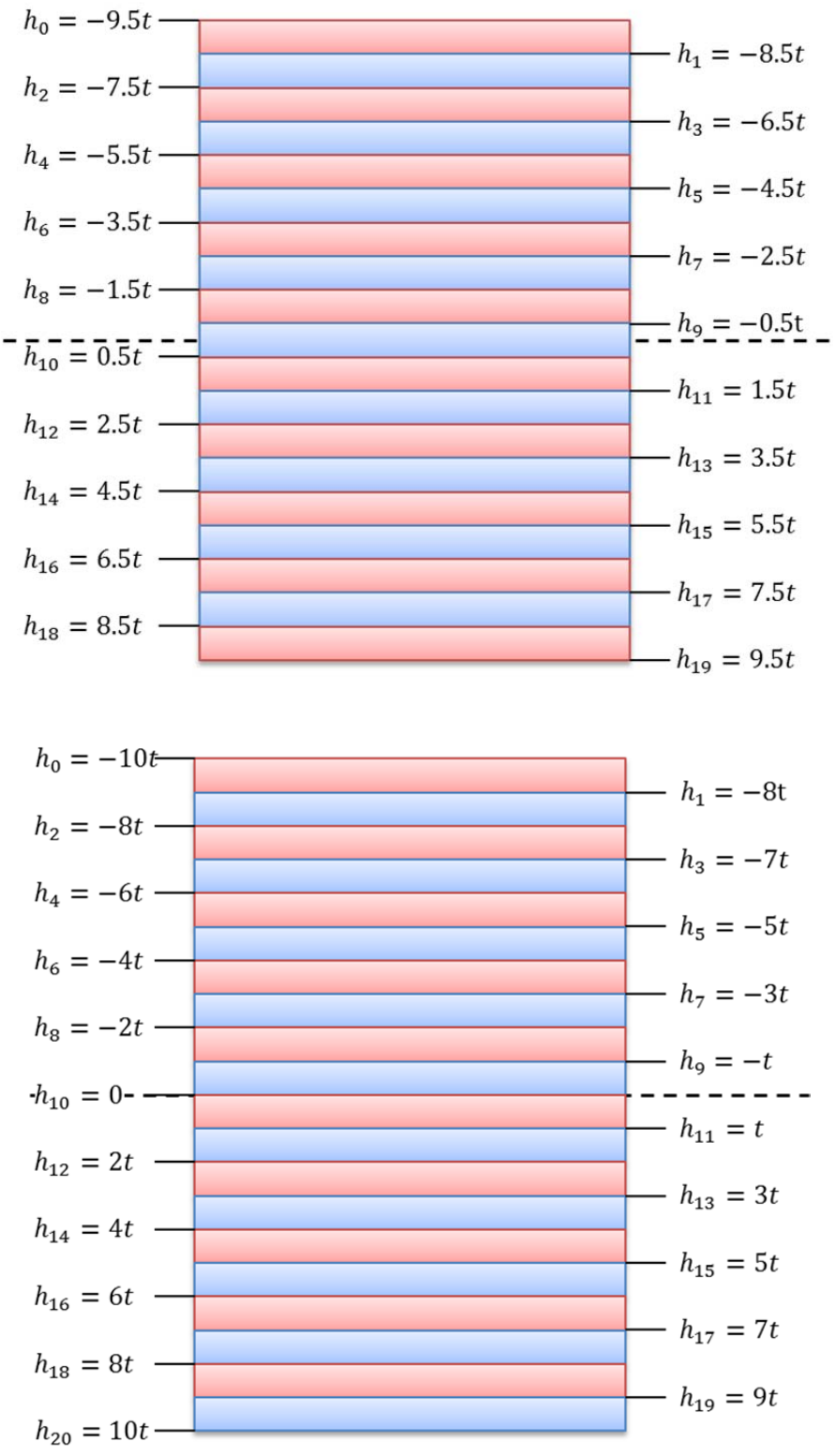

Figure 6.18: AF modeled as (top) 19 layer symmetric laminate and (bottom) 20 layer antisymmetric laminate , with t = 0.15 mm. Red layer represents -θ, blue +θ, where θ = 60°.

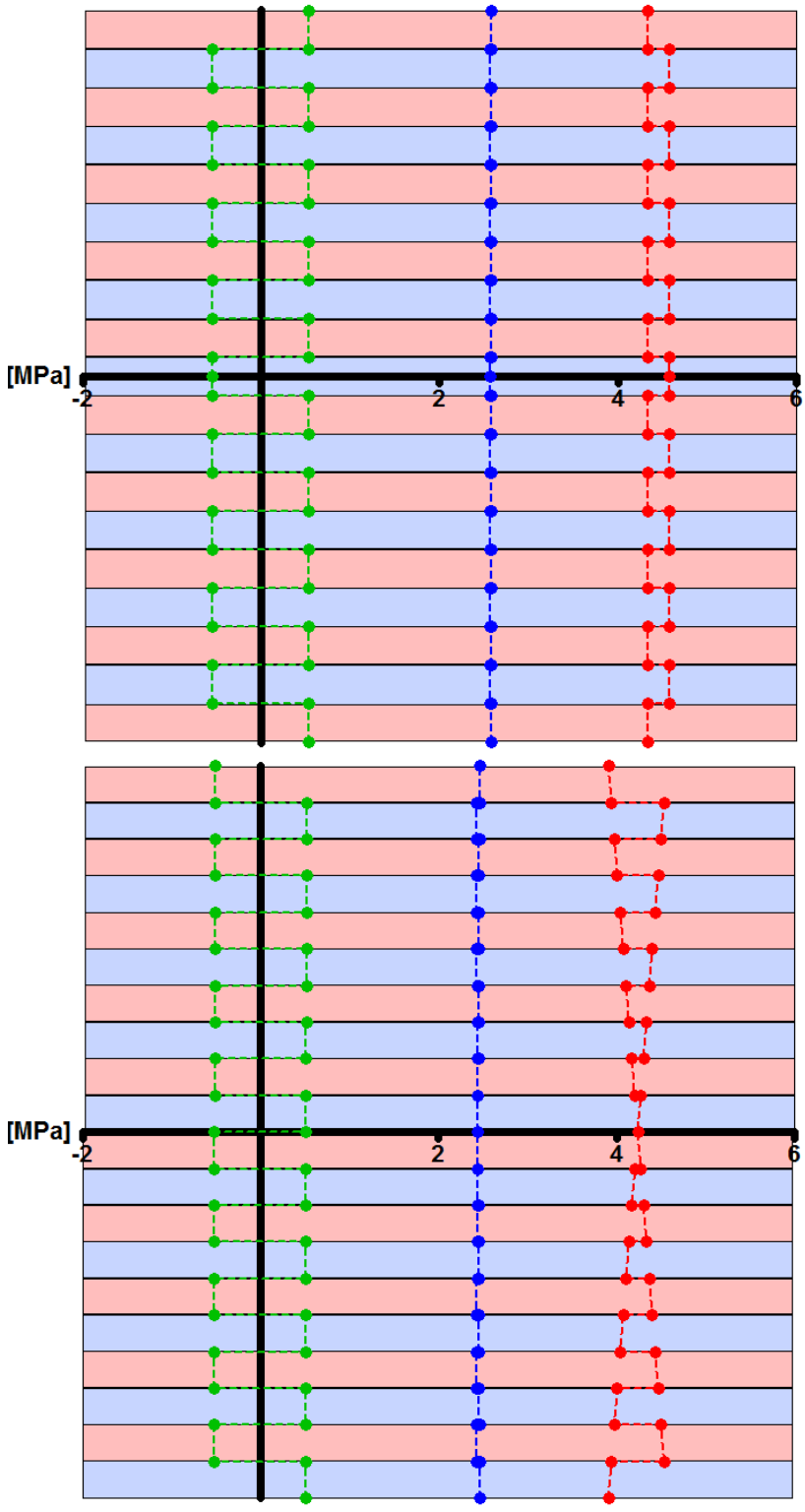

Figure 6.19: AF modeled as (top) 19 layer symmetric laminate and (bottom) 20 layer antisymmetric laminate, with t = 0.15 mm, showing the stresses through each layer in the principle coordinate system. ●σ_1, ●σ_2, ●τ_{12}. Red layer represents -θ, blue +θ.

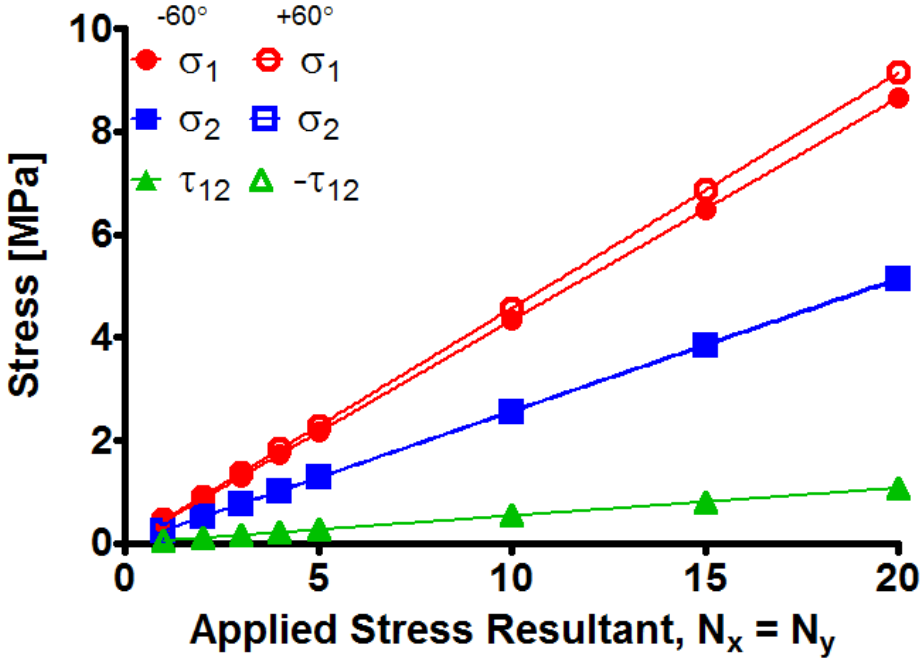

Figure 6.20: Stress through a symmetric angle-ply laminate (19 layer) based on the applied biaxial stress resultant applied (when $N_x = N_y$). Fit with a line, $R^2 = 1$.

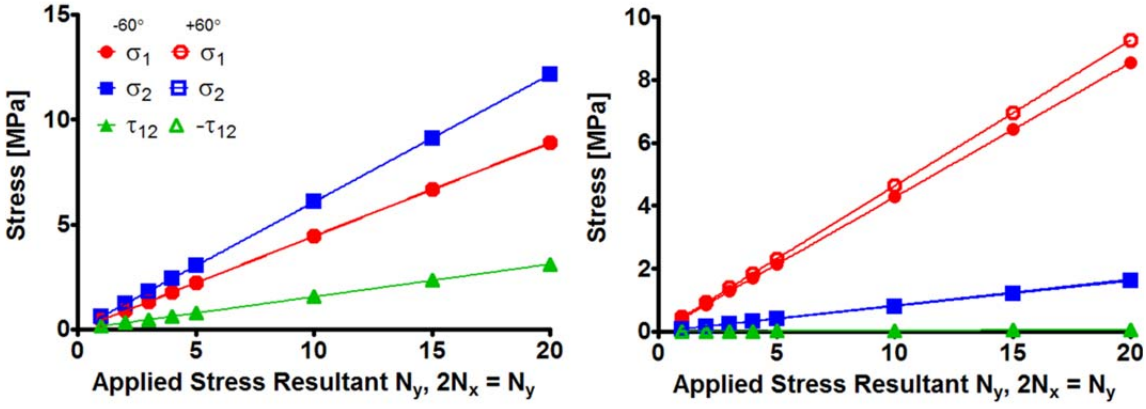

Figure 6.21: Stress through a symmetric angle-ply laminate (19 layer) based on the applied biaxial stress resultant applied being a multiple of the other. Fit with a line, $R^2 = 1$.

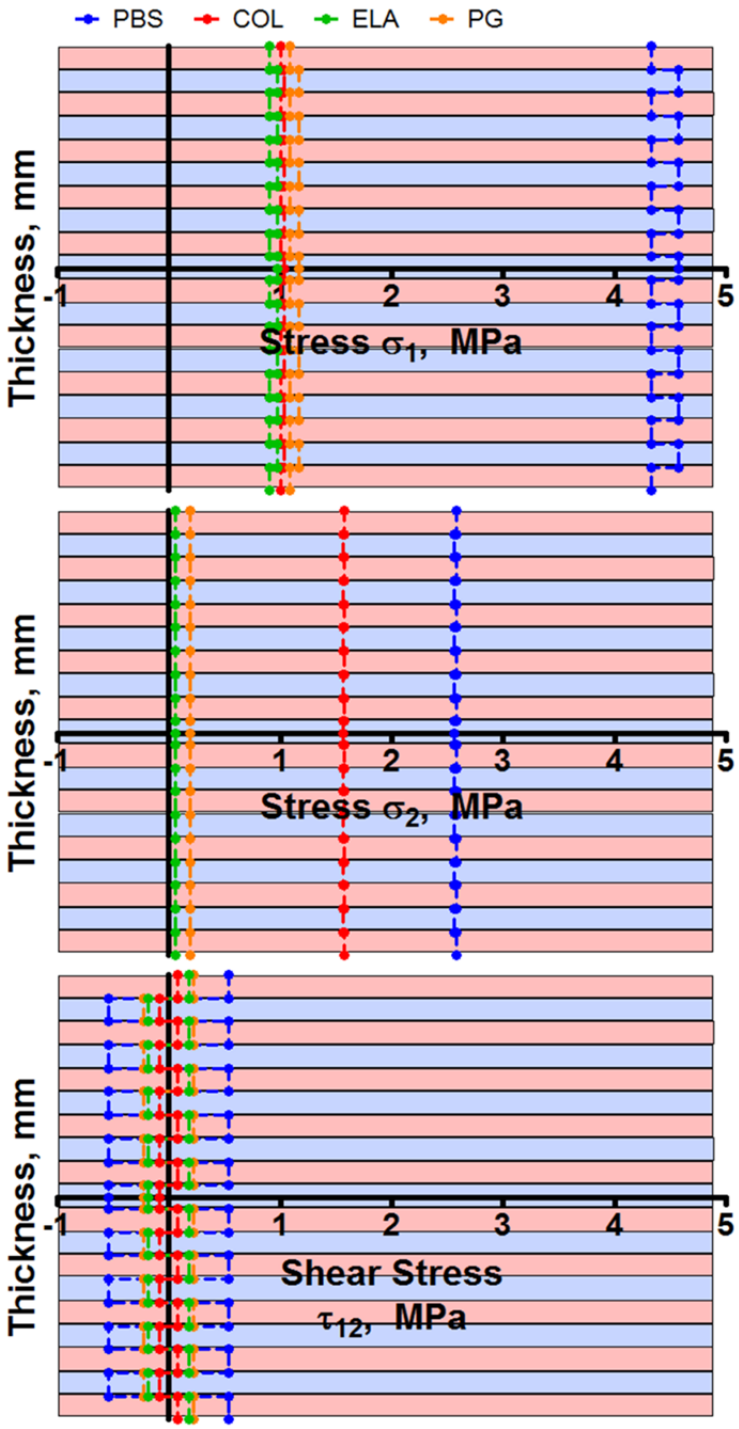

Figure 6.22: Stress distribution a modeled AF as 19 layer symmetric laminate, with t = 0.15 mm, showing the stresses through each layer in the principle coordinate system for digested samples subjected to a tensile load of +50 N acting on a 5 mm wide cube of the AF in both the circumferential (*y*) and axial directions (*x*). Red layer represents -θ, blue +θ.

Table 6.12: Calculation of stresses when biaxial stress resultant Nx = Ny = 10 N/mm applied to a symmetric 19 layer angle ply laminate.

Ply	z	θ	σ_x	σ_y	σ_{xy}	σ_1	σ_2	σ_{12}
1	-1.425	-60	3.48	3.43	-1.03	4.33	2.58	0.54
	-1.275	-60	3.48	3.43	-1.03	4.33	2.58	0.54
2	-1.275	+60	3.54	3.60	1.14	4.57	2.56	-0.54
	-1.125	+60	3.54	3.60	1.14	4.57	2.56	-0.54
3	-1.125	-60	3.48	3.43	-1.03	4.33	2.58	0.54
	-0.975	-60	3.48	3.43	-1.03	4.33	2.58	0.54
4	-0.975	+60	3.54	3.60	1.14	4.57	2.56	-0.54
	-0.825	+60	3.54	3.60	1.14	4.57	2.56	-0.54
5	-0.825	-60	3.48	3.43	-1.03	4.33	2.58	0.54
	-0.675	-60	3.48	3.43	-1.03	4.33	2.58	0.54
6	-0.675	+60	3.54	3.60	1.14	4.57	2.56	-0.54
	-0.525	+60	3.54	3.60	1.14	4.57	2.56	-0.54
7	-0.525	-60	3.48	3.43	-1.03	4.33	2.58	0.54
	-0.375	-60	3.48	3.43	-1.03	4.33	2.58	0.54
8	-0.375	+60	3.54	3.60	1.14	4.57	2.56	-0.54
	-0.225	+60	3.54	3.60	1.14	4.57	2.56	-0.54
9	-0.225	-60	3.48	3.43	-1.03	4.33	2.58	0.54
	-0.075	-60	3.48	3.43	-1.03	4.33	2.58	0.54
10	-0.075	+60	3.54	3.60	1.14	4.57	2.56	-0.54
	0.075	+60	3.54	3.60	1.14	4.57	2.56	-0.54
11	0.075	-60	3.48	3.43	-1.03	4.33	2.58	0.54
	0.225	-60	3.48	3.43	-1.03	4.33	2.58	0.54
12	0.225	+60	3.54	3.60	1.14	4.57	2.56	-0.54
	0.375	+60	3.54	3.60	1.14	4.57	2.56	-0.54
13	0.375	-60	3.48	3.43	-1.03	4.33	2.58	0.54
	0.525	-60	3.48	3.43	-1.03	4.33	2.58	0.54
14	0.525	+60	3.54	3.60	1.14	4.57	2.56	-0.54
	0.675	+60	3.54	3.60	1.14	4.57	2.56	-0.54
15	0.675	-60	3.48	3.43	-1.03	4.33	2.58	0.54
	0.825	-60	3.48	3.43	-1.03	4.33	2.58	0.54
16	0.825	+60	3.54	3.60	1.14	4.57	2.56	-0.54
	0.975	+60	3.54	3.60	1.14	4.57	2.56	-0.54
17	0.975	-60	3.48	3.43	-1.03	4.33	2.58	0.54
	1.125	-60	3.48	3.43	-1.03	4.33	2.58	0.54
18	1.125	+60	3.54	3.60	1.14	4.57	2.56	-0.54
	1.275	+60	3.54	3.60	1.14	4.57	2.56	-0.54
19	1.2	-60	3.48	3.43	-1.03	4.33	2.58	0.54
	1.425	-60	3.48	3.43	-1.03	4.33	2.58	0.54

Table 6.13: Calculation of stresses when biaxial stress resultant Nx = Ny = 10 N/mm applied to an antisymmetric 20 layer angle ply laminate.

Ply	z	θ	σ_x	σ_y	σ_{xy}	σ_1	σ_2	σ_{12}
1	-1.5	-60	3.265	3.111	-0.879	3.911	2.466	0.506
1	-1.35	-60	3.273	3.134	-0.894	3.943	2.463	0.507
2	-1.35	+60	3.401	3.556	1.174	4.534	2.423	-0.520
2	-1.2	+60	3.394	3.532	1.158	4.501	2.426	-0.519
3	-1.2	-60	3.280	3.158	-0.910	3.976	2.461	0.508
3	-1.05	-60	3.287	3.181	-0.925	4.009	2.459	0.509
4	-1.05	+60	3.387	3.509	1.143	4.468	2.428	-0.518
4	-0.9	+60	3.380	3.486	1.127	4.435	2.430	-0.518
5	-0.9	-60	3.294	3.205	-0.941	4.042	2.457	0.509
5	-0.75	-60	3.301	3.228	-0.957	4.075	2.454	0.510
6	-0.75	+60	3.373	3.462	1.112	4.402	2.432	-0.517
6	-0.6	+60	3.366	3.439	1.096	4.370	2.435	-0.516
7	-0.6	-60	3.308	3.251	-0.972	4.107	2.452	0.511
7	-0.45	-60	3.315	3.275	-0.988	4.140	2.450	0.511
8	-0.45	+60	3.358	3.415	1.081	4.337	2.437	-0.516
8	-0.3	+60	3.351	3.392	1.065	4.304	2.439	-0.515
9	-0.3	-60	3.323	3.298	-1.003	4.173	2.448	0.512
9	-0.15	-60	3.330	3.322	-1.019	4.206	2.446	0.513
10	-0.15	+60	3.344	3.368	1.050	4.271	2.441	-0.514
10	0	+60	3.337	3.345	1.034	4.239	2.443	-0.514
11	0	-60	3.337	3.345	-1.034	4.239	2.443	0.514
11	0.15	-60	3.344	3.368	-1.050	4.271	2.441	0.514
12	0.15	+60	3.330	3.322	1.019	4.206	2.446	-0.513
12	0.3	+60	3.323	3.298	1.003	4.173	2.448	-0.512
13	0.3	-60	3.351	3.392	-1.065	4.304	2.439	0.515
13	0.45	-60	3.358	3.415	-1.081	4.337	2.437	0.516
14	0.45	+60	3.315	3.275	0.988	4.140	2.450	-0.511
14	0.6	+60	3.308	3.251	0.972	4.107	2.452	-0.511
15	0.6	-60	3.366	3.439	-1.096	4.370	2.435	0.516
15	0.75	-60	3.373	3.462	-1.112	4.402	2.432	0.517
16	0.75	+60	3.301	3.228	0.957	4.075	2.454	-0.510
16	0.9	+60	3.294	3.205	0.941	4.042	2.457	-0.509
17	0.9	-60	3.380	3.486	-1.127	4.435	2.430	0.518
17	1.05	-60	3.387	3.509	-1.143	4.468	2.428	0.518
18	1.05	+60	3.287	3.181	0.925	4.009	2.459	-0.509
18	1.2	+60	3.280	3.158	0.910	3.976	2.461	-0.508
19	1.2	-60	3.394	3.532	-1.158	4.501	2.426	0.519
19	1.35	-60	3.401	3.556	-1.174	4.534	2.423	0.520
20	1.35	+60	3.273	3.134	0.894	3.943	2.463	-0.507
20	1.5	+60	3.265	3.111	0.879	3.910	2.465	-0.506

6.5.Laminate Failure

We previously explored a method to determine the stresses in each layer of the model AF laminate in the principle coordinate system. This, however, did not take into account that at some measured stress (or strain), determined experimentally, the lamina are subject to failure. We are able to predict the laminate strength based on the strengths and interactions of the lamina; since the stresses in the principle directions are known, these can be compared with the lamina failure criterions and be rescaled for the entire laminate.

Let us consider the 19 ply symmetric angle-ply laminate to model the AF. We are able to determine the principle stresses for every k^{th} lamina from combining equations 7.ix and 7.xxvii. In the case of the control laminate (PBS), this reduces to a function in terms of the resultant stresses and moments. Due to the change in angle, there are two equations governing the laminate, one for the +60° layers and one for the -60° layers.

$$\begin{bmatrix}\sigma_1\\ \sigma_2\\ \sigma_{12}\end{bmatrix}_k^{+60} = \begin{bmatrix}-0.012N_x + 0.47N_y + 0.78N_{xy} - 0.02M_x + 0.058M_y + 0.15M_{xy}\\ 0.35N_x - 0.095N_y - 0.05N_{xy} + 0.28M_x - 0.10M_y - 0.141M_{xy}\\ -0.1N_x + 0.05N_y - 0.015N_{xy} - 0.25M_x + 0.11M_y - 0.07M_{xy}\end{bmatrix}$$
$$\begin{bmatrix}\sigma_1\\ \sigma_2\\ \sigma_{12}\end{bmatrix}_k^{-60} = \begin{bmatrix}0.01N_x + 0.42N_y + 0.71N_{xy} - 0.008M_x + 0.03M_y - 0.13M_{xy}\\ 0.35N_x - 0.09N_y + 0.05N_{xy} + 0.27M_x - 0.08M_y + 0.14M_{xy}\\ 0.1 + N_x - 0.05N_y - 0.017N_{xy} + 0.25M_x - 0.125M_y - 0.1M_{xy}\end{bmatrix} \quad \text{(6.xxix)}$$

We have previously discussed the interactive failure criterion, the *Tsai-Hill* failure theory. If we recall, the failure strengths for the control samples in the longitudinal (X) and transverse (Y) directions are: $X = 2.37 \pm 0.26$ MPa and $Y = 0.33 \pm 0.03$ MPa. We can substitute these values into the Tsai-Hill failure theory and simplify to obtain the following.

$$\sigma_1^2 - \sigma_1\sigma_2 + \left(\frac{2.37}{0.33}\right)^2 \sigma_2^2 + \left(\frac{2.37}{S}\right)^2 \tau_{12}^2 = 5.62 \quad \text{(6.xxx)}$$

We are able to substitute the principle stress values (equation 6.xxix) into this failure and can determine if failure will occur in either the ±60° layers due to any loading condition. However, there exists no data for shear strength in the literature.

6.5.1. Determination of Shear Strength for Lamina

While there is no experimental or modeling technique in the literature to determine shear strength, we do have experimental values for the ultimate tensile stress in the circumferential direction (*y*-direction). We can use this, in order to calculate the shear strength needed in order to fulfill the failure theory correctly. We subject our AF laminate model to uniaxial tension in the circumferential direction only ($N_y \neq 0, N_x = N_{xy} = M_x = M_y = M_{xy} = 0$). Substituting the principle stresses into the Tsai-Hill, allows us to solve for the stress resultants that would cause the layers to fail.

$$N_y^{+60} = \frac{5.62}{0.73 + \frac{0.01}{S^2}}$$
$$N_y^{-60} = \frac{5.62}{0.66 + \frac{0.013}{S^2}} \quad \text{(6.xxxi)}$$

We can see that the failure stress resultant is dependent on the shear strength for each layer (Figure 6.23). We know from previous experiments, that the failure strength of the AF in the circumferential direction is$\sigma_{f,circ} = 1.27 \pm 0.28$ MPa. This must be transformed into the stress resultant by multiplying by thickness of the sample tested (0.15 mm): $\sigma = \frac{F}{A} = \frac{F}{ht} = \frac{N_y}{h}$; the circumferential samples had average dimensions of 5 x 2 x 0.15 mm – *L* x *h* x *t*. Therefore the stress resultant that caused the AF to fail in the circumferential direction experimentally is:$2.54 \frac{N}{mm}$. We can substitute this value into equation 7.xxxi to determine the values of the shear strength in order to make the

experimental tensile strength hold true. The shear strength is equal to $S = 0.23$ MPa for the +60 layers and to $S = 0.24$ MPa for the -60 layers. Using this same technique, we can also determine the shear strengths of the digested samples (Table 6.13)

6.5.1.1. Alternate Method for Calculation of Shear Strength

This methodology gives different values of the shear strength depending on the sign of the angle. However, in theory, the shear strengths should be equal to each other since we are oriented in the principle coordinate system. We hypothesize that this difference comes from the arbitrary form of the shear modulus that we determined earlier (G_{12} to be 0.3 MPa in the case of PBS samples [226], and a reduction of the control sample value for the digested samples).

Here, we try an alternate method to determine the shear strength and shear modulus concurrently. The shear strength of the lamina is a function of the shear modulus (Figure 6.24, Figure 6.25). The shape of the curves all follows the same trend, regardless of digestion or sign of fiber angle. There exists a vertical asymptote at some minimum value of lamina shear modulus, G_{12}, after which the curve evens to a slightly increasing line (slope PBS: 0.05 and 0.04 for +60° and -60° layers respectively). We can find the value of the lamina shear modulus which will give the same shear strength for each lamina. For the control samples (PBS), the shear modulus is calculated to be $G_{12} = 0.92$ MPa and shear strength, S = 0.24 MPa. We can also do this same technique for the digested samples (Figure 6.26). The shear moduli that allow the same shear strength for the ±θ can be seen in Table 6.15. These values are dependent on the fiber angle being exactly ±60°.

We can recalculate the laminate engineering constants, to determine the effect of this new shear modulus value (Table 7.15). The calculated laminate moduli all increase due to the increase in G_{12} and the Poisson's ratios slightly decrease. The axial elastic moduli and Poisson's ratios are still within the range of literature. The newly calculated circumferential modulus (E_y) is now also within the range of that in literature, including our experimental data. However, the laminate shear modulus is still being overestimated.

6.5.2. Failure Envelope

As the IVD is in compression, the AF is experiencing biaxial tension. Now that the shear strength is known, we are able to determine the failure stress resultants for any combination of loading conditions. In order to mimic *in vivo* conditions, we can subject our model AF laminate to biaxial stress in the *x*- and *y*- directions only (axial and circumferential, N_y and $N_x \neq 0, N_{xy} = M_x = M_y = M_{xy} = 0$). In the case of the control samples, the Tsai-Hill failure equation is now a function of two stress resultant conditions: N_y and N_x, which can be plotted leading to an elliptical failure envelope.

Figure 6.27 shows the failure envelopes for the control samples for both forms of determining the shear strength: by assuming $G_{12} = 0.3$ [226] and by assuming equal for both ±θ° layers and determining what value of G_{12} makes this true. We can see that the more conservative envelope is for the determination of G_{12} (same shear strength). This is the case for the digested samples as well (Figure 6.28). It is important to remember that the stress resultants are graphed here. In order to change into load, one would need to multiply by the thickness of the sample, and to put in terms of stress, divide by the height of the sample.

First, let us examine the failure envelopes for ±θ for the known G_{12} method. In the COL and PG groups, the envelopes for ±θ are very close to each other, while for PBS and ELA, one of the angles is more conservative of an estimate than the other. For all cases, except PG, the maximum stress resultants occur when a combination of both N_x and N_y are applied. This indicates that the unique angle ply composition of the laminate allows the most strength when loaded biaxially. Alternatively, the PG group, is able to stand more load until failure when loaded uniaxially in the circumferential direction and not a combination for the case of the known $G_{12} = 0.102$ MPa. We hypothesize that this is due to the fact that when the PG are removed in the system, the macromechanics adjust in the laminate which corresponds to the collagen fibers not as able to take on load in the transverse directions on the lamina scale. For all sample groups, the ellipse is tilted toward the circumferential axis (larger N_y); this is expected because the angle is taken from the axial orientation and in the circumferential direction $\theta=30°$, the laminate gets stronger as more strong as $\theta \rightarrow 0°$.

For the determination of G_{12} group (the alternate method), we see that in the case of the PBS, COL and ELA groups, the envelope is more conservative than the original method. The ellipses also shift toward the axial axis (N_x) in this alternate method. Again, the PG group is the exception. For this case, the failure envelope for equal shear strengths is shaped just as the other digestive groups. This indicates to us, that the shear modulus chosen in the first method, $G_{12} = 0.126$ MPa, was not a good assumption and thus resulted in a skewed failure envelope. Since the alternative determination of shear strength gives the more conservative failure stress resultants, we will compare this envelope for the different digestions: Figure 6.29. The size of the failure envelopes

correspond directly with the data seen experimentally on the lamina level: PBS > PG > ELA > COL. This is expected since the laminate failure theory is based on the lamina properties.

6.5.3. Sensitivity Analysis

It is interesting to examine the change in shape of the failure envelopes depending on the value of shear modulus used (the true difference between methodologies). A sensitivity analysis was performed for the failure envelopes of the control samples; in this case only the +60° layer was examined. Different values of G_{12} were used and the failure envelope determined based on determining shear strength from the circumferential failure stress (Figure 6.30).

The shape and size of the failure envelope changes with the lamina shear modulus. As the shear modulus increases, the stress resultant in the circumferential direction (N_y) decreases; however the value where it crosses the N_y axis stays constant, while the intercept on the N_x axis gets larger as the modulus increases. There is a need for an experimental value for shear modulus of an annular lamina. The shape and size of the failure envelope will be influenced by this value. An alternate method to determining shear modulus would be to determine the shear strength of the lamina and back calculate the shear modulus, as our alternative method did.

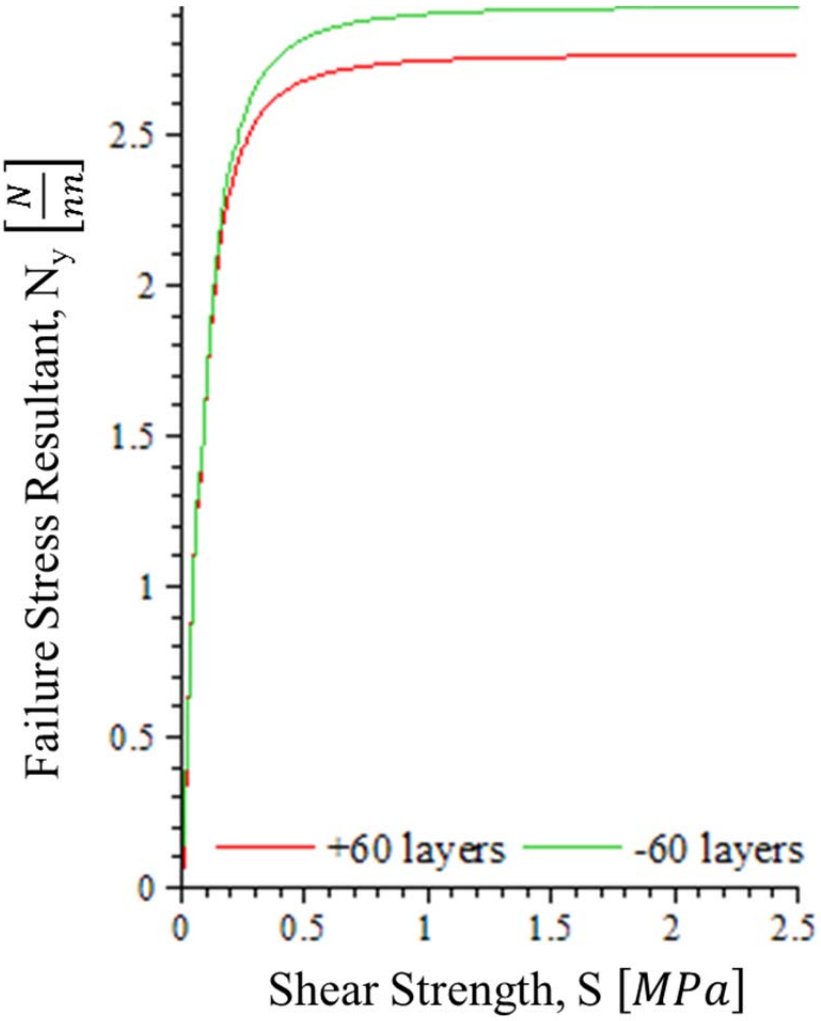

Figure 6.23: Failure stress resultant in the circumferential direction, N_y, when subjected to uniaxial tension is dependent on the shear strength of the lamina.

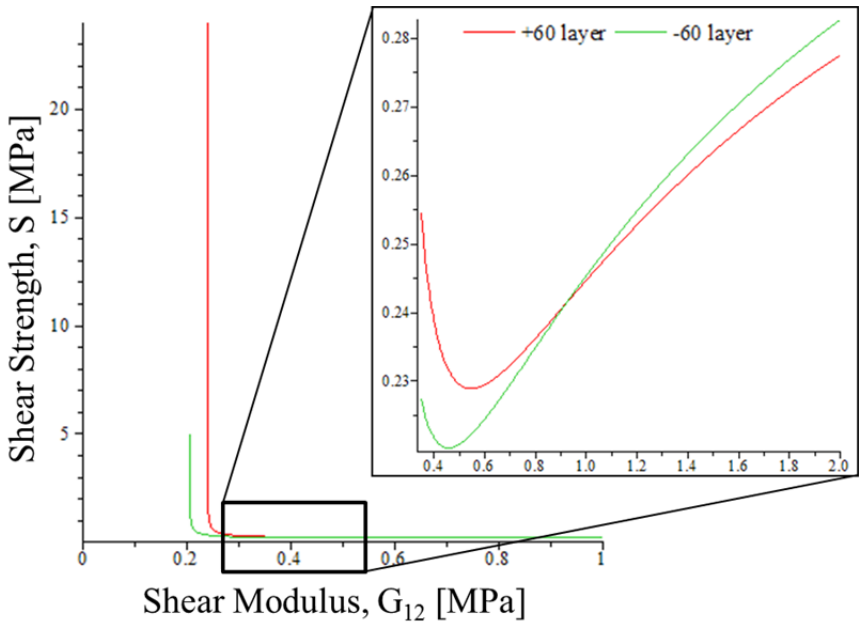

Figure 6.24: Shear strength is a function of shear modulus for lamina.

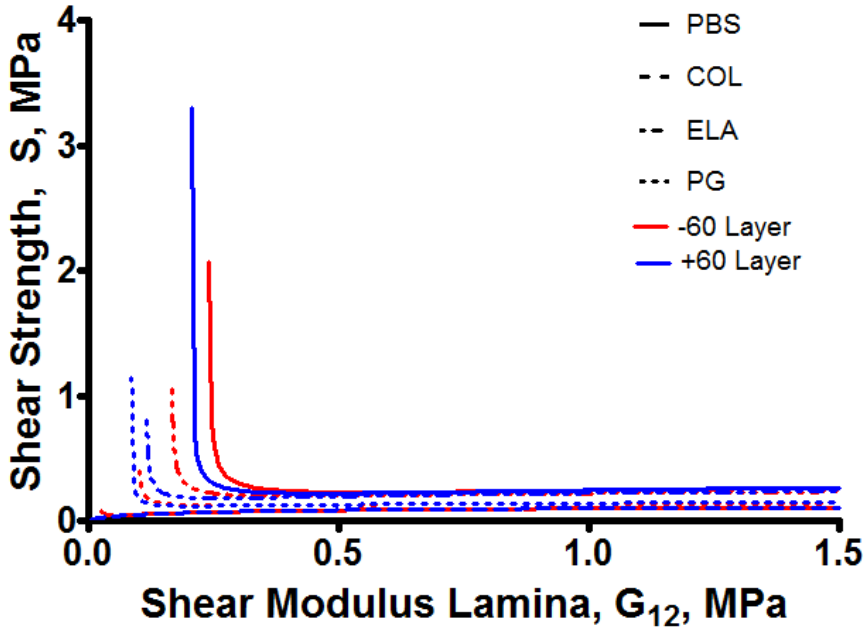

Figure 6.25: Shape of curves for shear modulus versus shear strength all follow same trend for digested groups.

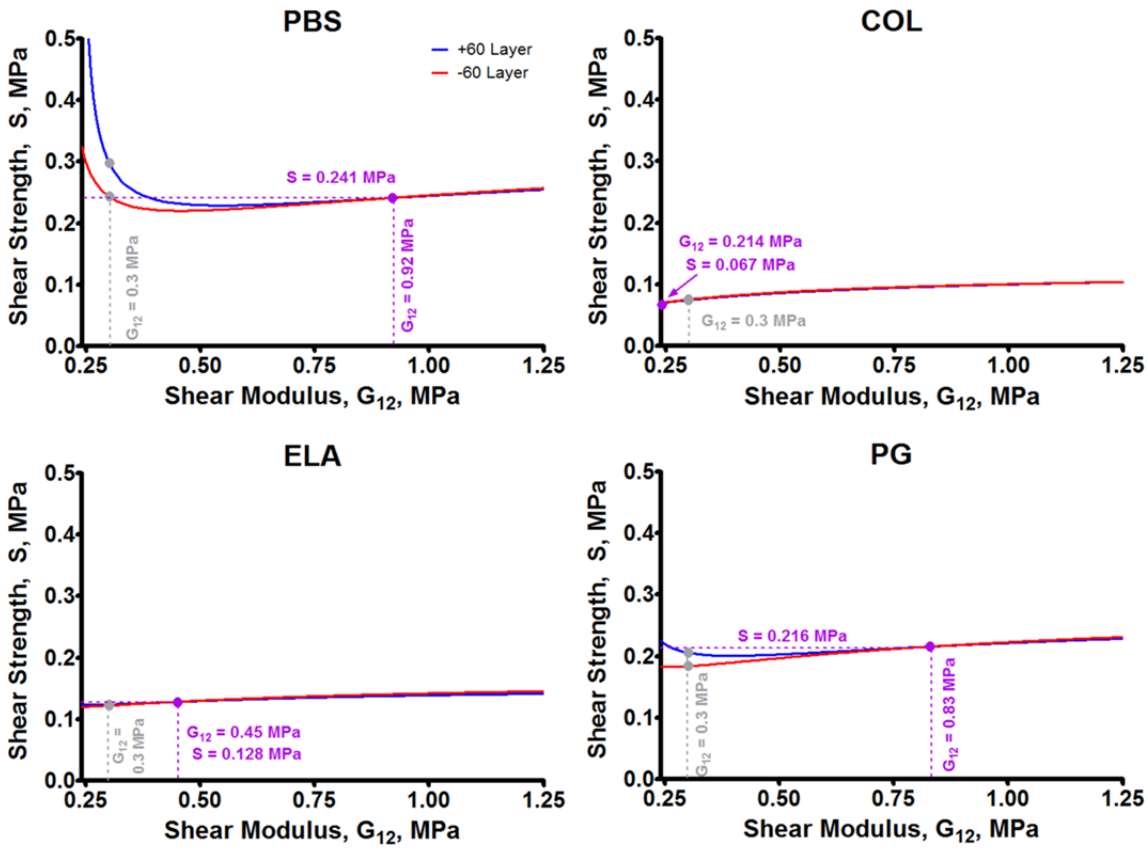

Figure 6.26: Shear strength as a function of shear modulus for lamina in all digestion groups. Shear strength when G_{12} = 0.3 MPa illustrated as well as location where shear strength is same for both ±θ lamina.

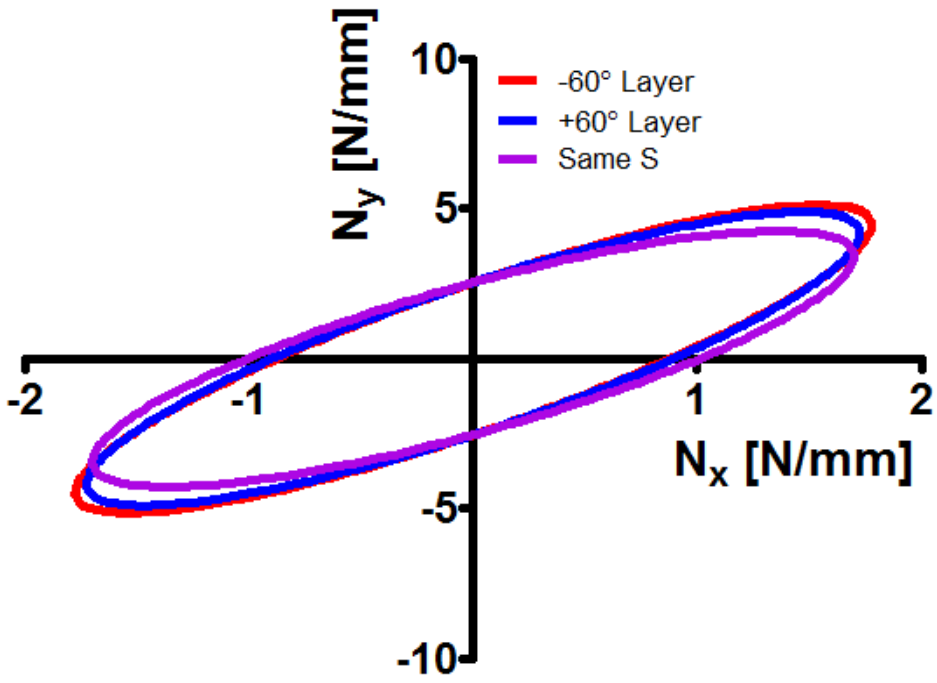

Figure 6.27: Failure envelope for control (PBS) samples when subjected to biaxial stress. Blue and red represents failures for the ±θ layers when G_{12} is taken from Iatridis & Gwynn (2004) to be 0.3 MPa [226]. Purple shows the failure envelope for the calculated G_{12} that gives same shear strength for both angled plies.

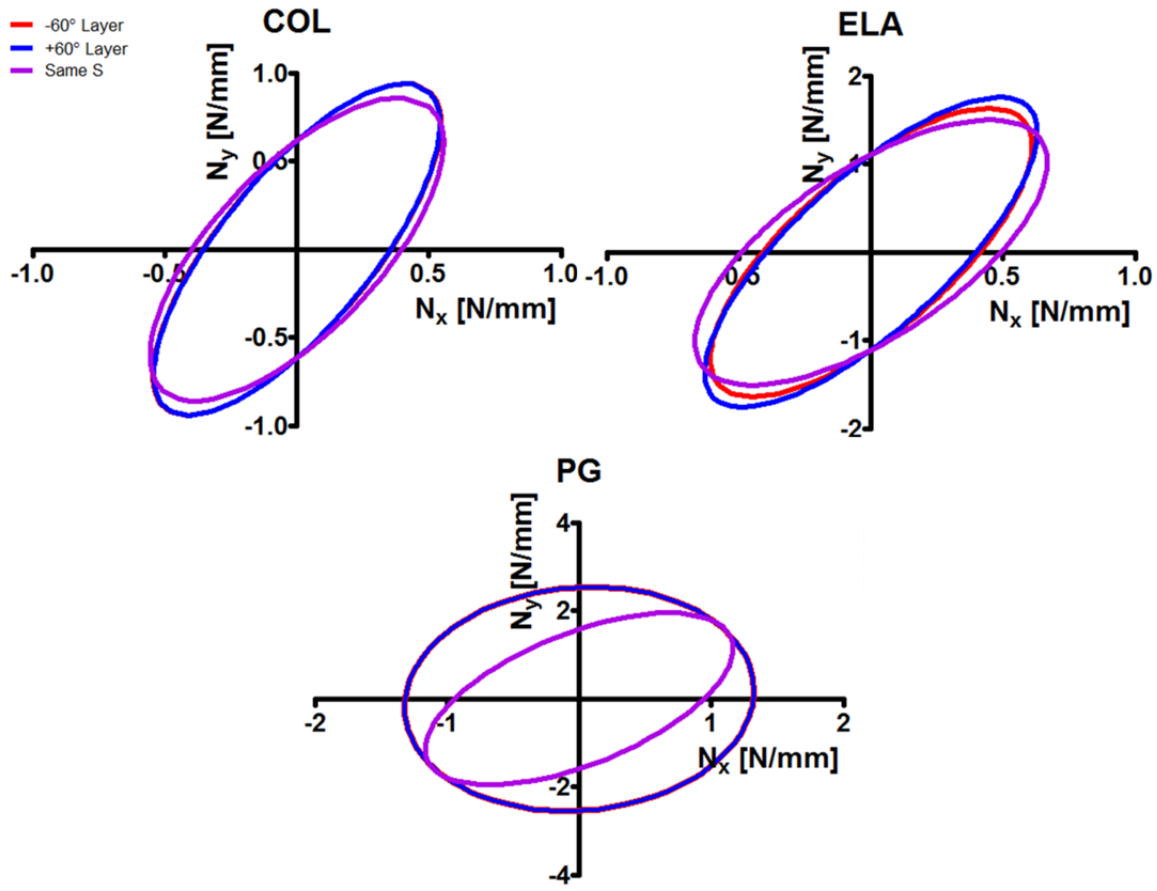

Figure 6.28: Failure envelope for digested samples when subjected to biaxial stress. Blue and red represents failures for the ±θ layers when G_{12} is taken to be the same decrease as elastic modulus from 0.3 MPa [226]. Purple shows the failure envelope for the calculated G_{12} that gives same shear strength for both angled plies.

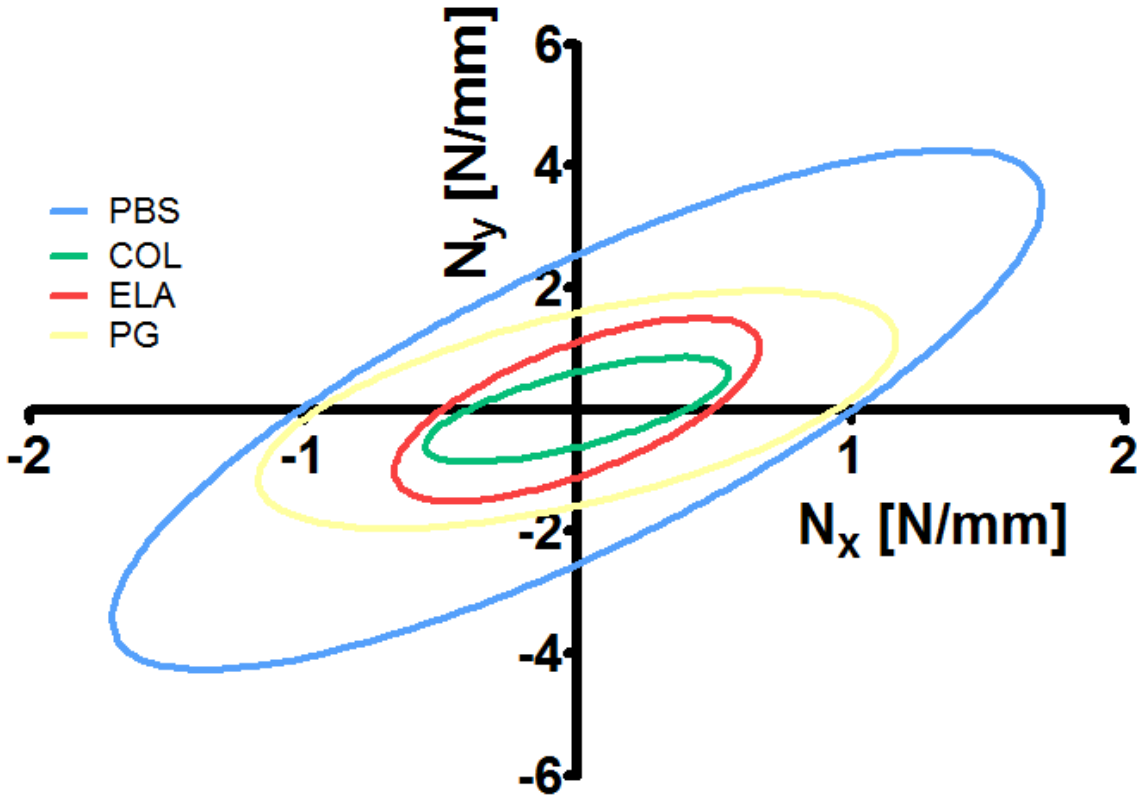

Figure 6.29: Failure envelope for digested samples when subjected to biaxial stress for different digestion groups. The failure envelopes are for alternate shear strength technique (calculated G_{12} to produce same S).

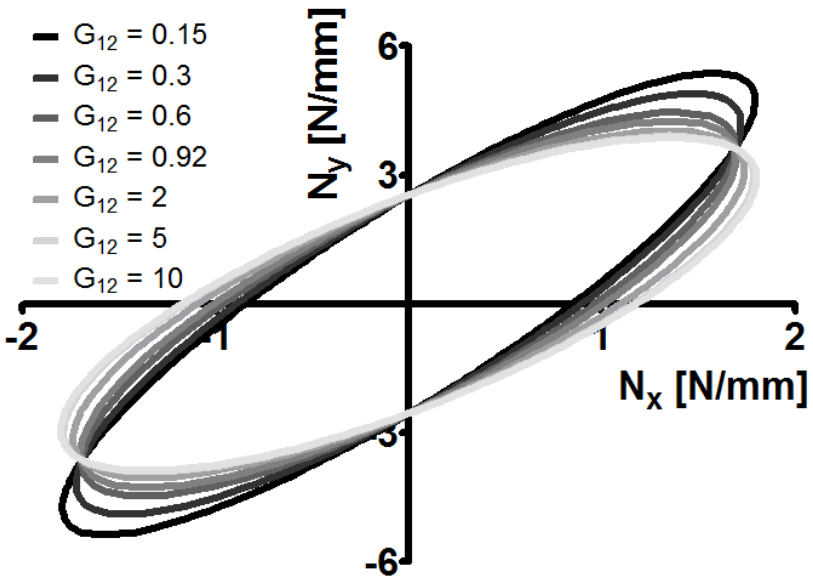

Figure 6.30: Failure envelope of biaxially loaded AF model showing dependence of lamina shear modulus, G_{12} (in MPa) for +60° layers. G_{12} = 0.3 MPa was previously reported in the model by Iatridis & Gwynn [226] and G_{12} = 0.92 MPa is the value that allows the shear strength for both ±60° to be equal.

Table 6.14: Calculated shear strengths for all digestion groups.

Digestion Group	Shear Strength, S [MPa]	
	+60° Layer	-60° Layer
PBS	0.298	0.243
COL	0.046	0.035
ELA	0.104	0.17
PG	0.078	0.093

Table 6.15: Calculated shear modulus and corresponding shear strength using alternate method for all digestion groups.

Digestion Group	Shear Modulus, G_{12} [MPa]	Shear Strength, S [MPa]
PBS	0.920	0.241
COL	0.214	0.067
ELA	0.45	0.128
PG	0.830	0.216

Table 6.16: Comparison of laminate engineering constants for control sample for shear modulus value taken from literature [226] and value calculated from the shear strength of ±θ lamina being equal.

	height (mm)	**Num. of Layers**	E_x (MPa)	E_y (MPa)	G_{xy} (MPa)	ν_{xy}	ν_{yx}
Elliott & Setton (2001) [82]	1.37 ± 0.30	11	0.82 ± 0.71	17.45 ± 14.29	–	0.66 ± 0.22	1.77 ± 0.65
Duncan & Lotz (1998) [231]	~2.5	16	2.2 ± 1.7	–	–	–	–
Fujita et al. (2000) [88]	3.2 ± 0.15	21	–	–	0.11 ±0.056	–	–
Wagner & Lotz (2004) [212]	~5	33	–	13.2 ± 5.00	–	0.40 ± 0.15	–
Ebara et al. (1996) [74]	~2.3	15	–	50 ± 30[a] 20 ± 15[b]	–	–	–
Acaroglu et al. (1995) [72]	~1.8	12	–	26 ± 17[a] 14 ± 10[b]	–	–	1.13 ± 0.67[a] 1.2 ± 0.4[b]
Guerin & Elliott (2006) [68]	2.83 ± 0.38	19	–	29.35 ± 21.92	–	–	4.64 ± 4.12
Iatridis et al. (1999) [87]	1.67 ± 0.24	12	–	–	0.1 – 0.4	–	–
Aim 1 Experimental Data	~2	13	–	11.04 ± 2.24	–	–	–
G_{12} = 0.3 MPa	2.85	19	1.24	4.67	3.27	0.378	1.42
G_{12} = 0.92 MPa	2.85	19	2.08	8.52	3.43	0.317	1.07

6.6.Conclusions

In the present aim, composite theory was used to build a model AF using classical lamination theory and experimentally determined laminar properties. This study builds on work completed by Iatridis and Gwynn (2004) who modeled the AF as an 8 ply symmetric laminate [226]. Lamination theory allowed us to calculate principle stresses in the annular layers. The Tsai-Hill failure theory was used in order to determine the shear strength by fitting to our experimental circumferential failure data. Using this shear strength, we were able to create biaxial failure envelopes for a 19-ply symmetric laminate model of the AF.

While this work advanced the application of using CLT for the AF, there are certain limitations that could possibly be addressed in future work. A more rigorous definition for the material properties of shear modulus and shear strength are needed. We showed that the failure envelopes are sensitive to these values. Shear testing of materials is difficult, especially thin plates, which are the annular lamina. This author suggests performing biaxial testing to determine the coupled failure strengths required for laminar failure. After the upper right quadrant of the strength envelope is populated with experimental data, the shear modulus can be determined by best fit.

This model is limited to tensile loading configurations. However, in the AF the collagen fibers loaded primarily in tension during loading of the IVD [144]. We are also limited to the AF experiences small strains. In the case of larger strains, the assumption of a constant fiber angle under deformation will not hold true. The use of CLT has some innate assumptions which limit the use of our model.

We assumed that the laminate was in a state of plane-stress; the normal and shear stress components in the *z* direction (radial) are negligible. However, delamination is a failure mechanism of the AF [209, 226]. This technique does not allow for investigations of interlaminar stresses which cause annular delamination. This could be explored in future work by implementing a computational model of the AF. Using finite element techniques allows for a three-dimensional annular model [142, 143, 154, 222, 231-234, 236, 237]; these models could be expanded to account for damage initiation. Another important assumption in the model was the perfectly bound lamina. Not allowing the lamina to slip in relation to each other artificially increases the shear modulus of the laminate. Computational annular models could be modified with the addition of deformable interfaces to account for this slip [238-242]. The properties of the interface elements could be determined based on fitting the behavior of the model to experimental data in the circumferential and radial directions (as determined in Chapter 4).

The assumption that the lamina behaved linear elasticity was made; however we have shown the AF has a nonlinear stress-strain curve (Figure 4.5). The goal of this aim was to examine the failure of the AF as a laminate structure, the failure stresses occur in the linear range of the stress-strain curve where the lamina behavior was linear. A goal of future work should be to account for the nonlinear behavior of the annular lamina.

It is important to note that the failure envelopes discussed here are an indication of an injury model as opposed to a degenerative one. This lends itself to a spontaneous disc herniation, where at some loading condition catastrophic failure will occur in the lamina of the AF. We were able to create failure envelopes which showed failure loadings as opposed to mechanisms for failure. Alternatively, a degenerative model

would allow for exploration of the roles of the macromolecules and the actual failure mechanisms that occur. Iatridis and Gwynn (2004) examined some of these failure patterns while viewing the AF under SEM [226]. They demonstrated the laminate structure of the AF using IVDs from mature Wistar rat tails using high-resolution SEM using a method described by Richards et al. (1999) [243]. They observed multiple failure patterns within a lamina: delamination, matrix cracking, and fiber failure. The paper also goes on to hypothesize that the failure modes could be dependent on the stress history applied and number of loading cycles [226].

In this study, we used composite theory techniques to model the AF as a fiber reinforced laminated composite. The use of CLT was able to predict the laminate properties for the elastic moduli and Poisson's ratio; however, the shear modulus was overestimated due to the assumption of perfectly bonded layers. The stresses in the principle directions were determined based on different loading configurations. We were able to expand this work to create biaxial failure envelopes with the interactive Tsai-Hill failure criteria. The main advantages of using this approach were the simplicity of use and that we were able to exploiting the symmetry properties of a symmetric angle-ply laminates within the context of deformation. This approach requires that the ply properties be known, showing the importance of determining an experimental lamina shear modulus.

7. CHAPTER SEVEN: CONCLUSIONS

7.1. Summary

Lower back pain is a major health problem in the United States of America, affecting close to 14% of people, resulting in 1.8 million missed worked days annually [2-6]. It can be caused by degeneration of the IVD or an injury to the disc. One type of catastrophic disc injury, herniation, is classified as the inner NP material initially bulging against the AF leading to eventual rupture (failure) of the AF, allowing the nuclear material to expulse out of the cavity. In a randomized MRI study of 98 subjects, 52% of the subjects had a bulge of the disc evident in at least one level, 27% had a protrusion, and 1% had an extrusion; Thirty-eight percent had an abnormality of more than one IVD level [90, 244]. It is the most prevalent musculoskeletal disorder, with a roughly 65-80% lifetime prevalence of lower back pain [245]. There have been previous studies characterizing the mechanical properties of the AF on both a laminate level [68, 72, 74, 82, 87, 88] and lamina level [35, 72, 73, 82, 86], however there is little literature on the failure mechanics of the AF.

7.1.1. Experimental Annular Mechanics

In this thesis, the mechanical properties of the AF were quantified on both a laminar (principle coordinate system) and laminate (global coordinate system) level using a custom designed micro-tensile device. In this work, we were able to build a more robust description of the characterization of the annulus fibrosus. The standard deviations for the experimentally determined properties ranged from 8 – 22% of the average value, which is stark contrast to the standard deviations previously reported in the literature which were sometimes up to 90% of the average value reported [35, 68, 72-74, 82, 86, 88]. We

hypothesize that our experimental values resulted in smaller standard deviations due to the small strain rate, consistency of sample dimension (thickness, 150μm), and consistency in testing technique. The samples showed multiple failure patterns, including fiber failure, matrix cracking, and delamination, which is constituent with other failure mechanisms observed [226].

This same testing technique was expanded to explore the role of macromolecules in annular mechanics. Using enzymatic digestion, collagen, elastin and proteoglycans were degraded using collagenase, elastase and chondroitinase ABC, respectively, to examine the mechanical role of each biomolecule. The mechanical and failure properties were determined for annular samples after degradation to give insight into the role of the biomolecules in the mechanical response of the AF.

Collagen fibers play a pivotal role in the tensile strength of the annulus on both a laminar and laminate level, shown by a decrease in failure stress and elastic modulus upon collagenase-treatment. Digestion of collagen allows the elastin fibers to play a greater role in the tensile strength of a single annular layer and between layers (radial samples), as seen by an increase in failure strain for the treated samples. Elastin fibers also significantly contributed to the tensile strength for both scales and all testing directions shown by a decrease in failure stress and elastic modulus upon elastase-treatment. The elastin fibers aid in deformation of the annulus in the out-of-plane testing directions as seen by a decrease in the failure strain for the transverse and radial samples. The proteoglycan matrix plays a more important role in laminar annular mechanics than on the laminate level, as seen by a decrease in failure stress and elastic moduli for the longitudinal and transverse directions after chondroitinase ABC-treatment. Proteoglycans

are not abundant between lamina in the AF, which we mechanically confirmed with the lack of statistical difference in properties for the laminate samples (circumferential and radial) to the control groups.

This study was limited due to the possibility of cross-degradation between digested groups [106]; biochemical assays could be performed in order to quantify the amount of each macromolecule degraded dependent on enzymatic protocol. However, despite this limitation, the digested properties provide insight into the mechanical behavior and molecular component interactions within the AF.

7.1.2. Laminated Annular Model

Based on fiber reinforced laminate composite theory, the experimentally determined laminar mechanical properties were used to model the AF as a 19-layer, symmetric, angle-ply composite. The mechanical properties of the modeled laminate were in the range of experimental literature values for the elastic moduli and Poisson's ratios of the AF [68, 72, 74, 82, 87, 88]. The shear modulus of the laminated AF was an order of magnitude higher than that reported in literature [87, 88]. We hypothesized that the assumption of perfectly bonded layers in the model was the reason for the discrepancy in shear modulus. In assuming that each layer is perfectly bonded, we negated the densely populated inter-laminar elastin area. With the addition of elastin, the stress-strain curve would allow high strain at the same stress, thus leading to a higher shear modulus. Other limitations of the annular laminate model included the assumption of plane stress, small strains, simplified rectangular geometry, single fiber angle and linear elastic behavior of the tissue. These assumptions are necessary in order to apply lamination theory to the annular material and are not physically relevant to how the AF

behaves *in vivo*. Despite these limitations, our model predictions for laminate properties of elastic moduli and Poisson's ratio were within the range of those reported in literature [68, 72, 74, 82, 212, 231]. The assumption of no slip between lamina (perfect bonds), did limit the shear modulus prediction value, and the model was an order of magnitude larger than shown in literature [87, 88].

A biaxial failure envelope was developed based on the Tsai-Hill failure criterion using the AF model. Due to the plane stress assumption, the role of the inter-laminar junctions was not explored (i.e. delamination) and only loading in the axial and circumferential directions was investigated. This failure model also did not take into account the different types of damage mechanisms evident in the AF; the model was indicative of a single, catastrophic, injury event. While these assumptions may not hold at failure stresses and strains, the goal was not to provide a validated constitutive model, instead to give insights into an injury model of the AF. The addition of a more complex AF behavior could be added in future analyses to create a more robust annular failure model: for example, three-dimensional geometry, non-linearly elastic behavior, complex fiber angle structure (fiber angle does not stay constant during loading [14, 68].

A complete failure model of the AF would be beneficial in prediction of catastrophic loadings that could lead disc herniation. Lumbar IVD herniation can cause severe symptoms such as pain, numbness, tingling or weakness in the lower extremities and repair of the herniation can require surgical intervention (discectomy), and physical therapy. Having a better understanding of the failure properties of the AF can lead to determination of the loading configurations that will result in this catastrophic injury depending on the health of the IVD. There has been a lot of work in techniques to

determine degenerative grade of a disc from an MRI [97-99, 103, 121, 246]; a failure model of the AF based on degenerative grade could lead to a clinician putting limitations on activities that would cause IVD loading that would exceed the failure loading based on the health of the IVD. Such a model could be created using computation techniques that incorporate the use of interface elements to integrate the deformation between lamina [238-242] and the nonlinear behavior of the lamina [144, 155, 214, 233, 236], and be subjected to physiologically relevant loading to mimic daily activities [63, 102].

7.2. Novel Contributions

- Characterization of the annular properties was experimentally determined for failure stress, failure strain, elastic moduli and Poisson's ratio.
- The role of collagen, elastin, and proteoglycan was investigated in both the lamina and laminate mechanics of the annulus fibrosus.
- Collagen fibers play an important role in the tensile strength of the annulus on both a laminar (longitudinal, transverse) and laminate (circumferential, radial) level.
- Elastin fibers play an important role in the tensile strength of the annulus on both a laminar (longitudinal, transverse) and laminate (circumferential, radial) level.
- Elastin fibers aid in deformation of the annulus in the out-of-plane (transverse, radial) testing directions .
- Proteoglycan matrix is more dominant in laminar (longitudinal, transverse) mechanics than laminate (circumferential, radial).
- Using classical lamination theory, an angle ply symmetric laminate was developed to model the AF.

- Shear strength of modeled annular lamina was calculated using classical lamination theory.
- Biaxial failure envelopes were developed for an annular model.

7.3. Future Work and Recommendations

Experimentally Determined Shear Modulus and Shear Strength

Our work showed that there is need for an experimentally determined value of shear modulus and shear strength for a single layer of the annulus fibrosus. In the literature, techniques for determination of the shear modulus of the laminated AF (axial-circumferential coordinate system) are discussed [87, 88], these can be expanded for use on the laminar level. An experimentally determined value for shear modulus (G_{12}) and shear strength (S) are needed to further the annular model.

Validation of Annular Model through Biaxial Testing

Experimental biaxial testing of the AF in the circumferential/axial orientation to failure would allow for validation of our proposed annular model. Using a predetermined failure criterion (for example, Tsai-Hill as used in previous aims), the value for shear strength can be calculated from the fit of the model and compared to an experimental value. Different composite failure criterion can be compared to the experimental values to determine the best technique.

Characterization Micromechanics of Degenerated Annulus Fibrosus

The enzymatic digestion technique allows for investigations into the role individual macromolecules play in annular mechanics. With the current technique,

digestion of multiple macromolecules is not possible to do the differences in activating buffers (including pH) for the different enzymes. A serial digestion technique could be designed in order to investigate the coupling of macromolecule removal – for example, treat with both collagenase and elastase and experimentally determine mechanical properties. Quantifying the amount of collagen, elastin and proteoglycan removed from the sample due to enzymatic digestion by using either FTIR analysis [247] or biochemical assays [248-252] can lead to developing a digestion model to mimic degeneration. In this thesis work, we have characterized the lamina mechanical and failure properties for normal and severely digested annular samples. The enzymatically digested samples represent extreme degeneration of singular macromolecules. Upon determining the biochemical makeup of different grades of degenerated AF, the current enzymatic digestion protocol could be modified, either time or concentration, in order to properly mimic a degenerated annular sample. However, to determine the mechanics of degenerative annular samples, the digested technique is not necessary when access to degenerated annular samples is available.

We propose obtaining sample from known degenerative grades of IVDs, with enough samples to populate an experiment for all 5 degenerative grades (for example, n=6 grade 1 single layer, n = 6 grade 1 inter-laminar samples, n=6 grade 2 single layer etc). The micromechanical testing technique can be used in order to create a database of properties for a wide range of degenerative grades. We hypothesize that the degenerative grades will be statistically significant from each other. This database of experimentally determined properties (E_1, E_2, ν_{12}, ν_{21}, G_{12}) for the four orientations (longitudinal, transverse, circumferential, and radial) would allow for input into various failure models

leading to determination of loading conditions that would cause catastrophic failure of an annular model depending on level of degeneration.

Creation of Three-dimensional Computational Annular Model for Catastrophic Injury

Using the previously discussed composite techniques, our annular model is limited to the axial-circumferential plane. Computational techniques would allow our model to be expanded to three-dimensions. We propose modeling the AF as a laminated angle-ply composited, allowing the lamina to initially have orthotropic, linearly elastic material properties. There is composite literature in which interface elements are used in order to allow movement between lamina [111, 114, 117-120, 122, 238]. We recommend using these interface elements between the lamina in order to remove the limitation of perfectly bonded lamina. The interface elements properties are not able to be experimentally determined, however we have experimental data for how the annular laminate as a whole should behave (from the circumferential and radial data). The laminate behavior can be fit to our experimental data to determine the mechanical properties of the interface elements. These interface areas could also be modeled as elements with adjustable friction coefficients in order to fit the experimental data.

The simplified modeled described, can be expanded to include the non-linearly elastic behavior of the annulus. After a validated model of the AF is computationally created, the stress concentrations due to various loading conditions can be investigated. The lamina properties can also be adjusted to account for degeneration and the changes in stress distributions explored.

This model would treat the annular lamina as homogenous materials with known properties in the global coordinate system (by transforming the principle material directions by some angle, θ). Incorporation of a failure criterion into the model would allow for investigations into loading conditions that would cause catastrophic injury to the disc. For example, it could be determined what compressive loading on the IVD would cause the AF to rupture (possibly leading to herniation) in a person with grade 4 IVD. An understanding of these failure loads subjected to the IVD could lead to clinical advisement on limitations of activities that would cause these failure loads. For instance, patients can be directed not to lift anything over a weight of *X* pounds – this *X* pounds, combined with the patient's body mass would put an IVD into compression with the AF feeling tensile loads greater a fracture criterion allows.

Creation of Three-dimensional Computational Annular Model for Degenerative Injury

The previous future work discussed, modeled the AF with homogenous lamina thus leading to an injury model. However, clinically, AF tears are evident prior to disc herniation and it is hypothesized that these annular tears will coalesce over time and eventually lead to a herniation [149, 150]. The creation of a three-dimensional computational model that represented the annular lamina as a homogenous matrix with embedded fibers would allow for investigation into annular tears [226, 253]. The current limitations of a model like this are determining values for the material and failure properties of the fibers and matrix, and the fiber volume fraction. These values could be determined experimentally through uniaxial testing and imaging techniques to determine fiber volume fraction. An alternate technique could be to use the properties of collagen

fibrils as the fiber element properties and then determine the matrix properties and fiber volume fraction to the experimental single layer data. A simplified model could have perfectly bond the fibers and matrix, then expanding to allow slip between the fibers and matrix, similar to what happens *in vivo*.

Having a validated three-dimensional fiber reinforced annular model would allow for investigations into the changes in stress concentrations when annular defects are created. For example, a small tear could be integrated within a single layer of the AF model parallel to the collagen fibers, through the matrix (Figure 7.1A) and the stress distributions explored in various loading conditions; other tear inclusions could include (Figure 7.1): fiber breakage (one fiber, multiple), tear perpendicular to the collagen fibers, tear between fiber/matrix interface, and delamination between two lamina.

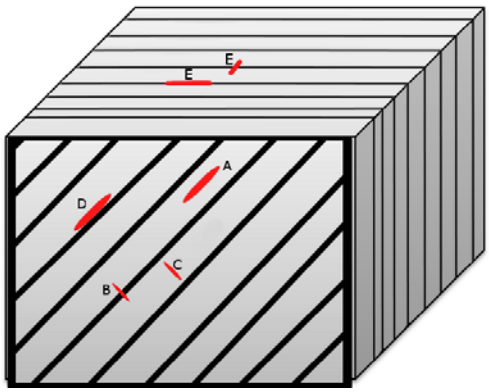

Figure 7.1: Representation of three-dimensional fiber reinforced annular composite. Types of annular tears are depicted in red: A) matrix tear, parallel to fibers B) fiber tear C) matrix tear, perpendicular to fibers D) fiber/matrix interface tear E) delamination.

It would be beneficial to include a failure criterion to the model. After the additional of any type of annular defect (tear), determine in different loading conditions where the locations of highest stress would be next and would exceed the failure strengths. This would allow for a model that could propagate tears in the AF. Investigations into how annular tears are able to coalesce and lead to a catastrophic injury

would greatly aid in clinical settings. Annular tears are able to be seen on MRI [17, 150, 254], understanding that certain types of annular tears are more likely to herniation, could lead to clinicians directing the patients to limited activity or alternate preventative actions.

Macromolecule Degeneration is responsible for Annular Tear Type

There has been previous work experimentally generating disc herniation in IVDs under compressive and bending loading [118, 120, 255]. However, there has been no direct link to the type of herniation or tear observed (radial, circumferential, rim lesion) and the loading protocol. We have shown on the laminar level the effect the digestive enzymes have on the failure properties of the AF. We hypothesize that the macromolecular breakdown of the tissue is the driving force behind the type of injury.

We propose soaking dissected anterior column units (vertebra-disc-vertebra, removal of posterior elements) in digestive enzymes (as the enzyme diffuses in toward the NP, the AF tissues will be digested) and subjecting them to herniation inducing loading protocols. We expect that different types of tears will occur depending on the digestive enzyme used. This could be further expanded, to explore the differences in annular tearing due to degenerative grade of the tissue.

APPENDIX A: LabVIEW Programs

Custom software programs were written using the LabView (National Instruments Corporation, Austin, TX) in order to record the load and have a webcam take an image every second during a uniaxial tensile test. The main program included a webcam subroutine which allowed for the user view the image and adjust the size and adjust the image contrast. The images were captured in color, and the user allowed to adjust the intensity, red, green, or blue coloring (240 x 320 pixel). Please refer to Figure 0.1 and Figure 0.2 for the block diagram and front panel of the webcam program.

The acquisition program (Figure 0.3) received and recorded the voltage (changed to force) output data from the load cell into a .csv file. It also allowed the user to specify the sampling rate for both the force and the image data. All force data was saved to a user specified folder and named in successive test number. For example, the first experiment run after the program was opened would be named ‘Test 1,’ the next ‘Test 2,’ and so on. This numbering would restart from one either when a new folder was specified or when the program was restarted. The images were also saved in a similar manner. Each image was saved into a large text file, each row containing one image’s data: intensity, and R, G, B coloring for each pixel. At the end of each test, the file will have columns representing the pixel information, and the number of rows corresponding to the number of images taken. The user saw a plot of the force on the front panel over the time of the test (Measurement, Figure 0.4). Also on the front panel, the user saw the image directly from the webcam, and when the program was not in use, a default image of a watch was shown. Within the LavView program, Matlab was opened and a program written in order to change the image to black and white. This new image was shown on the front panel

(intensity graph, Figure 0.4). An attempt was also made to calculate the displacement values directly from the images here (Dist, Figure 0.4). This was attempted by measuring the distance length of the white (negative) space in the black and white converted image. This proved to be unsuccessful, and displacement measurement was done as a posttest analysis, described in Appendix B: Matlab Programs (Page 214).

The final program written was the image program (Figure 0.5), which allowed the text image file recorded from the acquisition program to be read. The user would input the path of the folder where the image text file from the acquisition program was located (Figure 0.6), along with the name. The program would read the text file, line by line and reconstruct the image based on the information for the intensity and coloring of each pixel. After reconstruction each image would be saved as a .png (portable network graphic) file into the same folder. Images would be named in successive, ie 1.png, 2.png, etc. As the program was reconstituting each image, the user would see the image on the front panel Figure 0.6.

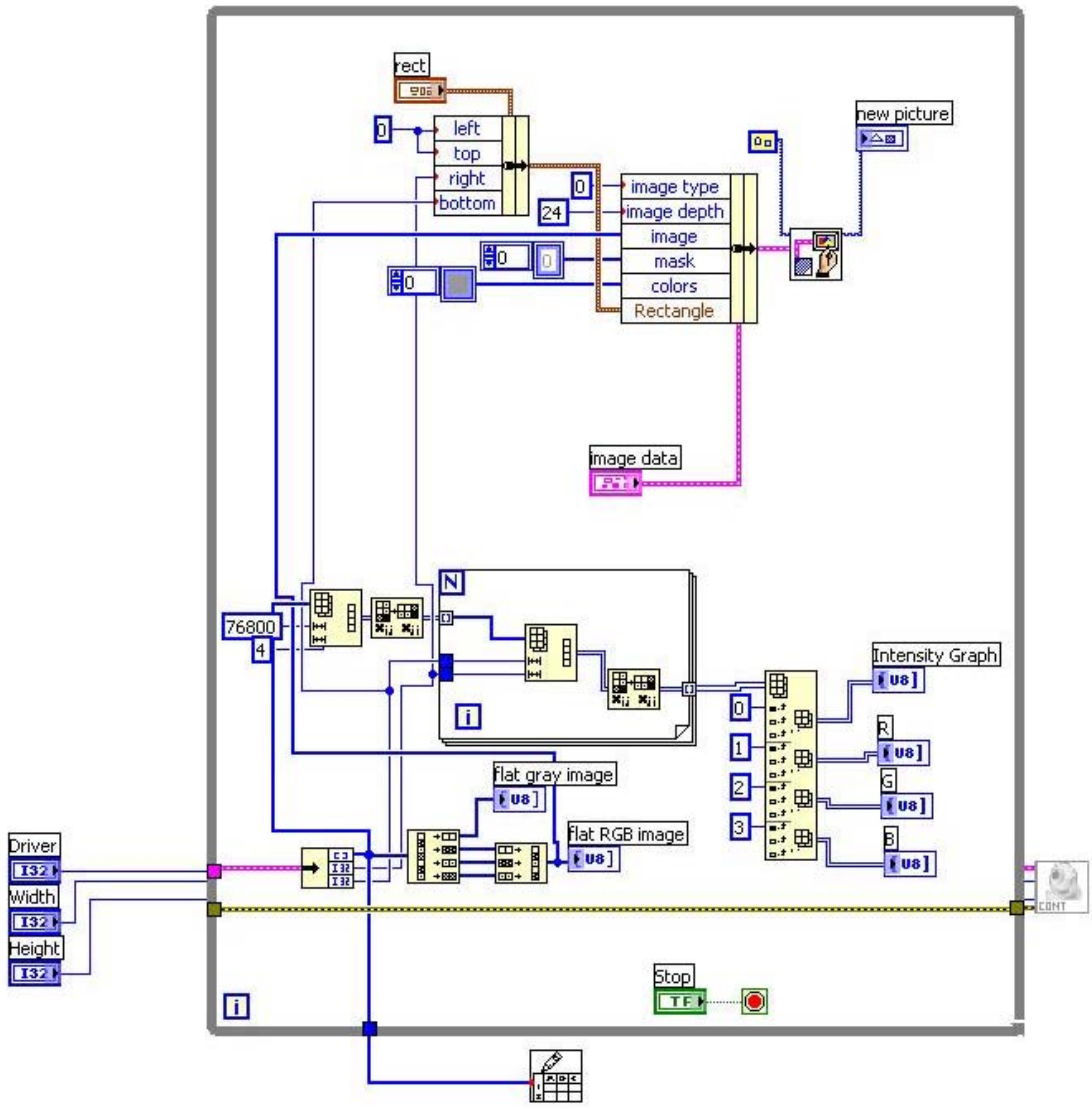

Figure 0.1: Block diagram of webcam LabView program. Allows user to adjust the image properties prior to data acquisition.

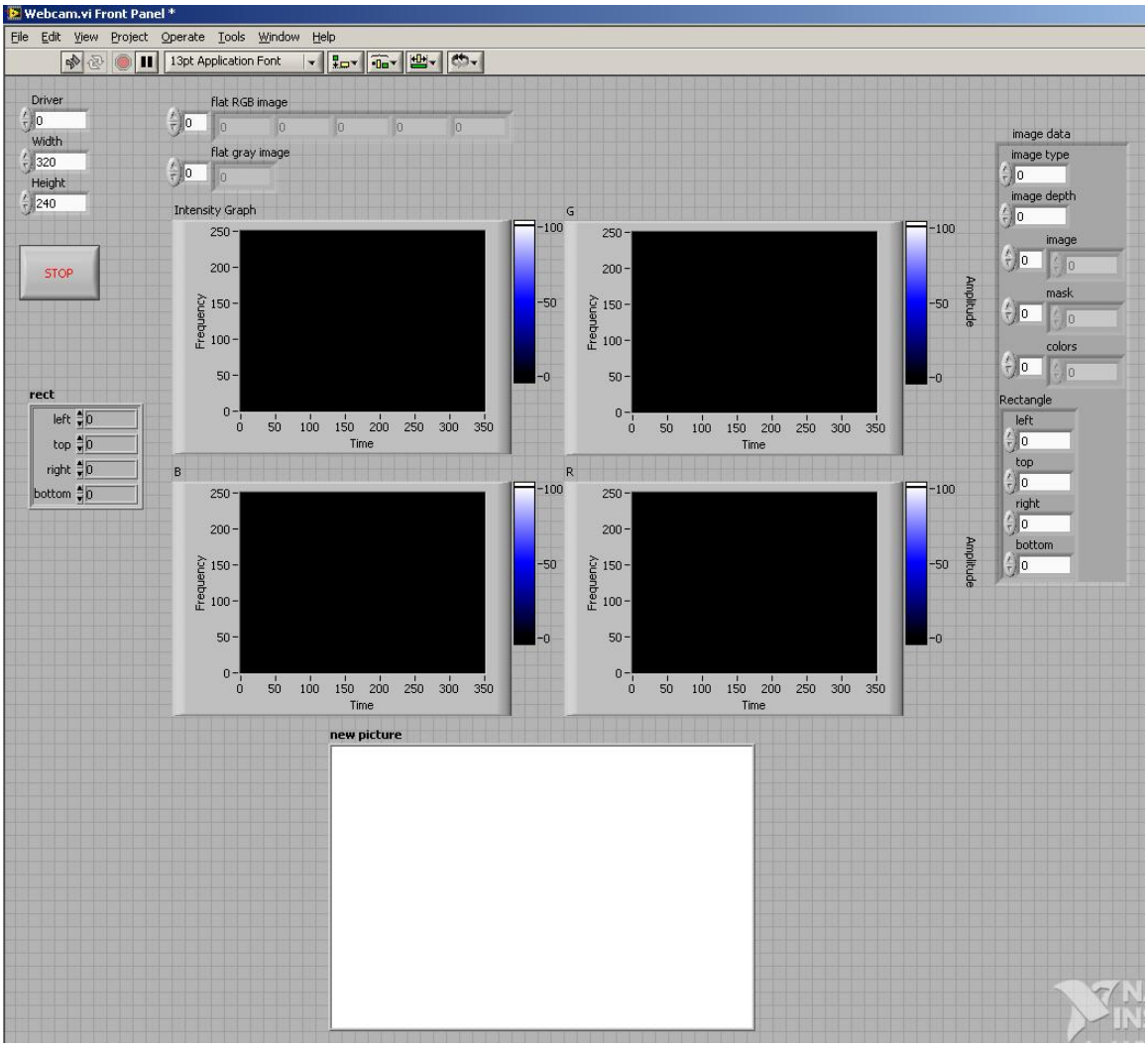

Figure 0.2: Front panel of webcam LabView program.

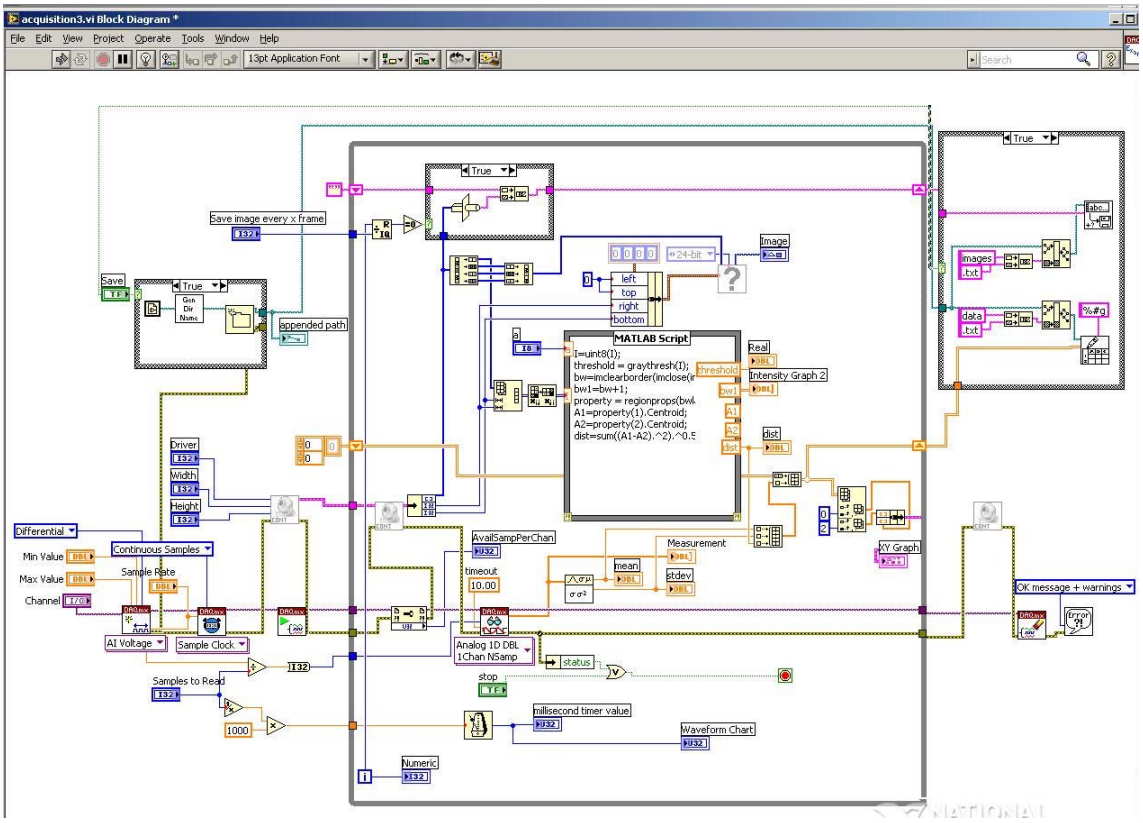

Figure 0.3 Block diagram of the acquisition LabView program.

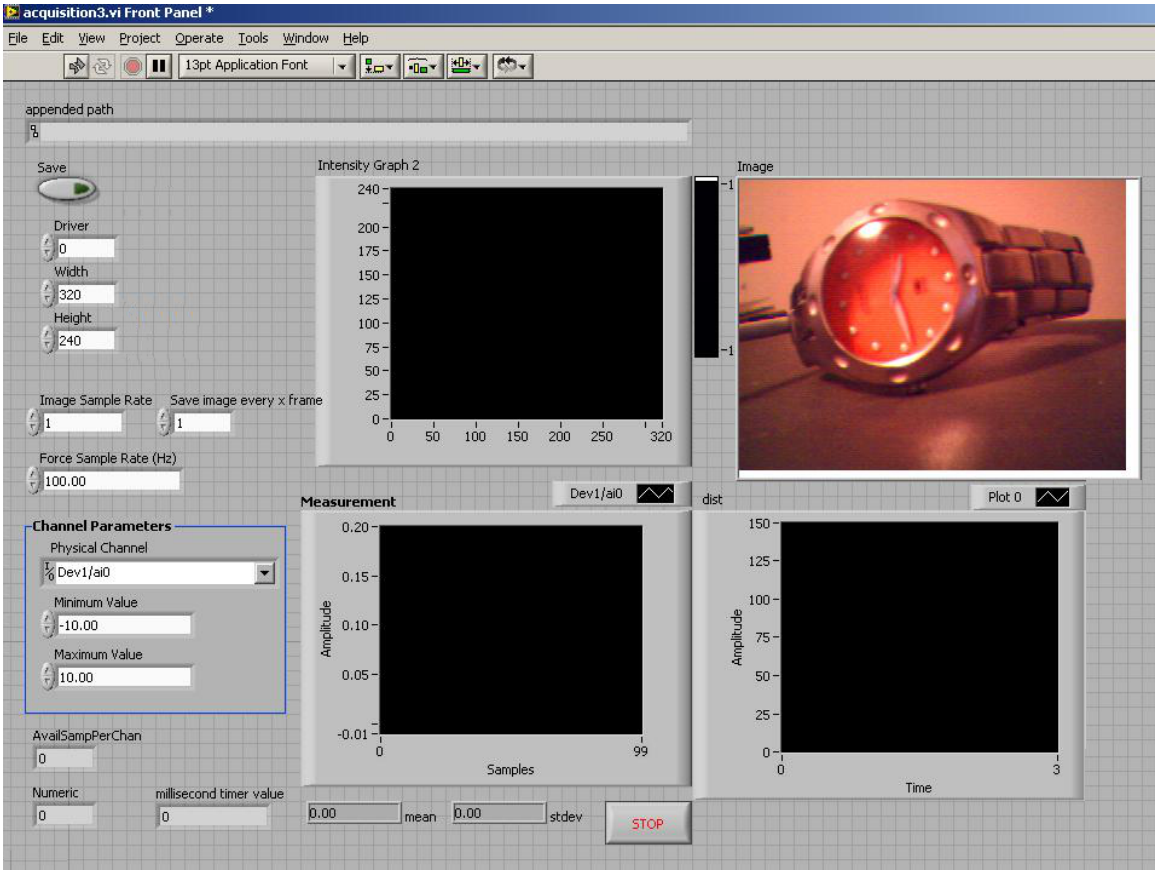

Figure 0.4: Front panel of data acquisition LabView program.

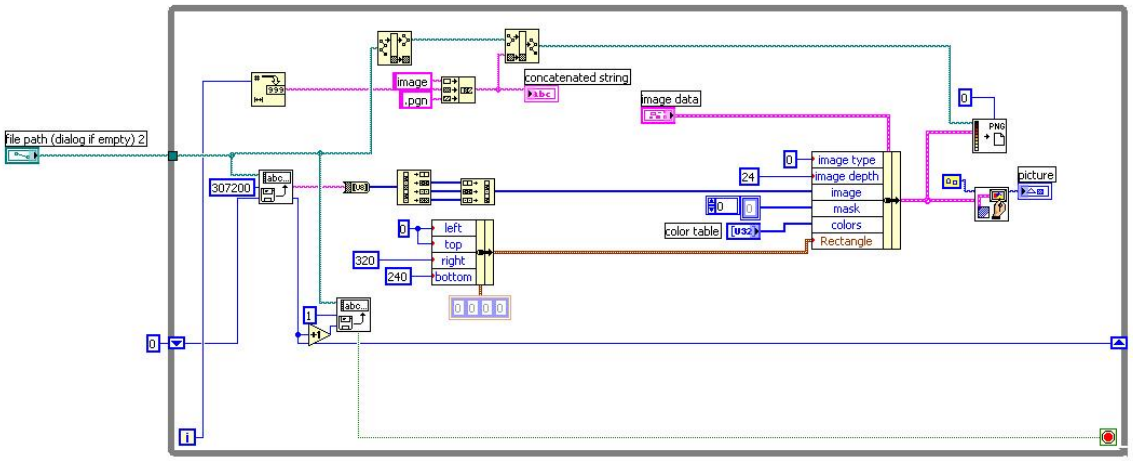

Figure 0.5: Block diagram of the image LabView program.

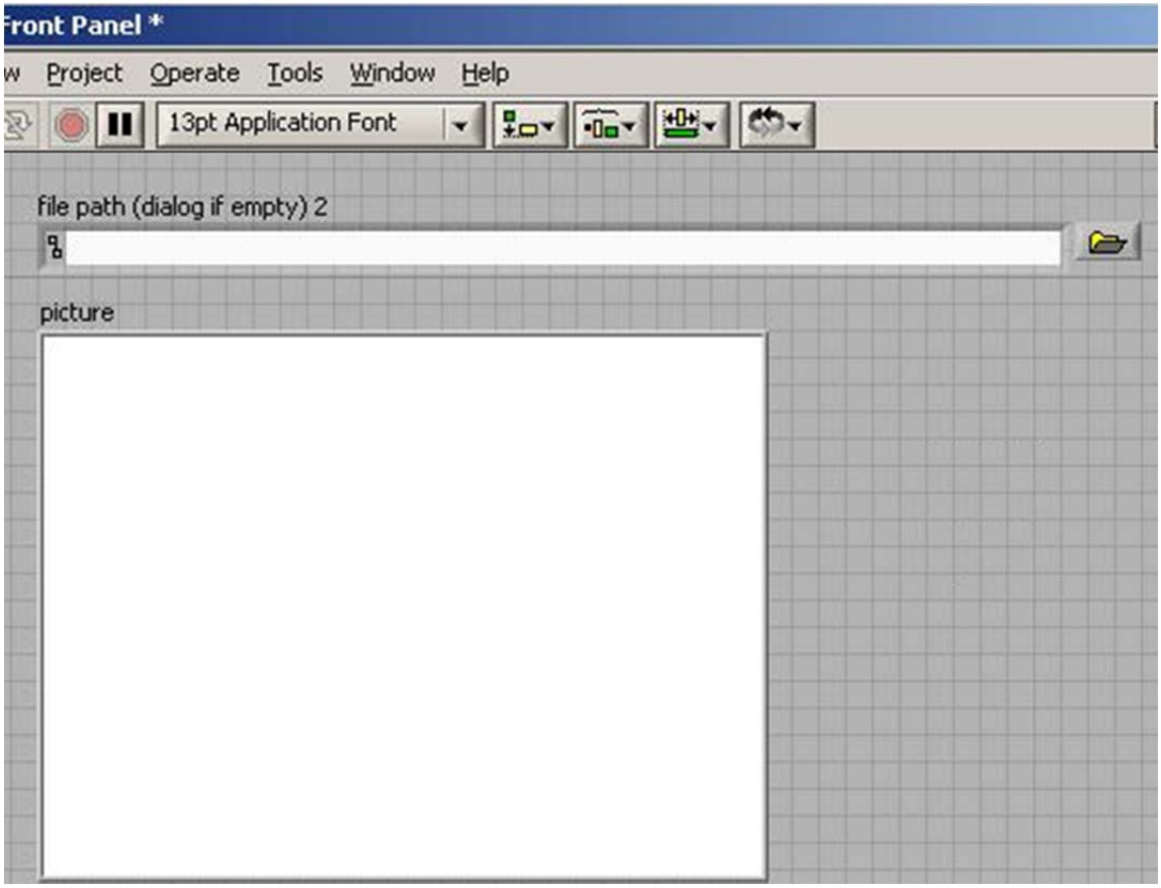

Figure 0.6: Front panel of image acquisition LabView program.

APPENDIX B: Matlab Programs

A series of Matlab (The MathWorks, Inc., Natick, Massachusetts) programs were written in order to analyze the sample images. All programs would convert the color images into black and white binary images. This would allow each pixel of the image to be represented by either one (white) or zero (black). The height of the image was measured from the first image 1 by averaging the averaging the sum of the columns of pixel data. The columns that are completely taken up by the grips will have a sum of zero (all black), and these values are disregarded). The columns with values are the sum of the negative (white) space; however we want the height of the sample. So the difference from the known 240 pixel height was taken for each column, giving the height in pixels of the sample in that column of the image. These were averaged and converted into mm; Preliminary studies showed that 0.0355 mm/pixels for the zoom setting on our microscope used to take images. The program was then readjusted (Program 1) to allow the user to input the locations of the columns in order to determine the height at different locations. This was changed to account for computer speed. The standard deviation of the average of heights was determine and evaluated to determine proper placement.

A similar displacement program was written (Program 2). Once the images were converted to binary, the sum of the rows were taken were taken at three locations along the top and three along the bottom grips of the samples. Since every white pixel is given a one in binary, this summation would give us the width, in pixels, between the samples (the sample width). These widths were averaged from all six locations and the standard deviation found. If the standard deviation was too large (greater than 10 pixels), then the

placement of the locations was changed; this occasionally happened due to the sample not being centered in the frame.

A final program combined the two previously explained and measured both the height and width of each sample. This was done so that both the height contraction and width expansion could be determined from the positions in order to calculate Poisson's ratio (Program 3).

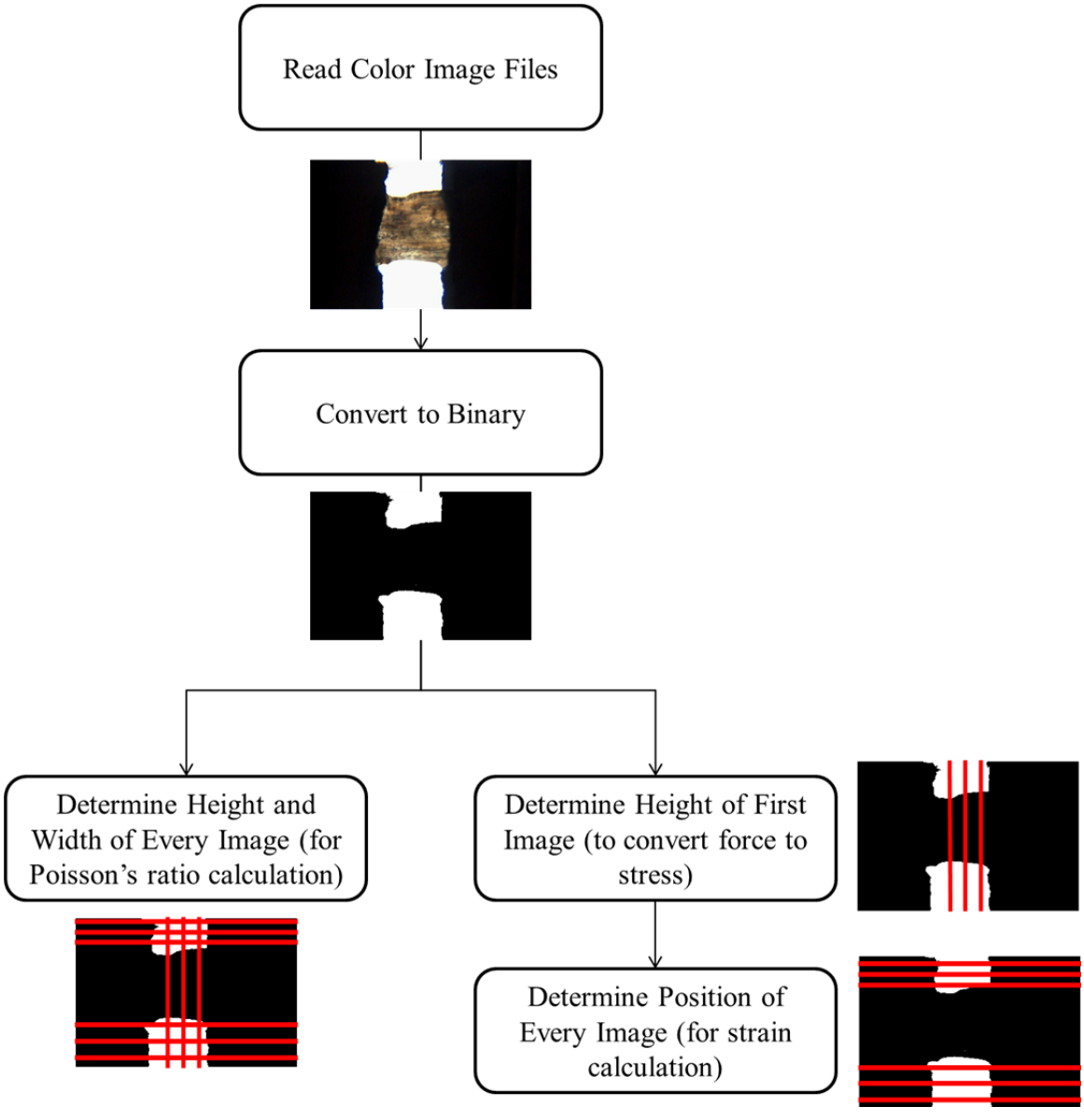

Figure 0.1: Flow chart of Matlab Programs to get position of samples from images, leading to determination of strain.

Program 1: Matlab Program to determine sample height

```
%Created by: Jessica L Isaacs
%This m-file calculates height in mm of a sample
clear
clc
cd('C:\Documents and Settings\...') % change cd to the path of the test
sequence that you want to analyze.
A = imread('image1.png');
bw = im2bw(A,0.94); %can change threshold
L1 = sum(bw(:,160)); %change column location in order to be over
various width locations of sample
L2 = sum(bw(:,170));%change column location in order to be over various
width locations of sample
L3 = sum(bw(:,180)); %change column location in order to be over
various width locations of sample
L4 = sum(bw(:,190)); %change column location in order to be over
various width locations of sample
L = [L1 L2 L3 L4];
Avg = sum(L)/4;
SD = std(L)
s=size(bw);
htpix=s(1)-Avg;
htmm = (1/0.0355)*htpix
```

Program 2: Matlab Program to determine sample displacement

```
%Created by: Jessica L Isaacs
%This m-file calculates the pixel position of the top and bottom grips
of images from the microtensile tester. Must change the path and the
top/bottom crop as well as the black/white threshold for each image
group.
clc
clear

% change cd to the path of the test sequence that you want to analyze.
cd('INSERT FILE LOCATION OF IMAGES HERE')

%This section crops the image to where you want the displacement taken;
at the top and then bottom grips.
topcrop1=10;
topcrop2=20;
topcrop3=30;
bottomcrop1=230;
bottomcrop2=220;
bottomcrop3=210;


bwthresh=0.8; %Change depending on image

Position=zeros(1000,1); %Allows for up to 1000 images

files = dir('image*.png');
for k = 1:numel(files)
    rgb = imread(files(k).name);
    bw=im2bw(rgb,bwthresh);
    Top1 = bw(topcrop1,:);
    Top2 = bw(topcrop2,:);
    Top3 = bw(topcrop3,:);
    Bottom1 = bw(bottomcrop1,:);
    Bottom2 = bw(bottomcrop2,:);
    Bottom3 = bw(bottomcrop3,:);
    A1=sum(Top1);
    A2=sum(Top2);
    A3=sum(Top3);
    B1=sum(Bottom1);
    B2=sum(Bottom2);
    B3=sum(Bottom3);
    Pos=(A1+A2+A3+B1+B2+B3)/6
    Position(k)=Pos;
end
```

Program 3: Matlab Program to determine sample Poisson's ratio

```
%Created by: Jessica L Isaacs
%This m-file calculates the height and width of each sample in order
for calculation of Poisson's ratio

clc
clear

%change cd to the path of the test sequence that you want to analyze.
cd('INSERT FILE LOCATION OF IMAGES HERE')

%This section crops the image to where you want the displacement taken.
topcrop1=10;
topcrop2=20;
topcrop3=30;
bottomcrop1=230;
bottomcrop2=220;
bottomcrop3=210;
midcrop1=160;
midcrop2=170;
midcrop3=180;
midcrop4=170;

bwthresh=0.85; %Change depending on image

Height=zeros(1000,2);  %Allows for up to 1000 images
Width=zeros(1000,2);

files = dir('image*.png');

for k = 1:numel(files)
    rgb = imread(files(k).name);
    bw=im2bw(rgb,bwthresh);
    wb=imcomplement(bw);
    Top1 = bw(topcrop1,:);
    Top2 = bw(topcrop2,:);
    Top3 = bw(topcrop3,:);
    Bottom1 = bw(bottomcrop1,:);
    Bottom2 = bw(bottomcrop2,:);
    Bottom3 = bw(bottomcrop3,:);
    Height1 = wb(:,midcrop1);
    Height2 = wb(:,midcrop2);
    Height3 = wb(:,midcrop3);
    Height4 = wb(:,midcrop4);
    Width(k,1) = (Top1+Top2+Top3+Bottom1+Bottom2+Bottom3)/6;
    Height(k,1) = (Height1+Height2+Height3+Height4)/4;
    Width(k,2) = STD(Width);
    HeightSD(k,2) = STD(Height);
end
```

APPENDIX C: Raw Data

Table 0.1: Raw Data for intralaminar control specimens for chapter 4.

	ε_F	σ_F	$E_{25\varepsilon F\%}$	$E_{50\cdot\varepsilon F\%}$	$E_{75\varepsilon F\%}$	ν
		[MPa]	[MPa]	[MPa]	[MPa]	
Longitudinal	0.137	1.890	12.015	16.533	16.856	0.552
	0.200	2.537	18.069	17.150	9.276	0.688
	0.071	1.200	11.969	19.475	20.792	0.357
	0.245	1.762	4.522	10.154	11.341	0.467
	0.265	1.676	9.569	15.448	10.466	0.402
	0.202	3.792	8.226	22.472	31.124	0.364
	0.240	2.767	4.434	12.448	19.495	0.500
	0.197	1.897	8.428	12.926	10.765	0.342
	0.175	2.699	9.136	18.459	12.133	0.208
	0.188	3.483	10.299	18.020	19.287	0.487
AVG	**0.192**	**2.370**	**9.667**	**16.309**	**16.153**	**0.437**
SD	*0.018*	*0.263*	*1.245*	*1.161*	*2.148*	*0.042*
Transverse	0.275	0.395	1.502	2.029	1.558	0.058
	0.211	0.173	0.603	1.228	1.038	0.075
	0.273	0.395	1.658	1.824	1.177	0.135
	0.302	0.389	1.171	1.212	1.303	0.110
	0.228	0.137	0.711	0.392	0.239	0.151
	0.184	0.423	2.201	2.682	2.382	0.127
	0.406	0.248	0.816	0.556	0.240	0.098
	0.120	0.387	1.501	3.740	5.174	0.130
	0.169	0.359	1.929	2.401	2.462	0.074
	0.205	0.419	1.728	3.063	2.934	0.012
AVG	**0.237**	**0.333**	**1.382**	**1.913**	**1.851**	**0.097**
SD	*0.025*	*0.034*	*0.171*	*0.344*	*0.466*	*0.013*

Table 0.2: Raw Data for interlaminar control specimens for chapter 4.

Orientation	ε_F	σ_F [MPa]	$E_{25\varepsilon F\%}$ [MPa]	$E_{50\cdot\varepsilon F\%}$ [MPa]	$E_{75\varepsilon F\%}$ [MPa]	ν
Circumferential	0.191	1.259	9.359	9.122	4.471	0.364
	0.131	0.920	8.256	10.173	6.675	0.358
	0.172	1.511	7.634	9.318	10.403	0.527
	0.121	1.828	15.065	21.033	17.504	0.402
	0.084	1.397	15.028	21.875	20.535	0.420
	0.211	0.608	2.175	3.121	3.749	0.384
	0.316	0.594	1.771	2.445	13.457	0.409
	0.179	3.445	18.374	19.638	19.025	0.358
	0.236	0.702	3.355	4.024	2.712	0.533
	0.107	0.476	2.207	4.452	6.685	0.682
AVG	**0.175**	**1.274**	**8.322**	**10.520**	**10.522**	**0.444**
SD	*0.022*	*0.281*	*1.932*	*2.415*	*2.116*	*0.036*
Radial	0.293	0.207	0.314	0.857	0.814	0.125
	0.145	0.287	0.837	1.748	2.333	0.171
	0.295	0.487	1.708	1.840	1.488	0.142
	0.469	0.302	0.565	0.756	0.720	0.153
	0.219	0.301	0.966	1.223	1.726	0.138
	0.178	0.413	0.677	1.659	3.287	0.128
	0.593	0.632	0.924	1.205	1.202	0.200
	0.492	0.447	0.924	1.135	0.897	0.203
	0.439	1.013	2.575	2.433	2.050	0.171
	0.367	0.968	2.604	3.172	3.041	0.157
AVG	**0.349**	**0.506**	**1.209**	**1.603**	**1.756**	**0.159**
SD	*0.047*	*0.089*	*0.257*	*0.236*	*0.289*	*0.009*

Table 0.3: Raw Data for longitudinal digested specimens in chapter 5

Digestion	ε_F	σ_F	E_{TOE}	E_{LIN}	ν
		[MPa]	[MPa]	[MPa]	
COL	0.418	0.261	0.312	0.745	0.242
	0.228	0.546	0.548	4.142	0.219
	0.286	0.222	0.499	1.261	0.343
	0.500	0.259	0.101	0.602	0.332
	0.529	0.175	0.508	1.049	0.491
	0.320	0.418	0.244	2.143	0.340
	0.203	0.265	0.133	2.817	0.418
	0.238	0.729	0.516	5.216	0.481
	0.290	0.943	0.515	5.299	0.322
	0.202	0.973	0.432	1.220	0.401
AVG	**0.313**	**0.433**	**0.366**	**2.582**	**0.353**
SD	*0.033*	*0.085*	*0.082*	*0.551*	*0.026*
ELA	0.171	0.337	0.552	1.995	0.692
	0.194	0.337	0.843	2.136	0.215
	0.196	1.278	3.754	9.123	0.182
	0.181	0.572	1.583	3.784	0.394
	0.320	1.556	2.271	9.442	0.303
	0.299	1.496	2.762	8.104	0.449
	0.132	0.353	2.385	4.675	0.515
	0.122	0.684	3.868	7.690	0.559
	0.101	0.394	1.877	6.131	0.462
	0.182	0.707	2.830	6.207	0.443
AVG	**0.195**	**0.761**	**2.102**	**5.526**	**0.419**
SD	*0.022*	*0.128*	*0.310*	*0.761*	*0.055*
PG	0.207	0.400	0.826	2.816	0.385
	0.151	0.496	4.026	6.370	0.418
	0.251	0.850	0.918	5.544	0.340
	0.278	0.271	0.812	1.856	0.264
	0.109	0.269	1.312	4.183	0.419
	0.101	0.381	1.858	3.125	0.229
	0.410	1.125	2.165	4.017	0.368
	0.194	2.021	3.911	13.913	0.334
	0.281	2.101	2.203	9.115	0.229
	0.090	0.843	5.976	14.276	0.305
AVG	**0.207**	**0.876**	**2.801**	**6.522**	**0.332**
SD	*0.032*	*0.217*	*0.767*	*1.419*	*0.025*

Table 0.4: Raw Data for transverse digested specimens in chapter 5

Digestion	ε_F	σ_F	E_{TOE}	E_{LIN}
		[MPa]	[MPa]	[MPa]
COL	0.671	0.016	0.030	0.021
	0.538	0.088	0.043	0.131
	0.426	0.665	0.504	3.752
	0.415	0.280	0.582	2.164
	0.435	0.126	0.192	0.615
	0.438	0.049	0.111	0.238
	0.479	0.018	0.023	0.106
AVG	**0.455**	**0.178**	**0.212**	**1.004**
SD	*0.035*	*0.088*	*0.075*	*0.607*
ELA	0.042	0.039	0.016	0.054
	0.130	0.103	0.082	0.141
	0.195	0.099	0.078	0.391
	0.055	0.140	0.059	0.404
	0.203	0.215	0.137	0.775
	0.176	0.133	0.004	0.495
	0.075	0.096	0.139	0.235
AVG	**0.125**	**0.119**	**0.075**	**0.353**
SD	*0.034*	*0.029*	*0.020*	*0.126*
PG	0.228	0.243	0.572	1.101
	0.309	0.487	0.782	1.491
	0.268	0.580	0.440	1.811
	0.239	0.138	0.054	0.831
	0.244	0.149	0.228	0.582
	0.448	0.413	0.155	1.073
	0.539	0.378	0.101	0.658
AVG	**0.323**	**0.332**	**0.336**	**1.060**
SD	*0.040*	*0.056*	*0.089*	*0.147*

Table 0.5: Raw Data for circumferential digested specimens in chapter 5

Digestion	ε_F	σ_F [MPa]	E_{TOE} [MPa]	E_{LIN} [MPa]
COL	0.249	0.988	2.260	5.968
	0.164	0.723	3.292	6.065
	0.179	1.199	2.462	10.124
	0.165	1.015	2.914	8.378
	0.127	0.701	2.957	7.463
	0.129	1.233	3.858	12.476
	0.080	0.410	2.317	6.112
	0.186	0.899	1.482	5.475
	0.151	0.325	1.426	2.576
	0.163	0.854	1.946	6.660
AVG	**0.154**	**0.773**	**2.364**	**6.664**
SD	*0.013*	*0.091*	*0.227*	*0.804*
ELA	0.274	0.675	0.856	3.969
	0.164	0.584	1.378	5.791
	0.183	0.582	1.223	6.868
	0.207	0.682	2.051	10.130
	0.194	1.575	1.356	3.322
	0.203	0.564	1.677	8.796
	0.126	0.863	1.213	2.934
	0.308	0.323	3.871	8.578
	0.155	0.942	1.828	6.754
	0.124	0.581	1.965	7.642
AVG	**0.194**	**0.744**	**1.717**	**6.349**
SD	*0.021*	*0.120*	*0.295*	*0.854*
PG	0.108	0.891	3.221	9.476
	0.116	1.498	5.476	16.561
	0.156	0.771	2.531	5.716
	0.123	0.361	1.001	4.786
	0.159	1.840	4.879	15.856
	0.088	1.528	6.630	18.703
	0.194	1.648	4.260	12.051
	0.088	0.875	4.786	13.564
	0.127	1.518	6.403	13.285
	0.155	1.721	4.686	14.019
AVG	**0.132**	**1.265**	**4.387**	**12.402**
SD	*0.011*	*0.157*	*0.548*	*1.434*

Table 0.6: Raw Data for circumferential digested specimens in chapter 5

Digestion	ε_F	σ_F [MPa]	E_{TOE} [MPa]	E_{LIN} [MPa]
COL	0.492	0.385	1.165	4.013
	0.559	0.208	0.499	1.139
	0.630	0.069	0.220	0.590
	0.545	0.269	1.111	1.281
	0.690	0.301	1.377	1.499
	0.666	0.446	0.498	2.209
	0.327	0.325	0.257	1.431
AVG	**0.559**	**0.286**	**0.732**	**1.737**
SD	*0.047*	*0.046*	*0.179*	*0.421*
ELA	0.248	0.237	0.297	2.224
	0.278	0.211	0.447	1.612
	0.298	0.503	0.303	3.481
	0.229	0.486	0.088	1.356
	0.263	0.317	0.152	1.802
	0.301	0.361	0.181	1.362
	0.345	0.197	0.269	0.959
AVG	**0.269**	**0.353**	**0.240**	**1.762**
SD	*0.012*	*0.050*	*0.052*	*0.363*
PG	0.560	0.194	0.439	0.266
	0.644	0.192	0.256	0.350
	0.797	0.594	0.331	1.022
	0.579	0.442	0.820	1.492
	0.306	0.315	0.706	2.779
	0.451	0.650	1.161	1.392
	0.274	1.096	2.057	4.500
AVG	**0.516**	**0.498**	**0.824**	**1.686**
SD	*0.070*	*0.121*	*0.237*	*0.567*

APPENDIX D: Calculation of Shear Strength

```
> restart
> with(linalg) : with(LinearAlgebra) : with(ArrayTools) : with(plots, implicitplot) :
> qb11 := q11·(cos(θ))^4 + 2·(q12 + 2·q66)·cos(θ)^2·sin(θ)^2 + q22
      ·sin(θ)^4 :
> qb12 := (q11 + q22 − 4·q66)·cos(θ)^2·sin(θ)^2 + q12·(cos(θ)^4
      + sin(θ)^4) :
> qb16 := -q22·cos(θ)·sin(θ)^3 + q11·cos(θ)^3·sin(θ) - (q12 + 2·q66)
      · cos(θ)·sin(θ)·(cos(θ)^2 - sin(θ)^2) :
> qb22 := q11·sin(θ)^4 + 2·(q12 + 2·q66)·cos(θ)^2·sin(θ)^2 + q22
      ·cos(θ)^4 :
> qb26 := -q22·sin(θ)·cos(θ)^3 + q11·sin(θ)^3·cos(θ) + (q12 + 2
      ·q66)· cos(θ)·sin(θ)·(cos(θ)^2 - sin(θ)^2) :
> qb66 := (q11 + q22 − 2·q12)·cos(θ)^2·sin(θ)^2 + q66
      ·(cos(θ)^2 - sin(θ)^2)^2 :
>
  Qbarplus60 := [[subs(theta = Pi/3, qb11), subs(theta = Pi/3, qb12),
      subs(theta = Pi/3, qb16)],
      [subs(theta = Pi/3, qb12), subs(theta = Pi/3, qb22), subs(theta
      = Pi/3, qb26)],
      [subs(theta = Pi/3, qb16), subs(theta = Pi/3, qb26), subs(theta
      = Pi/3, qb66)]] :
>
  Qbarminus60 := [[subs(theta = -Pi/3, qb11), subs(theta = -Pi/3, qb12
      ), subs(theta = -Pi/3, qb16)],
      [subs(theta = -Pi/3, qb12), subs(theta = -Pi/3, qb22), subs(theta =
      -Pi/3, qb26)],
      [subs(theta = -Pi/3, qb16), subs(theta = -Pi/3, qb26), subs(theta =
      -Pi/3, qb66)]] :
```

> $q11 := \frac{E_1}{1 - \nu_{12} \cdot \nu_{21}}$:

> $q22 := \frac{E_2}{1 - \nu_{12} \cdot \nu_{21}}$:

> $q12 := \frac{\nu_{12} \cdot E_2}{1 - \nu_{12} \cdot \nu_{21}}$:

> $q66 := G_{12}$:

> $E_1 := 16.15 : E_2 := 1.85 : \nu_{12} := 0.44 : \nu_{21} := 0.097$:

> $simplify(Qbarminus60)$

$$\left[\left[2.460253626 + 0.7500000000\, G_{12},\ 4.056898427 - 0.7500000000\, G_{12},\ -1.382734959 - 0.4330127020\, G_{12}\right],\ \left[4.056898427 - 0.7500000000\, G_{12},\ 9.929020602 + 0.7500000000\, G_{12},\ -5.085406978 + 0.4330127020\, G_{12}\right],\ \left[-1.382734959 - 0.4330127020\, G_{12},\ -5.085406978 + 0.4330127020\, G_{12},\ 3.206608031 + 0.2500000000\, G_{12}\right]\right]$$

> $simplify(Qbarplus60)$

$$\left[\left[2.460253626 + 0.7500000000\, G_{12},\ 4.056898427 - 0.7500000000\, G_{12},\ 1.382734959 + 0.4330127020\, G_{12}\right],\ \left[4.056898427 - 0.7500000000\, G_{12},\ 9.929020602 + 0.7500000000\, G_{12},\ 5.085406978 - 0.4330127020\, G_{12}\right],\ \left[1.382734959 + 0.4330127020\, G_{12},\ 5.085406978 - 0.4330127020\, G_{12},\ 3.206608031 + 0.2500000000\, G_{12}\right]\right]$$

> $A := \sum_{k=1}^{N} Q_k \cdot \left(h_k - h_{k-1}\right)$:

> $B := \frac{1}{2} \cdot \sum_{k=1}^{N} Q_k \cdot \left(\left(h_k\right)^2 - \left(h_{k-1}\right)^2\right)$:

> $d := \frac{1}{3} \cdot \sum_{k=1}^{N} Q_k \cdot \left(\left(h_k\right)^3 - \left(h_{k-1}\right)^3\right)$:

>
$h_0 := -9.5 \cdot t : h_1 := -8.5 \cdot t : h_2 := -7.5 \cdot t : h_3 := -6.5 \cdot t : h_4 := -5.5 \cdot t : h_5 := -4.5\, t : h_6 := -3.5 \cdot t : h_7 := -2.5 \cdot t : h_8 := -1.5 \cdot t : h_9 := -0.5 \cdot t : h_{10} := 0.5 \cdot t : h_{11} := 1.5 \cdot t : h_{12} := 2.5 \cdot t : h_{13} := 3.5 \cdot t : h_{14} := 4.5 \cdot t : h_{15} := 5.5 \cdot t : h_{16} := 6.5 \cdot t : h_{17} := 7.5 \cdot t : h_{18} := 8.5 \cdot t : h_{19} := 9.5 \cdot t$:

> $Q_1 := Qbarminus60 : Q_2 := Qbarplus60 : Q_3 := Qbarminus60 : Q_4 := Qbarplus60$:

$$Q_5 := Qbarminus60 : Q_6 := Qbarplus60 : Q_7 := Qbarminus60 : Q_8 := Qbarplus60 :$$

$$Q_9 := Qbarminus60 : Q_{10} := Qbarplus60 : Q_{11} := Qbarminus60 : Q_{12} := Qbarplus60 : Q_{13} := Qbarminus60 : Q_{14} := Qbarplus60 : Q_{15} := Qbarminus60 : Q_{16} := Qbarplus60 : Q_{17} := Qbarminus60 : Q_{18} := Qbarplus60 : Q_{19} := Qbarminus60 :$$

> $A := simplify(eval(subs(N = 19, A)))$

$$\left[\left[1.140000000\,10^{-7}\,t\left(4.10042271\,10^{8} + 1.25000000\,10^{8}\,G_{12}\right),\right.\right.$$
$$-1.900000000\,10^{-8}\,t\left(-4.056898427\,10^{9} + 7.50000000\,10^{8}\,G_{12}\right),$$
$$\left.-1.382734960\,t - 0.4330127020\,t\,G_{12}\right],$$
$$\left[-1.900000000\,10^{-8}\,t\left(-4.056898427\,10^{9}\right.\right.$$
$$\left.+ 7.50000000\,10^{8}\,G_{12}\right), 1.140000000\,10^{-7}\,t\left(1.654836767\,10^{9}$$
$$\left.+ 1.25000000\,10^{8}\,G_{12}\right), -5.085406983\,t + 0.4330127020\,t\,G_{12}\Big],$$
$$\left[-1.382734960\,t - 0.4330127020\,t\,G_{12}, -5.085406983\,t\right.$$
$$+ 0.4330127020\,t\,G_{12}, 1.900000000\,10^{-8}\,t\left(3.206608031\,10^{9}\right.$$
$$\left.\left.\left.+ 2.50000000\,10^{8}\,G_{12}\right)\right]\right]$$

> $B := simplify(eval(subs(N = 19, B)))$

$$\begin{bmatrix} 0. & 0. & 0. \\ 0. & 0. & 0. \\ 0. & 0. & 0. \end{bmatrix}$$

> $d := simplify(eval(subs(N = 19, d)))$

$$\left[\left[0.000003429500000\,t^3\left(4.10042271\,10^{8} + 1.25000000\,10^{8}\,G_{12}\right),\right.\right.$$
$$-5.715833333\,10^{-7}\,t^3\left(-4.056898427\,10^{9} + 7.50000000\,10^{8}\,G_{12}\right),$$
$$\left.-124.5613742\,t^3 - 39.00722755\,t^3\,G_{12}\right],$$
$$\left[-5.715833333\,10^{-7}\,t^3\left(-4.056898427\,10^{9}\right.\right.$$
$$\left.+ 7.50000000\,10^{8}\,G_{12}\right), 0.000003429500000\,t^3\left(1.654836767\,10^{9}\right.$$
$$\left.+ 1.25000000\,10^{8}\,G_{12}\right), -458.1104118\,t^3 + 39.00722755\,t^3\,G_{12}\Big],$$
$$\left[-124.5613742\,t^3 - 39.00722755\,t^3\,G_{12}, -458.1104118\,t^3\right.$$
$$+ 39.00722755\,t^3\,G_{12}, 5.715833333\,10^{-7}\,t^3\left(3.206608031\,10^{9}\right.$$
$$\left.\left.\left.+ 2.50000000\,10^{8}\,G_{12}\right)\right]\right]$$

> $t := 0.15 : ht := 19 \cdot t :$

> $Astar := MatrixInverse(A) - (-MatrixInverse(A).B).MatrixInverse(d - B.MatrixInverse(A).B).B.MatrixInverse(A) :$

```
> Bstar := -MatrixInverse(A).B.MatrixInverse(d - B.MatrixInverse(A).B) :
> Cstar := -MatrixInverse(d - B.MatrixInverse(A).B).B.MatrixInverse(A) :
> Dstar := MatrixInverse(d - B.MatrixInverse(A).B) :
>
```

$$Ep := Concatenate(1, Concatenate(2, Astar, Bstar), Concatenate(2, Bstar, Dstar)).\begin{bmatrix} Nx \\ Ny \\ Nxy \\ Mx \\ My \\ Mxy \end{bmatrix} :$$

```
> εx0 := Ep[1] : εy0 := Ep[2] : γxy0 := Ep[3] : Kx := Ep[4] : Ky := Ep[5] : Kxy := Ep[6] :
>
> Nx := 0 : Nxy := 0 : Mx := 0 : My := 0 : Mxy := 0 :
```

$$> \quad sigmaplus := simplify\left(Qbarplus60.\begin{bmatrix} \varepsilon x0 \\ \varepsilon y0 \\ \gamma xy0 \end{bmatrix} + \begin{bmatrix} Kx \\ Ky \\ Kxy \end{bmatrix}\right)$$

$$\left[\left[-\left(800.\left(5.368120980\,10^{9} + 3.259271060\,10^{9}\,G_{12} + 4.94226401\,10^{8}\,G_{12}^{2}\right)Ny\right)\Big/\left(-5.899374440\,10^{14} - 1.186335960\,10^{15}\,G_{12} - 8.874626174\,10^{13}\,G_{12}^{2} + 129.\,G_{12}^{3}\right)\right],\right.$$
$$\left[-\left(1.00000\,10^{5}\,Ny\left(2.227898466\,10^{9} + 4.195568338\,10^{9}\,G_{12} + 3.07436581\,10^{8}\,G_{12}^{2}\right)\right)\Big/\left(-5.899374440\,10^{14} - 1.186335960\,10^{15}\,G_{12} - 8.874626174\,10^{13}\,G_{12}^{2} + 129.\,G_{12}^{3}\right)\right],$$
$$\left.\left[-\left(20000.\,Ny\left(9.461126174\,10^{9} + 3.519163807\,10^{9}\,G_{12} + 2.16859724\,10^{8}\,G_{12}^{2}\right)\right)\Big/\left(-5.899374440\,10^{14} - 1.186335960\,10^{15}\,G_{12} - 8.874626174\,10^{13}\,G_{12}^{2} + 129.\,G_{12}^{3}\right)\right]\right]$$

$$> \quad sigmaminus := simplify\left(Qbarminus60.\begin{bmatrix} \varepsilon x0 \\ \varepsilon y0 \\ \gamma xy0 \end{bmatrix} + \begin{bmatrix} Kx \\ Ky \\ Kxy \end{bmatrix}\right)$$

$$\left[\left[\left(400.\left(9.662618465\,10^{9}+5.866687920\,10^{9}\,G_{12}+8.89607502\,10^{8}\,G_{12}^{2}\right)Ny\right)\Big/\left(-5.899374440\,10^{14}-1.186335960\,10^{15}\,G_{12}-8.874626174\,10^{13}\,G_{12}^{2}+129.\,G_{12}^{3}\right)\right],\left[-\left(20000.\,Ny\left(9.639038371\,10^{9}+2.066447449\,10^{10}\,G_{12}+1.574744111\,10^{9}\,G_{12}^{2}\right)\right)\Big/\left(-5.899374440\,10^{14}-1.186335960\,10^{15}\,G_{12}-8.874626174\,10^{13}\,G_{12}^{2}+129.\,G_{12}^{3}\right)\right],\left[\left(8000.\,Ny\left(2.128753389\,10^{10}+7.918118560\,10^{9}\,G_{12}+4.87934379\,10^{8}\,G_{12}^{2}\right)\right)\Big/\left(-5.899374440\,10^{14}-1.186335960\,10^{15}\,G_{12}-8.874626174\,10^{13}\,G_{12}^{2}+129.\,G_{12}^{3}\right)\right]\right]$$

> $Te := \begin{bmatrix} m^2 & n^2 & m\cdot n \\ n^2 & m^2 & -m\cdot n \\ -2\cdot m\cdot n & 2\cdot m\cdot n & m^2-n^2 \end{bmatrix} : Ts := \begin{bmatrix} m^2 & n^2 & 2\cdot m\cdot n \\ n^2 & m^2 & -2\cdot m\cdot n \\ -m\cdot n & m\cdot n & m^2-n^2 \end{bmatrix} : m := \cos(\text{theta}) : n := \sin(\text{theta}) :$

> $sigmaplusp := simplify\left(subs\left(\text{theta}=\frac{\pi}{3}, Ts.sigmaplus\right)\right)$

$$\left[\left[-\left(20000.\,Ny\left(1.660187608\,10^{10}+1.881365924\,10^{10}\,G_{12}+1.345635473\,10^{9}\,G_{12}^{2}\right)\right)\Big/\left(-5.899374440\,10^{14}-1.186335960\,10^{15}\,G_{12}-8.874626174\,10^{13}\,G_{12}^{2}+129.\,G_{12}^{3}\right)\right],\left[-\left(12000.\,Ny\left(-8.746098175\,10^{9}+3.824255485\,10^{9}\,G_{12}+3.52194147\,10^{8}\,G_{12}^{2}\right)\right)\Big/\left(-5.899374440\,10^{14}-1.186335960\,10^{15}\,G_{12}-8.874626174\,10^{13}\,G_{12}^{2}+129.\,G_{12}^{3}\right)\right],\left[-\left(25000.\,Ny\left(2.+5.814110220\,10^{9}\,G_{12}+4.38903687\,10^{8}\,G_{12}^{2}\right)\right)\Big/\left(-5.899374440\,10^{14}-1.186335960\,10^{15}\,G_{12}-8.874626174\,10^{13}\,G_{12}^{2}+129.\,G_{12}^{3}\right)\right]\right]$$

> $sigmaminusp := simplify\left(subs\left(\text{theta}=-\frac{\pi}{3}, Ts.sigmaminus\right)\right)$

$$\left[\left[-\left(20000.\,Ny\left(1.455518374\,10^{10}+1.821193916\,10^{10}\,G_{12}+1.345635473\,10^{9}\,G_{12}^{2}\right)\right)\Big/\left(-5.899374440\,10^{14}-1.186335960\,10^{15}\,G_{12}-8.874626174\,10^{13}\,G_{12}^{2}+129.\,G_{12}^{3}\right)\right],\left[-\left(4000.\,Ny\left(-2.554698869\,10^{10}+1.167600785\,10^{10}\,G_{12}+1.056582441\,10^{9}\,G_{12}^{2}\right)\right)\Big/\left(-5.899374440\,10^{14}-1.186335960\,10^{15}\,G_{12}-8.874626174\,10^{13}\,G_{12}^{2}+129.\,G_{12}^{3}\right)\right],\left[\left(10000.\,Ny\left(6.+1.483032646\,10^{10}\,G_{12}+1.184003107\,10^{9}\,G_{12}^{2}\right)\right)\Big/\left(-5.899374440\,10^{14}-1.186335960\,10^{15}\,G_{12}-8.874626174\,10^{13}\,G_{12}^{2}+129.\,G_{12}^{3}\right)\right]\right]$$

> $X := 2.37 : Y := 0.33 :$

> $Nyplus := solve\left(sigmaplusp[1]^2 - sigmaplusp[1]\cdot sigmaplusp[2] + \left(\frac{X}{Y}\right)^2 sigmaplusp[2]^2 + \left(\frac{X}{S}\right)^2 \cdot sigmaplusp[3]^2 = X^2, Ny\right)$

$$\left(2.370000000\left(-5.899374440\,10^{14}-1.186335960\,10^{15}\,G_{12}-8.874626174\,10^{13}\,G_{12}^{2}+129.\,G_{12}^{3}\right)S\right)\Big/\left(6.762622851\,10^{26}\,G_{12}^{4}+8.164318924\,10^{19}\,G_{12}+1.186706252\,10^{29}\,G_{12}^{2}+1.791674839\,10^{28}\,G_{12}^{3}+7.132433704\,10^{29}\,S^2-2.227197141\,10^{29}\,S^2\,G_{12}+2.064740672\,10^{29}\,S^2\,G_{12}^{2}+3.743513947\,10^{28}\,S^2\,G_{12}^{3}+1.531840282\,10^{27}\,S^2\,G_{12}^{4}+1.404225000\,10^{10}\right)^{1/2},$$

$$-\left(2.370000000\left(-5.899374440\,10^{14}-1.186335960\,10^{15}\,G_{12}-8.874626174\,10^{13}\,G_{12}^{2}+129.\,G_{12}^{3}\right)S\right)\Big/\left(6.762622851\,10^{26}\,G_{12}^{4}+8.164318924\,10^{19}\,G_{12}+1.186706252\,10^{29}\,G_{12}^{2}+1.791674839\,10^{28}\,G_{12}^{3}+7.132433704\,10^{29}\,S^2-2.227197141\,10^{29}\,S^2\,G_{12}+2.064740672\,10^{29}\,S^2\,G_{12}^{2}+3.743513947\,10^{28}\,S^2\,G_{12}^{3}+1.531840282\,10^{27}\,S^2\,G_{12}^{4}+1.404225000\,10^{10}\right)^{1/2}$$

> $$Nyminus := solve\left(sigmaminusp[1]^2 - sigmaminusp[1] \cdot sigmaminusp[2] + \left(\frac{X}{Y}\right)^2 sigmaminusp[2]^2 + \left(\frac{X}{S}\right)^2 \cdot sigmaminusp[3]^2 = X^2, Ny \right)$$

$$\left(2.962500000\left(-5.899374440\,10^{14} - 1.186335960\,10^{15}\,G_{12} - 8.874626174\,10^{13}\,G_{12}^2 + 129.\,G_{12}^3\right)S\right) \Big/ \left(3.159506250\,10^{10} + 2.393500440\,10^{27}\,S^2\,G_{12}^4 + 1.020454636\,10^{30}\,S^2 + 1.230332233\,10^{27}\,G_{12}^4 + 1.561883638\,10^{20}\,G_{12} + 1.930270354\,10^{29}\,G_{12}^2 + 3.082125134\,10^{28}\,G_{12}^3 - 4.009977036\,10^{29}\,S^2\,G_{12} + 3.137533311\,10^{29}\,S^2\,G_{12}^2 + 5.807937213\,10^{28}\,S^2\,G_{12}^3\right)^{1/2},$$

$$-\left(2.962500000\left(-5.899374440\,10^{14} - 1.186335960\,10^{15}\,G_{12} - 8.874626174\,10^{13}\,G_{12}^2 + 129.\,G_{12}^3\right)S\right) \Big/ \left(3.159506250\,10^{10} + 2.393500440\,10^{27}\,S^2\,G_{12}^4 + 1.020454636\,10^{30}\,S^2 + 1.230332233\,10^{27}\,G_{12}^4 + 1.561883638\,10^{20}\,G_{12} + 1.930270354\,10^{29}\,G_{12}^2 + 3.082125134\,10^{28}\,G_{12}^3 - 4.009977036\,10^{29}\,S^2\,G_{12} + 3.137533311\,10^{29}\,S^2\,G_{12}^2 + 5.807937213\,10^{28}\,S^2\,G_{12}^3\right)^{1/2}$$

> $$S1 := solve(Nyplus[1] = 1.27 \cdot 2, S)$$

$$\Big(1.27000\,10^{5}\Big(\Big(-2.646732634\,10^{34}+7.161240416\,10^{34}\,G_{12}^{2}+9.412$$
$$G_{12}^{3}+3.435531618\,10^{32}\,G_{12}^{4}+9.299030755\,10^{34}\,G_{12}$$
$$-1.286075504\,10^{21}\,G_{12}^{5}+9.34708329\,10^{8}\,G_{12}^{6}\Big)$$
$$\Big(4.746825008\,10^{23}\,G_{12}^{2}+7.166699356\,10^{22}\,G_{12}^{3}$$
$$+2.705049140\,10^{21}\,G_{12}^{4}+3.265727570\,10^{14}\,G_{12}+56169.\Big)\Big)^{1/2}\Big)$$
$$\Big/\Big(-2.646732634\,10^{34}+7.161240416\,10^{34}\,G_{12}^{2}$$
$$+9.412102897\,10^{33}\,G_{12}^{3}+3.435531618\,10^{32}\,G_{12}^{4}$$
$$+9.299030755\,10^{34}\,G_{12}-1.286075504\,10^{21}\,G_{12}^{5}$$
$$+9.34708329\,10^{8}\,G_{12}^{6}\Big),$$
$$-\Big(1.27000\,10^{5}\Big(\Big(-2.646732634\,10^{34}+7.161240416\,10^{34}\,G_{12}^{2}$$
$$+9.412102897\,10^{33}\,G_{12}^{3}+3.435531618\,10^{32}\,G_{12}^{4}$$
$$+9.299030755\,10^{34}\,G_{12}-1.286075504\,10^{21}\,G_{12}^{5}$$
$$+9.34708329\,10^{8}\,G_{12}^{6}\Big)\Big(4.746825008\,10^{23}\,G_{12}^{2}$$
$$+7.166699356\,10^{22}\,G_{12}^{3}+2.705049140\,10^{21}\,G_{12}^{4}$$
$$+3.265727570\,10^{14}\,G_{12}+56169.\Big)\Big)^{1/2}\Big)\Big/\Big(-2.646732634\,10^{34}$$
$$+7.161240416\,10^{34}\,G_{12}^{2}+9.412102897\,10^{33}\,G_{12}^{3}$$
$$+3.435531618\,10^{32}\,G_{12}^{4}+9.299030755\,10^{34}\,G_{12}$$
$$-1.286075504\,10^{21}\,G_{12}^{5}+9.34708329\,10^{8}\,G_{12}^{6}\Big)$$

> $S2 := solve(Nyminus[1] = 1.27 \cdot 2, S)$

$$\left(50800.\left(\left(3.435531618\,10^{32}\,G_{12}^{4}-2.258653389\,10^{34}+9.517861390\,10^{34}\,G_{12}+7.197833473\,10^{34}\,G_{12}^{2}+9.429157141\,10^{33}\,G_{12}^{3}-1.286075504\,10^{21}\,G_{12}^{5}+9.34708329\,10^{8}\,G_{12}^{6}\right)\left(4.931400214\,10^{23}\,G_{12}^{3}+1.968531573\,10^{22}\,G_{12}^{4}+5.05521\,10^{5}+3.088432566\,10^{24}\,G_{12}^{2}+2.499013821\,10^{15}\,G_{12}\right)\right)^{1/2}\right)\Big/\left(3.435531618\,10^{32}\,G_{12}^{4}-2.258653389\,10^{34}+9.517861390\,10^{34}\,G_{12}+7.197833473\,10^{34}\,G_{12}^{2}+9.429157141\,10^{33}\,G_{12}^{3}-1.286075504\,10^{21}\,G_{12}^{5}+9.34708329\,10^{8}\,G_{12}^{6}\right),$$

$$-\left(50800.\left(\left(3.435531618\,10^{32}\,G_{12}^{4}-2.258653389\,10^{34}+9.517861390\,10^{34}\,G_{12}+7.197833473\,10^{34}\,G_{12}^{2}+9.429157141\,10^{33}\,G_{12}^{3}-1.286075504\,10^{21}\,G_{12}^{5}+9.34708329\,10^{8}\,G_{12}^{6}\right)\left(4.931400214\,10^{23}\,G_{12}^{3}+1.968531573\,10^{22}\,G_{12}^{4}+5.05521\,10^{5}+3.088432566\,10^{24}\,G_{12}^{2}+2.499013821\,10^{15}\,G_{12}\right)\right)^{1/2}\right)\Big/\left(3.435531618\,10^{32}\,G_{12}^{4}-2.258653389\,10^{34}+9.517861390\,10^{34}\,G_{12}+7.197833473\,10^{34}\,G_{12}^{2}+9.429157141\,10^{33}\,G_{12}^{3}-1.286075504\,10^{21}\,G_{12}^{5}+9.34708329\,10^{8}\,G_{12}^{6}\right)$$

```
> plot([S1[1], S2[1]], G12 = 0..1, title
    = "Shear strength as a function of shear modulus", legend
    = ["+60 layer", "-60 layer"], labels
    = ["Shear Modulus, G12, MPa", "Shear Strength, S, MPa"],
    labeldirections = ["horizontal", "vertical"])
```

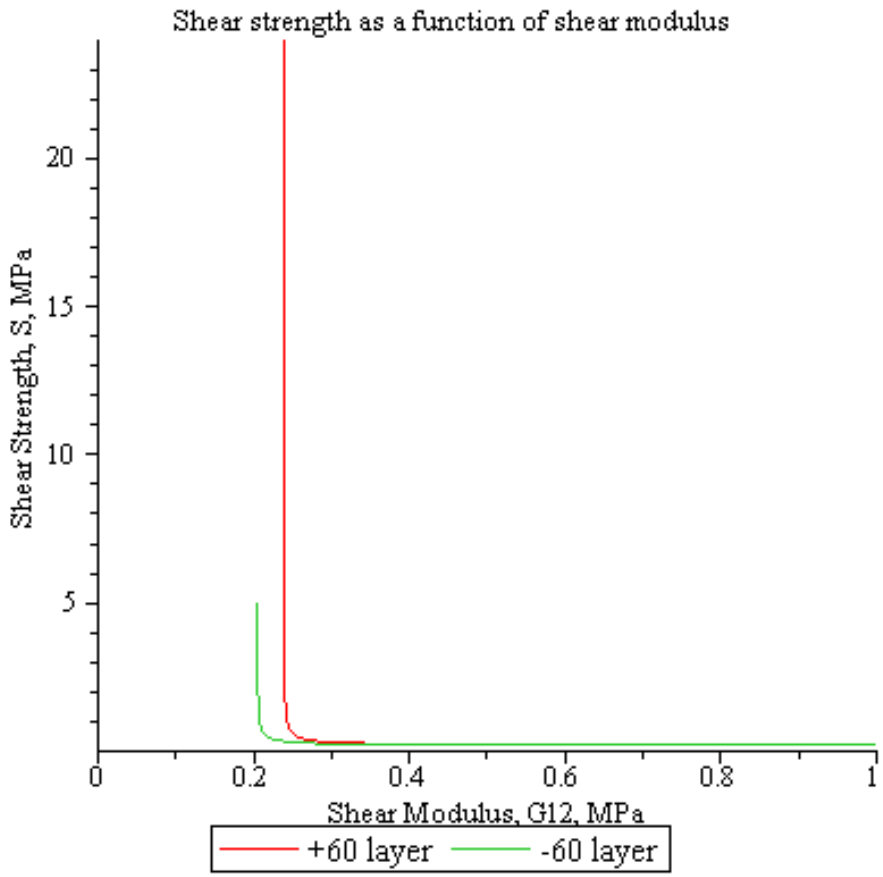

> $plot([S1[1], S2[1]], G_{12} = 0.3..2, title$
$= "Shear strength as a function of shear modulus: Zoomed", legend$
$= ["+60 layer", "-60 layer"], labels$
$= ["Shear Modulus, G12, MPa", "Shear Strength, S, MPa"],$
$labeldirections = ["horizontal", "vertical"])$

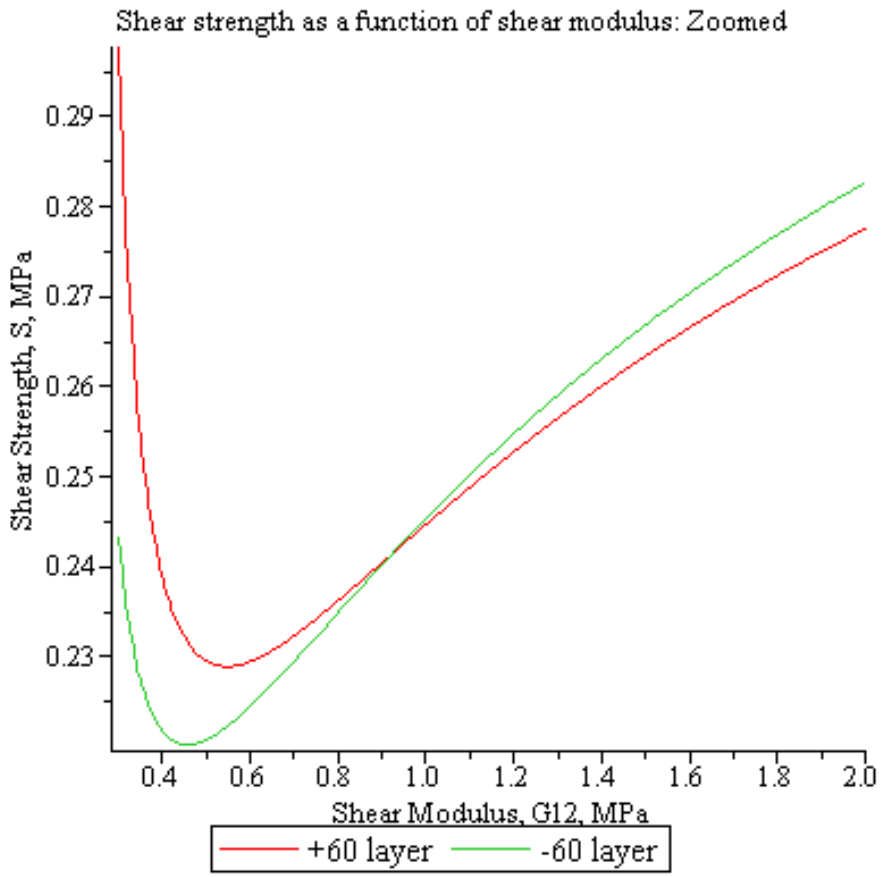

> $G_{12} := fsolve(S1[1] = S2[1], G_{12})$

0.9204679357

> $S := S1[1]$

0.2413368677

LIST OF REFERENCES

1. Luo X, Pietrobon R, X Sun S, Liu GG, Hey L. Estimates and patterns of direct health care expenditures among individuals with back pain in the United States. Spine. 2004;29(1):79.
2. Robertson JT. The rape of the spine. Surgical Neurology. 1993;39(1):5-12.
3. Nachemson AL. Spinal disorders. Overall impact on society and the need for orthopedic resources. Acta Orthop Scand Suppl. 1991;241:17-22.
4. Webster BS, Snook SH. The cost of compensable low back pain. J Occup Med. 1990;32(1):13-5.
5. Bonica J. The Nature of the Problem. In: Caron H, McLaughlin R, eds. Management of low back pain. Boston: John Wright PSG; 1982. p. 1-15.
6. Cooper BS, Rice DP. The economic cost of illness revisited. Soc Secur Bull. 1976;39(2):21-36.
7. Miller JA, Schmatz C, Schultz AB. Lumbar disc degeneration: correlation with age, sex, and spine level in 600 autopsy specimens. Spine. 1988;13(2):173-8.
8. Hickey DS, Hukins DW. Relation between the structure of the annulus fibrosus and the function and failure of the intervertebral disc. Spine. 1980;5(2):106-16.
9. Inoue H, Takeda T. Three-dimensional observation of collagen framework of lumbar intervertebral discs. Acta Orthop Scand. 1975;46(6):949-56.
10. Coventry MB, Ghormley RK, Kernohan JW. THE INTERVERTEBRAL DISC: ITS MICROSCOPIC ANATOMY AND PATHOLOGY: Part I. Anatomy, Development, and Physiology. J Bone Joint Surg Am. 1945;27(1):105-12.
11. Cassinelli EH, Hall RA, Kang JD. Biochemistry of intervertebral disc degeneration and the potential for gene therapy applications. Spine J. 2001;1(3):205-14.
12. Buckwalter J. The fine structure of the human intervertebral disc. In: White A, Gordon S, eds. AAOS symposium on idiopathic low back pain. St Louis: CV Mosby; 1982. p. 108-43.
13. Ayad S, Weiss J. Biochemistry of the intervertebral disc. In: Jayson M, ed. The lumbar spine and back pain. 3rd ed. Edinburgh, Scotland: Churchill Livingstone; 1987. p. 111-31.
14. Marchand F, Ahmed AM. Investigation of the laminate structure of lumbar disc anulus fibrosus. Spine. 1990;15(5):402-10.
15. Hukins DW. Disc Structure and Function. In: Ghosh P, ed. The Biology of the Intervertebral Disc. Boca Raton: CRC Press; 1988. p. 1-37.
16. Fujita Y, Duncan NA, Lotz JC. Radial tensile properties of the lumbar annulus fibrosus are site and degeneration dependent. J Orthop Res. 1997;15(6):814-9.
17. Stadnik TW, Lee RR, Coen HL, Neirynck EC, Buisseret TS, Osteaux MJ. Annular tears and disk herniation: prevalence and contrast enhancement on MR images in the absence of low back pain or sciatica. Radiology. 1998;206(1):49-55.
18. Natarajan RN, Ke JH, Andersson GB. A model to study the disc degeneration process. Spine. 1994;19(3):259-65.
19. White AA, Panjabi MM. Clinical biomechanics of the spine: Lippincott Philadelphia; 1990.
20. Raj PP, Fipp A. Intervertebral Disc: Anatomy-Physiology-Pathophysiology-Treatment. Pain Practice. 2008;8(1):18.

21. Bogduk N, Tynan W, Wilson AS. The nerve supply to the human lumbar intervertebral discs. J Anat. 1981;132(Pt 1):39-56.
22. Jackson HC, 2nd, Winkelmann RK, Bickel WH. Nerve endings in the human lumbar spinal column and related structures. J Bone Joint Surg Am. 1966;48(7):1272-81.
23. Lipson SJ, Muir H. Proteoglycans in experimental intervertebral disc degeneration. Spine. 1981;6(3):194.
24. Berthet-Colominas C, Miller A, Herbage D, Ronziere MC, Tocchetti D. Structural studies of collagen fibres from intervertebral disc. Biochimica et Biophysica Acta (BBA)-Protein Structure and Molecular Enzymology. 1982;706(1):50-64.
25. Inerot S, Axelsson I. Structure and composition of proteoglycans from human annulus fibrosus. Connective tissue research. 1991;26(1-2):47-63.
26. Eyre D. Collagens of the disc. In: Ghosh P, ed. The biology of the intervertebral disk. Boca Raton: CRC Press; 1988. p. 171-88.
27. Hayes A, Benjamin M, Ralphs J. Extracellular matrix in development of the intervertebral disc. Matrix Biology. 2001;20(2):107-21.
28. Errington R, Puustjarvi K, White I, Roberts S, Urban J. Characterisation of cytoplasm-filled processes in cells of the intervertebral disc. Journal of anatomy. 1998;192(3):369-78.
29. McNeilly C, Banes A, Benjamin M, Ralphs J. Tendon cells in vivo form a three dimensional network of cell processes linked by gap junctions. Journal of anatomy. 1996;189(Pt 3):593.
30. Kiani C, Liwen C, Yao Jiong WU, Yee AJ, Burton BY. Structure and function of aggrecan. Cell Research. 2002;12(1):19-32.
31. Inoue H. Three-dimensional architecture of lumbar intervertebral discs. Spine. 1981;6(2):139-46.
32. Bruehlmann SB, B Rattner J, R Matyas J, A Duncan N. Regional variations in the cellular matrix of the annulus fibrosus of the intervertebral disc. Journal of anatomy. 2002;201(2):159-71.
33. Cassidy J, Hiltner A, Baer E. Hierarchical structure of the intervertebral disc. Connective tissue research. 1989;23(1):75-88.
34. Horton WG. Further observations on the elastic mechanism of the intervertebral disc. J Bone Joint Surg Br. 1958;40-B(3):552-7.
35. Holzapfel GA, Schulze-Bauer CA, Feigl G, Regitnig P. Single lamellar mechanics of the human lumbar anulus fibrosus. Biomech Model Mechanobiol. 2005;3(3):125-40.
36. Tsuji H, Hirano N, Ohshima H, Ishihara H, Terahata N, Motoe T. Structural Variation of the Anterior and Posterior Anulus Fibrosus in the Development of Human Lumbar Intervertebral Disc| A Risk Factor for Intervertebral Disc Rupture. Spine. 1993;18(2):204.
37. Buckwalter JA, Mow VC, Boden SD, Eyre DR, Weidenbaum M. Intervertebral disk structure, composition and mechanical function. In: Buckwalter JA, Einhorn TA, Simon SR, eds. Orthopaedic Basic Science. 2nd ed. Rosemont, IL: American Academy of Orthopaedic Surgeons; 2000. p. 547-56.
38. Roughley PJ. Biology of intervertebral disc aging and degeneration: involvement of the extracellular matrix. Spine. 2004;29(23):2691-9.
39. Sigma Aldrich. Collagenase from Clostridium histolyticum. MSDS, No. C0130.

40. Bushell GR, Ghosh P, Taylor TF, Akeson WH. Proteoglycan chemistry of the intervertebral disks. Clin Orthop Relat Res. 1977;(129):115-23.
41. Ohshima H, Urban JP, Bergel DH. Effect of static load on matrix synthesis rates in the intervertebral disc measured in vitro by a new perfusion technique. J Orthop Res. 1995;13(1):22-9.
42. Oegema TR, Jr., Bradford DS, Cooper KM. Aggregated proteoglycan synthesis in organ cultures of human nucleus pulposus. J Biol Chem. 1979;254(21):10579-81.
43. Ayad S, Weiss JB. Biochemistry of the intervertebral disk. In: Jayson MIV, ed. The Lumbar Spine and Back Pain. 3rd ed. New York: Churchill-Livingstone; 1987. p. 100-37.
44. Iatridis JC, Weidenbaum M, Setton LA, Mow VC. Is the nucleus pulposus a solid or a fluid? Mechanical behaviors of the nucleus pulposus of the human intervertebral disk. Spine. 1996;21(10):1174-84.
45. Sigma Aldrich. Chondroitinase ABC, from Proteus vulgaris. MSDS, No. C3667
46. Gray WR, Sandberg LB, Foster JA. Molecular model for elastin structure and function. Nature. 1973;246(5434):461.
47. Mikawa Y, Hamagami H, Shikata J, Yamamuro T. Elastin in the human intervertebral disk. A histological and biochemical study comparing it with elastin in the human yellow ligament. Arch Orthop Trauma Surg. 1986;105(6):343-9.
48. Robb BW, Wachi H, Schaub T, Mecham RP, Davis EC. Characterization of an in vitro model of elastic fiber assembly. Mol Biol Cell. 1999;10(11):3595-605.
49. Buckwalter JA, Cooper RR, Maynard JA. Elastic fibers in human intervertebral discs. J Bone Joint Surg Am. 1976;58(1):73-6.
50. Hickey DS, Hukins DW. Collagen fibril diameters and elastic fibres in the annulus fibrosus of human fetal intervertebral disc. J Anat. 1981;133(Pt 3):351-7.
51. Johnson EF, Chetty K, Moore IM, Stewart A, Jones W. The distribution and arrangement of elastic fibres in the intervertebral disc of the adult human. J Anat. 1982;135(Pt 2):301-9.
52. Johnson EF, Berryman H, Mitchell R, Wood WB. Elastic fibres in the anulus fibrosus of the adult human lumbar intervertebral disc. A preliminary report. J Anat. 1985;143:57-63.
53. Yu J, Winlove PC, Roberts S, Urban JP. Elastic fibre organization in the intervertebral discs of the bovine tail. J Anat. 2002;201(6):465-75.
54. Mecham RP, Broekelmann TJ, Fliszar CJ, Shapiro SD, Welgus HG, Senior RM. Elastin Degradation by Matrix Metalloproteinases. CLEAVAGE SITE SPECIFICITY AND MECHANISMS OF ELASTOLYSIS. J Biol Chem. 1997;272(29):18071-6.
55. Bode W, Meyer E, Powers JC. Human leukocyte and porcine pancreatic elastase: x-ray crystal structures, mechanism, substrate specificity, and mechanism-based inhibitors. Biochemistry. 1989;28(5):1951-63.
56. Berg JM, Tymoczko JL, Stryer L. Lipids and cell membranes. Biochemistry 6th Edition WH Freeman & Co, New York. 2007:326-32.
57. Horner HA, Roberts S, Bielby RC, Menage J, Evans H, Urban JPG. Cells from different regions of the intervertebral disc: effect of culture system on matrix expression and cell phenotype. Spine. 2002;27(10):1018.

58. Chelberg MK, Banks GM, Geiger DF, Oegema Jr TR. Identification of heterogeneous cell populations in normal human intervertebral disc. Journal of anatomy. 1995;186(Pt 1):43.
59. Rufai A, Benjamin M, Ralphs J. The development of fibrocartilage in the rat intervertebral disc. Anatomy and embryology. 1995;192(1):53-62.
60. Neumann DA. Kinesiology of the Musculoskeletal System: Foundations for Rehabilitation: Mosby; 2010.
61. Seog J, Dean D, Plaas A, Wong-Palms S, Grodzinsky A, Ortiz C. Direct measurement of glycosaminoglycan intermolecular interactions via high-resolution force spectroscopy. Macromolecules. 2002;35(14):5601-15.
62. Adams M, Roughley P. What is intervertebral disc degeneration, and what causes it? Spine. 2006;31(18):2151.
63. Nachemson A. The load on lumbar disks in different positions of the body. Clinical orthopaedics and related research. 1966;45:107-22.
64. Nachemson A. The load on lumbar disks in different positions of the body. Clin Orthop Relat Res. 1966;45:107-22.
65. Nachemson AL. The Lumbar Spine An Orthopaedic Challenge. Spine. 1976;1(1):59-71.
66. Wilke HJ, Neef P, Caimi M, Hoogland T, Claes LE. New in vivo measurements of pressures in the intervertebral disc in daily life. Spine. 1999;24(8):755.
67. Klein JA, Hukins DWL. X-ray diffraction demonstrates reorientation of collagen fibres in the annulus fibrosus during compression of the intervertebral disc. Biochimica et Biophysica Acta (BBA)-General Subjects. 1982;717(1):61-4.
68. Guerin HAL, Elliott DM. Degeneration affects the fiber reorientation of human annulus fibrosus under tensile load. Journal of biomechanics. 2006;39(8):1410-8.
69. Klein JA, David WL H. Collagen fibre orientation in the annulus fibrosus of intervertebral disc during bending and torsion measured by X-ray diffraction. Biochimica et Biophysica Acta (BBA)-General Subjects. 1982;719(1):98-101.
70. McMillan D, Garbutt G, Adams M. Effect of sustained loading on the water content of intervertebral discs: implications for disc metabolism. Annals of the Rheumatic Diseases. 1996;55(12):880.
71. Lubliner J. Plasticity theory: Macmillan New York; 1990.
72. Acaroglu ER, Iatridis JC, Setton LA, Foster RJ, Mow VC, Weidenbaum M. Degeneration and aging affect the tensile behavior of human lumbar anulus fibrosus. Spine. 1995;20(24):2690-701.
73. Skaggs DL, Weidenbaum M, Iatridis JC, Ratcliffe A, Mow VC. Regional Variation in Tensile Properties and Biochemical Composition of the Human Lumbar Anulus Fibrosus. Spine. 1994;19(12):1310-9.
74. Ebara S, Iatridis JC, Setton LA, Foster RJ, Mow VC, Weidenbaum M. Tensile Properties of Nondegenerate Human Lumbar Anulus Fibrosus. Spine. 1996;21(4):452-61.
75. Panagiotacopulos N, Knauss W, Bloch R. On the mechanical properties of human intervertebral disc material. Biorheology. 1979;16(4):317-30.
76. Galante JO. Tensile properties of the human lumbar annulus fibrosus. Acta Orthop Scand Suppl. 1967;100:4-91.
77. Urban J, Maroudas A. Swelling of the intervertebral disc in vitro. Connect Tissue Res. 1981;9(1):1-10.

78. Urban JP, McMullin JF. Swelling Pressure of the Lumbar Intervertebral Discs: Influence of Age, Spinal Level, Composition, and Degeneration. Spine. 1988;13(2):179-87.
79. Best BA, Guilak F, Setton LA, et al. Compressive Mechanical Properties of the Human Anulus Fibrosus and Their Relationship to Biochemical Composition. Spine. 1994;19(2):S212-S21.
80. Green TP, Adams MA, Dolan P. Tensile properties of the annulus fibrosus II. Ultimate tensile strength and fatigue life. European Spine Journal 1993;2(4):209-14.
81. Adams MA, Green TP. Tensile properties of the annulus fibrosus I. The contribution of fibre-matrix interactions to tensile stiffness and strength. European Spine Journal. 1993;2(4):203-8.
82. Elliott DM, Setton LA. Anisotropic and inhomogeneous tensile behavior of the human anulus fibrosus: experimental measurement and material model predictions. J Biomech Eng. 2001;123(3):256-63.
83. Wu HC, Yao RF. Mechanical behavior of the human annulus fibrosus. J Biomech. 1976;9(1):1-7.
84. T. Brown, Hansen R, Yorra A. Some Mechanical Tests on the Lumbosacral Spine with Particular Reference to the Intervertebral Discs: A Preliminary Report J Bone Joint Surg Am. 1957;39:1135-64.
85. Pezowicz CA, Robertson PA, Broom ND. Intralamellar relationships within the collagenous architecture of the annulus fibrosus imaged in its fully hydrated state. J Anat. 2005;207(4):299-312.
86. Fujita Y, Duncan NA, Lotz JC. Radial tensile properties of the lumbar annulus fibrosus are site and degeneration dependent. Journal of orthopaedic research. 1997;15(6):814-9.
87. Iatridis JC, Kumar S, Foster RJ, Weidenbaum M, Mow VC. Shear mechanical properties of human lumbar annulus fibrosus. Journal of Orthopaedic Research. 1999;17(5):732-7.
88. Fujita Y, Wagner D, Biviji A, Duncan N, Lotz J. Anisotropic shear behavior of the annulus fibrosus: effect of harvest site and tissue prestrain. Medical engineering & physics. 2000;22(5):349-57.
89. Powell MC, Wilson M, Szypryt P, Symonds EM, Worthington BS. Prevalence of lumbar disc degeneration observed by magnetic resonance in symptomless women. Lancet. 1986;2(8520):1366-7.
90. Boden SD, Davis DO, Dina TS, Patronas NJ, Wiesel SW. Abnormal magnetic-resonance scans of the lumbar spine in asymptomatic subjects. A prospective investigation. J Bone Joint Surg Am. 1990;72(3):403-8.
91. Matsui H, Kanamori M, Ishihara H, Yudoh K, Naruse Y, Tsuji H. Familial predisposition for lumbar degenerative disc disease. A case-control study. Spine. 1998;23(9):1029-34.
92. Pope MH, Magnusson M, Wilder DG. Kappa Delta Award. Low back pain and whole body vibration. Clin Orthop Relat Res. 1998;(354):241-8.
93. Battie MC, Videman T, Gibbons LE, Fisher LD, Manninen H, Gill K. 1995 Volvo Award in clinical sciences. Determinants of lumbar disc degeneration. A study relating lifetime exposures and magnetic resonance imaging findings in identical twins. Spine. 1995;20(24):2601-12.

94. Battie MC, Videman T, Gill K, et al. 1991 Volvo Award in clinical sciences. Smoking and lumbar intervertebral disc degeneration: an MRI study of identical twins. Spine. 1991;16(9):1015-21.
95. Roughley PJ. Biology of intervertebral disc aging and degeneration: involvement of the extracellular matrix. Spine. 2004;29(23):2691.
96. Iatridis JC, Gwynn Ia. Mechanisms for mechanical damage in the intervertebral disc annulus fibrosus. J Biomech. 2004;37(8):1165-75.
97. Urban J, Roberts S. Degeneration of the intervertebral disc. Arthritis Research and Therapy. 2003;5(3):120-38.
98. Olczyk K. Age-related changes in proteoglycans of human intervertebral discs. Zeitschrift fur Rheumatologie. 1994;53(1):19.
99. Olczyk K. Age-related changes in glycosaminoglycans of human intervertebral discs. Folia histochemica et cytobiologica/Polish Academy of Sciences, Polish Histochemical and Cytochemical Society. 1993;31(4):215.
100. Olczyk K. Age-related changes in collagen of human intervertebral disks. Gerontology. 1992;38(4):196-204.
101. Yamauchi M, Woodley DT, Mechanic GL. Aging and cross-linking of skin collagen. Biochem Biophys Res Commun. 1988;152(2):898-903.
102. Nachemson A. Lumbar intradiscal pressure. Experimental studies on post-mortem material. Acta Orthop Scand Suppl. 1960;43:1-104.
103. Adams M, McMillan D, Green T, Dolan P. Sustained loading generates stress concentrations in lumbar intervertebral discs. Spine. 1996;21(4):434.
104. Lee TC, Midura RJ, Hascall VC, Vesely I. The effect of elastin damage on the mechanics of the aortic valve. Journal of biomechanics. 2001;34(2):203-10.
105. Schmidt MB, Mow VC, Chun LE, Eyre DR. Effects of proteoglycan extraction on the tensile behavior of articular cartilage. Journal of Orthopaedic Research. 1990;8(3):353-63.
106. Smith LJ, Byers S, Costi JJ, Fazzalari NL. Elastic fibers enhance the mechanical integrity of the human lumbar anulus fibrosus in the radial direction. Ann Biomed Eng. 2008;36(2):214-23.
107. Jacobs NT, Smith LJ, Han WM, Morelli J, Yoder JH, Elliott DM. Effect of orientation and targeted extracellular matrix degradation on the shear mechanical properties of the annulus fibrosus. Journal of the Mechanical Behavior of Biomedical Materials. 2011;4(8):1611-9.
108. Osti OL, Vernon-Roberts B, Moore R, Fraser RD. Annular tears and disc degeneration in the lumbar spine. A post-mortem study of 135 discs. J Bone Joint Surg Br. 1992;74(5):678-82.
109. Key JA, Ford LT. Experimental intervertebral-disc lesions. J Bone Joint Surg Am. 1948;30A(3):621-30.
110. Smith JW, Walmsley R. Experimental incision of the intervertebral disc. J Bone Joint Surg Br. 1951;33-B(4):612-25.
111. Yasuma T, Makino E, Saito S, Inui M. Histological development of intervertebral disc herniation. The Journal of bone and joint surgery American volume. 1986;68(7):1066.
112. Moore RJ, Vernon-Roberts B, Fraser RD, Osti OL, Schembri M. The origin and fate of herniated lumbar intervertebral disc tissue. Spine. 1996;21(18):2149.

113. Tampier C, Drake JDM, Callaghan JP, McGill SM. Progressive disc herniation: an investigation of the mechanism using radiologic, histochemical, and microscopic dissection techniques on a porcine model. Spine. 2007;32(25):2869.
114. Haughton VM. MR imaging of the spine. Radiology. 1988;166(2):297-301.
115. Mobbs RJ, Steel T. Migration of lumbar disc herniation: An unusual case. Journal of clinical neuroscience. 2007;14(6):581-4.
116. Adams MA, Hutton WC. Prolapsed intervertebral disc. A hyperflexion injury 1981 Volvo Award in Basic Science. Spine. 1982;7(3):184-91.
117. Gordon SJ, Yang KH, Mayer PJ, Mace Jr AH, Kish VL, Radin EL. Mechanism of disc rupture. A preliminary report. Spine. 1991;16(4):450.
118. Adams M, Hutton W. The effect of fatigue on the lumbar intervertebral disc. The Journal of bone and joint surgery British volume. 1983;65(2):199.
119. Aultman CD, Scannell J, McGill SM. The direction of progressive herniation in porcine spine motion segments is influenced by the orientation of the bending axis. Clinical Biomechanics. 2005;20(2):126-9.
120. Callaghan JP, McGill SM. Intervertebral disc herniation: studies on a porcine model exposed to highly repetitive flexion/extension motion with compressive force. Clinical Biomechanics. 2001;16(1):28-37.
121. Olczyk K. Age-related changes of elastin content in human intervertebral discs. Folia histochemica et cytobiologica/Polish Academy of Sciences, Polish Histochemical and Cytochemical Society. 1994;32(1):41.
122. Adams MA, Burton AK, Dolan P, Bogduk N. The biomechanics of back pain: Churchill Livingstone; 2007.
123. Case SW, Reifsnider KL. Fatigue of Composite Materials. In: Milne I, Ritchie RO, Karihaloo B, eds. Comprehensive Structural Integrity: Elsevier; 2003.
124. Mandell JF. Fatigue behavior of short fiber composite materials. In: Reifsnider KL, ed. Composite Materials Series: Fatigue of Composites. New York: Elsevier; 1990. p. 232-337.
125. lftekhar A. Biomedical Composites. In: Kutz M, ed. Standard Handbook of Biomedical Engineering and Design: McGraw-Hill; 2003.
126. Schwartz M. Composite Materials Handbook. 2 ed. New York: McGraw-Hill; 1992.
127. Gdoutos EE, Pilakoutas K, Rodopoulos CA. Failure Analysis of Industrial Composite Materials. New York: McGraw-Hill; 2000.
128. Mallick PK. Composites Engineering Handbook. New York: Marcel Dekker; 1997.
129. Talreja R. Fatigue of composite materials: damage mechanisms and fatigue-life diagrams. Fatigue of Composite Materials. Lancaster, PA: Technomic; 1987.
130. Corigliano A. Damage and Fracture Mechanics Techniques for Composite Structures. In: Milne I, Ritchie RO, Karihaloo B, eds. Comprehensive Structural Integrity Elsevier; 2003.
131. Hull D, Clyne TW. An Introduction to Composite Materials. Cambridge, UK: Cambridge University Press; 1996.
132. Wang J, Karihaloo BL. Cracked composite laminates least prone to delamination. Proc Roy Soc London. 1994;A444:17-35.

133. Pagano NJ, Pipes RB. Some observations on the interlaminar strength of composite laminates. Int J Mech Sci. 1973;15:679-88.
134. Iatridis JC, Setton LA, Foster RJ, Rawlins BA, Weidenbaum M, Mow VC. Degeneration affects the anisotropic and nonlinear behaviors of human anulus fibrosus in compression. Journal of biomechanics. 1998;31(6):535-44.
135. Rose CA, Herakovich CT. An approximate solution for interlaminar stresses in composite laminates. Composites Engineering. 1993;3(3):271-85.
136. Herakovich CT. Mechanics of fibrous composites. New York: John Wiley & Sons, Inc, 1998. 1998.
137. Goel V, Monroe B, Gilbertson L, Brinckmann P. Interlaminar shear stresses and laminae separation in a disc: finite element analysis of the L3-L4 motion segment subjected to axial compressive loads. Spine. 1995;20(6):689.
138. Yu J. Elastic tissues of the intervertebral disc. Biochem Soc Trans. 2002;30(Pt 6):848-52.
139. Skaggs D, Weidenbaum M, Iatridis J, Ratcliffe A, Mow V. Regional variation in tensile properties and biochemical composition of the human lumbar anulus fibrosus. Spine. 1994;19(12):1310-9.
140. Holzapfel G, Schulze-Bauer C, Feigl G, Regitnig P. Single lamellar mechanics of the human lumbar anulus fibrosus. Biomechanics and modeling in mechanobiology. 2005;3(3):125-40.
141. Smith LJ, Byers S, Costi JJ, Fazzalari NL. Elastic fibers enhance the mechanical integrity of the human lumbar anulus fibrosus in the radial direction. Annals of biomedical engineering. 2008;36(2):214-23.
142. Belytschko T, Kulak R, Schultz A, Galante J. Finite element stress analysis of an intervertebral disc. Journal of Biomechanics. 1974;7(3):277-85.
143. Lin H, Liu Y, Adams K. Mechanical response of the lumbar intervertebral joint under physiological (complex) loading. The Journal of bone and joint surgery American volume. 1978;60(1):41.
144. Shirazi-Adl SA, Shrivastava SC, Ahmed AM. Stress Analysis of the Lumbar Disc-Body Unit in Compression A Three-Dimensional Nonlinear Finite Element Study. Spine. 1984;9(2):120.
145. Elliott DM, Setton LA. Anisotropic and inhomogeneous tensile behavior of the human anulus fibrosus: experimental measurement and material model predictions. Journal of biomechanical engineering. 2001;123:256.
146. Hewitt J, Guilak F, Glisson R, Vail TP. Regional material properties of the human hip joint capsule ligaments. Journal of orthopaedic research. 2001;19(3):359-64.
147. Elliott DM, Narmoneva DA, Setton LA. Direct measurement of the Poisson's ratio of human patella cartilage in tension. Journal of biomechanical engineering. 2002;124:223.
148. Jones RM. Mechanics of composite materials: Hemisphere Pub; 1999.
149. Osti O, Vernon-Roberts B, Moore R, Fraser R. Annular tears and disc degeneration in the lumbar spine. A post-mortem study of 135 discs. Journal of Bone and Joint Surgery-British Volume. 1992;74(5):678.
150. Osti O, Fraser R. MRI and discography of annular tears and intervertebral disc degeneration. A prospective clinical comparison. Journal of Bone and Joint Surgery-British Volume. 1992;74(3):431.

151. Saal JS, Franson RC, Dobrow R, Saal JA, White AH, Goldthwaite N. High levels of inflammatory phospholipase A2 activity in lumbar disc herniations. Spine. 1990;15(7):674.
152. Yamashita T, Cavanaugh J, El-Bohy A, Getchell T, King A. Mechanosensitive afferent units in the lumbar facet joint. The Journal of bone and joint surgery American volume. 1990;72(6):865.
153. Natarajan R, Ke J, Andersson G. A model to study the disc degeneration process. Spine. 1994;19(3):259.
154. Spilker R, Jakobs D, Schultz A. Material constants for a finite element model of the intervertebral disk with a fiber composite annulus. Journal of biomechanical engineering. 1986;108:1.
155. Ueno K, Liu Y. A three-dimensional nonlinear finite element model of lumbar intervertebral joint in torsion. Journal of biomechanical engineering. 1987;109(3):200.
156. Klisch SM, Lotz JC. Application of a fiber-reinforced continuum theory to multiple deformations of the annulus fibrosus. Journal of Biomechanics. 1999;32(10):1027-36.
157. París F. A study of failure criteria of fibrous composite materials. NASA/CR. 2001;210661:2001.
158. Soden P, Kaddour A, Hinton M. Recommendations for designers and researchers resulting from the world-wide failure exercise. Composites Science and Technology. 2004;64(3-4):589-604.
159. Li Q. Strain energy density failure criterion. International journal of solids and structures. 2001;38(38-39):6997-7013.
160. Sun C, Quinn B, Tao J, Oplinger D. Comparative evaluation of failure analysis methods for composite laminates. Washington, DC: FAA, Office of Aviation Research, 1996. 1996.
161. Lynch HA, Johannessen W, Wu JP, Jawa A, Elliott DM. Effect of fiber orientation and strain rate on the nonlinear uniaxial tensile material properties of tendon. Journal of biomechanical engineering. 2003;125:726.
162. Staab GH. Laminar composites: Butterworth-Heinemann; 1999.
163. Hill R. The mathematical theory of plasticity: Oxford University Press, USA; 1950.
164. Tsai SW. Strength theories of filamentary structures. In: Schwartz RT, Schwartz HS, eds. Fundamental aspects of fiber reinforced plastic composites; Dayton, OH: Wiley Interscience; 1968. p. 3-11.
165. Azzi V, Tsai S. Anisotropic strength of composites. Experimental Mechanics. 1965;5(9):283-8.
166. Ebara S, Iatridis JC, Setton LA, Foster RJ, Mow VC, Weidenbaum M. Tensile properties of nondegenerate human lumbar anulus fibrosus. Spine. 1996;21(4):452.
167. Yu J, Peter C, Roberts S, Urban JPG. Elastic fibre organization in the intervertebral discs of the bovine tail. Journal of anatomy. 2002;201(6):465-75.
168. Gloeckner DG, Bihir KL, Sacks MS. Effects of mechanical fatigue on the bending properties of the porcine bioprosthetic heart valve. ASAIO journal. 1999;45(1):59.
169. Billiar K, Sacks M. Biaxial mechanical properties of the natural and glutaraldehyde treated aortic valve cusp—Part I: experimental results. Journal of biomechanical engineering. 2000;122:23.

170. Fithian DC, Kelly MA, Mow VC. Material properties and structure-function relationships in the menisci. Clinical orthopaedics and related research. 1990;252:19-31.
171. Proctor C, Schmidt M, Whipple R, Kelly M, Mow V. Material properties of the normal medial bovine meniscus. Journal of orthopaedic research. 1989;7(6):771-82.
172. Spilker RL, Donzelli PS, Mow VC. A transversely isotropic biphasic finite element model of the meniscus. Journal of Biomechanics. 1992;25(9):1027-45.
173. Smith LJ, Fazzalari NL. Regional variations in the density and arrangement of elastic fibres in the anulus fibrosus of the human lumbar disc. Journal of anatomy. 2006;209(3):359-67.
174. Gibson LJ, Ashby M, Schajer G, Robertson C. The mechanics of two-dimensional cellular materials. Proceedings of the Royal Society of London A Mathematical and Physical Sciences. 1982;382(1782):25-42.
175. Lakes R. Foam structures with a negative Poisson's ratio. Science. 1987;235:1038-40.
176. Ting T, Chen T. Poisson's ratio for anisotropic elastic materials can have no bounds. The quarterly journal of mechanics and applied mathematics. 2005;58(1):73-82.
177. Ting T, Barnett D. Negative Poisson's ratios in anisotropic linear elastic media. Journal of applied mechanics. 2005;72:929.
178. Caddock B, Evans K. Microporous materials with negative Poisson's ratios. I. Microstructure and mechanical properties. Journal of Physics D: Applied Physics. 1989;22:1877.
179. Yeganeh-Haeri A, Weidner DJ, Parise JB. Elasticity of α-cristobalite: a silicon dioxide with a negative Poisson's ratio. Science. 1992;257(5070):650.
180. Baughman RH, Shacklette JM, Zakhidov AA, Stafström S. Negative Poisson's ratios as a common feature of cubic metals. Nature. 1998;392(6674):362-5.
181. Baughman RH, Dantas SO, Stafström S, Zakhidov AA, Mitchell TB, Dubin DHE. Negative Poisson's ratios for extreme states of matter. Science. 2000;288(5473):2018.
182. Lakes R, Witt R. Making and characterizing negative Poisson's ratio materials. International Journal of Mechanical Engineering Education. 2002;30(1):50-8.
183. Lee T, Lakes R. Anisotropic polyurethane foam with Poisson'sratio greater than 1. Journal of Materials Science. 1997;32(9):2397-401.
184. Zhu HX, Knott JF, Mills NJ. Analysis of the elastic properties of open-cell foams with tetrakaidecahedral cells. Journal of the Mechanics and Physics of Solids. 1997;45(3):319-43.
185. Li K, Gao XL, Subhash G. Effects of cell shape and cell wall thickness variations on the elastic properties of two-dimensional cellular solids. International journal of solids and structures. 2005;42(5):1777-95.
186. Baker A, Dutton S, Kelly D. Composite Materials for Aircraft Structures (2nd Edition). American Institute of Aeronautics and Astronautics.
187. Adams M, Green T. Tensile properties of the annulus fibrosus. I. The contribution of fibre-matrix interactions to tensile stiffness and strength. European Spine Journal. 1993;2(4):203-8.
188. Green T, Adams M, Dolan P. Tensile properties of the annulus fibrosus. II. Ultimate tensile strength and fatigue life. European Spine Journal. 1993;2(4):209-14.

189. Bass E, Ashford F, Segal M, Lotz J. Biaxial testing of human annulus fibrosus and its implications for a constitutive formulation. Annals of biomedical engineering. 2004;32(9):1231-42.
190. Bruehlmann SB, Hulme PA, Duncan NA. In situ intercellular mechanics of the bovine outer annulus fibrosus subjected to biaxial strains. Journal of Biomechanics. 2004;37(2):223-31.
191. Nerurkar NL, Elliott DM, Mauck RL. Mechanics of oriented electrospun nanofibrous scaffolds for annulus fibrosus tissue engineering. Journal of orthopaedic research. 2007;25(8):1018-28.
192. Sarkar S, Schauer CL, Vresilovic E, Marcolongo M. Immobilization of Chondroitin Sulfate for Biomimetic Polymer Brush Synthesis Strategies. In Preparation. 2011.
193. Kiani C, Liwen C, Yao Jiong W, YEE AJ, Burton BY. Structure and function of aggrecan. Cell Research. 2002;12(1):19-32.
194. Raj PP. Intervertebral Disc: Anatomy Physiology Pathophysiology Treatment. Pain Practice. 2008;8(1):18-44.
195. Thompson J, Pearce R, Schechter M, Adams M, Tsang I, Bishop P. Preliminary evaluation of a scheme for grading the gross morphology of the human intervertebral disc. Spine. 1990;15(5):411-5.
196. Isaacs J, Gidvani S, Bonfiglio D, Doehring T, Vresilovic E, Marcolongo M. Characterization of Annulus Fibrosus Micromechanics. The Spine Journal. Submitted.
197. Panjabi MM. The stabilizing system of the spine. Part I. Function, dysfunction, adaptation, and enhancement. Journal of spinal disorders. 1992;5:383-.
198. Nachemson A. Lumbar spine instability: a critical update and symposium summary. Spine. 1985;10(3):290.
199. Nachemson AL, Schultz AB, Berkson MH. Mechanical properties of human lumbar spine motion segments: influences of age, sex, disc level, and degeneration. Spine. 1979;4(1):1.
200. Keller TS, HANSSON TH, ABRAM AC, SPENGLER DANM, PANJABI MM. Regional variations in the compressive properties of lumbar vertebral trabeculae: Effects of disc degeneration. Spine. 1989;14(9):1012.
201. Liu X, Wu H, Byrne M, Jeffrey J, Krane S, Jaenisch R. A targeted mutation at the known collagenase cleavage site in mouse type I collagen impairs tissue remodeling. The Journal of cell biology. 1995;130(1):227.
202. De Souza S, Pereira HM, Jacchieri S, Brentani R. Collagen/collagenase interaction: does the enzyme mimic the conformation of its own substrate? The FASEB journal. 1996;10(8):927.
203. Karlinsky JB, Snider GL, Franzblau C, Stone P, Hoppin Jr F. In vitro effects of elastase and collagenase on mechanical properties of hamster lungs. The American review of respiratory disease. 1976;113(6):769.
204. Mercer RR, Crapo J. Structural changes in elastic fibers after pancreatic elastase administration in hamsters. Journal of Applied Physiology. 1992;72(4):1473.
205. Morris SM, Stone PJ. Immunocytochemical study of the degradation of elastic fibers in a living extracellular matrix. Journal of Histochemistry & Cytochemistry. 1995;43(11):1145.

206. Nuismer R, Tan S. Constitutive relations of a cracked composite lamina. Journal of Composite Materials. 1988;22(4):306.
207. Gibson RF. Principles of composite material mechanics: McGraw-Hill New York; 1994.
208. Herakovich CT. Mechanics of Fibrous Composites. New York: John Wiley & Sons, Inc.; 1998.
209. Iatridis JC, MacLean JJ, Ryan DA. Mechanical damage to the intervertebral disc annulus fibrosus subjected to tensile loading. Journal of biomechanics. 2005;38(3):557-65.
210. Elliott DM, Setton LA. A linear material model for fiber-induced anisotropy of the anulus fibrosus. Journal of biomechanical engineering. 2000;122:173.
211. O'Connell GD, Guerin HL, Elliott DM. Theoretical and uniaxial experimental evaluation of human annulus fibrosus degeneration. Journal of biomechanical engineering. 2009;131:111007.
212. Wagner DR, Lotz JC. Theoretical model and experimental results for the nonlinear elastic behavior of human annulus fibrosus. Journal of Orthopaedic Research. 2004;22(4):901-9.
213. Hollingsworth NT, Wagner DR. Modeling shear behavior of the annulus fibrosus. Journal of the Mechanical Behavior of Biomedical Materials. 2011.
214. Kulak R, Belytschko T, Schultz A, Galante J. Nonlinear behavior of the human intervertebral disc under axial load. Journal of biomechanics. 1976;9(6):377-86.
215. Guo Z, Peng X, Moran B. A composites-based hyperelastic constitutive model for soft tissue with application to the human annulus fibrosus. Journal of the Mechanics and Physics of Solids. 2006;54(9):1952-71.
216. Peng X, Guo Z, Moran B. An anisotropic hyperelastic constitutive model with fiber-matrix shear interaction for the human annulus fibrosus. Journal of Applied Mechanics. 2006;73:815.
217. Wu HC, Yao RF. Mechanical behavior of the human annulus fibrosus. Journal of biomechanics. 1976;9(1):1-2, IN1, 3-7.
218. Spencer AJM. Constitutive Theory for Strongly Anisotropic Solids. Springer-Verlag New York, Inc, Continuum Theory of the Mechanics of Fibre-Reinforced Composites. 1984:1-32.
219. Nahas MN. Survey of failure and post-failure theories of laminated fiber-reinforced composites. ASTM J Compos Technol Res. 1986;8(4):138-53.
220. Kant T. A critical review and some results of recently developed refined theories of fiber-reinforced laminated composites and sandwiches. Composite Structures. 1993;23(4):293-312.
221. Orifici A, Herszberg I, Thomson R. Review of methodologies for composite material modelling incorporating failure. Composite Structures. 2008;86(1):194-210.
222. Ochoa OO, Reddy JN. Finite element analysis of composite laminates: Springer; 1992.
223. Campbell FC. Structural Composite Materials: ASM International; 2010.
224. Reissner E, Stavsky Y. Bending and stretching of certain types of heterogeneous aeolotropic elastic plates. Journal of Applied Mechanics. 1961;28:402.

225. Nettles AT. Basic mechanics of laminated composite plates. National Aeronautics and Space Administration, Huntsville, AL (United States). George C. Marshall Space Flight Center, 1994.
226. Iatridis JC, Ap Gwynn I. Mechanisms for mechanical damage in the intervertebral disc annulus fibrosus. Journal of biomechanics. 2004;37(8):1165-75.
227. Lempriere B. Poisson's ratio in orthotropic materials. AIAA Journal. 1968;6:2226-7.
228. Ashton J, Halpin JC, Petit PH. Primer on composite materials: analysis: Technomic Stamford, Connecticut; 1969.
229. Vinson JR, Sierakowski RL. The behavior of structures composed of composite materials: Springer; 2002.
230. Pister K, Dong S, editors. Elastic bending of layered plates1959.
231. Duncan NA, Lotz JC. Experimental validation of a porohyperelastic finite element model of the annulus fibrosus. In: Middleton J, Jones ML, Pande GN, eds. Computer Methods in Biomechanics & Biomedical Engineering. New York: Gordon and Breach; 1998. p. 527–34.
232. Eberlein R, Gerhard AH, Christian AJSB. An anisotropic model for annulus tissue and enhanced finite element analyses of intact lumbar disc bodies. Computer Methods in Biomechanics and Biomedical Engineering. 2001;4(3):209-29.
233. Shirazi-Adl SA, Shrivastava SC, Ahmed AM. Stress analysis of the lumbar disc-body unit in compression. A three-dimensional nonlinear finite element study. Spine. 1984;9(2):120.
234. Shirazi-Adl A. On the fibre composite material models of disc annulus--comparison of predicted stresses. Journal of biomechanics. 1989;22(4):357-65.
235. Yin L, Elliott DM. A biphasic and transversely isotropic mechanical model for tendon:: application to mouse tail fascicles in uniaxial tension. Journal of biomechanics. 2004;37(6):907-16.
236. Rao AA, Dumas GA. Influence of material properties on the mechanical behaviour of the L5-S1 intervertebral disc in compression: a nonlinear finite element study. Journal of Biomedical Engineering. 1991;13(2):139-51.
237. Spilker RL. Mechanical behavior of a simple model of an intervertebral disk under compressive loading. Journal of biomechanics. 1980;13(10):895-901.
238. Corigliano A. Formulation, identification and use of interface models in the numerical analysis of composite delamination. International Journal of Solids and Structures. 1993;30(20):2779-811.
239. Chaboche J, Girard R, Schaff A. Numerical analysis of composite systems by using interphase/interface models. Computational Mechanics. 1997;20(1):3-11.
240. Alfano G, Crisfield M. Finite element interface models for the delamination analysis of laminated composites: mechanical and computational issues. International Journal for Numerical Methods in Engineering. 2001;50(7):1701-36.
241. Bambole A, Desai Y. Hybrid-interface element for thick laminated composite plates. Computers & Structures. 2007;85(19-20):1484-99.
242. Aymerich F, Dore F, Priolo P. Prediction of impact-induced delamination in cross-ply composite laminates using cohesive interface elements. Composites Science and Technology. 2008;68(12):2383-90.

243. Richards R, Owen GR, Ap Gwynn I. Low voltage backscattered electron imaging (< 5 kV) using field emission scanning electron microscopy. Scanning Microscopy. 1999;13(1):55-60.
244. Jensen MC, Brant-Zawadzki MN, Obuchowsk Ni, Modic MT, Malkasian D, JS R. MRI imaging of the lumbar spine in people without back pai. N Engl J Med. 1994;331:369-73.
245. Manchikanti L. Epidemiology of low back pain. Pain physician. 2000;3(2):167.
246. Boos N, Weissbach S, Rohrbach H, Weiler C, Spratt KF, Nerlich AG. Classification of age-related changes in lumbar intervertebral discs: 2002 Volvo Award in basic science. Spine. 2002;27(23):2631.
247. Massey CJ, Sarkar S, Marcolongo M. Fourier Transform Infrared Spectroscopy Characterization of the Human Intervertebral Disc. In Preparation. 2011.
248. Kielty CM, Sherratt MJ, Shuttleworth CA. Elastic fibres. J Cell Sci. 2002;115(14):2817-28.
249. Osakabe T, Seyama Y, Yamashita S. Comparison of elisa and hplc for the determination of desmosine or isodesmosine in aortic tissue elastin. Journal of Clinical Laboratory Analysis. 1995;9(5):293-6.
250. Stegemann H. [Microdetermination of hydroxyproline with chloramine-T and p-dimethylaminobenzaldehyde.]. Hoppe Seylers Z Physiol Chem. 1958;311(1-3):41-5.
251. Blumenkrantz N, Asboe-Hansen G. New method for quantitative determination of uronic acids. Analytical Biochemistry. 1973;54(2):484-9.
252. Missirlis YF. Use of enzymolysis techniques in studying the mechanical properties of connective tissue components. J Bioeng. 1977;1(3):215-22.
253. Yin L, Elliott DM. A homogenization model of the annulus fibrosus. Journal of biomechanics. 2005;38(8):1674-84.
254. Ernst CW, Stadnik TW, Peeters E, Breucq C, Osteaux MJC. Prevalence of annular tears and disc herniations on MR images of the cervical spine in symptom free volunteers. European Journal of Radiology. 2005;55(3):409-14.
255. Wilder DG, Pope MH, Frymoyer JW. The biomechanics of lumbar disc herniation and the effect of overload and instability. Journal of spinal disorders. 1988;1(1):16.

VITA

Jessica L Isaacs was born on August 11, 1985 in Chester, Pa. She graduated from Strath Haven High School in Wallingford, Pa in 2002 (after completing her junior year). Jessica was enrolled at the University of Pittsburgh for three semesters pursuing a degree in Mechanical Engineering. She transferred to Widener University in the spring of 2004. Jessica received her B.S. in Mechanical Engineering from Widener University in 2006, receiving the College of Engineering's leadership and service award upon graduation.

In 2006, Jessica joined Drexel University, pursuing a Doctoral degree in Mechanical Engineering & Mechanics. She received her M.S. in Mechanical Engineering from Drexel in 2009. During her tenure at Drexel University, Jessica received the International Travel Award from Drexel (June 2012, Gothenburg, Sweden) as well as working as a freshman engineering design teaching fellow (2008-2009) and was also the event coordinator of a non-profit group called *Buzzing 4 Change*. Also during her time at Drexel, Jessica co-authored the following papers:

- Binetti V, Isaacs JL, Kita K, Fussell G, Marcolongo M, Lowman A. "Characterization of the Behavior of a PVA Hydrogel in Model Conditions: A Comparison of In Vitro and Synthetic Osmotic Models." Journal of Biomedical Materials Research Part B: Applied Biomaterials. ***In preparation.***
- Isaacs JL, Vresilovic E, Sarkar S, Marcolongo M. "Role of Biomolecules on Annulus Fibrosus Mechanics: Effect of Enzymatic Digestion on Micromechanics." Journal of Biomechanics. ***Submitted.***
- Isaacs JL, Gidvani S, Doehring T, Vresilovic E, Marcolongo M. "Characterization of Annulus Fibrosus Micromechanics." The Spine Journal. ***Submitted.***
- Cannella M, Isaacs JL, Allen S, Orana A, Vresilovic E, Marcolongo M. "Nucleus Implantation: The Biomechanics of Augmentation versus Replacement with Varying Degrees of Nucleotomy." The Spine Journal. ***Submitted.***

Jessica is the recipient of a prestigious Fulbright Post-Doctoral award which will enable her to conduct her post-doctoral research at Tel Aviv University under Professor Rami Haj-Ali starting October 2012.